THE UNIVERSITY *of* EDINBURGH

FREQUENCY-BASED STRUCTURAL DAMAGE IDENTIFICATION AND DYNAMIC SYSTEM CHARACTERISATION

Thesis submitted for the degree of
Doctor of Philosophy

Lei Mao

Institute of Infrastructure and Environment
School of Engineering
The University of Edinburgh

April, 2012

Declaration

I hereby declare that

This thesis was composed by myself and the work contained therein was solely the work of the author except otherwise acknowledged in the text.

No part of this thesis has been submitted for any other degree or professional qualification.

Signed:

Lei Mao
University of Edinburgh

Date submitted:

Abstract

This thesis studies structural dynamic system identification in a frequency-based framework. The basic consideration stems from the fact that frequencies may generally be measured with higher accuracy than other pertinent modal data such as mode shapes; however only a limited number of frequencies may be measured in the conventional context of natural frequencies. Being able to measure extra frequencies is a key to the success of a frequency-based method. The main part of the thesis is therefore organised around the involvement of the so-called artificial boundary condition (ABC) frequencies to augment the frequency dataset for general structural damage identification. In essence, the ABC frequencies correspond to the natural frequencies of the system with additional pin supports, but may be extracted from specially configured incomplete frequency response function matrix of the original structure without the need of physically imposing the additional supports.

In the first part of the research, a particular focus is placed on the actual extraction of these ABC frequencies from physical experiments through effective modal testing, data collection, data processing and analysis. The influences of key processes involved in a typical modal experimental procedure, including high-fidelity measurement of the (impact) excitation input, averaging, windowing, and an effective use of post-processing techniques, particularly the Singular Value Decomposition (SVD) technique, are scrutinised in relation to the extraction of the ABC frequencies. With appropriate implementation of testing and data processing procedures, results demonstrate that all one-pin and two-pin ABC frequencies from the first few modes can be extracted with good quality in a laboratory setting, and the accuracy of extracted ABC frequencies is comparable to natural frequencies of corresponding orders.

A comprehensive study is then carried out to investigate the sensitivities of ABC frequencies to damages. Two-pin ABC frequency sensitivity is formulated by extending the expression of anti-resonance sensitivity. On this basis, the mode shape contribution is adopted as a criterion for the selection of more sensitive ABC

frequencies to be employed in detailed parameter identification or finite element model updating procedures. The soundness of using ABC frequencies in structural parameter identification and the effectiveness of the above ABC frequency selection method are subsequently examined through case studies involving laboratory experiments and the corresponding FE model updating. Furthermore, a preliminary study is carried out to examine the possibility of formulating ABC frequency-based damage indicator, herein with an analogy to the mode shape curvature, for direct damage assessment.

As an extended investigation in the general framework of frequency-based dynamic identification, in the last part of the thesis, a complex dynamic system, namely a railway bridge under moving loads & masses, is evaluated with regard to the various frequency characteristics involved. The variation of the natural frequencies of the bridge-moving mass system, as well as the presence of the apparent frequencies from the trainloads, are analysed in detail. Besides simplified theoretical analysis, a computational model is developed to simulate the combined bridge-moving vehicle/train system, where the vehicle mass is coupled with the bridge via surface contact. The model is verified by comparison with field measurement data and theoretical predictions. Parametric studies enable a clear identification of the correlation of the frequency contents between the response and the trainload, and provide new insight into the significance of the so-called driving and dominant frequencies. It is found that much of the dynamic response phenomena, including the resonance effect, may be explained from the view point of the frequency characteristics of the trainload pattern, which is governed primarily by the ratio between the carriage length and the bridge length.

Finally, a resonance severity indicator (the Z-factor) is developed for the assessment of the resonance effect in the railway bridge response when the trainload moves at a resonance speed. Numerical results demonstrate that the proposed methods are effective for the determination of the critical speed and the resonance effects, including the situations where a significant carriage mass is incorporated.

Acknowledgements

The research work presented in this thesis was carried out in the School of Engineering, The University of Edinburgh. The scholarship was funded by the Edinburgh Research Partnership, for which I gratefully acknowledge.

I am deeply grateful of my supervisor Professor Yong Lu for his unreserved guidance, advice and encouragement throughout my PhD study. This research would not have been possible without his continuous support.

I would also like to thank my second supervisor Professor Peter Woodward for all the useful discussions and feedback.

I wish to thank my colleagues and friends at the Institute for Infrastructure and Environment, School of Engineering, for laugher, joy and fruitful discussions. Dr. Zhenguo Tu deserves special mention for helping me a lot at the beginning of my research.

I am grateful to the laboratory technicians at our institute for assisting me in preparing the test structures and conducting the laboratory works.

Finally, and most importantly, I wish to thank my parents, Xuewu Mao and Shixia Cao for their patience, understanding and always being there.

Table of Contents

Figures and Tables

1 Introduction

1.1 Background

Structural Health Monitoring (SHM) is an important subject in today's civil engineering practice. This is particularly true for large scale structures, for example, bridges and high-rise buildings, since severe damages or collapse of these structures will cause not only significant economic loss, but also loss of human lives. Therefore, the interest in the ability to monitor the structures and detect damage at an early stage becomes pervasive.

Among many other approaches to structural health monitoring and damage identification, model-based methods, in particular finite element model updating, have attracted extensive attention in the past few decades. In such a procedure, the errors in a computational finite element model are corrected by minimizing the discrepancy between the measured and simulated response data. The parameters after updating may serve as indicators of the structural or damage conditions, while the updated FE model as a whole can be used for current and future performance predictions for the structure in question. The most commonly used response data for FE model updating are the dynamic modal data, such as natural frequencies, mode shapes, and to a lesser extent damping. However, in practical conditions, the noise contained in the response data, especially in mode shapes, dictate that only a limited amount of such data as acquired from a physical test may be useful in the actual FE model updating operation.

Comparing to the mode shapes, modal frequencies are generally known to be measurable with higher accuracy. However, natural frequencies are not sensitive to local damages. Moreover, since each natural mode has only one frequency, the total number of natural frequencies that can be measured with high quality is always limited. These restrict the ability of using natural frequency alone in relatively

complex problems involving a large number of variable parameters. It would be highly desirable if additional modal frequencies can be generated to enhance the frequency dataset in the general damage detection and structural identification field.

The concept of perturbed natural frequencies of a structure under different (perturbed) boundary conditions opens up a new avenue where more modal frequency data may be generated for damage identification. The development of the theory of the artificial boundary condition (ABC) methodology, by which the above mentioned perturbed natural frequencies of the structure with additional pin supports could be derived from the incomplete FRF matrix measured from the original structure, as well as the subsequent studies on the effectiveness of such frequencies in structural identification, brings the incorporation of the perturbed natural frequencies a significant step closer to practical applications.

Despite the above advancements, the measurement aspects of the perturbed natural frequencies based on the ABC approach, hereinafter called the ABC frequencies, have not been systematically studied. Moreover, since a large variety of perturbed boundary conditions, or the ABC pin supports, may be configured for the ABC frequencies, appropriate criteria for the selection of better (or more sensitive) ABC frequencies for inclusion in the structural identification or FE model updating also need be developed. These pertinent topics have become the main theme of the present research study.

While expanding reliable modal dataset by resorting to additional frequency information is deemed to be crucial for improved structural identification and FE model updating, for complex systems a thorough understanding the frequency characteristics of the structure in a dynamic environment is equally important both for possible extraction of modal information under the dynamic loading and for control/moderation of the dynamic responses. Railway bridges represent such a class of structures whereby the dynamic characteristics under a normal working condition (under moving trains) can differ significantly from a static condition. Comparing to typical road bridges, the dynamic properties of railway bridges, especially those of small to medium sizes, can be strongly affected by the moving mass and the moving

wheel-axle loads from a passing train. Measuring the dynamic properties of a bare railway bridge can be less meaningful without considering such variations in a coupled train-bridge system. On the other hand, extracting pertinent modal information from measured bridge responses under a moving train can be highly complicated, since the trainload excitation can impart a strong presence in the frequency spectrum of the measured railway bridge responses. Therefore, it is necessary to examine the trainload excitation frequencies and their influencing parameters, and how such frequencies affect the measured dynamic response and the frequency spectrum in order to fully understand the dynamic behaviour of the railway bridges, especially the resonance effect.

1.2 Objectives and Scopes

In the research programme, a robust structural identification framework that involves the use of evolutionary optimization algorithms in conjunction with comprehensive dynamic measurement data, will be further developed. In particular, the focus is placed on the development of viable procedures to acquire artificial boundary condition (ABC) frequencies in a real structural and measurement environment.

To facilitate the selection of more sensitive ABC frequencies for structural identification and FE model updating, the sensitivities of the ABC frequencies to damages are investigated. The existing anti-resonance sensitivity expression is extended to formulate the expression of two-pin ABC frequency sensitivities. On this basis, a criterion for selecting ABC frequencies in the finite element model updating is put forward. The effectiveness of proposed methodology is validated using both numerical and experimental studies. Furthermore, based on the relationship between ABC frequencies and mode shapes at the same pin locations, a preliminary investigation is carried out to study the possibility of formulating ABC frequency-based damage index for a direct damage assessment in as similar fashion to the mode shape curvature.

On the dynamic characteristics of railway bridges, a comprehensive evaluation of the frequency characteristics of the railway bridge response under trainloads will be studied, with a special interest in examining the significance and variation trend of key frequency components from the passing trainloads. In the analysis, a finite element model is developed for the study and the influence of the moving mass is incorporated by simulating the vehicle as moving mass and coupling it to the bridge via surface contact.

Based on the frequency characteristics in the bridge and trainload excitation, the resonance of railway bridges is investigated by involving the varying resonance frequency of the bridge-vehicle system. A resonance indicator (Z-factor) is developed to analyze the bridge resonance under trainload with multiple carriages, which represents the rate of the bridge response amplitudes as the consecutive moving loads pass over a bridge at a potential resonance speed. The performance of defined Z-factor in determining the trainload speeds causing the most serious resonance effect is demonstrated using numerical studies.

1.3 Organization of the thesis

Following the Introduction, Chapter 2 presents the literature review. An overview of methods using modal data for structural identification and finite element model updating is given firstly, including representative studies employing modal frequencies, mode shapes and their derivatives, damping ratios, or a combination of them. Limitations of employing these modal data in real structures, especially using mode shape-based information, are described through relevant applications. Researches investigating the possibility of incorporating more reliable modal data, especially anti-resonances and the so-called ABC frequencies, and the effectiveness of these techniques in damage identification and model updating are then summarised and discussed. A general overview of the research studies related to the frequency characteristics in railway bridge response under trainloads is also presented.

In Chapter 3, a comprehensive experimental study on the acquisition of ABC frequencies from physical structures is presented. The focus is placed at devising an effective framework for the entire process of testing, data collection, and data processing such that high quality FRF data can be generated, from which reliable ABC frequencies can then be extracted. In particular, the singular value decomposition (SVD) techniques is examined in details, and its performance in extracting accurate ABC frequencies is validated using results from real tests. In the last section of Chapter 3, a preliminary study is carried out to examine the sensitivities of ABC frequencies to a certain damage using extracted ABC frequencies before and after the existence of damage.

In Chapter 4, the sensitivities of ABC frequencies to structural change (damage) are studied both theoretically and experimentally. The existing anti-resonance frequency sensitivity expression is extended to formulate the expressions for two-pin ABC frequency sensitivities. Based on this, the mode shape contribution is adopted as the criteria for the selection of the ABC frequencies in finite element model updating. With GA as a searching engine, the performance of selected ABC frequencies using the proposed criteria in FE model updating is examined with both numerical and experimental studies. A preliminary investigation into formulating an ABC frequency-based damage indicator for a fast damage assessment is carried out in the last part of this chapter.

Chapter 5 deals with the frequency characteristics of a variant dynamic system, in particular the railway bridges under trainload, with a special interest in examining the significance and the variation trend of key frequency components in the response arising from the trainload. The influence of moving mass is incorporated in the developed finite element model. The study provides systematic insight into the identification of the dynamic characteristics in different bridge-trainload systems and the general trends of the resonance effects.

Chapter 6 focuses on the quantification of the railway bridge resonance under trainload excitations, incorporating the influence of the moving mass. The variation of the critical speed under single moving vehicle with the moving mass is examined

firstly. A theoretical formulation is presented, which leads to the derivation of a resonance indicator, Z-factor, for the determination of the governing resonance speeds and resonance severity considering the moving mass effect. The performance of proposed Z-factor in determining the resonant speeds and resonance severity is verified through numerical studies.

Finally, the conclusions and directions for further research are given in Chapter 7.

2 Literature Review

Structural fault and damage detection is an important subject in civil engineering practice. This is particularly true for large scale structures, for example, bridge and high-rise buildings, as failure of such structures will have great economic and social consequences.

There is a large body of literature on various topics concerning structural damage identification and monitoring. Many vibration-based techniques have been developed to relate dynamic response data, chiefly natural frequency and mode shape information, to structural changes or damage, and these methods have been verified with different degrees of success through numerical or experimental studies. This chapter will aim to provide a focused review of the developments in the area of using modal information for structural identification, thus leading to a conclusion that seeking creatively for enhanced and expanded modal dataset with reliable measurement quality is a key to the success of vibration based techniques in practice. Modal frequencies under perturbed boundary conditions, and the artificial boundary condition (ABC) technique which facilitates the extraction of such frequencies, are deemed to be a potentially viable approach. The last part of this chapter is devoted to a brief review of studies related to identification of the frequency characteristics of railway bridges, which represent a special class of complex dynamic systems.

More specific review of techniques which are closely related to the developments in this thesis will be given in individual chapters.

2.1 Overview of modal data based damage identification techniques

In the last few decades, a variety of techniques have been developed using modal-data for structural identification and damage detection. Most techniques are oriented to construct appropriate damage indices to correlate with the change of the structural parameters. By comparing the indices before and after the damage, the location and degree of the damages could be determined. Modal data considered in these indices typically include natural frequencies, frequency response functions (FRF), mode shapes, modal strain energy, flexibility, as well as damping ratios.

Doebling et al. (1996) presented a comprehensive review of literature concerning the detection, location, and characterization of structural damages via techniques that employ changes in measured structural vibration responses. They categorise these techniques in accordance with the required response data and analysis methods. The response data include natural frequencies, mode shapes and their derivatives, flexibility coefficients, etc. The analysis methods stretch from those using property matrix updating technologies, nonlinear response methods, to artificial intelligence algorithms such as genetic algorithms and neural network. Furthermore, the applications of these structural identification methods in different types of structures, including beams, trusses, plates, shells, bridges, offshore platforms and other large civil structures, were also summarized in this report.

Sohn et al. (2004) extended the above review by reporting new technical developments published between 1996 and 2001 in the field of structural health monitoring (SHM). In particular, techniques using operational evaluation, data fusion and cleaning, feature extraction and information condensation, as well as statistical model development for feature discrimination, were presented.

The above reviews also highlighted several drawbacks in the development of damage identification techniques, including: 1) most methods rely on some sort of analytical models, which by themselves may have uncertainties; 2) many damage-sensitive indices may have difficulties when being applied in real structures, due to various uncertainties and data quality; 3) techniques based on the linearity of models will

have problems dealing with damages of non-linear nature; 4) advancement about interactions between global sensing system and local damage detection methods seems to lag behind.

As modal natural frequencies can generally be extracted with higher accuracy from real measurements, many investigations have been carried out to use natural frequencies for structural damage identification. Vandiver (1975) and Begg et al. (1976) studied the effects of structural damages on natural frequencies using offshore structure as a test bed. Results showed that the removal of member from such a structure could cause 5%-30% changes in modal frequencies, while the cracks have only little effect on modal frequencies. It is interesting to note that in Duggan et al. (1980), where the effects of varying environmental and operating conditions on natural frequencies were studied, the changes in frequencies from removal of a bracing member from an offshore platform could not be distinguished from changes due to varying operational conditions.

Stubbs, et al. (1990), Stubbs and Osegueda (1990) presented a method of using variations in natural frequencies to identify the changes of elemental stiffness. Hearn and Testa (1991) investigated the possibility of using the ratio of changes in natural frequencies from different modes to identify the damages. The basis was that the structural damage would not cause same changes to all elements of the structure, and the changes in natural frequencies could be expressed as a function of only damaged stiffness parameters. Leutenegger (1999) pointed out that, when the natural frequencies are employed to identify cracks, the non-linear effect caused by crack opening and closing should be included in the model.

Mroz and Lekszynski (2000) carried out a sensitivity analysis to determine the location of additional masses and the support locations using natural frequencies. Gomes and Silva (2008) compared the performance of natural frequencies in identifying the damages using modal sensitivity technique and genetic algorithm (GA). Results demonstrate that both methods can identify the damage location but fail to quantify the damage extent, even in a single damage scenario.

Zak et al. (1999) investigated the natural frequency changes due to a kind of indirect stiffness change, namely in a composite plate due to the delamination damages. Results demonstrated that the changes in natural frequencies could be identified clearly by varying delamination length and position. However, it was found that in some damage scenarios, additional vibration modes would be observed, which may cause difficulty when matching analytical and experimental natural frequencies.

Previous experiences of employing natural frequencies for damage identification have confirmed that natural frequencies are not sensitive to the local damages. Moreover, the natural frequencies may be susceptible to environmental changes such as temperature, which further restrict the applicability of natural frequency-based model updating techniques.

Numerous studies have been reported using mode shape information for damage identification, including mode shapes, mode shape derivatives and modal strain energy, with or without consideration of natural frequencies. Some examples include West, 1984; Yuen, 1985; Fox, 1992; Kim et al. 1992; Srinivasan and Kot, 1992; Ahmadian et al. 1997; Osegueda et al. 1992; Natke, 1997, Doebling and Farrar, 1997, et al. Among other mode shape derivatives, mode shape curvature has attracted most attention for identifying the structural damages. Pandey et al. (1991) suggested that the absolute mode shape curvature changes could be employed as an indicator for damages in a beam structure. Maeck and De Roeck (1999) applied mode shape curvature method in studying the Z24 pre-stressed concrete bridge in Switzerland and a reinforced concrete beam as the test beds.

Carrasco (1997) studied a method using changes in modal strain energy to identify the damage in truss model. Worden and Fieller (1999) used the modal strain energy to identify damage (simulated by cuts) in plate structures.

The possibility of extracting mode shape information for damage identification using auto-regressive moving average (ARMA) predication model have been studied by Garcia et al. (1998), Garcia and Osegueda (1999).

Wang, et al. (1997) employed a scaled model for a single span plate girder bridge and carry out modal analysis of the model. The vibration of the structures was excited using an impact hammer, and 24 accelerometers were employed to record the dynamic response. In the study, the damage was created in a girder flange, and the first 6 mode shape information before and after the damage were utilized to form the damage index. Results showed that damage could be successfully identified with developed damage index. However, this damage index could not identify multiple damages accurately.

Koh and Dyke (2007) presented the use of correlation-based damage detection methods and GA in long-span, cable-stayed bridges. This method was based on the multiple damage location assurance criteria (MDLAC), which gave the relationship between damage and the stiffness variation in the elements, this relationship could be obtained using the sensitivity matrix including natural frequencies. The locations of damage could be determined by iteratively searching for the maximum MDLAC value, which served as an indication that the damage correlated well with the stiffness changes in specific elements. The results demonstrated that the correlation-based method could successfully locate the multiple damage locations, but usually could not determine the damage severities. Moreover, the authors pointed out that the success of this method heavily depends on the involvement of particular sets of natural frequencies which were sensitive to the damage scenario, rather than simply the number of modes employed.

Gandomi et al. (2008) summarized mode shape-based technologies for damage identification. These methods were categorized based on the employed modal data, including mode shape changes and mode shape derivative changes. The authors concluded that mode shape curvature and modal strain energy were more sensitive to local changes in the structures, thus more suitable to detect structural faults. However, mode shapes are prone to measurement errors, and only limited number of mode shapes could be measured with good quality from the structures. Such issues could limit considerably the applicability of mode shape-based methods in practice.

As examples of using other forms of modal information, Modena, et al. (1999) studied the damping effect on the visually undetectable cracks in pre-cast reinforced concrete structures, and found that larger damping changes could be caused due to the cracks, while smaller changes could be observed in natural frequencies and lower order mode shapes. Agneni, et al. (2000) examined a damage detection method using measured frequency response functions (FRFs). In the method, the mass and stiffness matrices were obtained from the FRFs to identify the damages. However, it was found that when FRFs were obtained from time history signals, the truncation effect due to windowing may result in changes in mass and stiffness matrices, which may give rise to misleading results.

In parallel to the development of modal-data based damage indices, finite element model updating has become a widely employed vehicle for comprehensive structural parameter identification and damage assessment. In a typical FE model updating procedure, variable model parameters such as stiffness and damping of individual elements are updated so that the computed "responses" using the FE model, most commonly the natural frequencies and mode shapes, match the measured counterparts from the actual structure. In terms of the searching techniques, more recent years have seen a general shift from the traditional iterative-based methodology to more robust artificial intelligence computation techniques such as genetic algorithms.

Among numerous studies, Ruotolo and Surace (1997) compared the performance of genetic algorithm and simulated annealing in identifying multiple cracks in beam structures. The results demonstrate that both searching methods can successfully detect the multiple damage locations. Stubbs, et al. (1999) applied FE model updating on a four-lane highway bridge spanning Interstate 40. The vibration of the bridge was measured with 26 sensors on the deck and 4 sensors placed on the column. After field tests, modal parameters were extracted from measurement data, including natural frequencies and mode shapes of the first five modes. A FE model was developed based on data from the as-built plans of the bridge, and natural frequencies and mode shapes from the FE model were then compared to those from

field tests. Their results indicated that the damage positions as identified from the model updating match the surface crack patterns inspected visually.

Perera and Ruiz (2008) described a representative two-stage FE updating procedure for large-scale structures. In the first stage, the approximate damage locations were determined, while in the second stage the specific damage members and extents were identified by considering only the possible damage regions from the first stage. In their procedure, two objective functions, including the modal flexibilities and a damage location criterion which were dependent on the natural frequencies and mode shapes, were used in the Strength Pareto Genetic Algorithm (SPGA) to detect the damages. The method was applied to a continuous beam and a frame with numerical simulations and to the real I-40 bridge. The results showed that this method could determine the location and extent of the damage in the numerical study, even with a 5% noise influence in the modal data. In the real bridge application, this method also exhibited a robust and reliable performance.

Mehrjoo and Khaji (2008) presented a method to estimate the damages in the joints of truss bridge structures using a back-propagation neural network. In this method, the truss bridge was divided into several substructures and only the substructure with most joints was updated, thus reducing the number of output in the neural network. The first few natural frequencies and mode shapes were selected as inputs and the outputs contained the damage severity of the joints. This method was applied on both simple model truss and real truss bridge.

Generally speaking, the current state of the art in the vibration-based parameter identification and FE model updating indicates that the success of a particular technique will almost inevitably depend upon the size and quality of measurable modal-information related response dataset. Many existing techniques assume an ample supply of accurate modal parameters, especially mode shapes, for a mathematical implementation of an inverse solution. Such techniques seldom have a proven application record, due apparently to the fact that in a real application environment mode shapes are unlikely to be measured to a desired accuracy. Next

some studies related to the limitation of measured mode shape information in FE model updating will be reviewed and discussed.

2.2 Challenges in modal-data based structural damage identification techniques

Studies in the literatures have demonstrated that modal parameters may be employed with a variety of techniques for structural parameter identification, including FE model updating. The most commonly used modal data include natural frequencies, mode shape-based information, and to a lesser extent damping. However, when these measured modal parameters are employed in real applications, measurement errors and environmental noises dictate that only a limited amount of such data may be reliably derived from a physical test. This is particularly true for mode-shape data, as noted in a review article by Mottershead and Friswell (1993) among many other studies on modal data measurement errors (e.g., Gandomi et al, 2008; Yan et a. 2007). It has been observed that errors in elements of a mode shape vector can be as much as 20%, and such level of errors could well overshadow the changes in mode shapes due to some significant damage. Recent advancement in the measurement and data communication systems makes it possible to measure mode shapes at a large number of locations, but this still can not resolve issues with high errors in the individual mode shape components.

Jones and Turcotte (2002) elaborated the disadvantages of employing mode shape information for model updating in physical structures. Apart from errors contained in the measured mode shape date, which according to their experiences could be of order of 10%, the use of mode shape expansion or FE model reduction, which is usually necessary as the mode shape could not be measured at all DOFs of a system, could introduce extra errors. All these factors would affect the model updating results.

The limitations with the use of mode shape information have been evidenced in many studies on physical model or real structures. For example, Ratcliffe (1997)

presented a mode shape-based damage index and applied it in a physical beam structure. The method utilized mode shape from damaged beam to calculate Laplacian function, which identified the damage in a similar fashion to mode shape curvatures, but only used the damaged model, and damage locations could be indicated by the peaks in the Laplacian curve. A steel beam with dimension of $0.6\text{m} \times 0.25\text{m} \times 0.004\text{m}$ was employed for the investigation and the damage was simulated with the cut at the middle position, which produced about 30% stiffness reduction of the beam. 20×7 measurement points were used along the length and width to obtain mode shapes with impact testing method. The first five natural frequencies and damping ratios were extracted to identify the damage effect, while only the first two measured mode shapes could be obtained reasonably and employed to calculate Laplacian function and identify the damage position. Results showed that only the first mode shape could yield reasonable results.

Law et al. (1998) observed the limitations of using experimental mode shapes in a study involving the modal strain energy method for damage identification, In the study, the mode shape data were measured at selected DOFs of the frame structure, and a mode shape expansion technique was applied to the incomplete mode shape data. By using 10 sensors to record the dynamic responses of the frame structure, the first 6 natural frequencies and mode shapes before and after the damages could be extracted. By comparing to the numerical results from the FE model, it was observed that the obtained 6 natural frequencies matched very well with those from FE model, whereas only the mode shapes from the lowest two modes could be measured with good quality, even though the experimental mode shapes from the first 6 modes looked reasonable.

Qiao et al. (2007) utilized some most advanced instrumentations, including the scanning laser vibrometer (SLV), PZT actuators and polyvinylidenefluoride (PVDF) sensors, to measure mode shapes and identify damage positions using mode shape curvature-based techniques. An E-glass/epoxy composite plate with embedded delamination was used as the test structure. The plate had dimensions of $0.6069\text{m} \times 0.3048\text{m} \times 0.00508\text{m}$ and was divided into a measured grid of 74×46 for SLV+PZT and 17×12 for PVDF+PZT. The first five mode shapes were measured,

but in the study only the higher three measured mode shapes were employed, whereas the first two mode shapes contained more noises. Moreover, results demonstrated that due to a coarse mesh of PVDF, the measured mode shapes from SLV gave better results.

In summary, experiences from laboratory or field tests have consistently confirmed that measurement of mode shapes could normally produce only a limited number (usually the first two or three) of modes with a high quality. Even with advanced measurement systems, it is still difficult to get rid of the measurement errors and increase substantially the number of reliable mode shapes. In contrast, it is generally recognised that natural frequencies can be measured with high quality from physical tests (Mottershead and Friswell, 1993). However, natural frequencies are not sensitive to local damages. Moreover, since each natural mode has only one frequency, the total number of natural frequencies that can be measured with high quality is always limited. These restrict the ability of using natural frequency alone in relatively complex problems involving a large number of variable parameters. It would be highly desirable if additional modal frequencies can be generated to enhance the frequency dataset in the general damage detection and structural identification field.

2.3 Research studies on expanding modal dataset for structural damage identification and FRF processing

In attempt to expand the modal dataset, especially the frequencies, some special modal data have been investigated for their measurability and effectiveness in structural identification applications. These include the anti-resonances from frequency response function curves (FRFs) and the artificial boundary condition (ABC) frequencies.

Lallement and co-workers (1992, 1998) investigated the possibility of using zeros (anti-resonances) from FRFs for damage identification. The zeros from FRFs were deemed to contain much more useful information; and moreover, these zeros occur at

different frequencies for different measurement points, therefore there can be much more anti-resonances than resonances (natural frequencies).

Mottershead (1998) further investigated the information contained in the anti-resonances from FRFs. In the study, the sensitivity of the anti-resonances was derived as a linear combination of the natural frequency sensitivities and mode shape sensitivities. With numerical studies, it was observed that the sensitivity of an anti-resonance was pre-dominantly affected by the sensitivities of the nearest natural frequencies and mode shapes.

Ambrogio and Fregolent (2000) studied the effectiveness of anti-resonances in damage identification. It was found that anti-resonances from transfer FRFs (force and response are not at the same position) were not suitable for model updating purposes, as anti-resonances in such transfer FRFs would be greatly altered by small changes in the structural model, which may cause mismatch between experimental and analytical data, and thus giving rise to misleading results. On the other hand, the changes in the driving-point FRFs (force and response are at the same position) were of the same order as changes in natural frequencies. Thus it was concluded that anti-resonances from driving-point FRFs were more appropriate for damage identification.

The application of anti-resonances in damage identification has also been investigated by Jones and Turcotte (2002). In the study, a vertically erected 6m truss structure was employed for investigation, and the damages were created by removing diagonal elements or reducing half of the cross sectional area of the diagonal elements. The penalty method using sensitivity matrix was utilized to update the model. Two groups of modal data were used to form the sensitivity matrix, including natural frequencies alone, and natural frequencies plus anti-resonances. Results demonstrated that with natural frequencies and anti-resonances, remarkable improvements could be observed from the updating results.

The concept of perturbed natural frequencies of a structure under different (perturbed) boundary condition opens up another avenue where more modal data may be generated for damage identification (Li et al. 1995). Gordis (1996, 1999)

further demonstrated that the natural frequencies of a structure with additional pin supports at certain locations could be derived from the incomplete FRF matrix measured from the original structure. This eliminated the need of physically imposing additional supports, which would be almost impossible to realise in an actual structure case. The term of “artificial boundary condition (ABC)" reflects the fact that, although the frequencies thus derived are equivalent to the natural frequencies of the perturbed system, the perturbed boundary conditions need not be actually imposed.

It should be mentioned that when only one pin is added on the structure, the ABC frequencies degenerate to the anti-resonances (zeros) in the driving-point FRF curves of original structure.

The potential effectiveness of using ABC frequencies in finite element mode updating of frame structures has been investigated numerically by Tu and Lu (2008). The employed ABC frequencies included one-pin and two-pin ABC frequencies. Several frame structures of different configurations were created for the study, and different numbers of stiffness parameters were selected for updating. Two groups of modal data were used as response dataset, namely natural frequencies alone, and natural frequencies plus ABC frequencies. Results demonstrated that when ABC frequencies were added to the dataset, remarkable improvement in the updating results could be observed.

It is apparent that there could be a variety of different combinations (locations of the artificial pins) for the ABC frequencies, especially when more than one ABC pins are involved. However, it is generally established that, in an FE model updating procedure, usually the amount of modal data to be employed should be about 2-3 times of the number of unknown parameters to be identified (Friswell et al. 1998, He and Fu, 2001). This is because there always exists a certain level of measurement errors in the modal data, consequently using too many modal data could end up with a decreased degree of accuracy in the updating results. Consequently the selection of the ABC pin locations for the generation of ABC frequencies becomes a pertinent topic. However, so far there is only limited research in this regard.

In the context of anti-resonances, Friswell and Mottershead (1995) presented a trail-and-error approach, which employed the condition number of generalized sensitivity matrix to determine the anti-resonances for FE model updating. Hanson et al. (2007) proposed a method of evaluating the effect of anti-resonances in damage identification using a simplified 2-DOF representation of a beam system. Based on the formulation of anti-resonance sensitivity, the contribution of mode shape sensitivity could be calculated using the ratios between sensitivities of mode shapes and corresponding anti-resonance sensitivity. This ratio could be employed as the criterion to evaluate the effectiveness of anti-resonances in FE model updating. In the framework of ABC frequencies, Tu and Lu (2008) presented a method of selecting extra pin locations for ABC frequencies. In the method, the suitable pin locations were determined by searching all possible DOFs of the structures using a genetic algorithm based optimisation scheme, with the objective function being defined based on a sensitivity analysis.

On the measurability and measurement accuracy of ABC frequencies from physical tests, some preliminary studies were performed (Lu and Tu, 2008). It was generally observed that using the typical impact hammer testing method, one-pin ABC frequencies (anti-resonances of FRFs) from the lowest few modes could be obtained with acceptable accuracy, whereas identification of ABC frequencies in two-pin configurations could be problematic due to spurious peaks. Improved testing and data processing techniques would be required, particularly on the processing of the FRF curves as the extraction of ABC frequencies requires the inversion of the measured FRF matrix, and this poses significantly increased demand on the quality of the FRF curves.

Different curve fitting methods have been developed for improving FRF quality. Richardson and Formenti (1982) presented a rational fraction polynomial technique for improving FRF data. In the method, the FRF was expressed in a rational fraction form using a ratio of two polynomials, and unknown coefficients in numerator and denominator polynomials can be solved within single step. Moreover, the orthogonal polynomial was employed in the method to reduce ill-conditioning and computation costs based on previous results (Forsythe, 1957).

However, there exist several drawbacks in the above technique, for instance poor fitting in the low frequency range, inaccurate mode shape estimation, etc. In attempt to rectify these drawbacks, modifications to the above method have been presented. For example, Carcaterra and Ambrogio (1995) proposed a rational fraction polynomial technique based on an iterative procedure. By using iterative searching, the fitting error can be minimized efficiently. It should be mentioned that in order to apply this iterative technique, the number of modes in a given frequency range should be known in advance, and the method can only be applied reliably over a limited frequency range. Moreover, the anti-resonance information may get distorted with this method.

Another widely used technique to eliminate the noise influence in FRF data is the singular value decomposition (SVD) technique, and the effects of this method have been studied extensively (e.g. Tufts and Kumerasan, 1982; Juang and Pappa, 1986; Allemang and Brown, 1998). The technique is based on Eckart-Young theory, which is employed to estimate the best lower rank of a given matrix. In the method, the singular values can be obtained by decomposing the given matrix, and the rank of the matrix can be determined using the lowest non-zero singular value.

Continued research has been conducted to further improve the SVD technique in better eliminating the noise influence. Tufts et al. (1982) studied the possibility of estimating signals in the noisy data. Cadzow (1982) presented a method to extract the system parameters in the noisy data using SVD technique. Similar research was carried out by Braun and Ram (1987). Cakar and Sanliturk (2002) proposed a procedure of employing the SVD technique to eliminate the noise influence in FRF data. In the procedure, the measured FRF data were employed to form a FRF matrix, then the FRF matrix is decomposed using SVD technique, and subsequently the singular values representing noise components can be removed from singular value matrix using a pre-defined noise threshold. The noise-free FRF matrix can be re-formed using the singular value matrix after deleting the noise components. Numerical studies were carried out to validate the effectiveness of the proposed procedure in eliminating additive noise in FRF data.

The above procedure was further updated by Sanliturk and Cakar (2005). Compared to FRF matrix used in the above procedure, the modified procedure can be applied to a single curve of FRF data by constructing the Hankel matrix from the FRF data. The effectiveness of such a SVD technique in eliminating multiplicative noise was investigated by defining a proper threshold for the noise removal.

2.4 Studies on bridge dynamic characteristics under passing trains

When damage identification techniques are applied to real structures, complications can arise from a variety of sources. Apart from complexities and uncertainties which are inherent with the physical structures, variable dynamic characteristics due to environmental (e.g. temperature and humidity) and mechanical loading conditions pose further challenges. One representative class of structures whose dynamic characteristics may be altered significantly under working loads is railway bridges. In a broader context of structural identification and FE model updating, understanding the frequency characteristics railway bridges in a dynamic environment (under moving trains) can be particularly important when the outcome is to be employed for identification of the in-service parameters and prediction of the dynamic responses. In this respect, a study on the varying frequency characteristics, herein in railway bridges under moving trains, is pertinent to a comprehensive evaluation of structural identification based on frequencies.

An overview of the relevant researches in the field of bridge dynamics including the effect of passing trains, particularly concerning the frequency characteristic, is given in the following. More specific review of the relevant techniques will be provided later in the respective chapters.

Generally speaking, in order to investigate bridge responses to a moving train, the effect of the moving train should be properly modelled. Depending on the main purpose of the analysis, different models may be used to simulate the train, for

example moving load model, moving mass model, sprung mass model, and some more sophisticated train dynamics models.

Early research on the bridge dynamic response due to moving vehicles may be traced back to Stokes (1849) and Willis (1849). These works have been credited as the first to bring the vehicle impacts to the bridge designs. They investigated the collapse of the Chaster Rail Bridge in England in 1847, which was the first case of railway bridge collapse in history, and modelled the vehicle as a concentrated moving load without considering the inertial effect.

A comprehensive review of the bridge-train/vehicle interaction study was presented by Yang et al. (2004). The review classifies the research on bridge dynamic responses before the 1940s as using mainly analytical or approximate solutions for simple and fundamental problems, for example Timoshenko (1922), Jeffcott (1929), Inglis(1934) and Lowan (1935). After that, analysis with more realistic bridge and vehicle models became possible with the advent of digital computers, such as analysis based on moving load model by Timoshenko and Young (1955) and Biggs (1964).

In the last few decades, there is a tendency of increasingly resorting to more realistic vehicle models to account for the vehicle effect in bridge dynamic response. Lou (2007) developed a train-track-bridge model with the finite element method to analyse the detailed effects of different vehicle models on the maximum dynamic responses of the train, rail track and the bridge. In the model, the train was simulated with a series of identical vehicles, and each vehicle consists of a mass-spring-damper system including a car body, two bogie frames, four wheel-sets and two stage suspension system.

Majka and Hartnett (2008) investigated the effects of different parameters, such as speed parameter, frequency parameter, mass parameter and span parameter in bridge dynamic response using a so-called Dynamic Bridge-Train Interaction (DBTI) model. The model included multi-body train and bridge subsystems.

In the study by Liu et al. (2009), the train was modelled with a varying degree of sophistication to allow for a representation of the dynamic train-bridge interaction with different train models. Several parameters, including the vehicle-to-bridge mass ratio, the vehicle-to-bridge natural frequency ratio, the train speed, and the damping of the bridge, were incorporated.

While sophisticated or high-fidelity models may be advantageous for the analysis of the detailed dynamic response in the complex train-bridge system, they may not always be necessary or instrumental for examining the primary dynamic characteristics. As a matter of fact, inclusion of too many parameters, some of which are of secondary effect, could overshadow the evaluation on the key variables. For this reason, relative simple models which accommodate only key features as moving load and moving mass have been employed effectively in some recent studies to identify the key parameters governing the dynamic response of the bridge.

Li and Su (1999) used a model in which the train was first modelled as a series of moving loads to study the dynamic response of a girder bridge under high-speed trains. As a general observation, it was found that the bridge resonant vibration occurs when the frequencies of the moving loads were close to the bridge resonance frequencies. Using the model they also investigated the effect of L_b/v (with L_b being the bridge span and v is the train speed), the number of moving loads and the damping ratio on the bridge resonant vibration. Subsequently, a more realistic train model incorporating the moving mass was employed. Resonances were found to be at similar speeds as those using only the moving load model, but the bridge response amplitudes were different. This indicated that the absolute bridge response would be dependent upon the amount of vehicle mass.

Yau (2001) further investigated the resonant vibration of a continuous bridge using a model in which the train was modelled as a series of moving loads. Results showed that with increased number of bridge spans, the number of main resonant peaks in the response of the continuous bridge would increase, but the bridge resonant response amplitude would decrease.

Xia et al. (2006) studied the bridge resonant vibrations under different loading scenarios. In addition to the basic parameters of d/v (with d being the distance between two consecutive vehicles) and L_b/v, the periodical action of sway forces from running vehicles due to rail irregularities was also considered as a factor. Furthermore, the time histories of load series for a train passing through bridges with different lengths were illustrated, to indicate that the trainloads applied to the bridge may exhibit different shapes.

Although several key parameters affecting the bridge response may be investigated using a simple moving load model, due to the ignorance of the vehicle/carriage mass, the moving load model will become deficient when the inertial effect due to the mass of a moving train tends to be significant, and this can occur due to high train speed and/or relatively large train mass.

When the moving mass enters into play, one immediate effect is the changing resonant frequency of the responding bridge, and the amount of variation will depend upon the carriage-to-bridge mass ratio. Li et al. (2003) investigated the variation of bridge natural frequency during the passage of moving train. In the study, both numerical integration method and approximate formula were employed to solve the bridge-train dynamic interaction. As expected, results showed that with passage of the moving train, the resonant frequency would vary in a periodic fashion. The variation of the resonant frequency in turn influenced the resonant vibration and the dynamic response in general.

With regard to the possible effect of the contact area of a moving mass on the bridge response, Esmailzadeh and Ghorashi (1995) observed that an increased length of the mass block could lead to sharp changes of the slope of the deflection curves, causing additional dynamic effect. Furthermore, by comparing the results from a moving mass model with a moving force model, it was found that the maximum deflection from the moving mass model was larger, and the speed causing the largest beam deflection, i.e., the “critical speed”, became smaller in the moving mass model.

The critical speed is another subject of major interest concerning the bridge dynamic response to moving trainload. The existing formulation usually relates the critical

speed to the fundamental natural frequency of the bridge (Fryba, 1999, Yang et al. 2004, etc.), and this apparently is applicable to the cases where the moving mass is negligible. Whereas the introduction of a moving mass generally reduces the critical speed, Dehestani, et al.(2009) demonstrated that the critical speed increases with stiffening the support constraints. These studies provide general understanding with regard to the potential effect of the moving mass on the bridge response. However, more systematic information about the quantification of such effect on the varying dynamic system properties, particularly the resonant frequencies, is still required.

With regard to the frequency contents in the bridge response under a moving train, Yang and Lin (2004) pointed out that the way by which bridge-train system interact with each other was mainly determined by the frequencies from two subsystems. Several researches have been devoted to investigate this problem. Paultre et al. (1995) analyzed the bridge dynamic response due to passing trains, and pointed out that certain peaks in the power spectral density (PSD) curves corresponded to the bridge-train interaction and did not represent the bridge natural frequencies. They argued that the contact force acting on the bridge was caused by the passing train and thus certain frequency components pertaining to the trainload excitation would inevitably be presented in the bridge response. Wu and Yang (2003) studied the response of a moving vehicle, and found that the vibration of bridge caused by the passing vehicle contained significant frequencies related to the vehicle speed and the vehicle length, i.e., d/v, which echoed the finding by Bolotin (1964).

Yang and Lin (2004) investigated the response measured in a moving vehicle and characterised the corresponding frequencies into the following groups, a) driving frequencies, which are associated with the duration of a vehicle passing over the bridge, b) vehicle natural frequencies, and c) bridge natural frequencies. In Yang and Chang (2009) the authors further investigated the effects of various parameters on the frequency contents in the vehicle response using a sprung mass model, and identified key influencing parameters, including the vehicle speed, bridge and vehicle length ratio, etc. On the other hand, studies by Ju and Lin (2003) and Fryba (2001) indicated that the so-called dominant frequencies, which originate from repeated wheel-axle loads (hence are related to the time interval between two

consecutive wheel-axle loads, could play an important role in the bridge dynamic response. If the first few dominant frequencies are close to the first few natural frequencies of the bridge, significant resonance may be produced. In this respect, the velocity of the passing train should ideally be regulated to avoid significant resonance effect due to the trainload dominant frequencies. It should be pointed out that, without more specific information on the orders of the frequencies involved, such a general guide would be of limited practical value. This is a topic which will be treated in detail later in this thesis.

According to above results, numerous publications exist in the literature regarding the bridge dynamic response and the train–bridge interactions. It is well recognised that the dynamic response of a railway bridge is influenced by a combination of factors, chiefly the bridge natural frequency, train speed, and bridge and carriage lengths. However, the intrinsic relationships among these parameters in terms of their effect on the bridge response have generally not been presented in a dynamics-explicit manner. It is not straightforward to implement a general recommendation, for instance resonance could take place under certain normalized speeds, without specific information with regard to the magnitude and the reasons behind the trend of variations. This intrinsic relationship will be further investigated in this study using comprehensive evaluation of the frequency characteristics of a railway bridge response under trainload.

3 Experimental study of extraction of ABC frequencies from modal testing

3.1 Introduction

The current state of the art in vibration based parameter identification and FE model updating, as discussed in the literature review (Chapter 2), indicates that the success of a particular technique will almost inevitably depend upon the size and quality of measurable modal-information related response dataset. The inclusion of anti-resonances and ABC frequencies in modal dataset can greatly improve the FE model updating results in numerical studies, provided that comparable measurement accuracy as in natural frequency data can be achieved.

However, anti-resonance and ABC frequencies have distinctive features from natural frequencies; successful extraction of such frequencies requires the availability of high quality frequency response function (FRF) curves not just in regions around the resonance peaks, but more so in regions of the anti-resonance "valleys", for which there exist only limited knowledge and experience in the literature with regard to the specific characteristics and the pertinent data processing demands. Therefore, in order to bring the utilization of such frequency data a significant step further towards applications in real practice, it is deemed to be of critical importance to investigate systematically into the experimental aspects of extracting such frequencies from physical tests.

This chapter is devoted to a comprehensive experimental study on the extraction of ABC frequencies from real measurements. To minimise complications from structural uncertainties, which are beyond the scope of the present investigation, the experiments have been conducted on laboratory models, and the test method is confined to the conventional modal testing. The focus has been placed at devising an effective framework for the entire process of testing, data collection, and data

processing such that high quality FRF data can be generated, from which reliable ABC frequencies can then be extracted. In particular, the singular value decomposition (SVD) technique is examined in detail, and its effectiveness and appropriate implementation are investigated in close association with the underlining characteristics of the FRF curves around the anti-resonance regions. It will be shown that, with appropriate modal testing and data processing techniques, reliable ABC frequencies in a variety of artificial boundary condition configurations can be extracted for parameter identification and damage detection purposes. Furthermore, experimental ABC frequencies before and after the introduction of certain damage will be extracted and compared in order to illustrate the general sensitivity of such frequencies to damage.

3.2 Brief overview of the theory

Modal frequencies of a give structure with however added (perturbed) supports provide extended modal information which can be incorporated to enhance the response dataset in a parameter identification, particularly a finite element model updating procedure. The practicality of such an idea is hindered by the fact that imposing actual added supports on a real structure is not normally feasible. A breakthrough for the potential implementation of the idea was brought about when Gordis (1996, 1999) presented a theoretical approach of deriving artificial boundary condition (as opposed to the actual physical boundary) frequencies from an incomplete frequency response function matrix of a structure. By partitioning between the measured and unmeasured coordinate (DOF) sets, the steady state response of a linear system at a forcing frequency ω (rad/s) can be written as:

$$\left(\begin{bmatrix} \mathbf{k}_{mm} & \mathbf{k}_{mo} \\ \mathbf{k}_{om} & \mathbf{k}_{oo} \end{bmatrix} - \omega^2 \begin{bmatrix} \mathbf{m}_{mm} & \mathbf{m}_{mo} \\ \mathbf{m}_{om} & \mathbf{m}_{oo} \end{bmatrix} \right) \begin{Bmatrix} \mathbf{x}_m \\ \mathbf{x}_o \end{Bmatrix} = \begin{Bmatrix} \mathbf{f}_m \\ \mathbf{f}_o \end{Bmatrix} \tag{3.1}$$

where $\mathbf{k}$ and $\mathbf{m}$ are stiffness and mass matrices, $\mathbf{x}$ and $\mathbf{f}$ are vectors of generalized response and excitation amplitudes, respectively. Subscript '*m*' represents measured coordinates or DOFs and subscript '*o*' refers to the unmeasured DOFs (‘omitted

coordinate set' or OCS). Clearly the OCS is effectively a reduced system, where all the measured DOFs are restrained or pinned to the ground.

Introducing the impedance matrix, $\mathbf{Z} = \mathbf{k} - \omega^2 \mathbf{m}$, Eq. (3.1) can be re-written as:

$$\begin{bmatrix} \mathbf{Z}_{mm} & \mathbf{Z}_{mo} \\ \mathbf{Z}_{om} & \mathbf{Z}_{oo} \end{bmatrix} \begin{Bmatrix} \mathbf{x}_m \\ \mathbf{x}_o \end{Bmatrix} = \begin{Bmatrix} \mathbf{f}_m \\ \mathbf{f}_o \end{Bmatrix} \tag{3.2}$$

Assuming no excitations are imposed on the omitted coordinates, i.e., $f_o=0$, from Eq. (3.2) we can get:

$$(\mathbf{f}_m) = \left(\mathbf{Z}_{mm} - \mathbf{Z}_{mo}\mathbf{Z}_{oo}^{-1}\mathbf{Z}_{om}\right)(\mathbf{x}_m) \tag{3.3}$$

Re-arranging:

$$\frac{\mathbf{f}_m}{\mathbf{x}_m} = \mathbf{H}_{mm}^{-1} = \left(\mathbf{Z}_{mm} - \mathbf{Z}_{mo}\mathbf{Z}_{oo}^{-1}\mathbf{Z}_{om}\right) \tag{3.4}$$

where $\mathbf{H}_{mm} = \mathbf{x}_m / \mathbf{f}_m$ is the incomplete frequency response function (FRF) matrix measured from the existing structure as it is.

Eq. (3.4) establishes the inherent relationship between the inverse of $\mathbf{H}_{mm}$ and the dynamic characteristics of the OCS represented by $\mathbf{Z}_{oo}$, such that at the natural frequencies of the OCS, $\mathbf{Z}_{oo}^{-1}$ is singular, so $\mathbf{H}_{mm}^{-1}$ is also singular, and vice versa. That is to say, by identifying the singularities (resonance frequencies) from the elements of $\mathbf{H}_{mm}^{-1}$, one can determine the natural frequencies of the OCS, i.e., the frequencies of the structure as if it was physically pinned at the measured DOFs. This can be more conveniently illustrated using an example shown in Fig. 3.1, where (a) shows the actual simply-supported beam, (b) depicts a perturbed boundary condition with two additional pin supports at "i" and "j", for which the modal frequencies are to be evaluated, and (c) shows the actual measurement settings. Instead of physically imposing the two additional pins as indicated in Fig. 3.1(b), the modal frequencies

under such a boundary condition can be determined by measuring the (2x2) FRF matrix on the original beam at points "i" and "j" shown in Fig 3.1(c), and subsequently identifying the singularities from the inverted FRF matrix. The term of "artificial" reflects the fact that the modal frequencies under a particular altered boundary condition are determined by particular FRF measurements from the original structure, without the need of physically imposing the required additional supports.

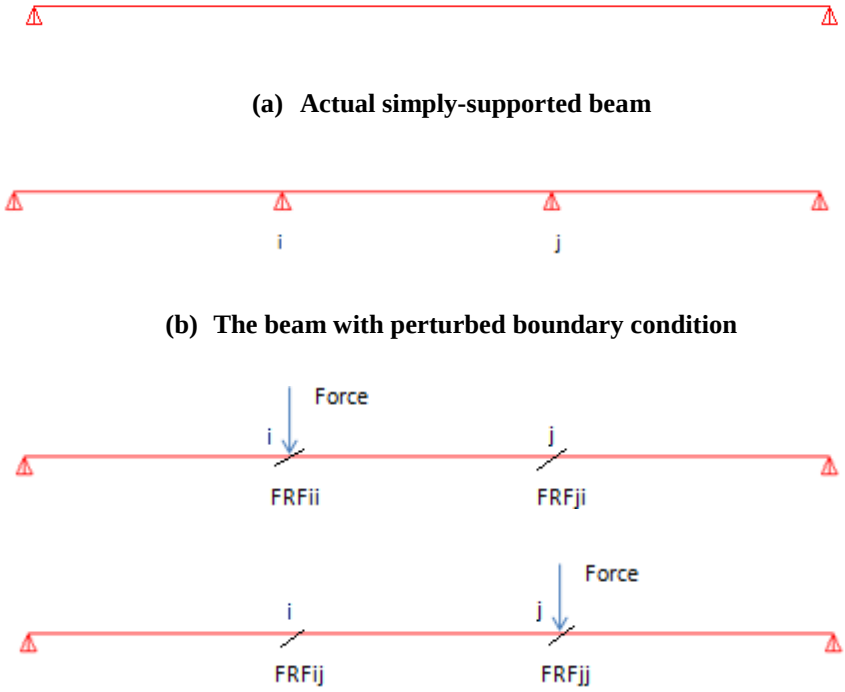

(a) Actual simply-supported beam

(b) The beam with perturbed boundary condition

(c) Artificial boundary condition frequency measurements

Figure 3.1 Illustration of artificial boundary condition frequency measurement settings

3.3 Experimental study – general procedure of modal testing for ABC frequencies

As mentioned, previous studies (e.g., Lu and Tu, 2007) have demonstrated the effectiveness of incorporating ABC frequencies with one to two pins in the

identification of structural parameters and detection of structural faults. The key to bringing the approach of involving ABC frequencies towards more practical applications lies upon the reliability and accuracy in the acquisition of the ABC frequencies from measured responses. In this section, an experimental exploration on extracting ABC frequencies from measurements on physical structures is presented with a laboratory model experiment. Issues and possible improvements with regard to the quality of FRF measurements from a modal testing point of view are highlighted and discussed. More advanced FRF processing, particularly using the SVD technique, and the eventual extraction of the ABC frequencies for various ABC configurations, will be given in subsequent sections.

3.3.1 Test set-up, experimental equipment and test procedure

The present experimental study focuses on a real measurement environment, while the test structures are kept to be relatively simple to avoid complications from the structural uncertainties. For this reason, a steel beam and an aluminium slab with flat cross sections were chosen, with modal properties of these model structures being representative of typical beams and slabs in actual construction.

The model beam had a length of 1 m, and a cross-section of 50mm (width) $\times$ 6mm (depth), while the dimension of the slab was 1,000 mm $\times$500 mm $\times$3mm. The beam and the slab were clamped at both ends, simulating fixed-end supports. Fig. 3.2 shows the set-up of the test beam and the slab, and the type of light-weight accelerometers used in the testing.

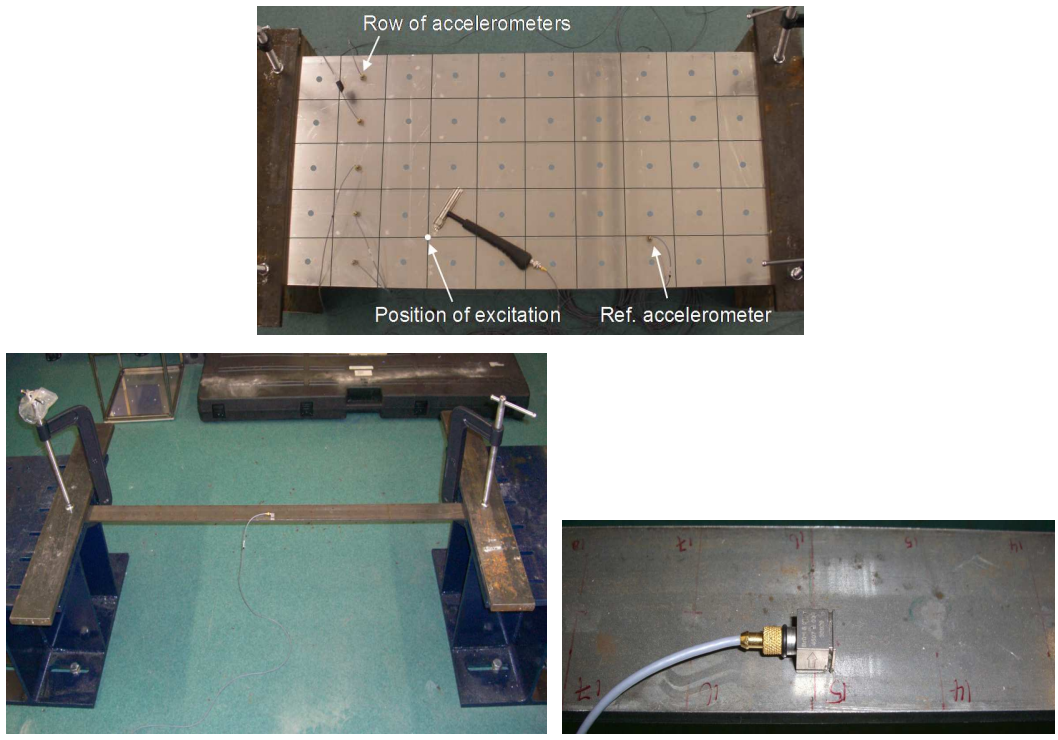

(a) Test slab / beam set-ups and attachment of accelerometers

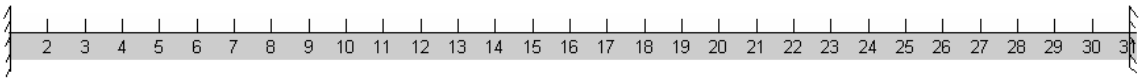

(b) Arrangement of the measurement points for the beam

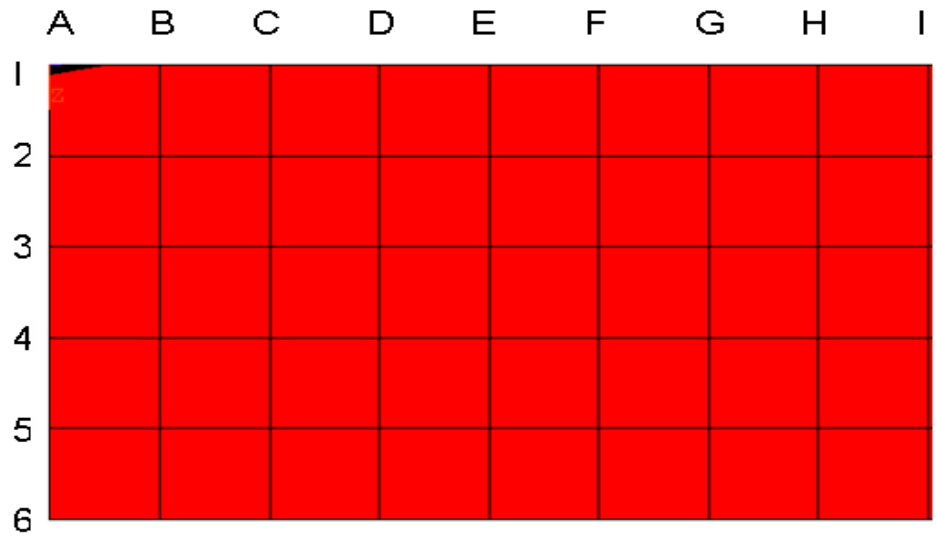

(c) Arrangement of the measurement points (nodes of the grid) for the slab

Figure 3.2 Test set-up for the model beam and slab

During the experiment, a measurement array was arranged by dividing the beam into 30 segments along its length, giving rise to 29 measurement points (the two end supports are excluded from the measurements), as shown in Fig. 3.2(c). For the slab, 10× 5 measurement grids were divided to give a total of 54 nodal points (points near two ends are excluded from the measurements) for extraction of ABC frequencies, as depicted in Fig. 3.2(d).

Strainbook 616 and WBK18 (dynamic signal conditioning modules) were employed to record input and response signals during the modal testing. Strainbook 616 is an Ethernet based data acquisition system which can accommodate strain gauge measurements in itself and also provides data acquisition support to other modules such as WBK18, which is an 8-channel unit for accelerations. In this experiment the entire DAQ system consisted of a Strainbook 616 and a WBK18, as shown in Fig. 3.3. The system is controlled via a PC through user-designed interface with Labview.

Figure 3.3 The main DAQ system used in the modal testing, consisting of Strainbook616, WBK18 and a PC

In the experiment, an impact hammer was used to excite the test structures. The impact force time history was measured by a built-in load cell in the impact hammer. Meanwhile, the responses of the test structure (accelerations) were recorded by accelerometers attached to the test structure. The accelerometers used were B & K DeltaTron type small-size accelerometers. The mass of the accelerometer is small enough (4.9g) as compared to the mass of each segment of the test structure, thus the influence to the beam mass due to the attachment of the accelerators was considered as negligible.

For simplicity and without losing generality, only one- and two-pin ABC frequencies are examined in the experimental study. The use of one- and two-pins would already allow for a large number of support variations. Moreover, the extraction of ABC frequencies involves inversion of the incomplete FRF matrix whose dimension increases with the number of (artificial) pins, therefore using more than 2-pins is expected to complicate the process, especially when measurement errors are taken into account.

To cover one- and two-pin configurations, two accelerometers are required and these are attached to two measurement points on the test structure at any one time, say locations *i* and *j*. The excitation (impact) is firstly applied at location *i* while the responses are measured at both *i* and *j*, resulting in FRF(*i*,*i*) and FRF(*j*,*i*). Subsequently the excitation is applied at *j* while the response are measured again at *i* and *j*, leading to FRF(*i*,*j*) and FRF(*j*,*j*). Thus, four FRF curves are obtained, including two driving-point FRFs and two transfer FRFs. This completes the measurement for the two-pin configuration of (*i, j*). The same procedure is repeated for any other intended two-pin configurations. It should be mentioned that in this study, the FRF curve is calculated using Equation (3.5) due to its presumable advantage of yielding FRF with a relatively higher signal-to-noise ratio (SNR) at around anti-resonances (Ambrogio and Fregolent, 1999, He and Fu, 2001), which is particularly desirable for extraction of the ABC frequencies:

$$H(w) = \frac{S_{FX}(w)}{S_{FF}(w)} \tag{3.5}$$

where S_{FX} is the cross power spectrum density of the excitation force and response, and S_{FF} is the auto power spectrum density of the excitation force.

Finally, with the obtained FRF curves, ABC frequencies can be extracted using the method described in Section 3.2. One-pin ABC frequencies with the pin at point *i* can be obtained by inverting the driving-point FRF curve at the same point, and indentifying the peaks in the inverted curve. In fact, these one-pin ABC frequencies are simply the anti-resonances (zeros) of the original FRF curves. In order to

calculate two-pin ABC frequencies with pins at i and j, the four FRF curves obtained from the respective test are employed to form a 2×2 FRF matrix, which is then inverted to obtain ABC matrix. Each element in the ABC matrix can be used to determine the two-pin ABC frequencies from the peaks in that ABC curve. The results from individual ABC curves may be used for counter-checking and assurance purposes, and elimination of spurious peaks due to measurement noise and the inverting operation.

3.3.2 Measurement of impact force and sampling frequency

From the above descriptions, it can be understood that the quality of extracting the ABC frequencies depend directly upon the quality of the constructed FRF curves, which in turn depends upon the accuracy of the measured force and response signals. Therefore, ensuring the accuracy in the measured force and response signals, and improvement of the constructed FRF curves are two key aspects determining the quality of the extracted ABC frequencies.

With regard to accurate measurement of the force and response signals, a crucial consideration is about an appropriate sampling frequency. In standard modal testing, usually the sampling frequency is selected according to the Nyquist theory, i.e. the sampling frequency should be at least two times of the maximum modal frequency that is contained in the signal and is considered to be of significance. While this general rule applies for the response signals (often with the consideration of a safety factor), it is far from sufficient when it comes to the measurement of the impact force. The impulse force applied to the test structure has a very short duration (usually several milliseconds), thus high sampling frequency would be required so that the force pulse can be measured with a satisfactory accuracy.

In this study, different sampling frequencies were examined to measure inputs and responses, and a proper sampling frequency was determined based on the quality of signals as well as the consistency of the constructed FRF curves. Fig. 3.4 depicts typical measured impulse forces when a medium impact tip was used (which

represents the impact condition in most of the tests) and the corresponding FRF curves from the test beam using different sampling frequencies. It should be noted that before calculating the FRF curve using Eq. (3.5), apparent noises in the measured impact force were removed using a rectangular window; the details will be described in the following Section 3.3.3.

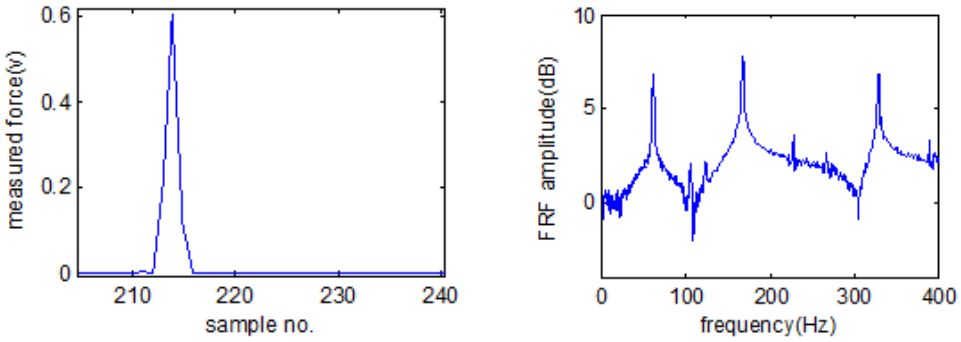

(a) 1,000Hz sampling frequency

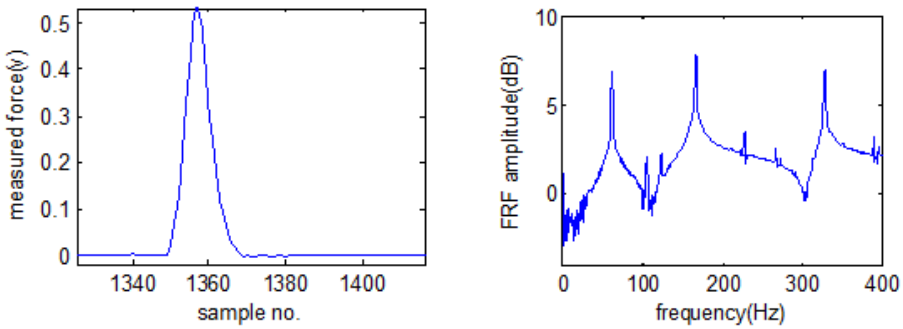

(b) 5,000Hz sampling frequency

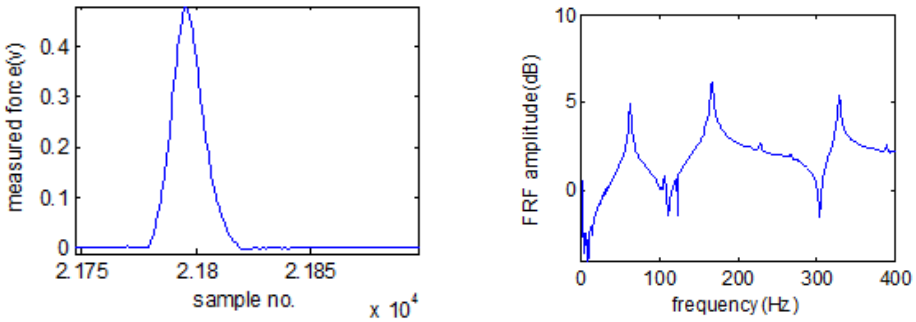

(c) 10,000Hz sampling frequency

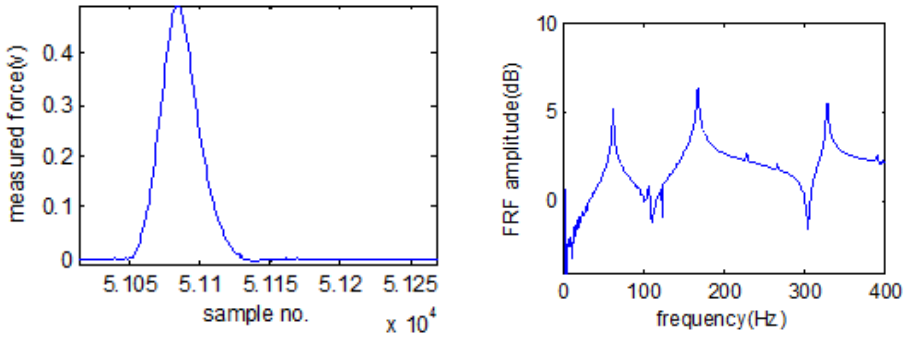

(d) Measured impulse force and corresponding FRF with 20,000Hz sampling frequency

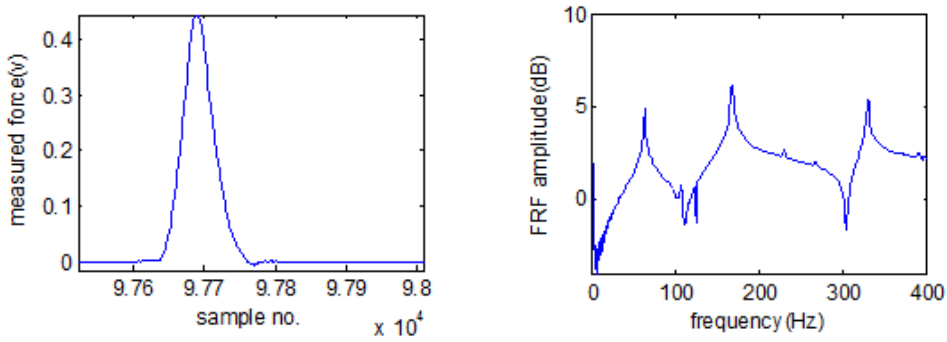

e) 30,000Hz sampling frequency

Figure 3.4 Measured impulse forces (left) and corresponding FRF curves (right) using different sampling frequencies for the test beam

From the above results, it can be seen clearly that when an insufficient sampling frequency was used (below 5,000Hz herein, giving less than 10 sample points over the impact duration), the impulse force could not be captured with good accuracy in the detailed force shape, which consequently affects notably the computed FRF with high “noise” level in the FRF curves. When the sampling frequency increases to 10,000Hz herein, the measured impulse force shape became rather stable and the noises in the FRF curves become minimal. Further increase of the sampling frequency does not appear to improve much further the FRF curves.

Considering both the accuracy and measurement-processing efficiency, a sampling frequency of 20,000Hz was employed in most of the laboratory model tests with a similar (or softer) impact tip, and necessary checks were performed to ensure the measured force was smooth enough in a particular test.

Besides the consideration of the particular demand on the sampling frequency for measuring the impact force, several data processing techniques were applied to measured signals and FRF curves to remove noises and maximise the quality of FRF for onwards calculation of the ABC frequencies. The main techniques employed will be described and discussed in detail in the following section.

3.3.3 Data processing for improvement of FRF calculation

From Fig. 3.4, even with force and response signals using proper sampling frequency (20,000Hz in the study), the obtained FRF curves still contain noises and spurious peaks, which will directly affect the further computation and extraction of the ABC frequencies, especially for ABC frequencies with more than one pin, where the inverting operation of FRF matrix is needed. Therefore, before calculating the FRF curves, the noises in the measured signals should be removed or reduced as much as possible. Moreover, irregularities (minor spurs) as observed in the obtained FRF curves (Fig.3.4) will have an effect on the quality of FRF matrix inversion, and hence the extracted ABC frequencies, as will be illustrated later, and such irregularities also need be treated properly. For these purposes, standard signal processing techniques, including windowing, averaging, filtering, as well as more advanced techniques particularly the Singular Value Decomposition (SVD), are employed in the experimental study.

3.3.3.1 Windowing

As described above, a sampling frequency of 20,000Hz was selected in the experiment, and the measurement period was in most cases fixed at 10s. Fig. 3.5 depicts typical measured force and response signals from the test beam and the slab. It can be seen that the 10s measurement period was enough to capture the vibration response in full.

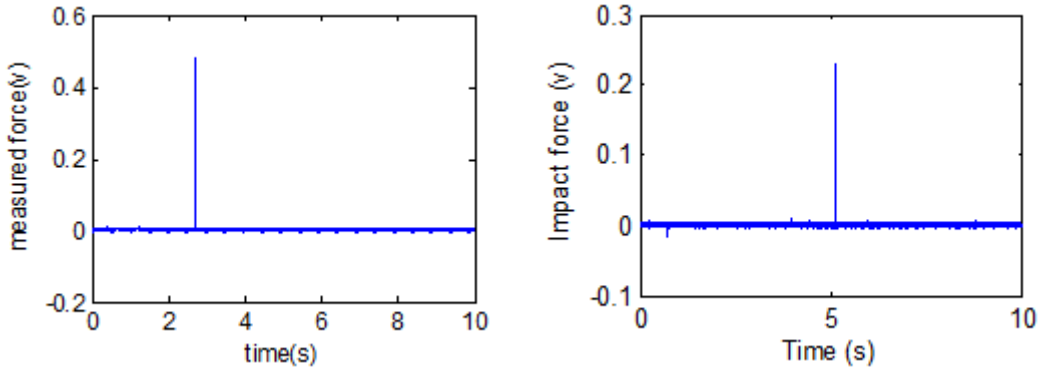

(a) Measured impulse force from the test beam (left) and test slab (right)

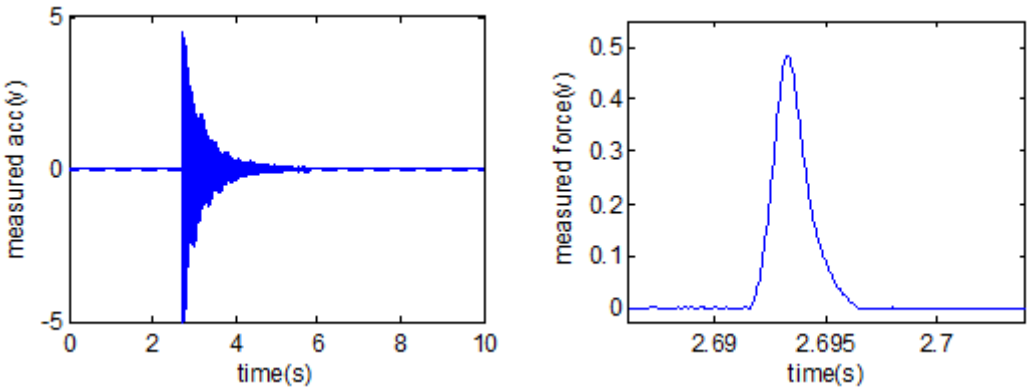

(b) Measured acceleration from the beam (c) Impact force from the beam (zoom-in)

Figure 3.5 Typical measured force and response signals from the test structures

From the measured force in Fig. 3.5, it can be seen that the impact force lasts only within a very short duration and it only takes a small portion in the signal, and remaining signal can be assumed as measurement noise since no useful information is contained in these portions. Thus these noises in the measured impact force can be removed without distorting the impulse force. As in typical modal tests where impact excitation is adopted, this may be easily done using a rectangular window (e.g. He and Fu, 2001), as illustrated in Fig. 3.6.

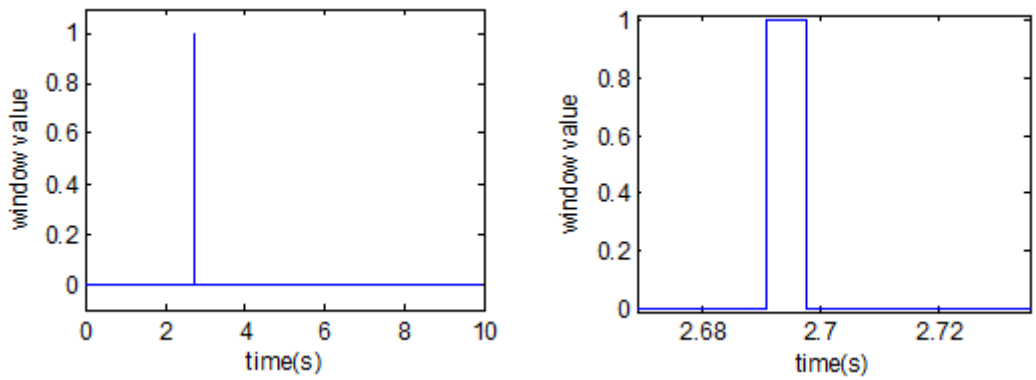

(a) Rectangular window **(b) Rectangular window (zoom in)**

Figure 3.6 Rectangular window used in the experiments

Fig. 3.7 presents the FRF curves before and after applying the rectangular window. It can be seen that after removing noises in the measured force, the FRF curves are noticeably smoother, especially in regions around the anti-resonances. Although such improvements do not appear to affect the FRF curves overall or the resonance peaks, they can result in meaningful improvement in ABC curves due to the inversion operation of FRF matrix. This will be illustrated further later.

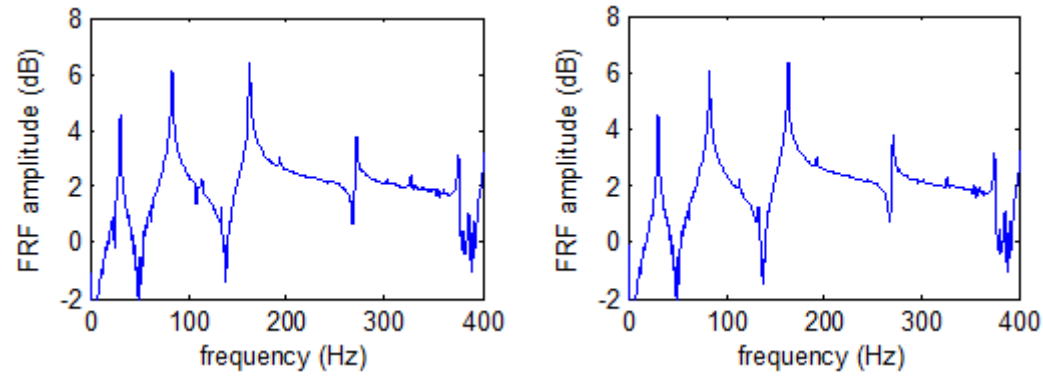

(a) FRF before windowing input **(b) FRF after windowing input**

From the beam

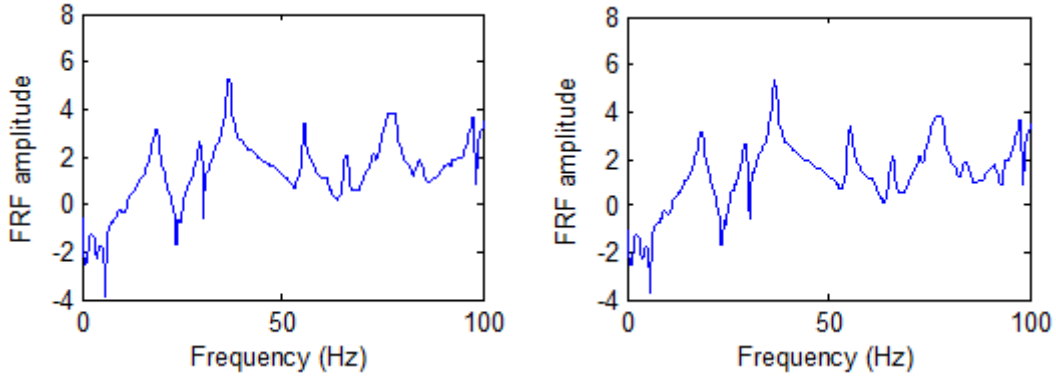

(c) FRF before windowing input **(d) FRF after windowing input**

From the slab

Figure 3.7 Effect of windowing on the impact force on FRF curves

Applying an exponential window was not considered in the present experiment because of the sufficiently long duration of the recorded signals. Such processing would become necessary if the measured duration is shorter than the sensible vibration timeframe in order to minimise the leakage errors.

3.3.3.2 Filtering

From Fig. 3.4 and Fig. 3.7, it can be seen clearly that in the obtained FRF curves, some marked noises appear in the low frequency range (lower than 10Hz herein), and this issue is more significant in FRF data from the test slab. This noisy region may exhibit different spectral shapes, even when the FRF curves are obtained at the same measurement point. It can be expected that when the FRF curves are employed, without clearing the low frequency noises, the calculated ABC curves in the low frequency region may be overwhelmed by noises. To alleviate such a problem, it is necessary to investigate the reasons behind the high level of noises in the low frequency region so that appropriate treatment may be applied to reduce this noise influence.

As described in section 3.1, the present experiment uses small size modal testing accelerometers (B & K DeltaTron in particular), taking advantage of their light

weight. The measurement frequency range is specified as from 0.2Hz to 6,000Hz, and a typical frequency response of these accelerometers is as shown in Fig. 3.8.

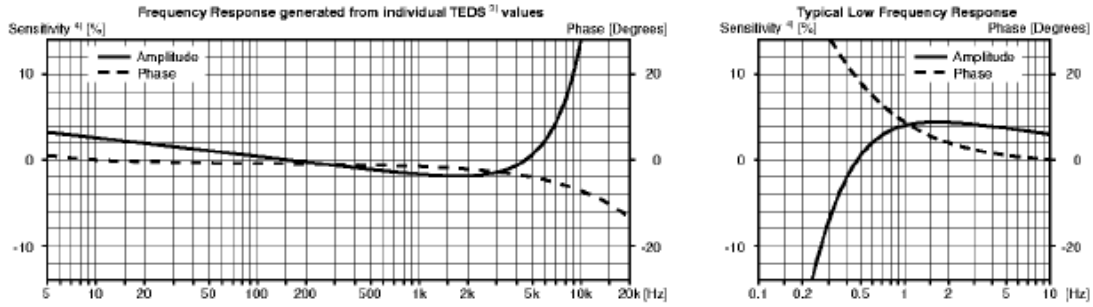

Figure 3.8 Frequency response of the light-weight accelerometers (adapted from DeltaTron Datasheet)

From Figure 3.8, it is found that the sensitivity of the accelerometer is noticeably larger in the low frequency range. Note that in the lower frequency range the measured responses from the test structures (below the 1st resonance) are dominated by random noises as no real response information is contained within this range. Thus, with high sensitivity of accelerometers at low frequency range, it is no surprise to find high level of noises in the FRF curves in the lower frequency region and without a fixed pattern.

When it is ascertained that the low frequency contents in the FRF curves contain just noises, removal of such contents becomes straightforward. In this study, a high-pass filter is utilized to reduce the noise level in the low frequency range of the signals. Considering the flat pass-band and stop-band characteristics, the high-pass Butterworth filter is employed to filter out the low frequency (below 10Hz herein) contents in the measured response signals.

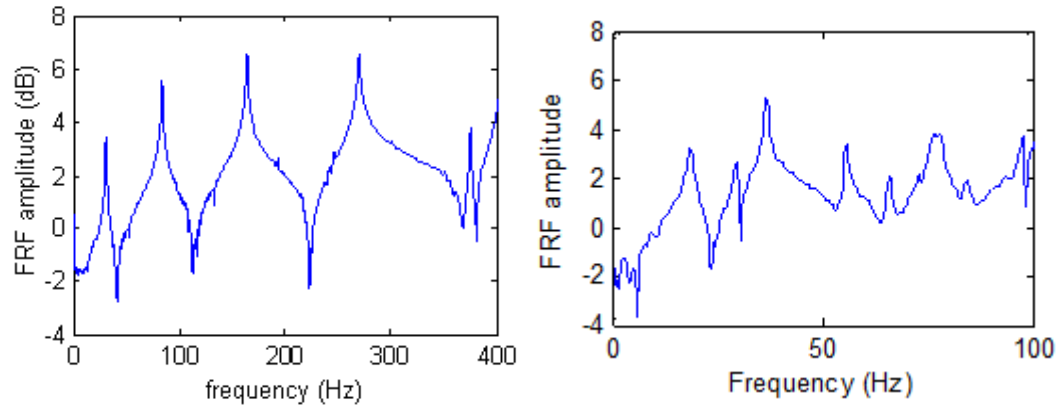

(a) FRF curves from the beam (left) and the slab (right) before filtering

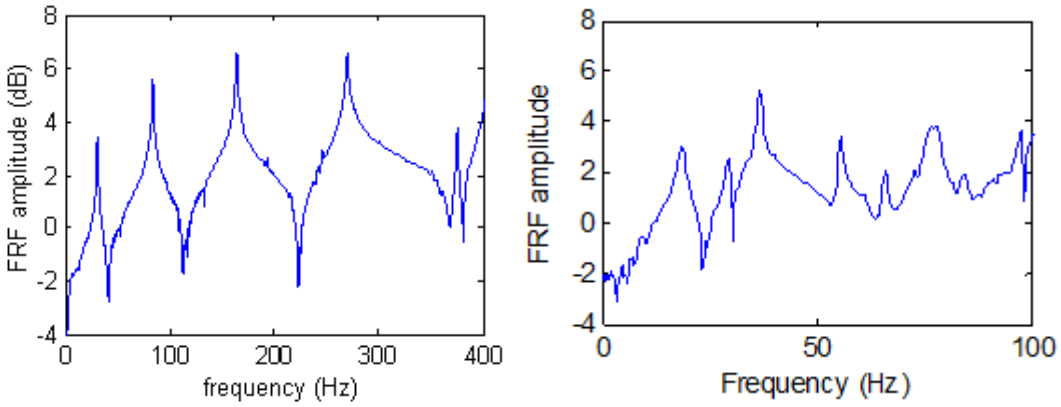

(b) FRF curves from the beam (left) and the slab (right) after filtering

Figure 3.9 Effect of filter on the FRF curves measured at the same point but at different times

Fig. 3.9 depicts the original FRF curves and the FRFs after applying the filtering process on the response signals. It can be seen from Fig. 3.9(a) that the two original FRF curves exhibit visible differences in the low frequency range, and in the FRF curve from the test slab there is a spurious 'anti-resonance' before the first real anti-resonance (which can be identified as being situated between the first and second natural modes). After filtering, the noise level at low frequency is markedly reduced in both cases, and the spurious 'anti-resonance' effectively disappears. As a result, when the processed FRFs are employed to calculate ABC frequencies, the chances of getting confused with possible misleading results in the low frequency range in the ABC curves are minimised.

3.3.3.3 Averaging

It is generally known that much of the measurement noises is random in nature, thus by taking multiple measurements for the same measurement set and averaging the resulting FRF curves, the random noises can be reduced effectively.

In this experimental exploration, several repeated tests were performed for each measurement configuration. From each test, the measured force and responses were used to calculate auto-power spectrum density and cross-power spectrum density, and these auto-power and cross-power spectrum density results from all tests were then averaged before calculating FRF using Eq. (3.5). Different numbers of measurements for averaging were tried to observe the effect under the particular test and structure settings.

Fig. 3.10 shows typical FRF curves from the test beam and the slab with averaged auto-power spectrum densities and cross-power spectrum densities with different numbers of measurements for averaging. From the results it can be seen that with just 1 measurement (no repeats for averaging), there exist marked noises, especially around the anti-resonance regions, due to environmental noises and other imperfect test conditions (such as misalignment between impact position and accelerometer position) compounded by low SNR at anti-resonances. When several measurements are taken and averaged to obtain FRF, the noises can be reduced significantly. It should be noted that when the averaging number increases beyond a certain level (10 herein), the averaged FRF curves do not appear to improve further. Therefore, in the present study, ten measurements were deemed to be sufficient for averaging purpose.

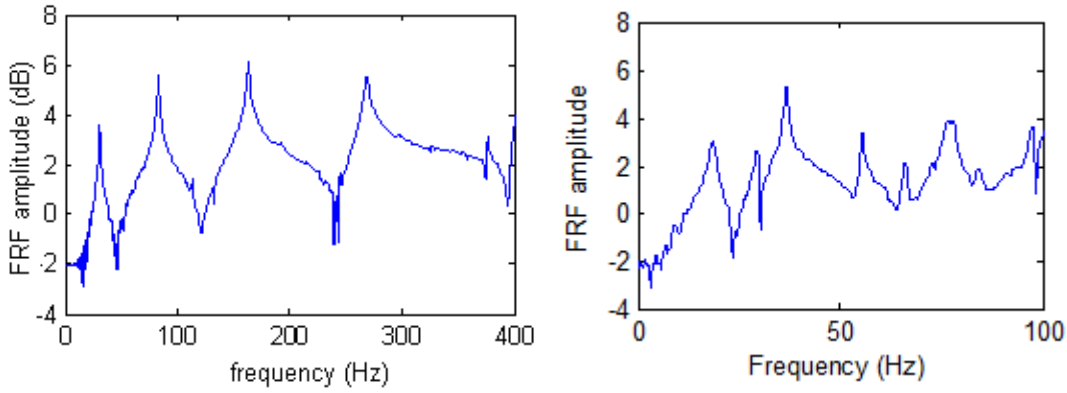

(a) 1 measurement: beam (left) and slab (right)

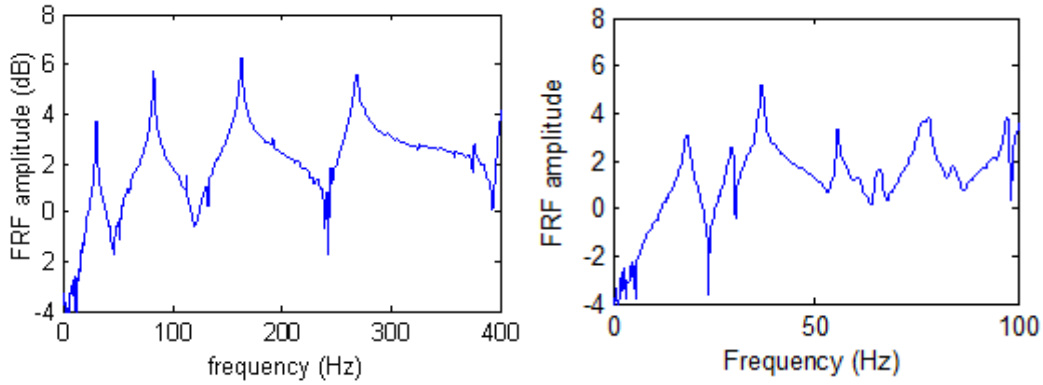

(b) 5 measurements: beam (left) and slab (right)

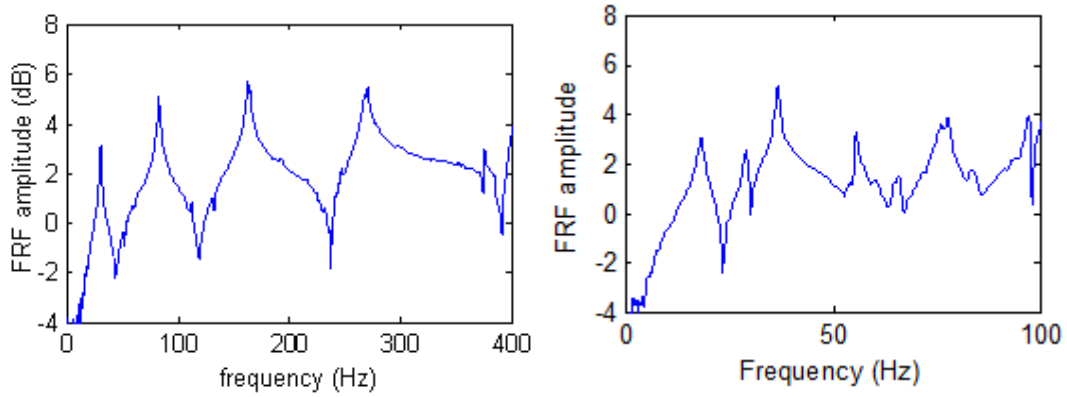

(c) 10 measurements: beam (left) and slab (right)

Figure 3.10 FRF curves with different number of measurements for averaging (left = beam; right = slab)

3.4 Singular Value Decomposition (SVD) technique and specific considerations associated with ABC frequency extraction

3.4.1 Overview and general considerations

With the implementation of the general techniques described above, the noises in FRF curves can be effectively reduced, allowing for resonances and anti-resonances to be identified with good accuracy from individual FRF curves. However, when these FRF curves are employed for the construction of the ABC curves, particularly for 2-pin ABCs (and similarly for ABCs with more than 2 pins, which are not considered here), those minor or secondary irregularities (spurs) that still exist in the FRF curves (shown in Fig. 3.10) tend to cause larger errors in the inverted FRF matrix, and thus affect the extraction of ABC frequencies and the accuracy, as will be illustrated in the next section. Therefore, further processing techniques need to be considered in order to remove these minor spurs and produce further smoothed FRF curves.

Singular Value decomposition (SVD) is an important linear algebra tool which has been used in many dynamic applications. A major application of SVD is for modal parameter identification (e.g. Tufts and Kumerasan, 1982; Cadzow, 1982). In this method, the FRF matrix of the system is decomposed to determine the system modes. SVD has also been found effective in eliminating the measurement noises in the FRF data (Sanliturk and Cakar, 2002, 2005). With the SVD technique, both additive and multiplicative noises can be eliminated effectively, leading to increased reliability of applications relying on FRF data.

In the SVD technique, given an [A] matrix of dimensions $m \times n$ and with rank R (Noting [A] contains noises), where $R \le n$, its singular value decomposition (SVD) can be expressed as:

$$[A] = [U][\Sigma][V]^T \tag{3.6}$$

where diagonal elements in $[\Sigma]$ are the singular values of [A], $[U]$ and $[V]$ are unitary matrices.

If the corresponding uncontaminated data can be expressed using a matrix $[\overline{A}]$, which has the rank r ($r \le R$), it can be calculated using the following equation:

$$[\overline{A}] = [U][\overline{\Sigma}][V]^T \tag{3.7}$$

where $[\overline{\Sigma}]$ is obtained by setting to zero all but its largest r singular values in [A], as it is assumed that the remaining singular values are dominated by noises.

Using Eq. (3.7), the noises in the matrix [A] can be effectively removed with a properly selected rank r.

According to previous researches, when the SVD technique is employed to reduce the noise in the FRF data, Hankel matrix should be firstly formed. Two different techniques can be employed to form the Hankel matrix. The first method utilizes the FRF data directly, and if the FRF with L elements can be expressed as $H = [H_1, H_2, \ldots, H_L]$, the Hankel matrix with size m×n can be formed as follows:

$$A = \begin{bmatrix} H_1 & H_2 & H_3 & \cdots & H_n \\ H_2 & H_3 & H_4 & \cdots & H_{n+1} \\ \vdots & \vdots & \vdots & \vdots & \vdots \\ H_m & H_{m+1} & H_{m+2} & \cdots & H_L \end{bmatrix} \tag{3.8}$$

In the second method, the impulse response function (IRF) is firstly obtained from FRF data using inverse Fourier transform, and these IRF data are used to form Hankel matrix in the similar fashion to Eq. (3.8). According to Sanliturk and Cakar (2005), the second method could give better distribution curve of singular values for determination of the rank of Hankel matrix, because of the clearly asymptotic trend that can be found in the singular value distribution curve. Thus in the present investigation, the IRF data is obtained from FRF data and then used to form the Hankel matrix.

With the formed Hankel matrix, SVD method can be employed to remove the noises (see e.g. Allemang and Brown, 1998; Sanliturk and Cakar, 2002, 2005). As described above, the rank of the Hankel matrix is determined with the help of the singular

value distribution curve. The proper rank (noise threshold) should be selected so that the elements with higher singular numbers are rendered as noises, and thus be eliminated by setting the corresponding singular values to zeros. Finally, the Hankel matrix is re-formed with processed matrices $[\overline{\Sigma}]$ using Eq. (3.7), and with Fourier transform, the cleared (presumably uncontaminated) FRF data are obtained.

Therefore, two parameters need to be determined for the implementation of SVD technique. Firstly the size of Hankel matrix should be decided properly, since different sizes can lead to different results. Since the noises are removed by setting the values of singular numbers larger than the selected rank to zeros, it is clear that the column of Hankel matrix should be larger than the actual system rank, i.e., n of the contaminated matrix [A] in Eq. (3.6) should be larger than rank r of the matrix $[\overline{A}]$ without measurement noises. If the number of columns in the Hankel matrix is less than the rank of the system, the Hankel matrix can not represent the system behaviour, and the system will be distorted. On the other hand, it the number of columns is too large it would require unnecessary computations. It is generally recommended that a square or nearly square Hankel matrix is adopted when considering both the accuracy and computation cost (Sanliturk and Cakar, 2005). Therefore, a square Hankel matrix is formed and used for implementation of the SVD technique in this investigation.

Another important parameter in the SVD technique is determination of the rank of the Hankel matrix, which is used to distinguish useful information and noises in FRF data. Theoretically, the singular numbers which are larger than the system rank should be zero. However, in actual experimental data, the singular values will not become zero due to measurement noise (Allemang and Brown, 1998). A widely used method is to plot the singular value distribution curve of [Σ] in Eq. (3.6), so that a proper rank can be determined when the singular value approaches an asymptote (Pickrel, 1996, Allemang and Brown, 1998). This method can ensure that the additive noises, which are caused by the measurement environment and have similar singular values, could be fully removed.

Next several cases will be employed to demonstrate the application of SVD techniques in FRF data containing different kinds of noises.

Firstly an illustrative example from Sanliturk and Cakar (2005) is employed to demonstrate the effectiveness of SVD techniques in removing noise from FRF data. In this example, the FRF data is generated from the FE model of a structure including 14 modes, and noises are added to the FRF curve to simulate a measured FRF curve. In this case 10% additive noise is added to the FRF curve, and the resulting noisy FRF curve is depicted in green (light) colour in Fig. 3.11(a). The noisy FRF data is then transferred into the IRF data to form the Hankel matrix, which has 200 columns, and the SVD technique is subsequently applied on the Hankel matrix. The distribution of the singular values is shown in Fig. 3.11(b).

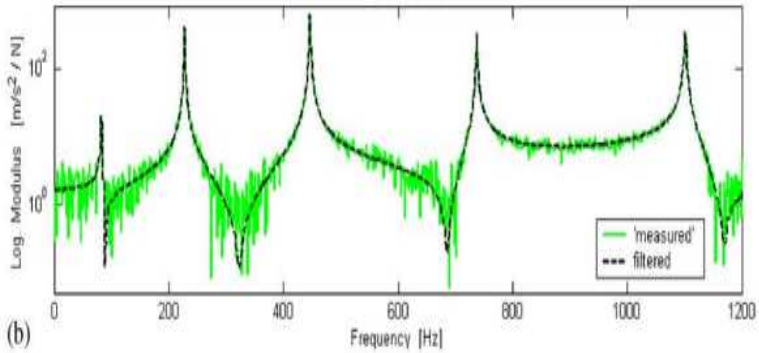

(a) FRF curves before (green/light colour) and after (dark/black colour) application of SVD

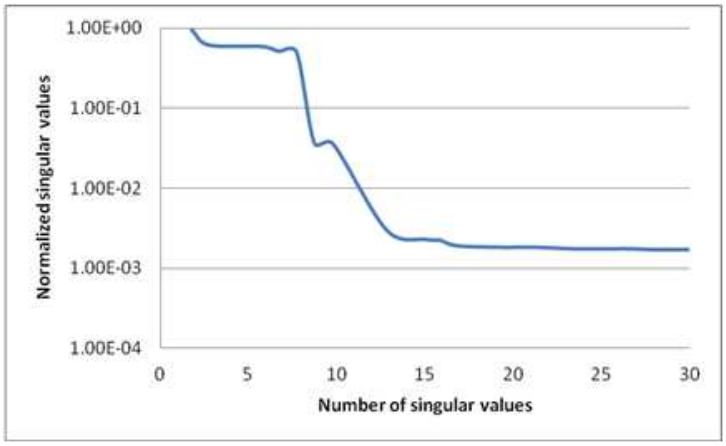

(b) Distribution of singular values from IRF data

Figure 3.11 FRF with additive noises and effect of applying SVD, after Sanliturk and Cakar (2005)

From Fig. 3.11(b), it can be found that the singular numbers have similar values after around 12, and therefore the contents with singular numbers larger than 12 may be assumed as noises. This number of 12 can be used as the rank of the Hankel matrix. With the selected rank, the Hankel matrix is re-formed and transferred back to the FRF data, which is shown in Fig. 3.11(a) (black colour). From the result it can be found clearly that the noises are fully removed in this case and an accurate FRF curve is obtained. The outcome also indicates that the selected rank based on the singular value distribution curve is appropriate for the removal the measurement noises, which are additive noises in this case.

However, when multiplicative noise is included in the FRF data (Fig. 3.12(a)), the rank of Hankel matrix will not be as obvious as in the case of additive noises from the singular value distribution curve. Fig. 3.12(b) depicts the singular value distribution curve of the Hankel matrix from noisy FRF data with 10% multiplicative noise. Note that the original FRF data is the same as that used in the above additive noise case. Since the rank can no longer be identified in the similar fashion as in the additive noise situation, Sanliturk and Cakar (2005) suggested that several candidates be tried to determine the possible rank. In this case, the rank is selected as 30. Fig. 3.11(a) depicts the FRF data before and after applying SVD technique with a rank of 30. It can be seen that with the selected rank, the noises are reduced effectively. However, it should be noted that the 4^{th} anti-resonance in FRF data is shifted after using this rank. This has particular implication for the ABC-oriented data processing, in that a selected rank may be suitable for normal FRF processing, but may be detrimental to ABC frequency extraction. This will be discussed in more detail later.

From the above examples, it can be observed that When FRF data is contaminated only by additive noises, the rank of Hankel matrix can be determined easily from the distribution of the singular values and these noises can be removed (almost) completely using the identified rank. This is because the additive noise is mainly caused by the environment noise and is independent or separable from the true FRF information.

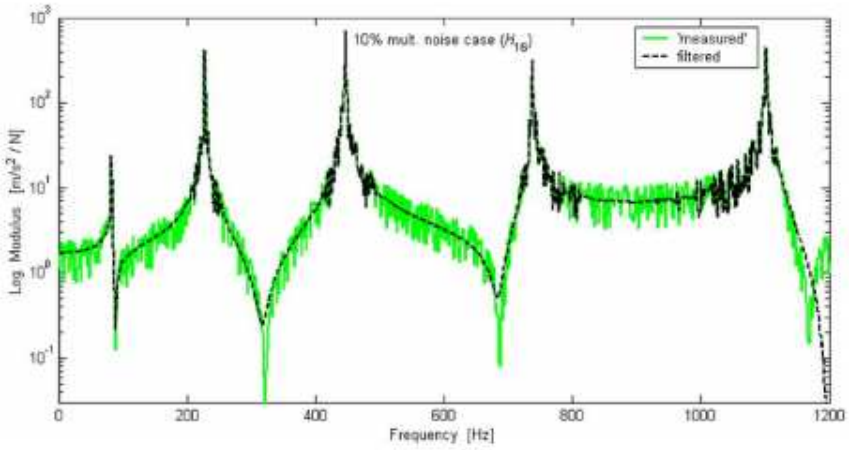

(a) FRF curves before (green/light colour) and after (dark/black colour) application of SVD

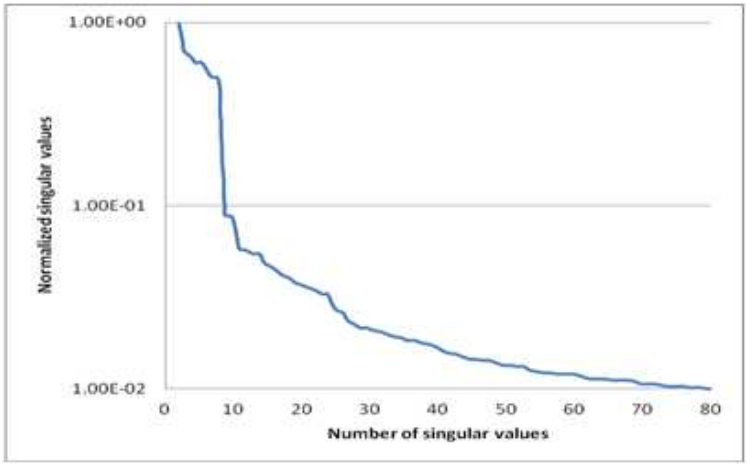

(b) Distribution of singular values from IRF data

Figure 3.12 FRF with multiplicative noises and effect of applying SVD, after Sanliturk and Cakar (2005)

However, when the FRF data includes multiplicative noises, the rank of Hankel matrix may not be identified clearly (Fig. 3.12(b)). This may be explained by the fact that the multiplicative noise is the product of the probabilistic nature of the signal amplifying technologies in typical charge-coupled devices, thus it varies with the underlying true FRF information. As the multiplicative noise is to some extent correlated with the true FRF data, this makes it difficult to remove such kind of noise completely and without affecting the true FRF data.

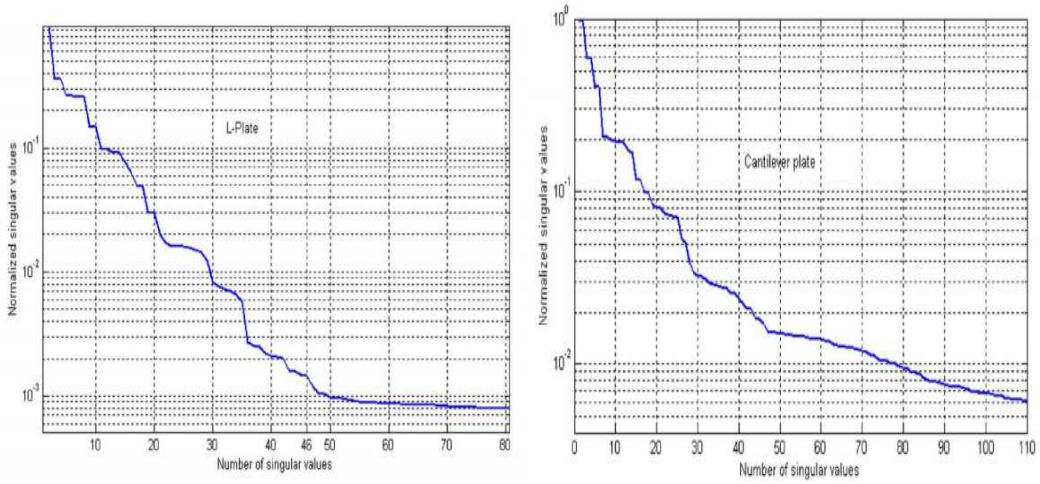

(a) free-free plate **(b) cantilever plate**

Figure 3.13 Distribution of singular values using FRF data from plates with different boundary conditions

Multiplicative noise may also be caused by other sources. Examining the test results in Sanliturk and Cakar (2005), when a free-free plate is used to measure FRF data, the singular value distribution curve clearly exhibits the rank, as shown in Fig. 3.13(a), indicating that only the additive noise is contained in measured FRF data. On the other hand, however, when FRF data is measured from the cantilever plate, where one plate end is fixed, the rank can no longer be identified from the singular distribution curve, as depicted in Fig. 3.13(b), indicating multiplicative noise. The clear distinction between these results suggests that the involvement of a support could be a source of multiplicative noises. As a matter of fact, in practical tests no perfect support conditions can actually be achieved; consequently, the supporting part of the test setup could be excited to a varying extent and thus contributing to the measured vibration responses. With the increase of structural rigidity and increase of the order of frequencies to higher modes, the vibration of supports can be expected to become more involved in the obtained FRF data, making it increasingly more difficult to distinguish between the real response of the test structure and that of the vibration in the support system. This situation can be worsened by the less good performance of sensors in high frequency range, causing further added noises in the

FRF data, especially for stiffer structures. Because the effect of such imperfections is dependent upon structural response of the test structure, the noises attributable to these sources are considered as of multiplicative nature in the present study.

3.4.2 Implementation of SVD and investigation of multiplicative noises

In the present investigation, the SVD technique is used for the removal of noises in the obtained FRF data. Considering the presence of multiplicative noise, and the particular need of preserving detailed information in the FRF around the anti-resonance regions for the onwards ABC frequency computation, the determination of the rank of Hankel matrix warrants more careful considerations. For example the result shown in Fig. 3.12(a) would not be satisfactory when it comes to the inverting operation of the FRF matrix.

To give a more systematic illustration of the application and effects of SVD technique on the obtained FRF data, two examples from the present test structures, including the beam and slab, are presented in what follows. As per the chosen procedure, firstly IRF data are obtained using FRF data from these test structures and Hankel matrices (in square form as mentioned earlier) are formed using the transformed IRF data. Fig. 3.14 depicts the singular value distribution curves using different number of columns for the Hankel matrix. The particular FRF data is from the test beam, and it contains 1,600 data points. Note that the rank of the system is found to be about 30 as will be discussed later with adequate SVD processing

From the distribution curves, it can be seen clearly that if the number of columns of the Hankel matrix is smaller or only slightly larger than the system rank, the system behaviour will be distorted by the operation and it is impossible to determine the rank of Hankel matrix. On the other hand, if the number of columns is sufficiently larger than the system rank, the results tend to converge. Therefore, in order to ensure that the Hankel matrix can express the system behaviour and the reasonable

computing cost, the column of Hankel matrix is selected as half size of IRF data (about 800 herein), and the square Hankel matrix could be formed.

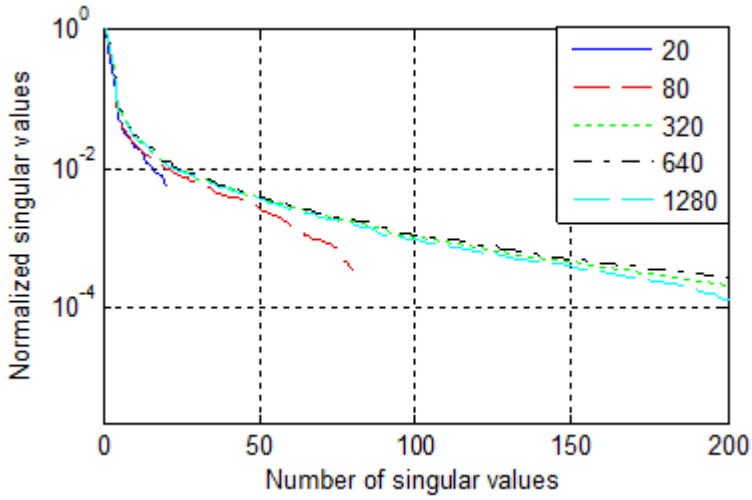

Figure 3.14 Distribution of singular values from Hankel matrix with different numbers of columns

SVD is then applied to the well-formed Hankel matrices to obtain the distribution of the singular values using Eq. (3.6), and typical results are shown in Fig. 3.15. As can be seen, the curves for both the beam and slab do not exhibit a clear asymptote, indicating the presence of multiplicative noises in the obtained FRF data. Further discussion about relation between the multiplicative noise and the support vibrations in the present tests will be given in the later part of this section.

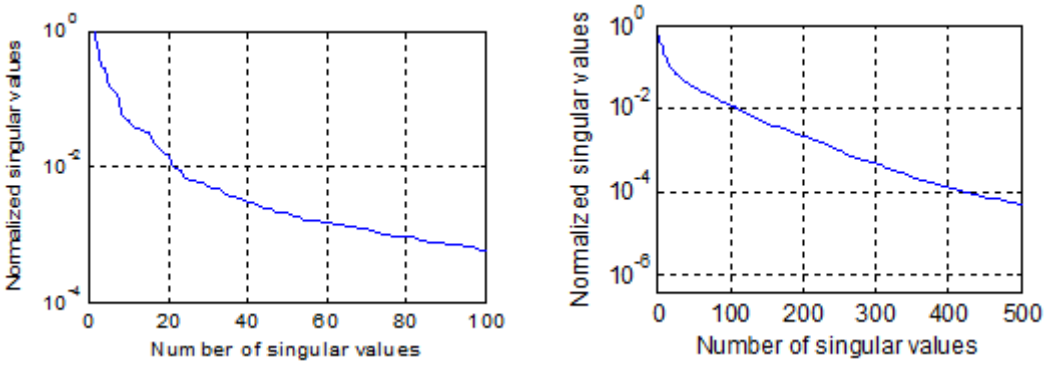

(a) From test beam **(b) From test slab**

Figure 3.15 Typical distributions of the singular values using the IRF data from test structure

Several candidate ranks are used for the SVD application to determine the rank of the Hankel matrix. Fig. 3.16 depicts the FRF curves before and after applying the SVD technique with different ranks.

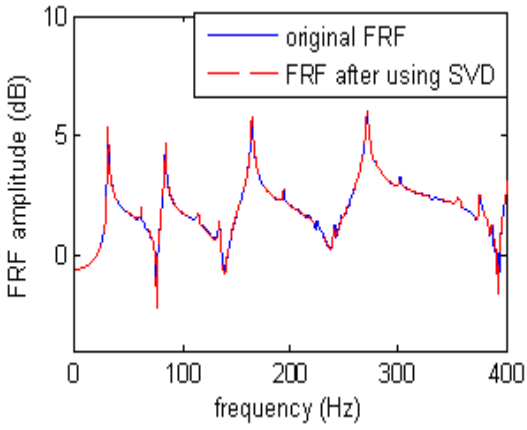

Rank 40

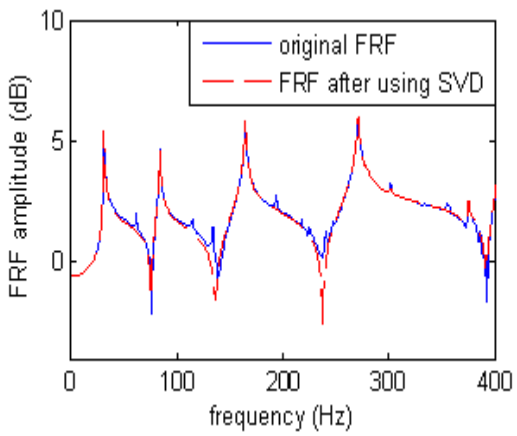

Rank 30

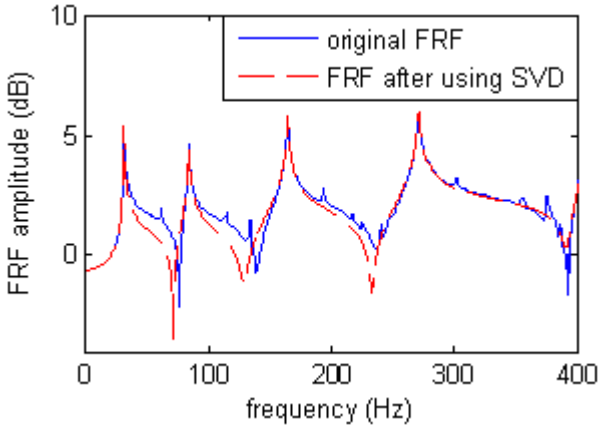

Rank 20

(a) FRF from test beam

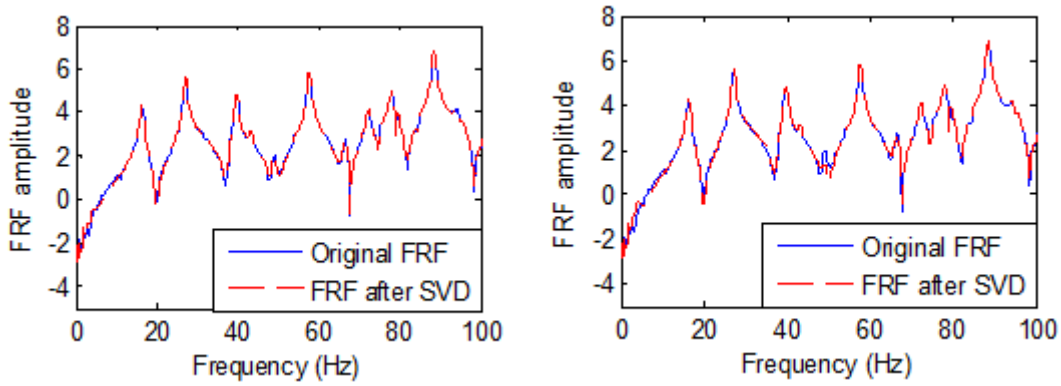

Rank 200 **Rank 190**

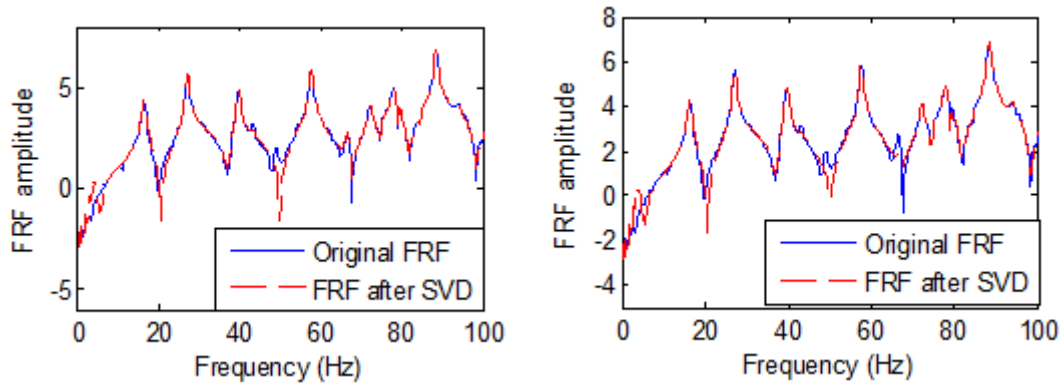

Rank 150 **Rank 140**

(b) FRF from test slab

Figure 3.16 FRF curves before and after applying SVD with different ranks

The selection of the proper rank for SVD application should be decided in accordance with the resulting FRFs. For the present test beam and slab, the proper rank appears to be on the order of 30 and 190, respectively. With these selected ranks, some multiplicative noises are seen to be removed effectively, while details of the FRF curves, especially around the anti-resonances, are not distorted.

From Fig. 3.16, it can be observed that even with a small change of the rank, the anti-resonance areas could be affected significantly. As mentioned before, the reason behind this is that in the impact test, the impact signal has low energy density, whereas the test structure theoretically has no response at anti-resonances

(Richardson, 1999; Avitabile, 2001; He and Fu, 2001) and consequently should have small singular values at these frequencies. Such small singular values may be similar to or even smaller than the singular values of multiplicative noises caused by the vibrations of supports. Therefore, a slight change in the rank will tend to introduce some equally sensible effect on the anti-resonances and multiplicative noises.

It is worth noting that a larger singular number is used in the case of the test slab than in the case of the test beam (190 vs. 30 herein). This is because in the test slab the response involves many more modes, due to torsion as well as bending, than the beam, while the singular value number represents the number of modes that are effectively involved in the vibration. Therefore, a larger singular number would become natural and necessary in the slab case for the SVD application.

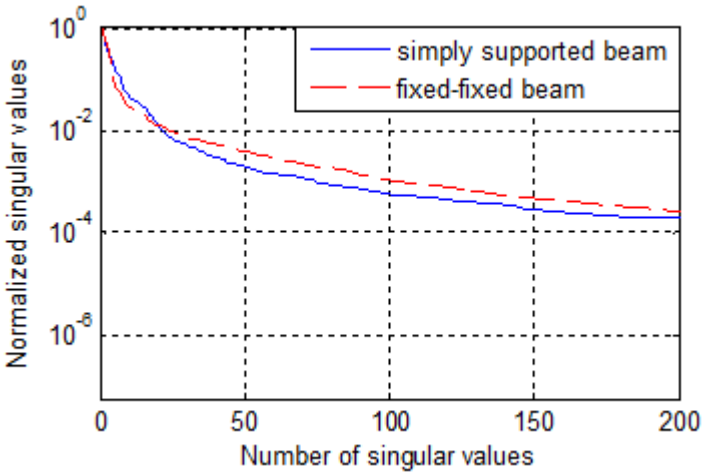

Figure 3.17 Distributions of singular values from FRF data of the tests under two different boundary conditions

In order to further confirm that the multiplicative noises in the obtained FRF data are mainly caused by the support vibration in the test, the same test structure may be purposely subjected to different boundary conditions which would incur different levels of support vibration, and examine the resulting singular value distributions. For example, a fixed-fixed condition can potentially involve a much more significant participation of the support vibration as compared to a simply supported condition, and therefore is more susceptible to multiplicative noises. Fig. 3.17 shows the

singular value distributions from FRF data using the above two different boundary conditions for the test beam.

It can be found that for high order singular numbers, larger singular values occur in the fixed-fixed beam as compared to the simply-supported beam, indicating that more significant multiplicative noises are included in FRF data from fixed-fixed beam. A further evidence of different levels of multiplicative noises may be found from comparing directly the FRF data under different boundary conditions. Fig. 3.18 shows the original FRF data from simply supported beam. Comparing to the original FRF data from the fixed-fixed beam shown earlier in Fig. 3.16(a), the simply supported beam appears to involve much less noise and hence less minor spurs.

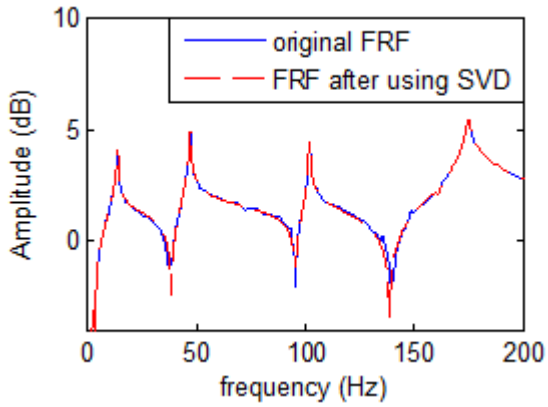

Figure 3.18 FRF data before and after applying SVD method from the simply-supported boundary condition

An additional perspective of the relation between the multiplicative noises and the support vibration may be gained by testing beams of different stiffness on the same supports. Herein this is done by using the same beam under the fixed-fixed condition but bringing the supports 50% closer, thus effectively reducing the span length by half and increasing the overall beam stiffness by 8 times. The singular value distribution curves for the beam with the original and reduced lengths are compared in Fig. 3.19.

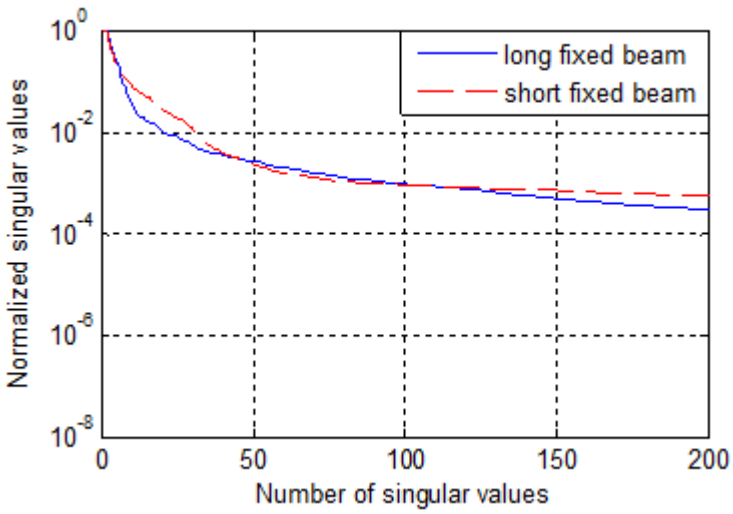

Figure 3.19 Distributions of singular values from FRF data of test beam with different span lengths

It can be seen clearly that the values of higher order singular numbers from the shorter beam are larger, indicating a higher level of multiplicative noises in the FRF data. It confirms that with a shift of the system natural frequencies to higher values, more support vibrations will be involved in the obtained data, making the FRF data more susceptible to multiplicative noises.

In conclusion of the above illustrative investigation on the multiplicative noises, as anti-resonances have singular values as small as those of the multiplicative noises, the selection of a smaller rank in the SVD application in order to remove the multiplicative noises may risk the distortion of the anti-resonance information and hence adversely affect the onwards ABC frequency identification. Where possible, the supports should be made enough rigid in the first place so that its vibration frequency is far higher than the maximum modal frequency of the test structure concerned. Furthermore, sensors should have satisfactory performances in the high frequency range of interest. In cases where significant multiplicative noises do occur, the rank for SVD application should be selected carefully through a trial process so that as much multiplicative noises can be removed while ensuring that the anti-resonance information is not distorted.

3.5 Extraction of ABC frequencies: outcome and discussion

With the processed FRF curves, one-pin and two-pin ABC frequencies can be identified from the elements of the inverted FRF matrix. In this section, the qualities of extracted one-pin and two-pin ABC frequencies are investigated with the application of the aforementioned data processing and SVD techniques. Moreover, the accuracy of the extracted ABC frequencies is also examined in light of the frequency changes due to damages, especially those representing early-stage damages.

To generally cover all possible 1-pin and 2-pin ABC scenarios, a detailed test routine was organized such that a large variety of artificial pin configurations can be obtained by combining the impact and measurement scenarios tested during the experiment.

3.5.1 Benchmark FE models

To give a general idea about the frequency characteristics of the test structures, Table 3.1 lists the first 3 measured natural frequencies of the test beam and the slab. For comparison, simple FE models were also set up for the test beam and slab using ANSYS software. In the FE models, 30 BEAM3 elements were used to model the test beam, with beam rigidity (EI) and density being 169.2 $N.m^2$ and 7800kg/ m^3, respectively, as in the test beam. The plate element in ANSYS was used to model the test slab, with density and Young's modulus being 2700kg/ m^3 and 70GPa, respectively, representing the test slab which was made of aluminium, which is schematically illustrated in Fig. 3.20. The computed natural frequencies of the beam and slab are also listed in Table 3.1. It can seen that the computed and measured frequencies agree very well, indicating that the FE models are accurate enough to be employed in assisting the experimental explorations, for example, in confirming the extracted ABC frequencies as will be discussed later.

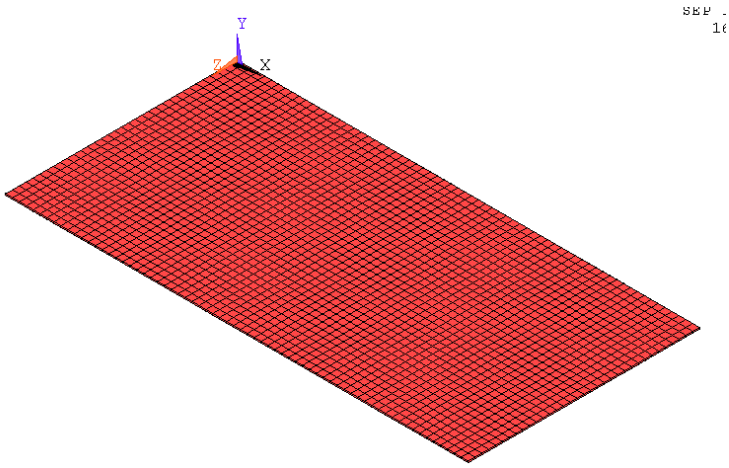

Figure 3.20 Benchmark FE models for the slab

Table 3.1 Experimental natural frequencies from the test beam

Mode number	1st	2nd	3rd
Experimental(beam)	30.5Hz	82.9 Hz	162.7 Hz
Numerical	30.2 Hz	83.1 Hz	163.1 Hz
Experimental(slab)	16.27Hz	26.49Hz	40.18Hz
Numerical	16.17Hz	26.85Hz	39.47Hz

3.5.2 One-pin ABC frequencies

For the one-pin cases, the measured FRF matrix reduces to a single driving-point FRF, and the ABC frequencies are actually the anti-resonances in the FRF curves. In line with the general ABC approach, these can be identified from peaks on the inverted driving-point FRF.

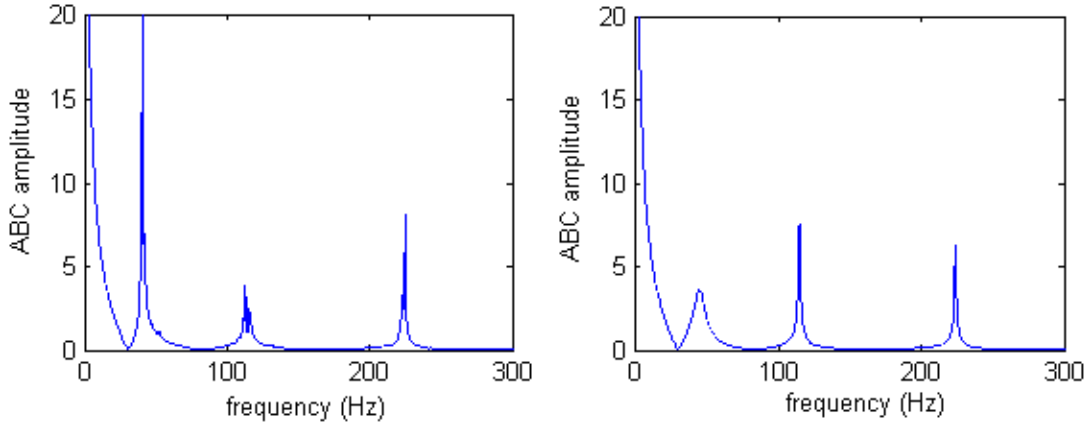

ABC curve from FRF before SVD **ABC curve from FRF after SVD**

(a) One-pin ABC curves with pin at point 6

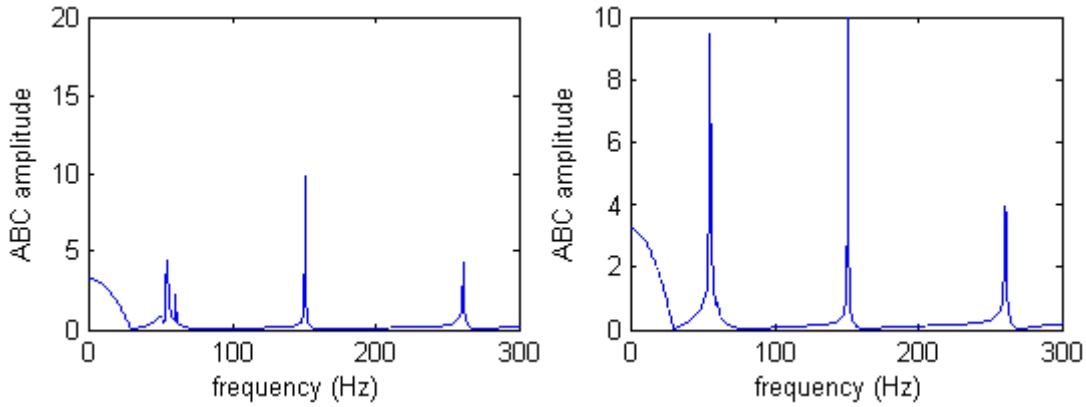

ABC curve from FRF before SVD **ABC curve from FRF after SVD**

(b) One-pin ABC curves with pin at point 22

Figure 3.21 Typical one-pin ABC curves from the test beam (location numbers refer to Fig. 3.2b)

Fig. 3.21 depicts two typical one-pin ABC curves (inverted driving-point FRF) from the test beam before and after applying SVD. From these curves, the first few peaks can be clearly and exclusively identified, and the corresponding frequencies are deemed to be the ABC frequencies, and they are listed in the Table 3.2. For a verification and comparison, the natural frequencies of the beam with an actual added pin support at the respective ABC location are obtained using the FE model,

and the results are also listed in the Table 3.2. It can be seen that the experimentally identified ABC frequencies (first three modes) agree well with the FE results, indicating that these frequencies are indeed the ABC frequencies and they have been determined with good accuracy.

From the results shown in Fig. 3.21, it can be observed that after applying the SVD technique on the FRF curves, with adequate selection of the rank as discussed in Section 3.4.2, the resulting ABC curves become smoother and the one-pin ABC frequencies (anti-resonances in driving-point FRF curves) are more clearly identifiable.

It should be noted that, as is the case in the general modal testing, if the sensor happens to be at a nodal point of a natural mode, the corresponding modal information will not be measured. The implication for the ABC frequencies extraction is that, if that natural mode happens to be an ABC mode as well, such an ABC mode will not be identifiable from that measurement. Fig. 3.22 depicts such a scenario, where the sensor is placed at the centre point, which is the nodal point of the second natural mode of the beam. As a result, the second natural mode, which happens to be the first ABC mode when an added pin is inserted at the mid-span, is not measured. From the one-pin ABC curve, only the second ABC frequency can be found, and this is confirmed by the associated FE analysis results shown in Table 3.2.

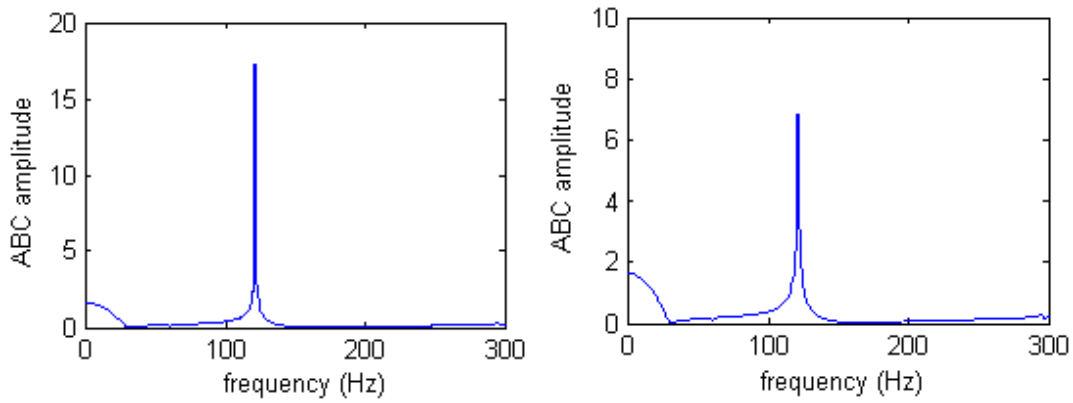

Before SVD **After SVD**

One-pin ABC curves with pin at point 16 (mid span)

Figure 3.22 One-pin ABC curves with sensor on nodal point (location numbers refer to Fig. 3.2b)

Table 3.2 One-pin ABC frequencies from the experiment and FE model analysis (the latter numbers are results from FE analysis)

Scenario	Frequencies (Hz)		
	1st	2nd	3rd
Fig. 3.21(a)	39.9/38.79	105.2/104.8	210.3/206.43
Fig. 3.21(b)	54.2/53.7	152/150	261/262.7
Fig. 3.22(a)	/83.5	122/121.1	/270.4

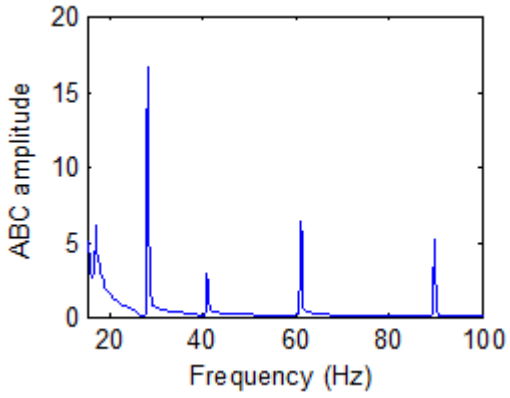

(a) One-pin ABC curves with pin at A1

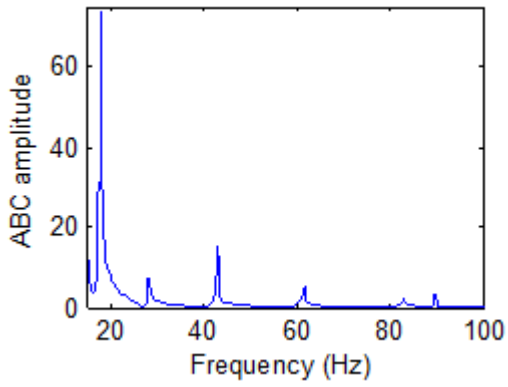

(b) One-pin ABC curves with pin at I2

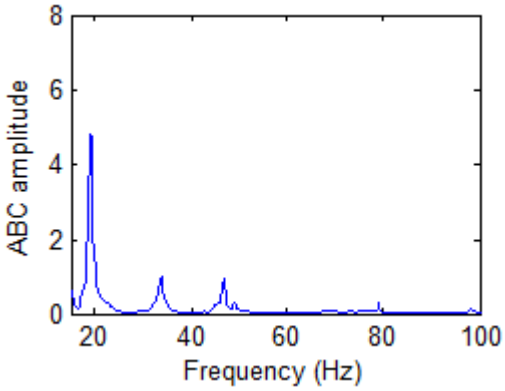

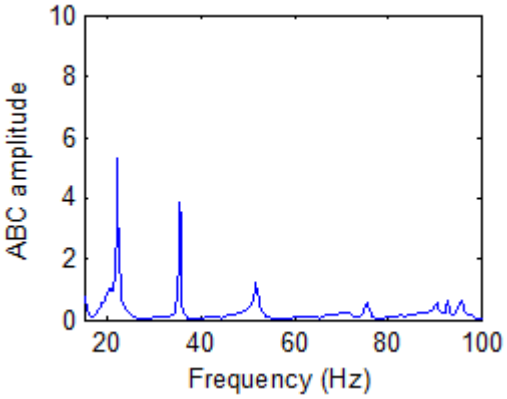

(c) One-pin ABC curves with pin at G6 **(d) One-pin ABC curves with pin at D2**

Figure 3.23 Typical one-pin ABC curves from the test slab (location numbers refer to Fig. 3.2c)

Fig. 3.23 presents some typical one-pin ABC curves from the test slab, and the extracted first three modes of the ABC frequencies are listed and compared with the respective FE modelling results in Table 3.3. These results demonstrate that using a similar procedure, the first 3 ABC frequencies in a one-pin configuration for the test slab can be extracted with good quality as well.

Table 3.3 One-pin ABC frequencies from experiment / FE model analysis (the latter numbers are results from FE analysis)

Pin Position	The 1st mode (Hz)	The 2nd mode (Hz)	The 3rd mode (Hz)
A1	16.78/16.68	28.08/27.79	40.89/41.16
I2	18/17.61	28.38/27.89	43.03/44.73
G6	18.92/18.58	33.57/34.09	46.69/47.92
D2	21.97/21.56	35.4/37.58	51.57/53.1

Based on the above results, it may be concluded that it is possible to obtain the first few (three herein) ABC frequencies for any arbitrary one-pin configuration from the inverted FRF curves, provided that appropriate procedure for the testing and data acquisition, as well as processing of the FRF curves with the SVD technique, are carefully implemented. The acquired ABC frequencies are of equivalent accuracy to the natural frequencies of similar orders, and thus may be employed in a similar fashion as the natural frequencies in a subsequent structural damage identification procedure.

Next, we shall examine the extraction of two-pin ABC frequencies from the FRF matrix and discuss the identifiability and accuracy of such ABC frequencies.

3.5.3 Two-pin ABC frequencies

As mentioned earlier, for two-pin ABC frequencies the FRF matrix will be a 2×2 matrix, consisting of four FRF curves. This matrix is then inverted to yield the required $\mathbf{H}_{mm}^{-1}$ matrix, which is also 2×2, with four elements representing four ABC curves. The ABC frequencies may be identified from any of these curves, and in practice the curves from other elements may be used for cross-checking and assurance purposes.

There are obviously a variety of configurations with arbitrary locations of the two pins. To allow for a systematic observation in a better organised manner, representative pin positions are chosen to cover essentially all possible combinations, and they are classified into closely-located pins and well-separated pins. Similar to the one-pin scenarios, the two-pin ABC curves from the test beam are examined firstly, and followed by two-pin ABC curves from the test slab to ascertain that reliable two-pin ABC frequencies can be extracted from different test structures using a similar procedure. The effect of the SVD treatment is also observed in the extraction of two-pin ABC frequencies.

3.5.3.1 Two pins at closely-located positions

In this scenario, two accelerometers are placed closely to obtain FRF curves, and the two-pin ABC curves are subsequently calculated by inverting the 2x2 FRF matrices. Fig. 3.24 depicts some typical two-pin ABC curves. For a comparison, the results before and after applying the SVD treatment on the FRFs are both included.

From these curves, the first few peaks can be identified clearly and almost exclusively, although the smoothness of these curves is not as good as in the one-pin scenarios, which is quite expected due to the involvement of four FRF functions and the inverting operation. In fact, even in a physical test where two additional pin supports are actually imposed, the frequency response function could be subject to

increased “noises” due to the increased rigidity of the beam and the shift of the modal frequencies towards a higher range.

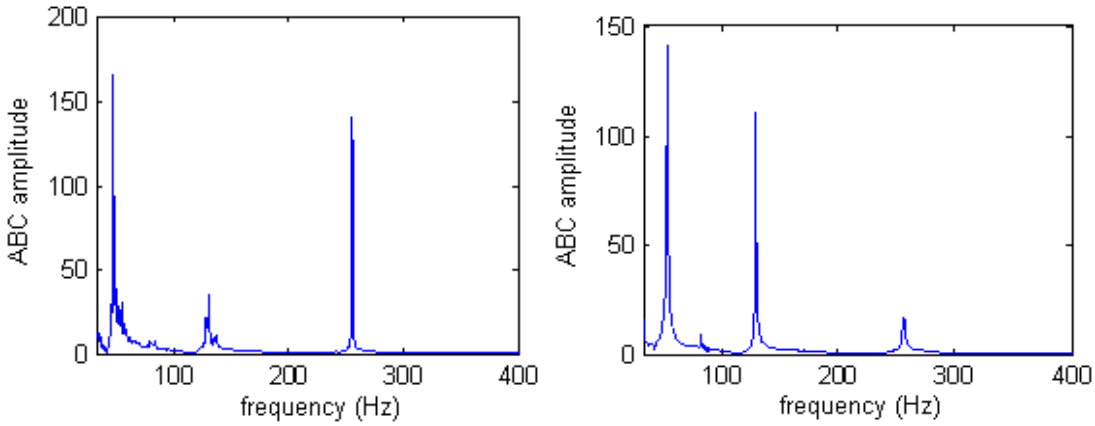

Before SVD **After SVD**

(a) ABC “Pins” at points 6 and 7

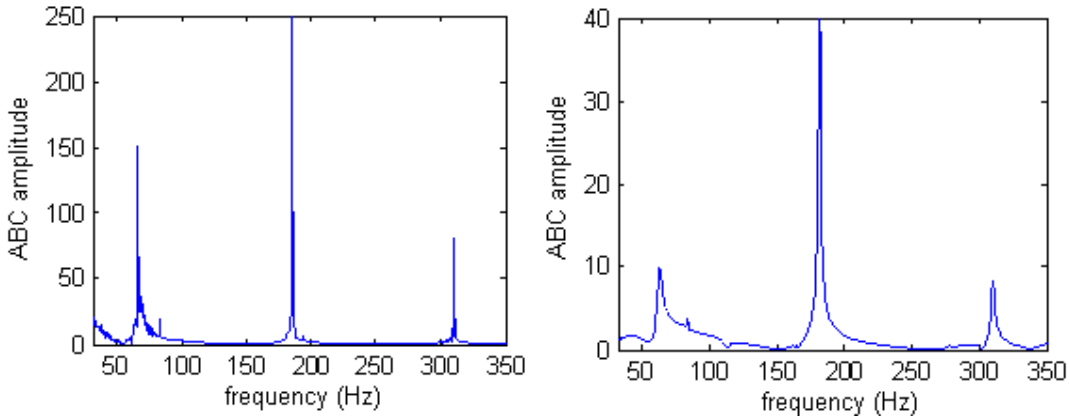

Before SVD **After SVD**

(b) ABC “Pins” at points 10 and 11

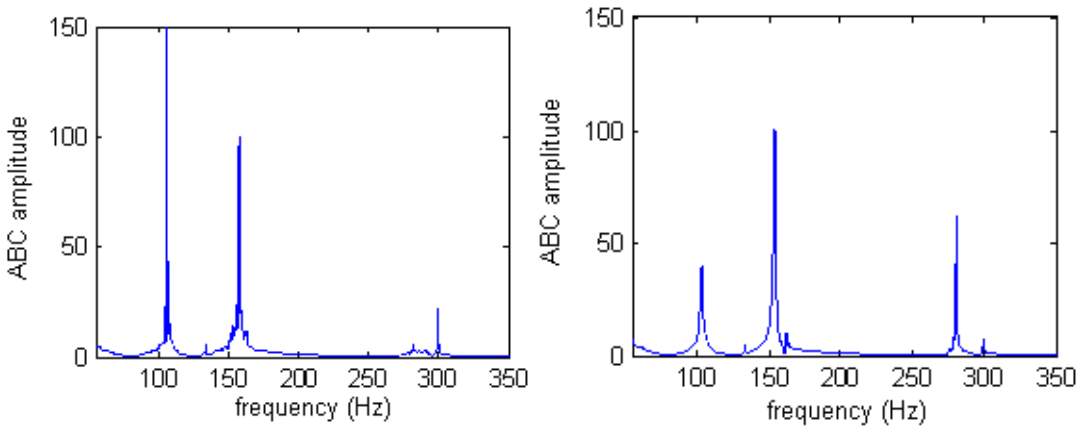

Before SVD **After SVD**

(c) ABC "Pins" at points 14 and 15

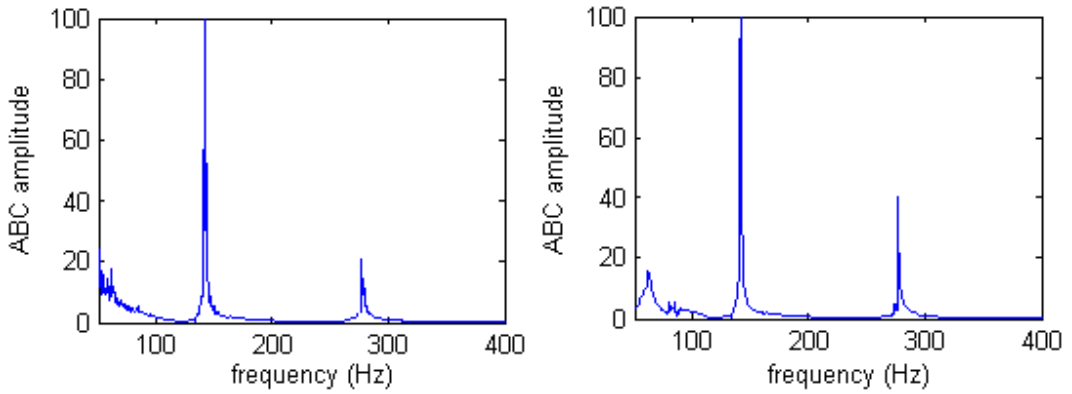

Before SVD **After SVD**

(d) ABC "Pins" at points 24 and 25

Figure 3.24 Typical two-pin ABC curves for cases with closely-located pins (location numbers refer to Fig. 3.2b)

Table 3.4 lists the two-pin ABC frequencies as extracted from the inverted 2x2 FRF matrices through the above procedure. The results from the FE model analysis by adding two actual pins at the corresponding positions are also shown. It can be seen that, similar to the one-pin cases, the experimentally identified two-pin ABC frequencies match well with the FE results for these scenarios where the two pins are at closely-located positions.

Comparing to the one-pin cases, the effect of the SVD treatment tends to be more pronounced in the extraction of two-pin ABC frequencies. This may be explained by the fact that, due to the FRF matrix inversion operation, relatively minor errors (noisy spurs) in individual FRF curves tend to have a compounded effect. As such, employing the SVD (or alike) technique to enhance the quality of individual FRF curves becomes even more important for extracting ABC frequencies with two (or more) pins.

Table 3.4 Two-pin ABC frequencies from experiment / FE model analysis for cases with closely-located pins (the latter numbers are results from FE analysis)

Case	Frequencies (Hz)		
	1st	2nd	3rd
a	47.1/46.2	128.5/127.3	256/249.7
b	64.8/66	180/182.3	311.4/316.2
c	103.1/102.3	153.5/154.6	280.8/282.9
d	49.1/50	137.3/138.7	277.1/272.1

3.5.3.2 Two pins at well-separated positions

In these scenarios, two accelerometers are placed at two well-separated points (with a larger distance). Similarly the two-pin ABC curves are constructed by inverting the 2x2 FRF matrices. Fig. 3.25 depicts some typical two-pin ABC curves for these scenarios. The two-pin ABC frequencies identified from these curves are listed in Table 3.5, with comparison to the corresponding FE analysis results.

From these results, it can be seen that the first few peaks can be found clearly from the two-pin ABC curves for these cases with well-separated pins, and the results

agree well with the corresponding FE analysis. The overall extraction condition is similar to the cases with two closely-located pins.

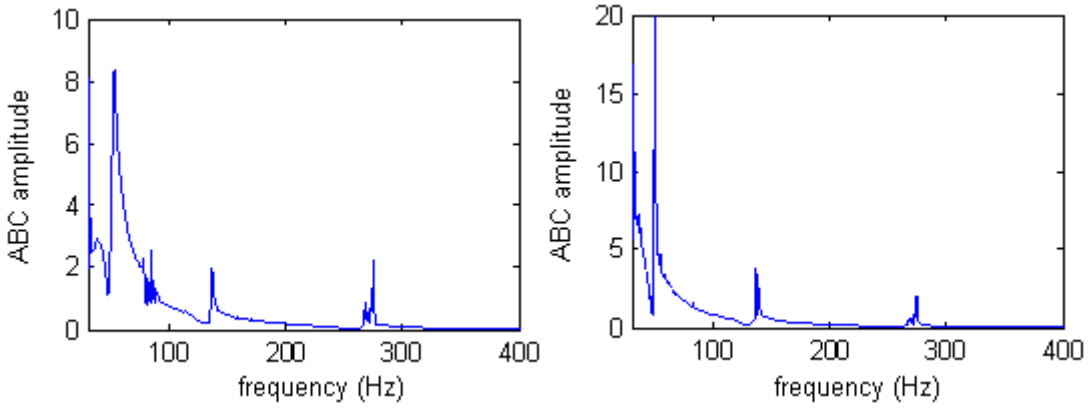

Before SVD **After SVD**

(a) ABC "Pins" at points 5 and 8

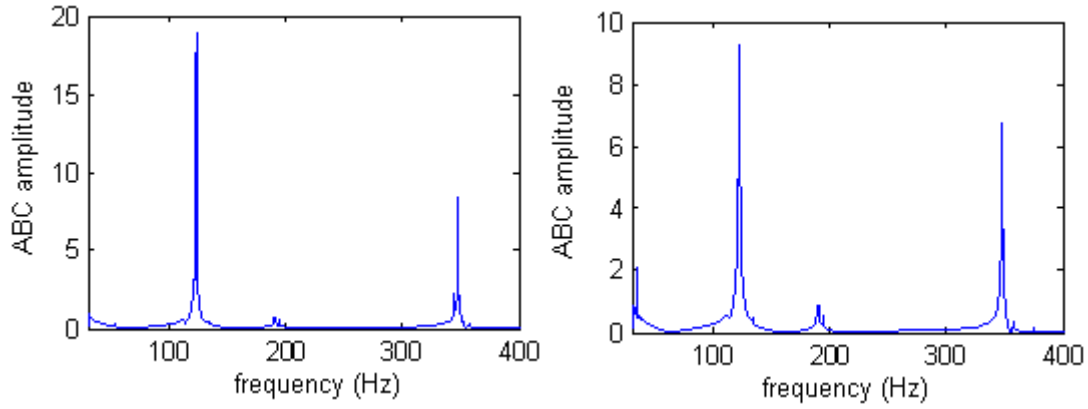

Before SVD **After SVD**

(b) ABC "Pins" at points 15 and 20

Figure 3.25 Typical two-pin ABC curves for cases with well-separated pins (location numbers refer to Fig. 3.2b)

Table 3.5 Two-pin ABC frequencies from experiment / FE analysis for cases with well-separated pins (the latter numbers are results from FE analysis)

Case	Frequencies (Hz)		
	1st	2nd	3rd

a	50.1/48.3	135.5/134	271.6/263.8
b	121.6/120.8	190.4/191.5	346.8/340.7

Fig. 3.26 shows some typical ABC curves when the two pins are located with further increased distance. The extracted ABC frequencies are listed in comparison with the FE analysis results in Table 3.6. Once again, the overall results are satisfactory and the extraction condition is comparable with other cases involving two pins.

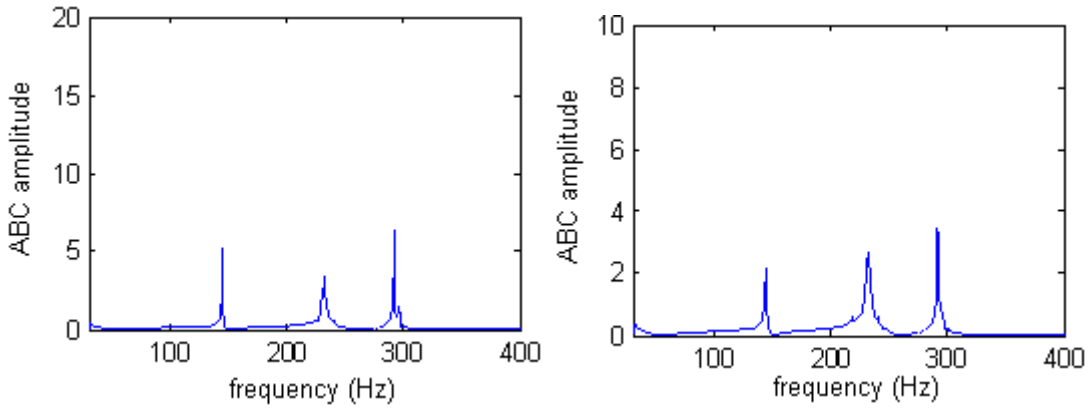

Before SVD **After SVD**

(a) ABC "Pins" at points 10 and 21

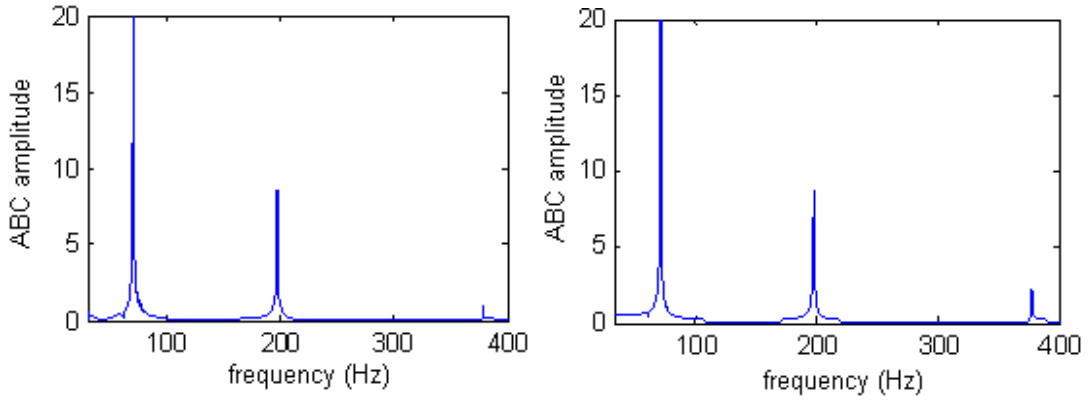

Before SVD **After SVD**

(b) ABC "Pins" at points 7 and 25

Figure 3.26 Typical two-pin ABC curves for cases with further separated pins (location numbers refer to Fig. 3.2b)

Table 3.6 Two-pin ABC frequencies from experiment / FE model analysis for cases with further separated pins (the latter numbers are results from FE analysis)

Scenario	Frequencies (Hz)		
	1st	2nd	3rd
a	141.7/139.85	232.8/233.27	292.7/291.93
b	67.25/66.8	191.1/189.86	374.9/372.97

The results described above demonstrate comprehensively that extracting ABC frequencies for a beam-like structure from a normal modal test is feasible and practical for one-pin and two-pin configurations. This observation is generally valid in the test slab as well. Fig. 3.27 shows some example two-pin ABC curves generated from the test slab following a similar procedure as for the beam. It can be observed that similar to the beam scenario, the first 3 two-pin ABC frequencies can be identified clearly and exclusively from the test slab. Comparison of the extracted ABC frequencies with the FE modelling results, as shown in Table 3.7, indicates that the accuracy of the extracted two-pin ABC frequencies from the test slab is similar to the test beam.

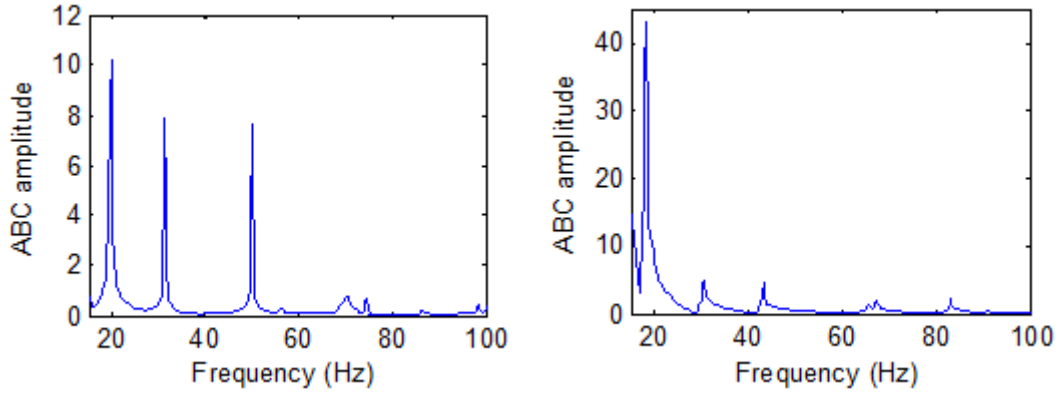

(a) One-pin ABC curves with pin at A1B5 **(b) One-pin ABC curves with pin at A1I2**

Figure 3.27 Typical two-pin ABC curves from the test slab (location numbers refer to Fig. 3.2c)

Table 3.7 Two-pin ABC frequencies from experiment / FE model analysis for the test slab (the latter numbers are results from FE analysis)

Pin Position	The 1st mode (Hz)	The 2nd mode (Hz)	The 3rd mode (Hz)
A1B5	19.84/20.02	31.43/31.59	50.05/51.42
A1I2	18.31/17.93	30.52/29.57	43.33/45.28

Summarising the above results and observations, it may be concluded that effectively all one-pin and two-pin ABC frequencies can be extracted for a beam or slab. The proposed data processing procedure in association with an impact testing approach appears to work well in improving the quality of the measured FRF functions, and subsequently improves the quality of extracted ABC frequencies. The extracted one-pin and two-pin ABC frequencies are poised to have similar accuracy as natural frequencies, thus these data can be employed for damage identification purpose.

In the section that follows, the effectiveness of using the experimentally extracted ABC frequencies for damage identification will be illustrated by observing the sensitivity of the extracted one-pin and two-pin ABC frequencies to certain damage. A more comprehensive discussion on using ABC frequencies for damage identification will be presented in Chapter 4 in association with an FE model updating application.

3.6 Effectiveness of using ABC frequencies for damage identification - illustrative experimental observations

For illustration, a kind of damage is created in the test beam, and ABC frequencies before and after creating the damage are extracted using the same procedure as described in previous sections. The changes of the ABC frequencies due to the damage are calculated and compared to the changes of natural frequencies of similar order to observe their comparative sensitivities.

Fig. 3.28 depicts the damaged test beam. The damaged area is located at about 0.33m-0.36m to the left end of the beam. It is noted that several cuts are made to create a relatively uniform reduction of the section stiffness over the damaged area, instead of a single cut which would cause a varying stiffness zone in the vicinity of the cut and hence introducing unnecessary complexity for the evaluation. By creating a (relatively) uniform stiffness reduction area, it also makes an analysis using a simple FE model for comparison more straightforward. With verification from an FE model, the cuts resulted in a reduction of stiffness by about 30% over a length of 100mm (10% of the total beam length).

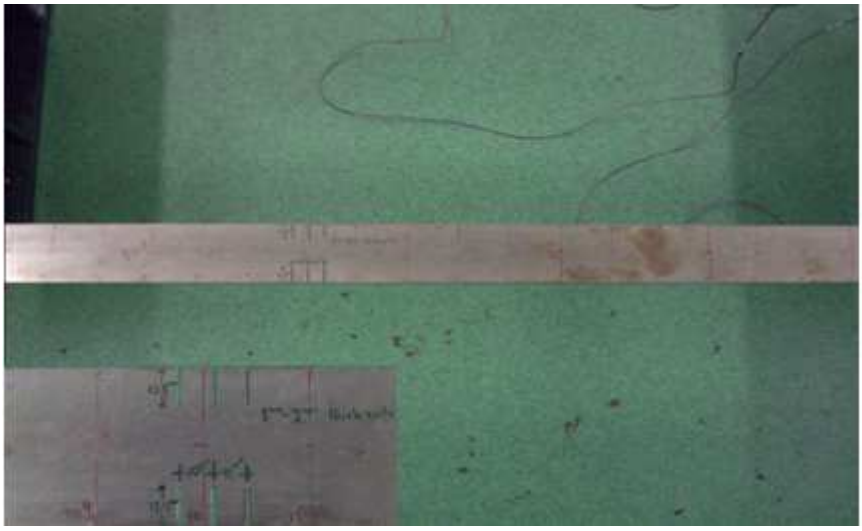

(a) Actual damage in the test beam

(b) Illustrative figure showing cut dimension in the beam

Figure 3.28 Test beam with damage

The natural frequencies of the damaged beam are measured firstly, and the changes of natural frequencies due to damages are calculated. The results are listed in Table 3.8. It can be seen that the damage leads to a change (reduction) of the natural frequencies in a range of 0.7-2.7%, with the highest reduction occurring to the

second mode. This is expected as the damage location is at about one-third length of the beam.

Table 3.8 Experimental natural frequencies and corresponding changes from the damaged beam

Mode number	1st	2nd	3rd
Experimental (with cuts)	29.8Hz	80.6Hz	161.6Hz
Experimental (without cuts)	30.5Hz	82.9Hz	162.7Hz
Changes due to damages	-2.3%	-2.8%	-0.68%

To get an idea about the sensitivity of one-pin ABC frequencies to the damage, Fig. 3.29 shows two typical FRF curves measured at points near the damaged area before and after damage is introduced. From the curves it can be found clearly that the anti-resonances (one-pin ABC frequencies) exhibit similar trends of shift due to the damage as the natural frequencies. The actual one-pin ABC frequencies extracted from these curves, along with those from several other one-pin positions, are summarised in Table 3.9.

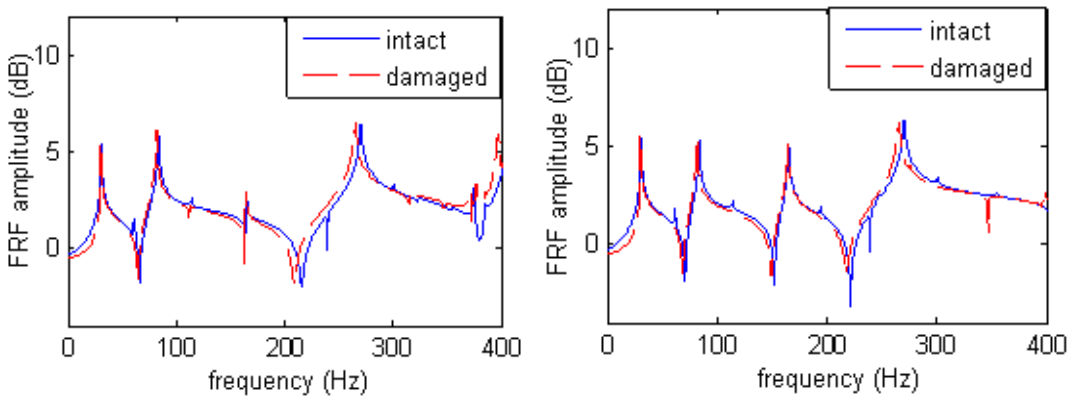

(a) FRF measured at point 12 **(b) FRF measured at point 13**

Figure 3.29 Measured FRF curves before and after damages

According to the results in Table 3.9, a majority of the one-pin ABC frequencies exhibit changes at a comparable level as the natural frequencies, whereas some exhibit smaller changes, for example the 2nd ABC frequency with a pin at point 8. This is no surprise as the damage location would inevitably locate at or near a nodal point for certain ABC modes (the same can happen to natural modes as well).

Table 3.9 Variation of one-pin ABC frequencies due to the damage

Pin Position	1st	2nd	3rd
4	-1.57%	-2.85%	-1.75%
8	-0.18%	-0.01%	-1.81%
12	-1.31%	-1.06%	-1.4%
18	-2.06%	-0.39%	-1.2%
21	-1.76%	-1.05%	-0.92%
24	-2.13%	-1.31%	-2.54%

Fig. 3.30 shows some typical two-pin ABC frequency curves before and after the damage. The extracted two-pin ABC frequencies and their percentage changes are listed in Table 3.10.

It can be observed that similar to one-pin ABC frequencies, sensible changes occur in the two-pin ABC frequencies and different degrees of change take place for different positions of the pins, as can be expected. It is particularly worth noting that changes in some two-pin ABC frequencies are markedly higher, indicating higher sensitivity in these ABC frequencies to the particular damage. With a large variety of available two-pin configurations, this indicates that there is good scope and necessity for an appropriate selection, and possibly optimisation, of the two-pin ABC frequencies for the onwards application in the parameter and damage identification. In lieu of a sophisticated procedure, e.g. using an optimisation algorithm (Tu and Lu, 2007), it is advisable to carry out preliminary studies to identify more sensitive ABC frequencies for certain targeted damage scenarios before undertaking the

measurement and identification operations. Further discussion on the sensitivity of the ABC frequencies to damage, with relation to mode shapes, will be given in Chapter 4.

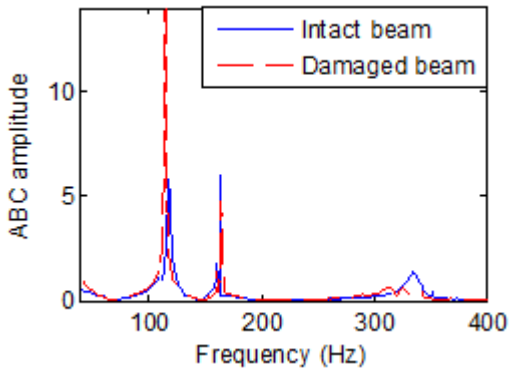

Pins at 12 and 18

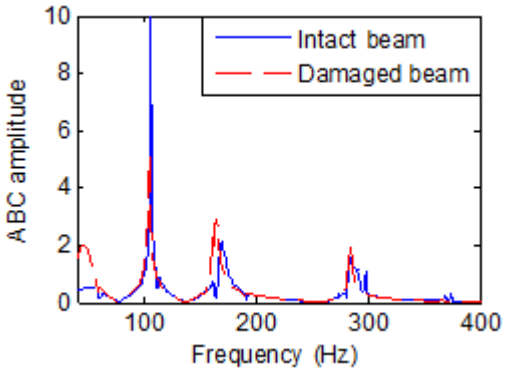

Pins at 18 and 21

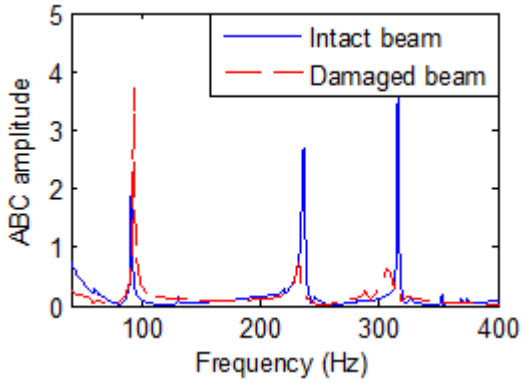

Pins at 18 and 27

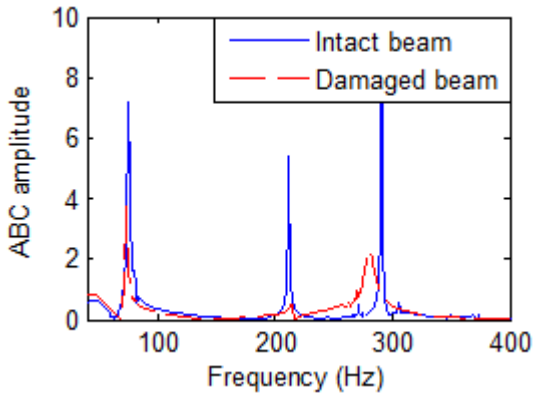

Pins at 21 and 24

Figure 3.30 Measured ABC curves before and after damages

Table 3.10 Variation of two-pin ABC frequencies due to the damage

Pin Position	1st	2nd	3rd
12,18	-4.34%	-0.96%	-1.96%
18,21	-1.42%	-2.54%	-0.11%
18,27	-0.83%	-1.69%	-3.28%
21,24	-2.85%	-1.13%	-3.81%

While the use of ABC frequencies for parameter identification can always be realised through a model-based technique, particularly finite element updating, it would also be desirable if the ample supply of the ABC frequency data can be exploited to facilitate a rapid assessment of the structural condition without the need of going through a sophisticated parameter identification procedure. An ABC frequency-based damage index would serve such a purpose, and this will be the topic of Chapter 4.

3.7 Conclusions

This chapter presents a comprehensive experimental investigation on the acquisition of ABC frequencies on physical structures in a laboratory setting. The effects of general modal testing operation, data acquisition and signal processing are examined systematically in the context of acquiring ABC frequencies, particularly with regard to producing smooth FRF curves in their entirety rather than focusing only on the modal

The implementation of the singular value decomposition (SVD) technique for the purpose of extracting reliable and accurate ABC frequencies is investigated thoroughly. The presence of multiplicative noises in the FRF data, particularly in terms of the singular value distributions, is deemed to be linked (at least partly) to the involvement of support vibration, and this is confirmed by specially designed experiments. This paves a way for controlling such noises during an experiment in the first place. On the removal of such noises, the SVD rank is found to play a critical role; but a precise determination of the SVD rank without affecting significantly the FRF information around the anti-resonance regions still requires further investigation.

Results from the representative beam and slab experiments demonstrate that, with a careful implementation of testing, data acquisition and processing procedures as outlined in the chapter, effectively all one-pin and two-pin ABC frequencies in the first few ABC modes can be obtained with quality and accuracy matching the comparable orders of natural frequencies. Comparison of the ABC frequencies between undamaged and (slightly) damaged beam cases shows that different ABC frequencies can possess markedly different sensitivities to a particular damage. As such and considering the availability of a large variety of possible one- and two-pin ABC configurations, it would be possible to select and even optimise the combinations of ABC frequencies for a particular parameter identification task. This subject is to be examined in the next chapter.

It should be noted that the test structures employed have been relatively simple, which is deemed necessary for the present stage of experimental evaluation on the

extraction of ABC frequencies, It can be expected that, as the structures become more sophisticated, additional complexities could arise in the process of extracting the ABC frequencies, and such complexities need be investigated in future research.

4 ABC frequency sensitivity evaluation and application in finite element model updating

4.1 Introduction

In Chapter 3, it has been demonstrated that with appropriate testing and data processing operations it is possible to extract a large number of ABC frequencies for the first few ABC modes from one-pin and two-pin combinations, and the accuracy of the extracted ABC frequencies can be as good as the natural frequencies.

In the above respect, and considering the fact that some ABC frequencies are more sensitive and some are less to a particular damage, it is necessary to select only those ABC frequencies which are generally more sensitive to the parameters being identified for use in the actual model updating or structural damage identification procedure. For this purpose, an appropriate criterion should be developed for the selection of ABC frequencies from all possible candidates so as to achieve the best outcome while at the same time reduce unnecessary effort in the measurements and data processing operations.

In the study presented in this chapter, the sensitivities of ABC frequencies to the damages are investigated. For simplicity and without losing generality, only one-pin and two-pin ABC frequencies are employed. In the present study, the approach of deriving anti-resonance sensitivity expression is adopted and is extended to two-pin ABC frequencies. On the basis of the expressions of one-pin and two-pin ABC frequency sensitivities, the contributions of the underlying mode shapes in the ABC frequencies can be calculated, and this enables the selection of more sensitive ABC frequencies for FE model updating. Following the basic formulation, numerical studies are then used to examine the performance of the selected ABC frequencies in FE model updating.

Also presented in this Chapter is a numerical study to investigate the effect of the size of the ABC frequency dataset in FE model updating. The proposed ABC frequency selection criterion and appropriate size are further examined through application to the FE model updating on a physical test beam (the experimental beam described in Chapter 3).

Finally, in light of the intrinsic relationship between the ABC frequencies and the underlying mode shapes, a preliminary effort to construct ABC frequency-based damage indices aiming at a direct indication of the structural condition is described in the last part of this chapter. In particular, the possibility of formulating an ABC frequency-based damage index in an analogy to the mode shape curvature is investigated using numerical studies, and the direction for future work is commented.

4.2 Theory of ABC frequency sensitivities

4.2.1 Sensitivity of driving point anti-resonances (one-pin ABC frequencies) and mode shape contributions

In modal analysis, the frequency response function (FRF) can generally be expressed as follows:

$$h_{ij}(\omega) = \sum_{k=1}^{n} \frac{\varphi_{ik}\varphi_{jk}}{\left(\omega_k^2 - \omega^2\right)} \tag{4.1}$$

where i, j represent positions of the excitation force and the response, respectively. φ_{ik}, φ_{jk} are the k-th order mode shape at points i and j, respectively, and ω_k is the k-th order natural frequency.

When the applied force and measured response are at the same position, the corresponding FRF reduces to the driving-point FRF as:

$$h_{ii}(\omega) = \sum_{k=1}^{n} \frac{\varphi_{ik}^2}{\left(\omega_k^2 - \omega^2\right)} \tag{4.2}$$

According to Mottershead (1998), Eq.(4.2) can be rearranged as follows:

$$h_{ii}(\omega) = \sum_{k=1}^{n} \frac{\varphi_{ik} \det\left(\Lambda - \omega^2 I\right)_k \varphi_{ik}}{\det\left(\Lambda - \omega^2 I\right)} \tag{4.3}$$

where $\det\left(\Lambda - \omega^2 I\right)_k = \left(\omega_1^2 - \omega^2\right)\left(\omega_2^2 - \omega^2\right)\cdots\left(\omega_{k-1}^2 - \omega^2\right)\left(\omega_{k+1}^2 - \omega^2\right)\cdots\left(\omega_n^2 - \omega^2\right)$

The driving point anti-resonance frequencies, which are just one-pin ABC frequencies, can be obtained by setting Eq.(4.3) to zero, thus:

$$\sum_{k=1}^{n} \varphi_{ik} \det\left(\Lambda - \omega_{1-pin\_i}^2 I\right)_k \varphi_{ik} = 0 \tag{4.4}$$

where ω_{1-pin_i} denotes anti-resonance from driving-point FRFs measured at point i (i.e. one-pin ABC frequency with pin at point i).

Differentiating each term in Eq. (4.4) with respect to a variable parameter p:

$$\begin{aligned} \frac{\partial}{\partial p}\left(\varphi_{ik} \det\left(\Lambda - \omega_{1-pin\_i}^2 I\right)_k \varphi_{ik}\right) = {} & \frac{\partial \varphi_{ik}}{\partial p} \det\left(\Lambda - \omega_{1-pin\_i}^2 I\right)_k \varphi_{ik} \\ & + \varphi_{ik} \frac{\partial}{\partial p}\left(\det\left(\Lambda - \omega_{1-pin\_i}^2 I\right)_k\right)\varphi_{ik} + \varphi_{ik} \det\left(\Lambda - \omega_{1-pin\_i}^2 I\right)_k \frac{\partial \varphi_{ik}}{\partial p} \end{aligned} \tag{4.5}$$

Based on Mottershead (1997), substituting Eq. (4.5) into Eq. (4.4) yields:

$$\frac{\partial \omega_{1-pin\_i}^2}{\partial p} = 2 \times \frac{\sum_{k=1}^{n} \frac{\partial \varphi_{ik}}{\partial p} \det\left(\Lambda - \omega_{1-pin\_i}^2 I\right)_k \varphi_{ik}}{\sum_{k=1}^{n} \varphi_{ik} \left(\sum_{\substack{p=1 \\ p \neq k}}^{n} \det\left(\Lambda - \omega_{1-pin\_i}^2 I\right)_{k,p} \right) \varphi_{ik}} + \frac{\sum_{p=1}^{n} \frac{\partial \omega_p^2}{\partial p} \left(\sum_{\substack{k=1 \\ k \neq p}}^{n} \det\left(\Lambda - \omega_{1-pin\_i}^2 I\right)_{k,p} \varphi_{ik} \varphi_{ik} \right)}{\sum_{k=1}^{n} \varphi_{ik} \left(\sum_{\substack{p=1 \\ p \neq k}}^{n} \det\left(\Lambda - \omega_{1-pin\_i}^2 I\right)_{k,p} \right) \varphi_{ik}} \tag{4.6}$$

From Eq. (4.6), it is clear that the sensitivity of the one-pin ABC frequencies to a particular structural parameter is a combination of the respective sensitivity of mode shapes at the same point and the sensitivity of the natural frequencies.

Hanson et al. (2007) also proposed the expression of anti-resonance sensitivity. A two-DOF system was used in their study, leading to a simplified expression of the FRF from Eq. (4.2) with n=2, and the subsequent sensitivity of the anti-resonance is effectively a special case of Eq. (4.6).

Theoretically speaking, based on Eq. (4.6), it is possible to calculate the contributions ("footprint") of the mode shapes in the driving-point anti-resonance (one-pin ABC) frequency sensitivities. Hanson et al. (2007) employed a ratio to represent the mode shape contributions in the sensitivities of the anti-resonances, with the following expression:

$$C = \frac{|\Phi|}{|\Omega| + |\Phi|} \tag{4.7}$$

where C is the relative mode shape contribution ratio, Ω denotes the natural frequency contribution in the anti-resonance (1-pin ABC) sensitivity, and Φ is the mode shape contribution in the anti-resonance (1-pin ABC) sensitivity,

$$\Omega = \frac{\sum_{p=1}^{n} \frac{\partial \omega_p^2}{\partial p} \left(\sum_{\substack{k=1 \\ k \neq p}}^{n} \det\left(\Lambda - \omega_{1-pin\_i}^2 I\right)_{k,p} \varphi_{ik} \varphi_{ik} \right)}{\sum_{k=1}^{n} \varphi_{ik} \left(\sum_{\substack{p=1 \\ p \neq k}}^{n} \det\left(\Lambda - \omega_{1-pin\_i}^2 I\right)_{k,p} \right) \varphi_{ik}} \tag{4.7a}$$

$$\Phi = 2 \times \frac{\sum_{k=1}^{n} \frac{\partial \varphi_{ik}}{\partial p} \det\left(\Lambda - \omega_{1-pin\_i}^2 I\right)_{k} \varphi_{ik}}{\sum_{k=1}^{n} \varphi_{ik} \left(\sum_{\substack{p=1 \\ p \neq k}}^{n} \det\left(\Lambda - \omega_{1-pin\_i}^2 I\right)_{k,p} \right) \varphi_{ik}} \tag{4.7b}$$

The effectiveness of using the ratio in a two-DOF system has been verified with both numerical and experimental studies (Hanson et al. 2007). Thus, the (1-pin) ABC frequencies that contain a larger mode shape contribution are expected to be

relatively more sensitive to damage and hence should be selected for the FE model updating.

4.2.2 Two-pin ABC frequency sensitivity and mode shape contributions

The above method of evaluating the anti-resonance (1-pin ABC) frequency sensitivity can be extended to two-pin ABC frequencies, thus Eq. (4.7) can also be employed to obtain mode shape contributions in the two-pin ABC frequency sensitivities.

As described in Chapter 3, two-pin ABC frequencies can be obtained by inverting the 2×2 FRF matrix measured at these two pin points, and each element (ABC curve) in the inverted matrix can be used to determine the two-pin ABC frequencies by identifying the singular (peak) frequencies.

For simplicity, consider only the first three natural modes in the structural response, the 2×2 FRF matrix can then be expressed as:

$$H = \begin{bmatrix} h_{ii} & h_{ij} \\ h_{ji} & h_{jj} \end{bmatrix} \tag{4.8}$$

where h_{ii} is the FRF containing the first three modes of information,

$$h_{ii} = \frac{\varphi_{i1}^2}{\omega_1^2 - \omega^2} + \frac{\varphi_{i2}^2}{\omega_2^2 - \omega^2} + \frac{\varphi_{i3}^2}{\omega_3^2 - \omega^2} \tag{4.8a}$$

Inverting the above matrix yields:

$$H^{-1} = \frac{1}{\left| h_{ii}h_{jj} - h_{ij}h_{ji} \right|} \begin{bmatrix} h_{jj} & -h_{ij} \\ -h_{ji} & h_{ii} \end{bmatrix} \tag{4.9}$$

From Eq. (4.9), the singular (peak) frequencies in the inverted matrix, i.e. the two-pin ABC frequencies, can be calculated by setting $\left| h_{ii}h_{jj} - h_{ij}h_{ji} \right|$ to zero:

$$\left(\frac{\varphi_{i1}^2}{\omega_1^2-\omega_{2-pin}^2}+\frac{\varphi_{i2}^2}{\omega_2^2-\omega_{2-pin}^2}+\frac{\varphi_{i3}^2}{\omega_3^2-\omega_{2-pin}^2}\right)\left(\frac{\varphi_{j1}^2}{\omega_1^2-\omega_{2-pin}^2}+\frac{\varphi_{j2}^2}{\omega_2^2-\omega_{2-pin}^2}+\frac{\varphi_{j3}^2}{\omega_3^2-\omega_{2-pin}^2}\right)- \left(\frac{\varphi_{i1}\varphi_{j1}}{\omega_1^2-\omega_{2-pin}^2}+\frac{\varphi_{i2}\varphi_{j2}}{\omega_2^2-\omega_{2-pin}^2}+\frac{\varphi_{i3}\varphi_{j3}}{\omega_3^2-\omega_{2-pin}^2}\right)^2=0 \tag{4.10}$$

From Eq. (4.10), the two-pin ABC frequencies with pins at *i* and *j* can be represented as:

$$\omega_{2-pin}^2=\frac{A1\times\omega_3^2+A2\times\omega_2^2+A3\times\omega_1^2}{A1+A2+A3} \tag{4.11}$$

where $A1=\left(\varphi_{i1}\varphi_{j2}-\varphi_{i2}\varphi_{j1}\right)^2$, $A2=\left(\varphi_{i1}\varphi_{j3}-\varphi_{i3}\varphi_{j1}\right)^2$, $A3=\left(\varphi_{i2}\varphi_{j3}-\varphi_{i3}\varphi_{j2}\right)^2$

The derivative of two-pin ABC frequencies with respect to a variable parameter p can be further expressed as follows:

$$\frac{\partial\omega_{2-pin}^2}{\partial p}=\frac{\left(\frac{\partial A1}{\partial p}\omega_3^2+\frac{\partial\omega_3^2}{\partial p}A1+\frac{\partial A2}{\partial p}\omega_2^2+\frac{\partial\omega_2^2}{\partial p}A2+\frac{\partial A3}{\partial p}\omega_1^2+\frac{\partial\omega_1^2}{\partial p}A3\right)(A1+A2+A3)}{(A1+A2+A3)^2} - \frac{\left(\frac{\partial A1}{\partial p}+\frac{\partial A2}{\partial p}+\frac{\partial A3}{\partial p}\right)\left(A1\times\omega_3^2+A2\times\omega_2^2+A3\times\omega_1^2\right)}{(A1+A2+A3)^2} \tag{4.12}$$

where $\frac{\partial A1}{\partial p}=2\left(\varphi_{i1}\varphi_{j2}-\varphi_{i2}\varphi_{j1}\right)\left(\frac{\partial\varphi_{i1}}{\partial p}\varphi_{j2}+\varphi_{i1}\frac{\partial\varphi_{j2}}{\partial p}-\frac{\partial\varphi_{i2}}{\partial p}\varphi_{j1}-\varphi_{i2}\frac{\partial\varphi_{j1}}{\partial p}\right)$

$$\frac{\partial A2}{\partial p}=2\left(\varphi_{i1}\varphi_{j3}-\varphi_{i3}\varphi_{j1}\right)\left(\frac{\partial\varphi_{i1}}{\partial p}\varphi_{j3}+\varphi_{i1}\frac{\partial\varphi_{j3}}{\partial p}-\frac{\partial\varphi_{i3}}{\partial p}\varphi_{j1}-\varphi_{i3}\frac{\partial\varphi_{j1}}{\partial p}\right) \tag{4.13}$$

$$\frac{\partial A3}{\partial p}=2\left(\varphi_{i2}\varphi_{j3}-\varphi_{i3}\varphi_{j2}\right)\left(\frac{\partial\varphi_{i2}}{\partial p}\varphi_{j3}+\varphi_{i2}\frac{\partial\varphi_{j3}}{\partial p}-\frac{\partial\varphi_{i3}}{\partial p}\varphi_{j2}-\varphi_{i3}\frac{\partial\varphi_{j2}}{\partial p}\right)$$

According to Eq. (4.12) and (4.13), it can be observed clearly that similar to one-pin ABC frequency sensitivity, the sensitivity of two-pin ABC frequency can also be

expressed with a combination of the natural mode shape sensitivities at the same points and the natural frequency sensitivities.

The mode shape contribution in the two-pin ABC frequency sensitivities can also be evaluated using Eq. (4.7), but the values of the mode shape sensitivity and natural frequency sensitivity are now expressed as:

$$\Phi = \frac{\left(\frac{\partial A1}{\partial p}\omega_3^2 + \frac{\partial A2}{\partial p}\omega_2^2 + + \frac{\partial A3}{\partial p}\omega_1^2 + \right)(A1 + A2 + A3)}{(A1 + A2 + A3)^2} - \frac{\left(\frac{\partial A1}{\partial p} + \frac{\partial A2}{\partial p} + \frac{\partial A3}{\partial p}\right)(A1 \times \omega_3^2 + A2 \times \omega_2^2 + A3 \times \omega_1^2)}{(A1 + A2 + A3)^2}$$

$$\Omega = \frac{\left(\frac{\partial \omega_3^2}{\partial p} A1 + \frac{\partial \omega_2^2}{\partial p} A2 + \frac{\partial \omega_1^2}{\partial p} A3\right)(A1 + A2 + A3)}{(A1 + A2 + A3)^2} \tag{4.14}$$

In what follows, a numerical case is employed to illustrate the outcome and the soundness of the one-pin and two-pin ABC frequency sensitivities with the above equations, before utilizing them in the process of selecting ABC frequencies for FE model updating.

4.3 Numerical verification of one-pin and two-pin ABC frequency sensitivities

A beam model is used for the numerical verification. Both one-pin and two-pin ABC frequency sensitivities are calculated using equations in Section 4.2, and these results are compared with those from the direct method, where the ABC frequency sensitivity is calculated using the ABC frequencies of the beam before and after the damage.

The beam has the same properties as the test beam described in Chapter 3. It is 1m long, and the cross section is 50 × 6 mm, and is made of steel. The beam is fully fixed at both ends. The rigidity (EI) of the beam is slightly tuned from the theoretical value to 162 $N.m^2$ so that its natural frequencies match those from the test beam with

the same dimension and boundary condition, allowing for easy comparisons in other aspects such as ABC frequencies where needed.

The first three natural frequencies from the FE model beam are 29.6Hz, 81.6Hz and 160Hz, respectively. The beam is divided into ten elements, thus nine measurement points can be employed to obtain ABC frequencies, as depicted in Fig. 4.1.

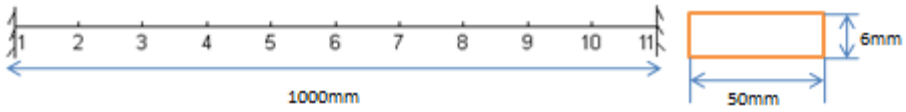

Figure 4.1 FE model of beam

For convenience, only the first order ABC frequencies are employed in the verification here. Similar observations can be extended to higher (2^{nd} and 3^{rd}) ABC frequencies as well.

A damage scenario is simulated with a 1% stiffness reduction at element 3, which is shown in Fig. 4.2.

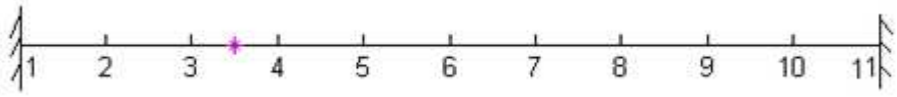

Figure 4.2 An arbitrary damage scenario in the beam

One-pin ABC frequency sensitivity is examined firstly. Given the beam properties, the sensitivity of one-pin ABC frequencies can be obtained using Eq. (4.6). It is noted that in the present calculation only the first three natural modes are used to form the FRF data.

Fig. 4.3 compares the results using the sensitivity equations with those calculated directly from the ABC frequencies before and after damage (direct method). The vertical axis is the sensitivity of squared one-pin ABC frequency, which is shown in Eq. (4.6).

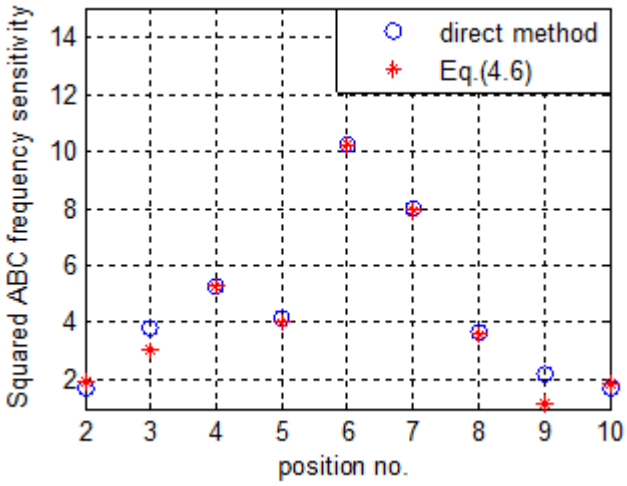

Figure 4.3 One-pin ABC frequency sensitivities (to damage in segment 3) obtained using different methods

It can be seen that the one-pin ABC frequency sensitivities calculated using Eq. (4.6) compare well with the direct results. The slight difference may be attributed to the fact that only the first few modes are employed to calculate the one-pin ABC frequency sensitivity using the equations. The variation of the sensitivity indicates that the one-pin ABC frequency (first order herein) shows the highest sensitivity when the pin is positioned at point 6, i.e. the mid-span. This is explicable as the first order ABC frequency when the pin is in the middle has the highest curvature over segment 3 where the particular damage is located.

Next, the sensitivity of two-pin ABC frequencies is examined. The two-pin ABC frequency sensitivities calculated using Eq. (4.12) and (4.13) are compared with the direct results of the two-pin ABC frequencies before and after damage. Fig. 4.4 shows the comparison. Note that numbers in the x-label indicates the two pin positions, for example, “12” means pins located at points 1 and 2. The vertical axis is the sensitivity of squared two-pin ABC frequency shown in Eq. (4.12).

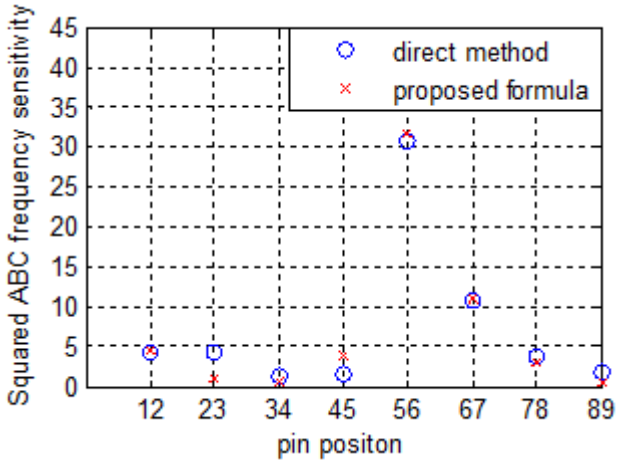

Figure 4.4 Two-pin ABC frequency sensitivities using different methods

It can be observed that the sensitivities evaluated using Eq. (4.12) and (4.13) agree well with the direct results. Similar to comparison results of one-pin ABC frequency sensitivity, the difference may be attributed to the fact that only the first few modes are used in the calculation with Eq. (4.12) and (4.13).

The above comparisons confirm that both one-pin and two-pin ABC frequency sensitivities can be satisfactorily evaluated using equations described in Section 4.2, which also indicates that these sensitivities are closely correlated with the first few (three herein) natural modes. This paves a way for the proposal of a methodology to select the ABC frequencies to be measured / included in a particular damage identification procedure.

4.4 Selection of ABC frequencies for effective FE model updating

In this section, a methodology for selecting ABC frequencies for FE model updating will be proposed and verified. As can be generally understood and also confirmed by previous studied (Hanson et al. 2007), when the updating parameter was sensitive to the mode shape data, the inclusion of anti-resonance with high mode shape contribution can significantly improve the convergence of updating results. A ratio expressing the mode shape contributions in the corresponding ABC frequency

sensitivities can be calculated and provided as a basis to select sensitive ABC frequencies.

4.4.1 Selection methodology

The sensitivity of an ABC frequency is defined with respect to a particular structural parameter, as expressed in Eq. (4.6), (4.12) and (4.13). For a set of different structural parameters, a set (vector) of ABC frequency sensitivities can be obtained. Therefore, depending upon whether or not prior knowledge about the damage positions is available, the selection method will differ.

4.4.1.1 Selection of ABC frequencies with prior knowledge of damage positions

When prior knowledge about the damage (stiffness reduction in particular) positions is available, the selection process is straightforward. The sensitivity of one-pin and two-pin ABC frequencies with respect to the stiffness of the damaged element can be calculated using Eq. (4.6), (4.12) and (4.13), then the mode shape contributions in the corresponding ABC frequency sensitivities can be obtained using Eq. (4.7). The ABC frequencies which exhibit higher mode shape contributions are selected, subject to a desirable total number, for FE model updating.

4.4.1.2 Selection of ABC frequencies without prior knowledge of damage positions

When the damage positions are not known beforehand, as in most practical applications, the selection needs to be based on the overall sensitivity of the ABC frequency with respect to all possible damage positions.

Generally speaking, assuming a structure with n elements, for a particular ABC frequency, its sensitivity to a damage (stiffness reduction) in element i is defined as S_i, thus in total n sensitivities of the ABC frequency can be obtained, the sensitivity vector S containing these sensitivities can be written as (S_1, S_2, …, S_{n-1}, S_n). For each ABC frequency sensitivity, the mode shape contribution index C can be calculated using Eq. (4.7), thus a vector of index C can be formed as **C** = (C_1, C_2, …, C_{n-1}, C_n). Based on the mode shape contribution vector **C**, the overall sensitivity of a ABC frequency may be expressed as:

$$\overline{C} = \mu_C + \mu_C / \sigma_C \tag{4.15}$$

where μ_C and σ_C are mean value and standard deviation of the vector **C**.

With the above index $\overline{C}$, the ABC frequencies with higher mean value and smaller standard deviation value will be selected, which means these ABC frequency sensitivities have collectively higher mode shape contributions to all possible damage scenarios.

Take the beam with ten elements shown in Fig. 4.1 as an example. There could be ten possible single damage positions. For each ABC frequency, a sensitivity vector **S** includes ten sensitivities with respect to elemental stiffness of ten possible positions, which can give ten mode shape contributions in vector **C**. Subsequently the $\overline{C}$ value in Eq. (4.15) can be calculated for the selection of ABC frequencies.

Fig. 4.5 depicts the index values of different ABC frequencies from the above beam, these frequencies include the first two orders of one-pin ABC frequencies and the first order two-pin ABC frequencies. From the figure it can be seen that the proposed index values stretch over a diverse range, from 20 to 60 herein, and this indicates that separation (selection) of the more sensitive ABC frequencies can be made using the index without ambiguity.

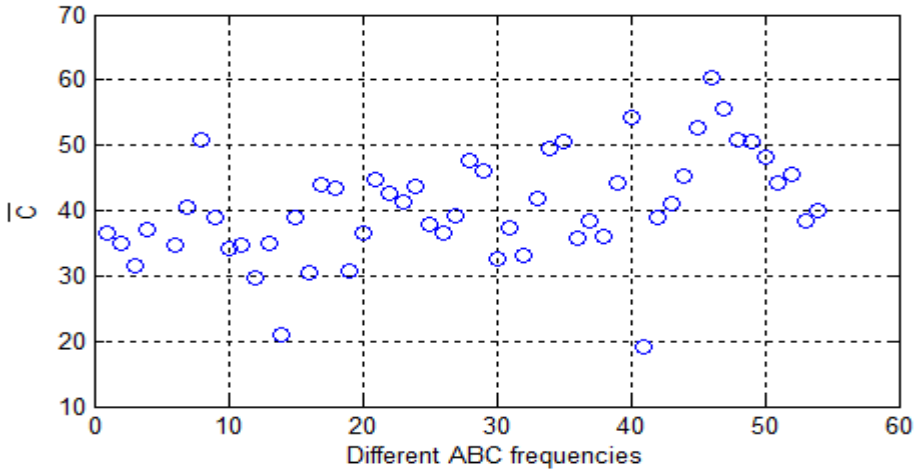

Figure 4.5 ABC frequency sensitivity index (mode shape contribution ratio) values

4.4.2 Numerical verification of the selection method with prior knowledge of damage positions

The same beam model mentioned above (shown in Fig. 4.1) is used to verify the performance of the selection method in FE model updating.

For first scenario with prior knowledge of the damage position, an arbitrary single damage is simulated by a 50% stiffness reduction at the 3rd element. The candidate ABC frequencies include the first two orders of one-pin ABC frequencies and the first order two-pin ABC frequencies. For comparison, two different sets of ABC frequencies are used for FE model updating. The first set includes ten ABC frequencies having larger mode shape contributions, while the second set includes ten ABC frequencies having smaller mode shape contributions. It should be mentioned that for the present verification, the ABC frequencies are free of noises (no noises added), and thus the difference in the updating results is only attributable to the performance of the selected ABC frequencies.

The actual FE model updating is carried using a genetic-algorithm powered model updating procedure. More details of this procedure will be given in Section 4.6.

Fig. 4.6 depicts the updating results using the two different sets of ABC frequencies datasets, the corresponding root mean square errors and the maximum percentage errors in the updating results. It is noted that the parameters being updated are represented by a stiffness ratio, which is defined as the ratio between the variable elemental rigidity and the original (undamaged) elemental rigidity.

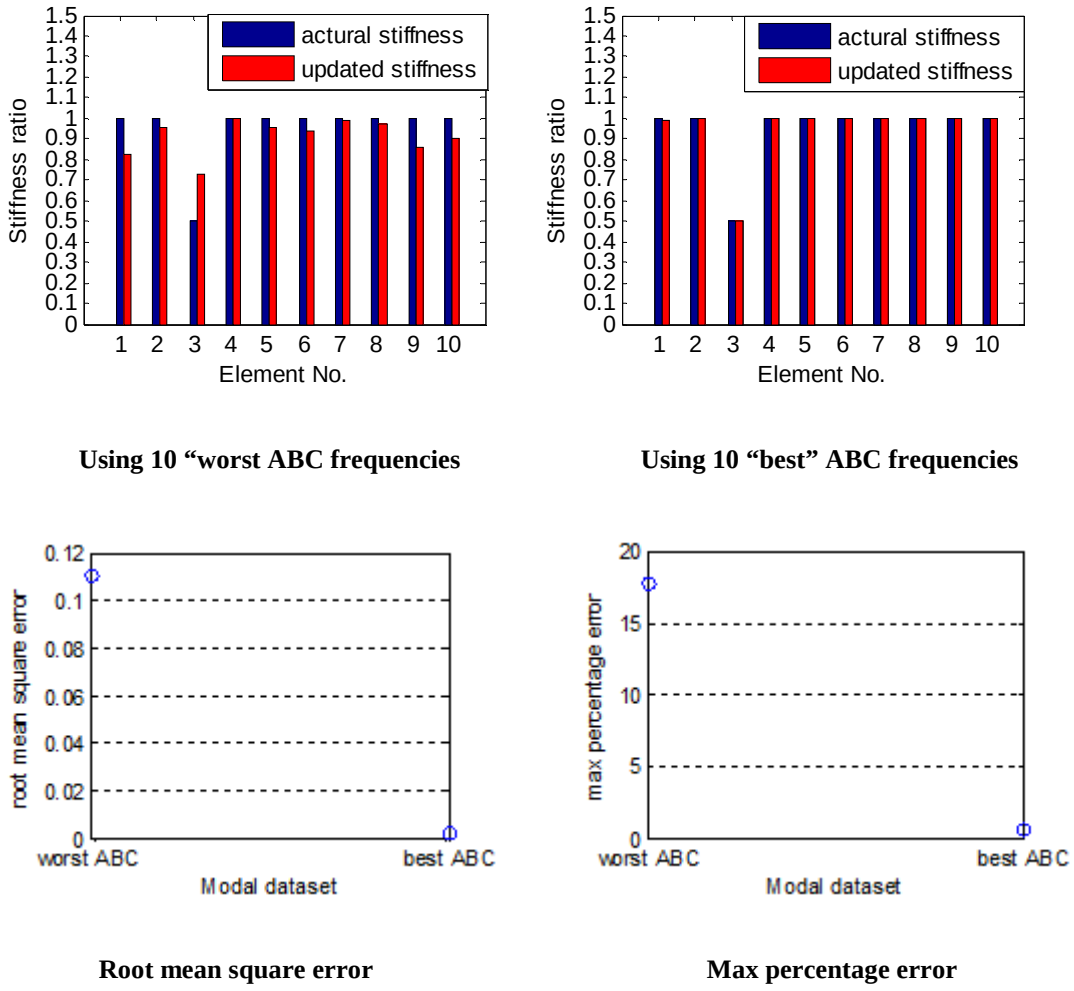

Using 10 "worst ABC frequencies

Using 10 "best" ABC frequencies

Root mean square error

Max percentage error

Figure 4.6 Updating results using different ABC frequencies (noise-free) and comparison

From the updating results shown in Fig. 4.6, it can be seen that the performance of the "best" 10 ABC frequencies selected by the mode shape contribution criterion is superior over that of the 10 "worst" ABC frequencies. Without the influence of measurement noises, the accuracy of the updating results using the 10 "best" ABC frequencies is almost perfect, with a root mean square error (RMSE) and maximum percentage error (MPE) approaching zero. On the other hand, with the "worst" 10

ABC frequencies, the RMSE and MPE of the updated results are about 11% and 18%, respectively.

To further evaluate the effect of the selection method under practical conditions, the computed (exact) ABC frequencies are treated by injecting measurement noises before they are employed in the FE updating procedure. For this purpose, a 1% uniformly distributed random error is added to the ABC frequencies to simulate more realistic ABC frequencies as would be extracted from an experiment. Fig. 4.7 shows the FE model updating results using noise-contaminated ABC frequencies. For comparison, results using 4 sets of ABC frequencies, ranging from collectively the "worst" to the "best" sets according to the different ABC frequency sensitivity index ($\overline{C}$) values calculated using Eq. (4.15), are presented. It should be mentioned that the same number (ten) ABC frequencies is used in each set.

The results and comparison further confirm that, even with the inclusion of the measurement noises in the ABC frequencies, the employment of "better" ABC frequencies that contain higher mode shape contributions tends to yield better updating results. When the "worst" set of ABC frequencies with ABC frequency sensitivity value $\overline{C}$ less than 35 is used, the updated results exhibit errors as large as 15% in terms of RMSE and 25% in terms of MPE. On the other hand, when the "best" set of ABC frequencies is used, the updating results are very good with only about 2% RMSE and 3% MPE.

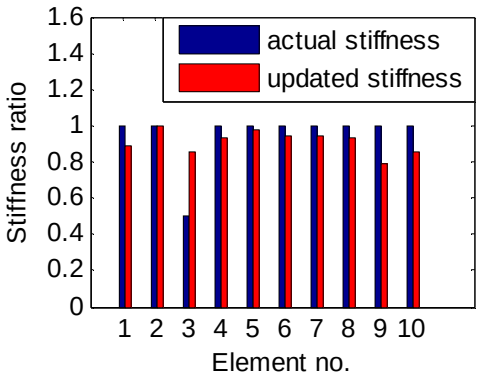

$\overline{C}$ < 35

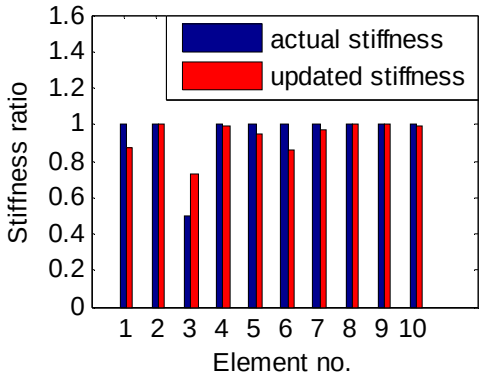

35< $\overline{C}$ <40

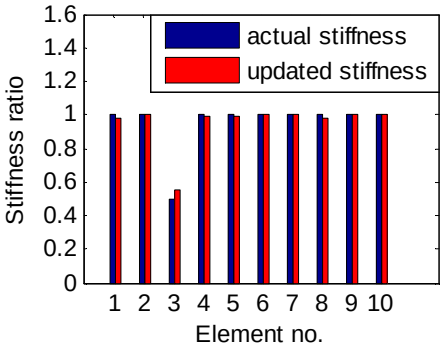

40< $\overline{C}$ <47

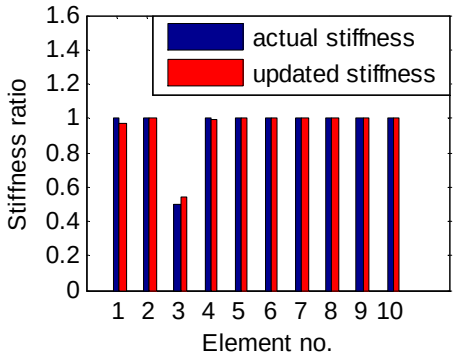

$\overline{C}$ >47

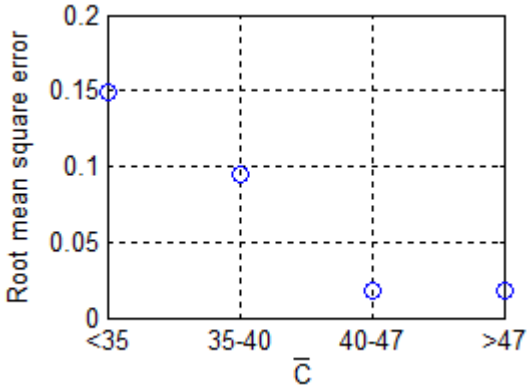

Root Mean Square Error

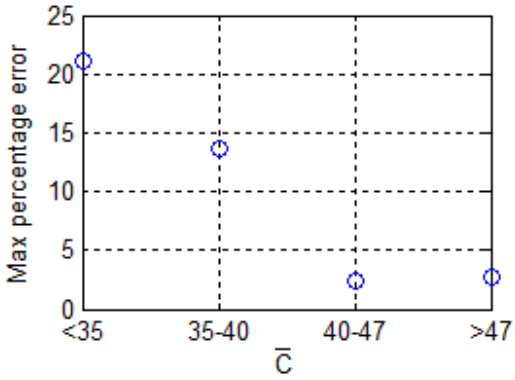

Max percentage error

Figure 4.7 Updating results using different ABC frequencies (noise added) and comparison

4.4.3 Numerical verification of the selection method without prior knowledge of damage positions

For this verification, different damage scenarios are considered to examine the performance of the proposed index in Eq. (4.15). Similar to the analysis in the above section, two datasets of ABC frequencies are employed in the FE model updating procedure. The first dataset includes ten ABC frequencies having the largest sensitivity index values (in terms of the mode shape contributions), while ten ABC frequencies with the smallest index values are used in the second dataset. 1% uniformly distributed random noises are added to the ABC frequencies to simulate measurement errors in all the ABC frequencies. The updating results are illustrated in Fig. 4.8.

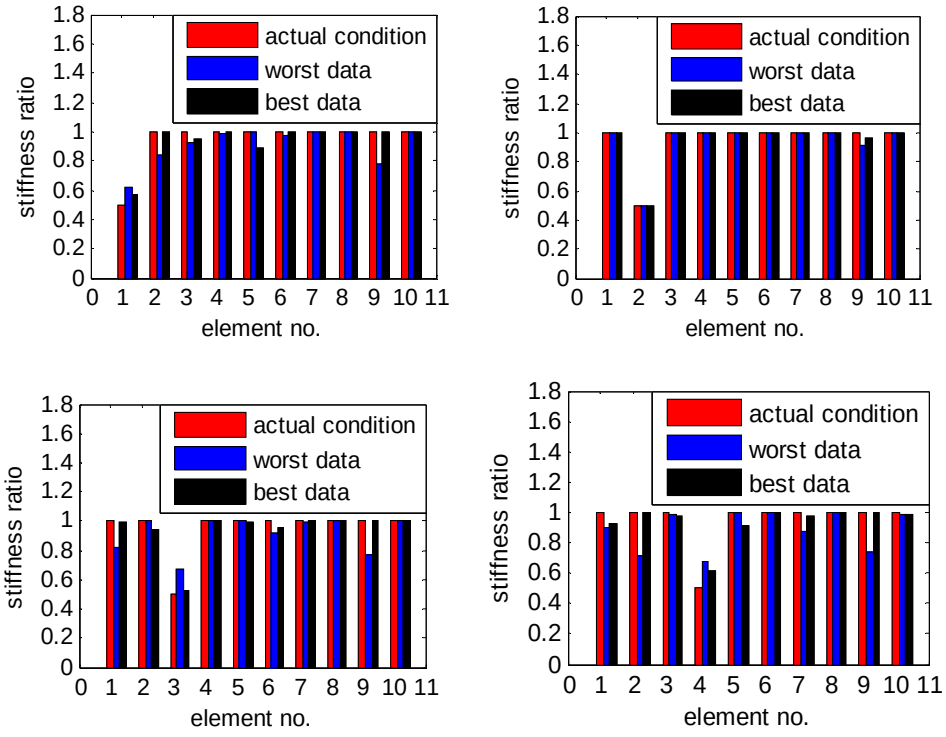

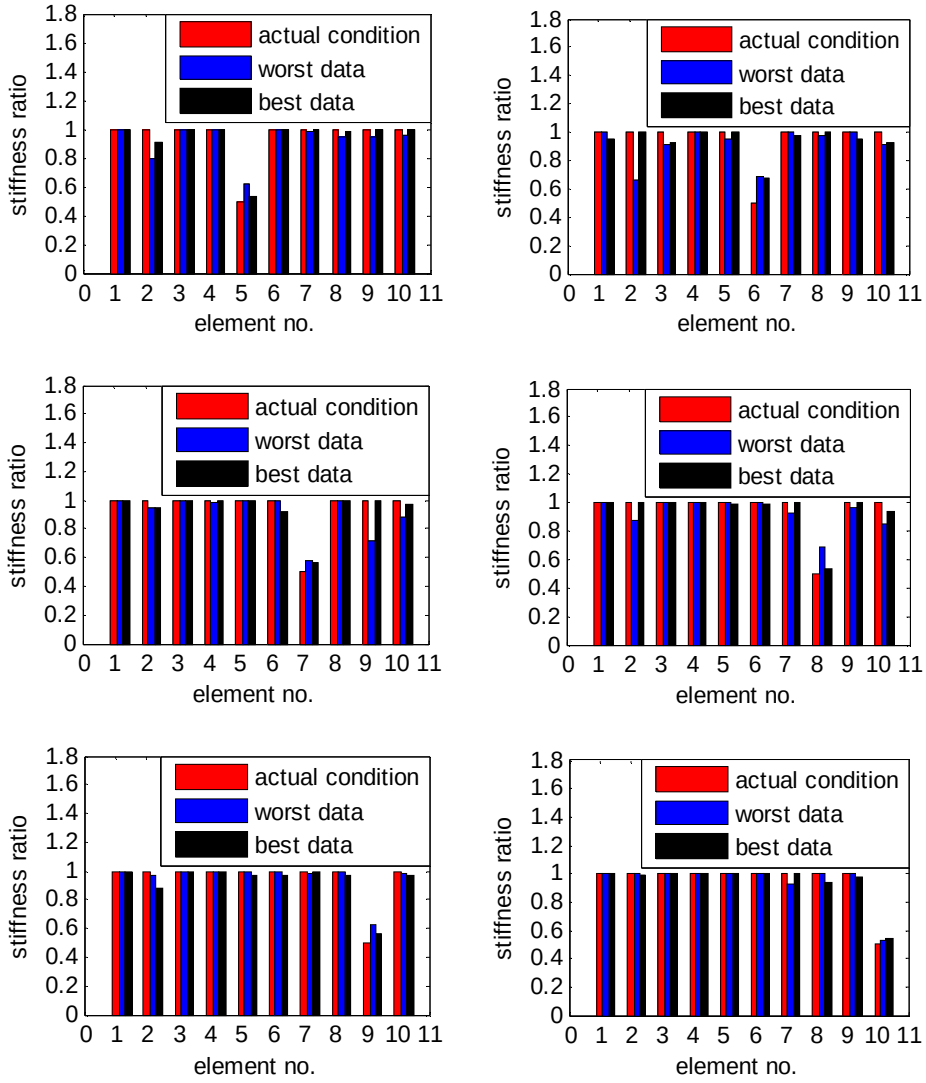

(a) Updating results for damage in element 1 to 10 consecutively

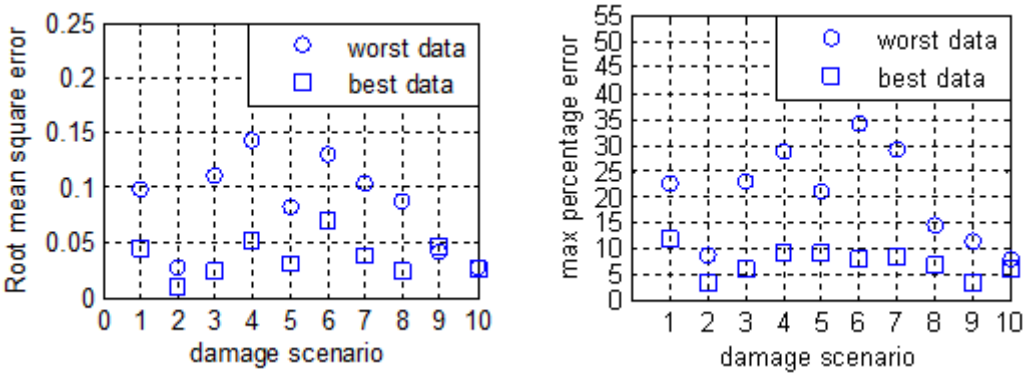

(b) Updating errors (RMSE and MPE) for each damage scenario

Figure 4.8 Updating results using the "best" and "worst" sets of ABC frequencies for various damage scenarios

From the results shown in Fig. 4.8, it can be seen that the performance of the “best” ten ABC frequencies is clearly and consistently superior over the “worst” ten ABC frequencies. Using the ten “best” ABC frequencies, the maximum RMSE and MPE of updated results are about 7% and 12%, respectively; whereas with the “worst” ten ABC frequencies the maximum RMSE and MPE in the updating results can approach as high as 15% and 35%, respectively.

It is worth noting that there exists differences in the updating results for the symmetrical damage scenarios, while theoretical speaking, the updating results for symmetrical cases should be exactly the same. These differences can be attributed to two factors; one is that the added 1% noise in the frequencies may cause variation in the updating results, and another is that the searching path in GA may not be the same in each case, which will also give different updating results.

It should be pointed out that in all the above numerical simulations, only a single damaged element has been assumed in each individual case. This is mainly for the convenience of presenting and comparing the results across different damage scenarios. In fact, during the model updating, all elements have been assumed to have variable damage (stiffness) parameters. Therefore, as far as the model updating procedure is concerned, the observations are generally applicable, regardless whether the problem involves just one or multiple damage locations. For illustration, two multiple-damage cases are considered and the updating is performed also using the ‘best’ and ‘worst’ ten ABC frequencies, respectively. The results are shown in Fig. 4.9. It can be observed that for multiple damage scenarios, the ‘best’ ten ABC frequencies still perform better than the ‘worst’ ten ABC frequencies.

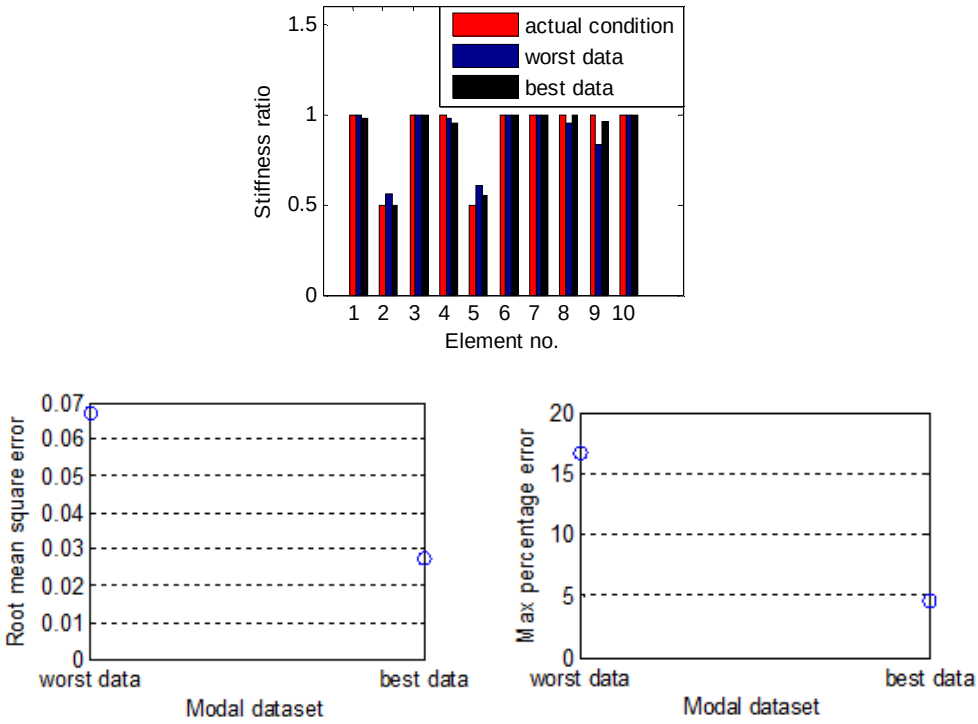

(a) 50% stiffness reductions at elements 2 and 5

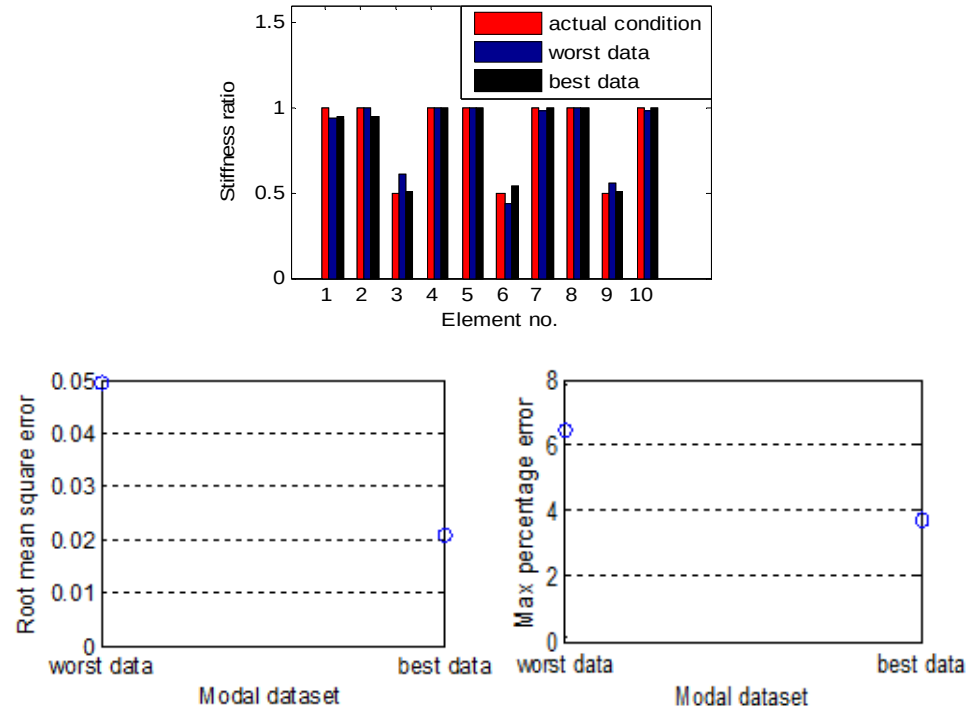

50% stiffness reductions at elements 3, 6 and 9

Figure 4.9 Updating results using the "best" and "worst" sets of ABC frequencies for multiple damage scenarios

It should be pointed out that in the above numerical examples, ten unknown parameters are updated using only ten ABC frequencies, which is deemed adequate for cross-comparison between the use of different sets of ABC frequencies (with different ranges of the sensitivity index). A general examination with regard to the effect of the ABC data size on the updating results will be carried out in the next section.

4.5 Investigation of size of ABC frequency dataset in FE model updating

As mentioned in Section 4.1, there is an optimum range of the amount of modal data to be included in a FE model updating procedure. It is generally understood that the number of modal data should be 2-3 times the number of parameters being updated in order to achieve a satisfactory result (Kwon and Lin, 2003). Due to inevitable measurement errors, employing too many modal data could introduce conflicting tendencies during the updating process and thus adversely affect the updating results, and evidences of such phenomenon have been reported in a number of occasions (e.g. Xia and Hao, 2000, He and Fu, 2001, Zhang et al. 2006). The use of the rule of "2-3 times" has been adopted in many previous studies (e.g. Friswell et al. 1998, Xia and Hao, 2000, Lu and Tu, 2003 and 2008, Zhang et al. 2006).

In this section, we shall examine whether the above general observations also apply in the case of using ABC frequencies. Firstly, two groups of twenty ABC frequencies are employed for the model updating; one group includes ABC frequencies with larger sensitivity index ($\overline{C}$) values, and the other includes ABC frequencies having smaller sensitivity index values. Thus, the two groups are effectively the expanded sets from the cases using 10 ABC frequencies in Section 4.4. The updating results and their percentage errors are shown in Fig. 4.10.

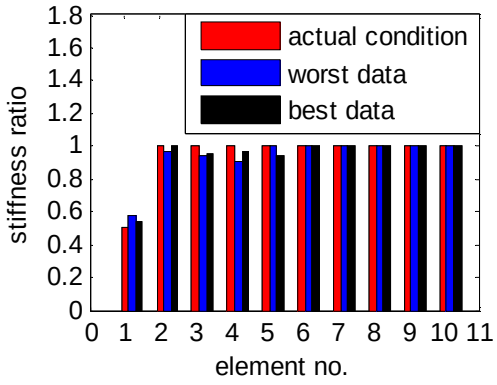
actual condition
worst data
best data
stiffness ratio
element no.

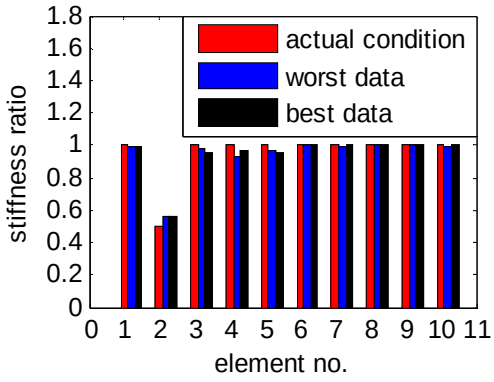
actual condition
worst data
best data
stiffness ratio
element no.

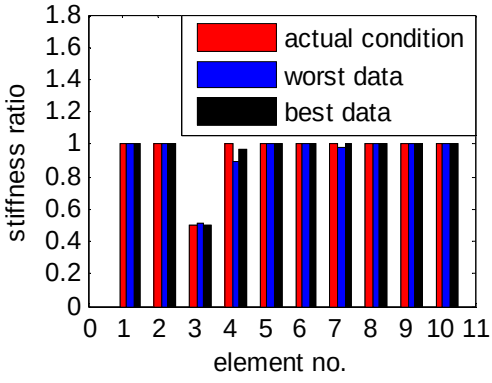
actual condition
worst data
best data
stiffness ratio
element no.

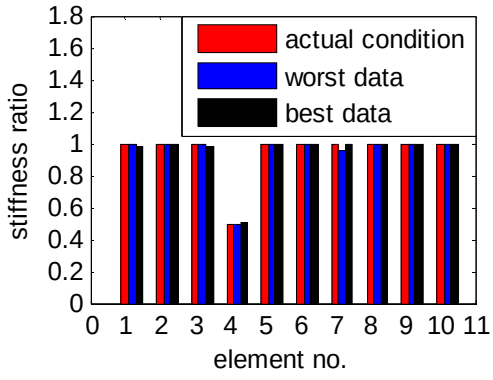
actual condition
worst data
best data
stiffness ratio
element no.

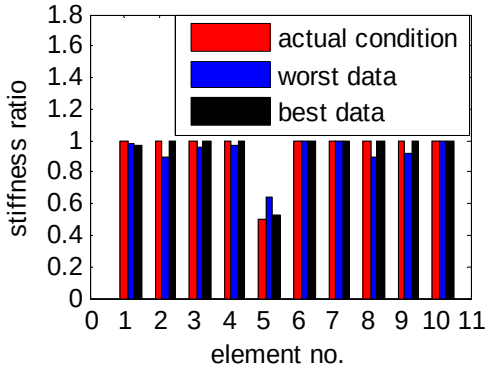
actual condition
worst data
best data
stiffness ratio
element no.

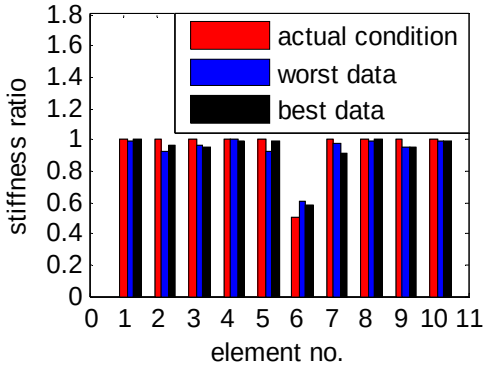
actual condition
worst data
best data
stiffness ratio
element no.

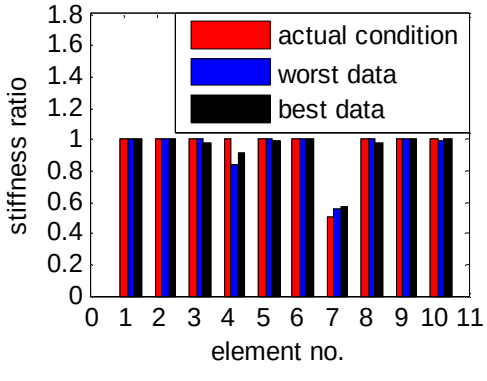
actual condition
worst data
best data
stiffness ratio
element no.

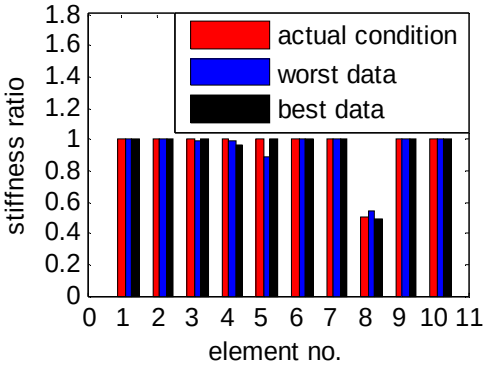
actual condition
worst data
best data
stiffness ratio
element no.

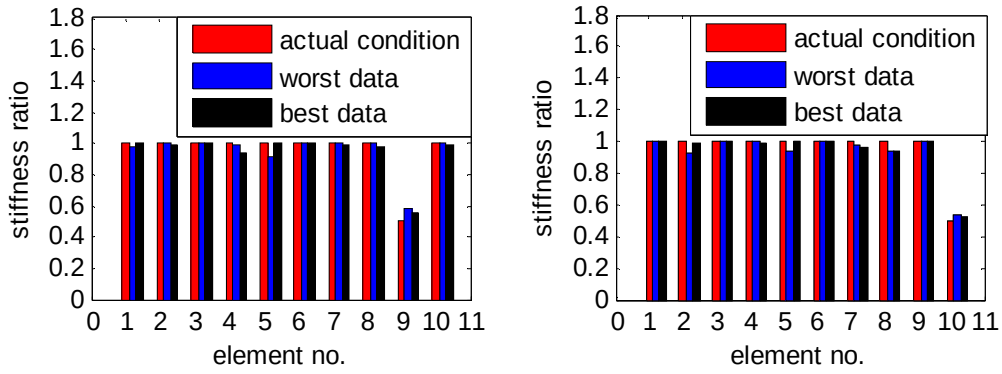

(a) Updating results for damage in element 1 to 10 consecutively

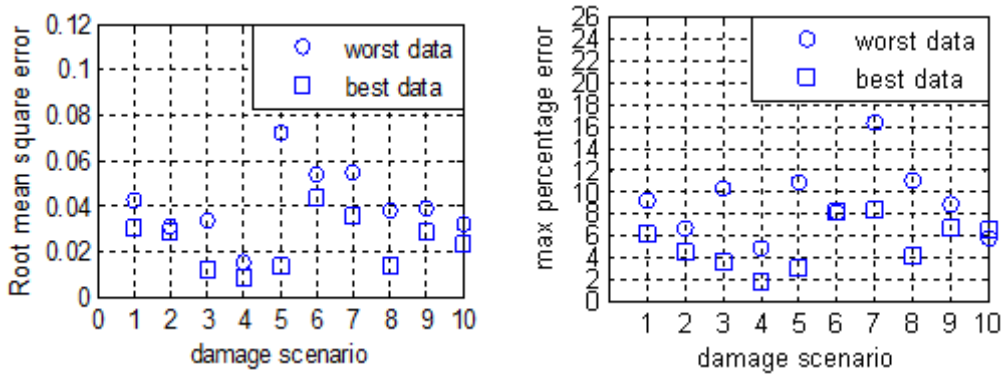

(b) Updating errors (RMSE and MPE) for each damage scenario

Figure 4.10 Updating results using 20 ABC frequencies for various damage scenarios

It can be seen that, when 20 ABC frequencies are employed for the updating of 10 parameters, the results from the set of ABC frequencies having higher $\overline{C}$ index values still produce better results. However, comparing with the results using ten ABC frequencies (Fig. 4.8(b)), increasing to twenty ABC frequencies does not improve the results much further for the case with the "best" ABC frequencies, indicating that the "best" ABC frequencies as selected according to the ABC sensitivity index (mode shape contributions) indeed contain more significant information. On the other hand, increasing to twenty ABC frequencies in the case of the "worst" ABC frequencies does improve the updating results markedly, and this is expected according the "2-3 times" rule mentioned before. In the particular case with ABC frequencies herein, this may be explained by the fact that, although the ABC frequencies with a smaller index contains less (sensitive) mode shape information, by

increasing the number of ABC frequencies, the overall mode shape information gets enhanced.

Next, we shall examine the updating results when too many ABC frequencies are involved. For this purpose all 54 ABC frequencies, including one-pin ABC frequencies from the first two modes and two-pin ABC frequencies from the first mode, are employed in the model updating for each damage scenario. Similar to the previous cases, 1% uniformly distributed random noises are added to ABC frequencies to simulate measurement errors. Fig. 4.11 shows the results in terms of the RMSE and MPE from using 20 ABC frequencies having larger index values and using all 54 ABC frequencies.

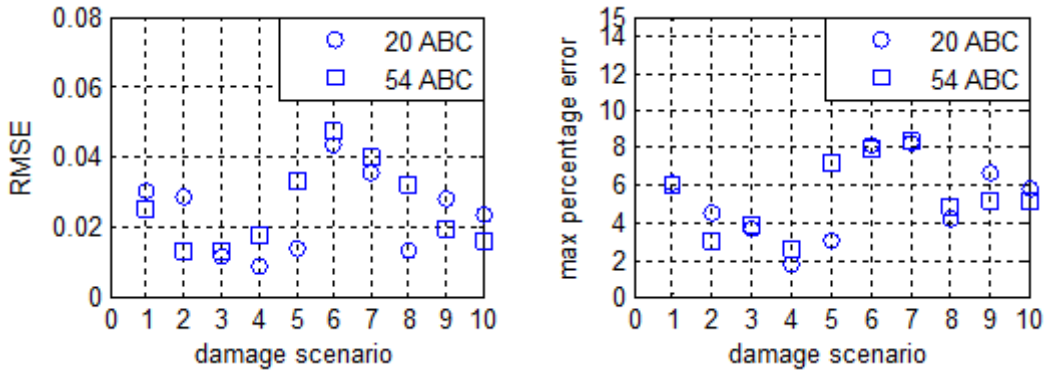

Figure 4.11 Updating results using different numbers of ABC frequencies

It can be found clearly that by further increasing ABC frequencies for the model updating, results do not show appreciable further improvement. In fact, some results using all 54 ABC frequencies exhibit even larger RMSE and MPE errors than those using 20 ABC frequencies, for example in damage scenarios 4,5,6,7 and 8.

The detailed accuracy profiles will understandably vary as the level of measurement errors (herein assumed 1%) in the ABC frequencies and structural setting vary. However, the results presented above tend to suggest that with ABC frequencies, the general rule on the amount of modal data to be included in the FE model updating still holds. In order words, when employing ABC frequencies in practice (containing some normal level of measurement noises) for model updating, the number of ABC

frequencies should be kept about 2-3 times of the number of unknown parameters in order to achieve an effective and efficient FE model updating process.

4.6 Comprehensive application: FE model updating of a physical test beam

In this section, an application of the above ABC frequency selection and size proposals on a physically tested beam, with the ABC frequencies extracted from the actual experiment, is presented. To provide a complete picture, the GA-powered FE model updating procedure, which is employed in all FE model updating processes in this thesis, is briefly described before going into the case study.

4.6.1 Overview of FE model updating with Genetic Algorithms (GAs)

In the context of structural identification and damage diagnosis, finite element model updating may be regarded as the most comprehensive model-based approach. In this procedure, variable model parameters, such as stiffness of individual elements, are updated so that the predicted response from the FE model matches the measured counterparts from the real structure. Clearly, the effectiveness and reliability of such a procedure depends upon a) the availability of a sufficient amount of sensitive and accurate response data, and b) a robust parameter search / optimization algorithm.

As an alternative to mode shape data, which is generally known as being difficult to measure with high accuracy, the present study proposes to resort to the ABC frequencies, which, together with any amount of natural frequencies, can form a sufficient dataset for the identification of a large number of parameters in the structure.

Once a desirable set of ABC frequencies are acquired according to the measurement and data processing procedure described in Chapter 3 and the selection criterion presented in the earlier sections of this chapter, the FE model updating procedure can

proceed. In this process, the variable parameters (stiffness factors) are adjusted in each round of updating such that the difference between the measured response data (herein natural and ABC frequencies) and the FE predicted counterparts falls within an acceptable margin of error or the updating has undergone a predefined number of iterations.

The traditional techniques for FE model updating is iterative based methods, such as sensitivity based analysis, which employs the sensitivity matrix to correct the predicted response based on actually measured data (e.g. Ricles, 1991, Hemez, 1993). However, it has been recognised that these iterative based techniques may often be trapped into a local optimum instead of a global solution, and moreover, the sensitivity matrix used in the analysis should be updated in each step, which may makes the calculation rather time-consuming (Mottershead and Friswell, 1993, Doebling and Farrar, 1997). In this respect, utilisation of artificial intelligence algorithms, particularly GAs as employed in the present study, has profound advantages.

A detailed treatment of GA-powered finite element model updating and relevant background literature can be found in Tu and Lu (2007). A brief overview of the key operations, along with the definition of a specific objective function incorporating the ABC frequencies, is given in what follows.

GA is a powerful global optimization technique that is derived from the process of natural selection and evolution in biology, following the rule of ‘survival of the fittest’. Compared to traditional optimization methods, GA searches from a population of points, not a single point, and it uses the information in the objective function itself to evaluate the results.

The basic elements in GA are “chromosome”, which code the information about different variables using different number of “genes”. The quality of the solution represented by the chromosome, i.e. the “fitness”, is determined by the value of a pre-defined objective function. Several steps are performed in the GA optimization procedure in searching for the variable (known) parameters, including initialization, selection, crossover and mutation.

As the procedure of FE model updating using GA optimization technique is essentially to adjust (through evolution) the unknown structural parameters to minimize the objective function, so that the predicted responses from the updated model match well with the experimental counterparts, the definition of the objective function is crucial. Herein the modal dataset includes natural frequencies (where needed) and ABC frequencies, the objective function is therefore defined to include two parts relating to natural frequency errors J_ω and ABC frequency errors J_{ABC}, respectively, with appropriate weighting:

$$J = W_\omega J_\omega + W_{ABC} J_{ABC} \tag{4.16}$$

where W_ω and W_{ABC} are weighting factors. In view of the general tendency that the ABC frequencies under one-pin and two-pin conditions in the first three modes may be extracted with similar accuracy as natural frequencies, the same weighting for W_ω and W_{ABC} can be used.

By organizing the natural frequency errors and ABC frequency errors, Eq. (4.16) can be re-written as:

$$J = \sum_{i=1}^{N} \left(\frac{\omega_{mi} - \omega_{ai}}{\omega_{mi}} \right)^2 \tag{4.17}$$

or in a modified form:

$$J = \frac{1}{N} \sum_{i=1}^{N} \left| \frac{\omega_{mi} - \omega_{ai}}{\omega_{mi}} \right| \tag{4.18}$$

where ω_{mi} and ω_{ai} denotes the measured and analytical frequencies, respectively, N is the number of frequencies in the dataset.

The variables for updating are the uncertain structural parameters. In the beam case considered herein, the flexural stiffness in all individual beam segments are assumed to be unknown and need be identified (updated). For normalisation, the stiffness factor, which is defined as the ratio between the “actual” elemental stiffness and the

"intact" elemental stiffness, is used in the updating process. Thus, the range for the stiffness factor to be updated is between 0 and 1, with 1 indicating no change (no damage) and 0 indicating total failure.

Real coding GA is used in this study, and accordingly a heuristic crossover method is employed. In this method, if the parent A is better than parent B (by comparing fitness – i.e. objective function – values), the following operation will be carried out to obtain the next generation:

$$\begin{aligned} A' &= A + r(A - B); \\ B' &= A; \end{aligned} \tag{4.19}$$

where A' and B' are the descendants, r is the random value taken from 0 to 1.

In the mutation step, uniform mutation method is selected. With this method, the selected gene is replaced with a random number taken within the boundary.

According to previous studies, in most cases, the probabilities for crossover and mutation can be selected within 0.6-0.9 and 0.01-0.02 to achieve reasonable solutions, but a lower crossover probability and higher mutation probability should be used for real coding GA. Therefore, in this study, the probabilities for crossover and mutation are selected as 0.7 and 0.02, respectively. These parameters are listed in the Table 4.1 .

Table 4.1 GA configuration

Max generation	1,000
Selection method	Ranking selection
Crossover method	Heuristic crossover
Crossover probability	0.7
Mutation method	Uniform mutation
Mutation probability	0.02

4.6.2 FE model updating with ABC frequencies for the test beam

The test beam with damage introduced by multiple cuts in a local region (Fig. 3.28) is employed in this analysis. Fig. 4.12 shows a schematic of the damage in terms of the stiffness change over the length of the beam. The damage is located at about 0.33-0.36m from the left beam end, and the stiffness factor in the damaged region was about 0.7 (or 30% reduction) and the damaged length was about 100mm. In the FE model for updating, which includes 10 beam elements, the damage is in beam element 4.

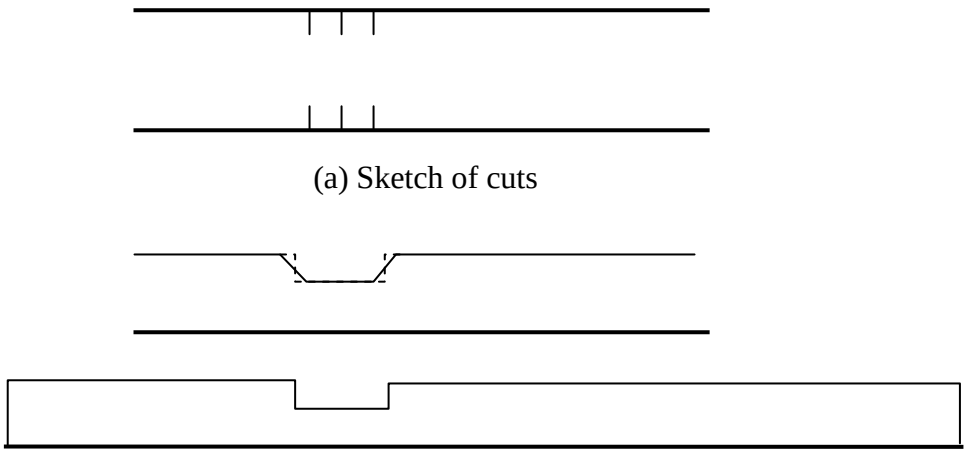

(a) Sketch of cuts

(b) Equivalent stiffness reduction

Figure 4.12 Schematic of damage and the corresponding stiffness change

As described in Chapter 3, using the recommended test and data analysis procedure, the one-pin and two-pin ABC frequencies from the lowest three modes can be extracted clearly and exclusively in this test beam case.

With the selection method described in Section 4.4.1, 20 ABC frequencies having higher mode shape contributions are selected from the entire set of measured one-pin and two-pin ABC frequencies. Note that for this application the lowest three natural

frequencies are also extracted and included in FE model updating. The model updating results and corresponding percentage errors are shown in Fig. 4.13.

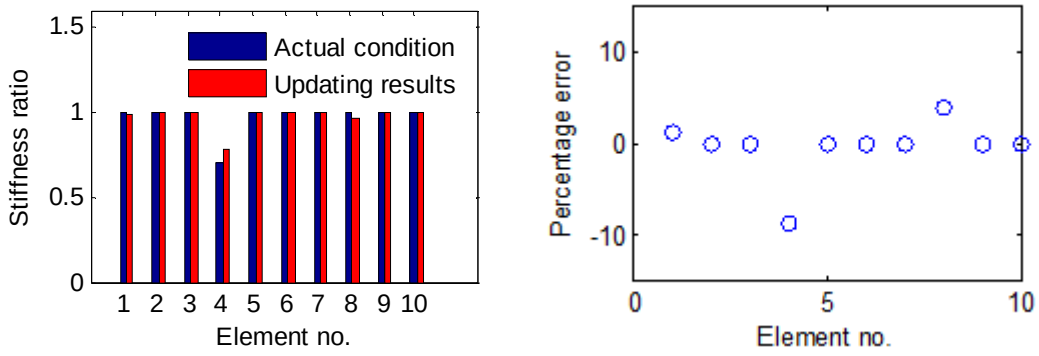

Figure 4.13 Model updating results using 20 selected ABC frequencies (left) and corresponding percentage errors (right)

The results prove to be very good; the stiffness ratios for most of the 10 beam elements are predicted within a margin of error of 3%, while the predicted stiffness in the damaged element has an error of less than 10%. The average percentage error in all stiffness parameters is 1.38%, which is of similar accuracy as in the numerical examples using 20 selected ABC frequencies described in Section 4.4. Such results demonstrate that, using experimental ABC frequencies, both the damage location and the severity could be successfully identified in physical structures when a similar test condition could be achieved.

4.7 Possible formulation of direct ABC frequencies-based damage index: a mode-shape curvature analogy

4.7.1 Formation of ABC-based damage index

Since ABC frequencies are derived from the inverted incomplete FRF function matrix, it is understandable that the ABC frequencies will reflect in a certain way the essential modal information contained in the FRF functions, including the mode

shapes and natural frequencies, which have been confirmed with the ABC frequency sensitivity expression. Therefore, it is reasonable to expect that an appropriate combination of the ABC frequencies could yield indication of the location and severity of damage in the structure. In particular, if an analogy between a collection of the ABC frequencies and the natural mode shapes may be established, one could extend some existing damage indices using the mode shape information to ABC frequencies. Such an analogy is examined in this section. For simplicity and without losing generality, we shall confine to the collection of one-pin ABC frequencies.

To simplify the formulation, herein the one-pin ABC frequencies are to be expressed considering their relationship with the first two natural modes. In this case, the driving-point FRF at the i-th DOF can be represented by the following truncated expression:

$$FRF_{ii}(\omega) = \frac{\phi_{i1}^2}{\omega_1^2 - \omega^2} + \frac{\phi_{i2}^2}{\omega_2^2 - \omega^2} \tag{4.20}$$

where ϕ_{i1}, ϕ_{i2} denote the first two mode shapes at the i-th DOF, and ω_1, ω_2 are the first two natural frequencies of the original system.

For a particular driving point (i-th DOF), anti-resonance occurs at frequencies where Eq. (4.20) becomes zero. Accordingly, the anti-resonance frequencies at measurement point i can be obtained as:

$$\omega_{i,1}^2 = \gamma_i \omega_1^2 + (1 - \gamma_i)\omega_2^2 \tag{4.21}$$

where $\omega_{i,1}$ is the first order one-pin ABC frequency at point i, and $\gamma_i = \left(1 + \left(\phi_{i1}^2 / \phi_{i2}^2\right)\right)$

From Eq. (4.21) it can be seen that anti-resonances (one-pin ABC frequencies) has a direct relationship to the mode shape displacements at the same DOF. As such, a mode shape-based damage index may be extended to using the one-pin ABC frequencies instead of the mode shape information. Herein we shall examine the mode shape curvature method when it is extended to using the one-pin ABC

frequencies, and whether such an ABC-frequency curvature index will be effective in damage detection.

Similar to the mode shape curvature, the ABC frequency curvature at point i may be approximated using the following equation:

$$\omega_{i,k}^{"} = \frac{\omega_{i+1,k} + \omega_{i-1,k} - 2\omega_{i,k}}{(\Delta h)^2} \tag{4.22}$$

where Δh is the distance between two adjacent measurement points, and $\omega_{i,k}$ is the k-th order ABC frequency with pin at point i.

Analogous to the employment of mode shape curvature in damage detection, the difference between the ABC frequency curvatures calculated with Eq. (4.22) before and after damage is expected to be larger at locations where damage (stiffness reduction) occurs, and hence may be used as a damage location indicator. This damage index is defined as the normalized curvature difference before and after damage

$$D_{i,k} = \frac{\Delta\omega_{i,k}^{"}}{\omega_{i,k}^{"}} = \frac{\left|\omega_{i,k}^{"} - \omega_{i,k}^{d"}\right|}{\omega_{i,k}^{"}} \tag{4.23}$$

4.7.2 Numerical examples

Unlike the mode shape curvature, the above defined ABC frequency curvature actually contains mode shape information from more than one modes, as well as information natural frequencies in a complex combination. Therefore it is expected that the representativeness of the above ABC frequency curvature-based damage index will not be straightforward. This is examined in the numerical examples that follow.

The same beam as used before is simulated for the verification of ABC frequency curvature effects. Herein the beam model is divided into 30 elements, which is

consistent with the arrangement of the measurement points shown in Fig. 3.1(b). The damage is simulated as the rigidity reduction in individual beam elements.

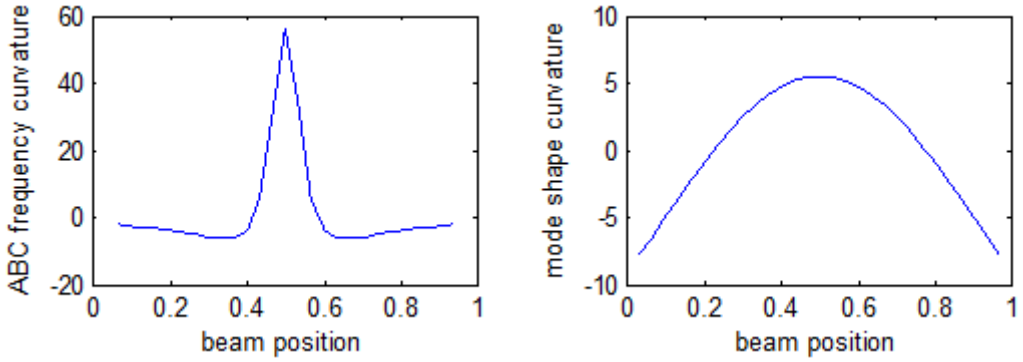

a) First mode

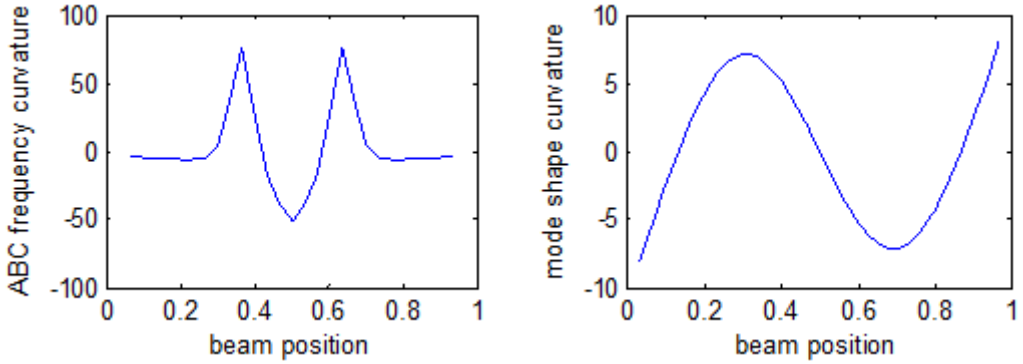

b) Second mode

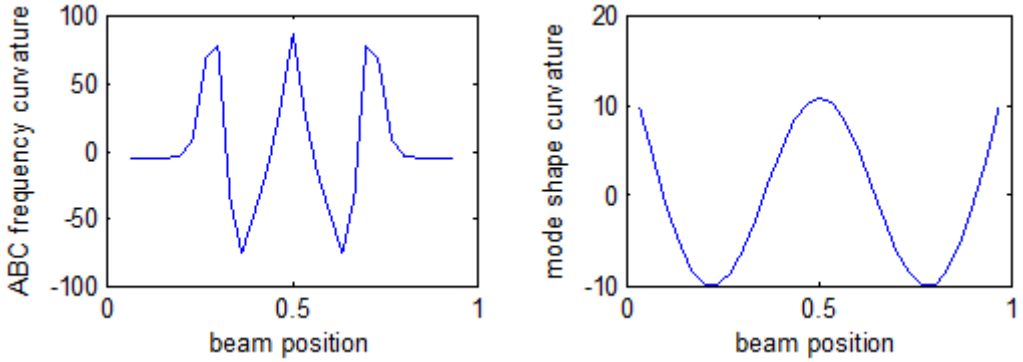

c) Third mode

Figure 4.14 One-pin ABC frequency curvatures vs. natural mode shape curvatures for the first three modes

Firstly the one-pin ABC frequency curvatures along the beam are calculated, and the results are depicted in Fig. 4.14. For comparison, the natural mode shape curvatures for the first three modes are also calculated and shown in Fig. 4.14. It is noted that before calculating the curvature values, the mode shapes and ABC frequencies in each mode have been normalized such that the maximum value is unity.

From the comparison, it can be observed that the ABC frequency curvatures exhibit more concentrated peak regions than the mode shape curvatures. This is expected to affect the sensitivity to damages around or away from the peaks regions significantly.

Three damage scenarios are used in the study to investigate the effectiveness of one-pin ABC frequency curvature-based damage index. The damage is simulated with 10% stiffness reduction in the damage element, and the damages are located at 0.07m, 0.21m and 0.5m from the left support of the beam (beam length = 1m), respectively. Using Eq. (4.22) and (4.23), the ABC frequency curvature-based damage index, $D_{i,k}$(i=1,2,...,29, k=1,2,3), can be calculated from the first three orders of ABC frequencies, and the results are depicted in Fig. 4.15.

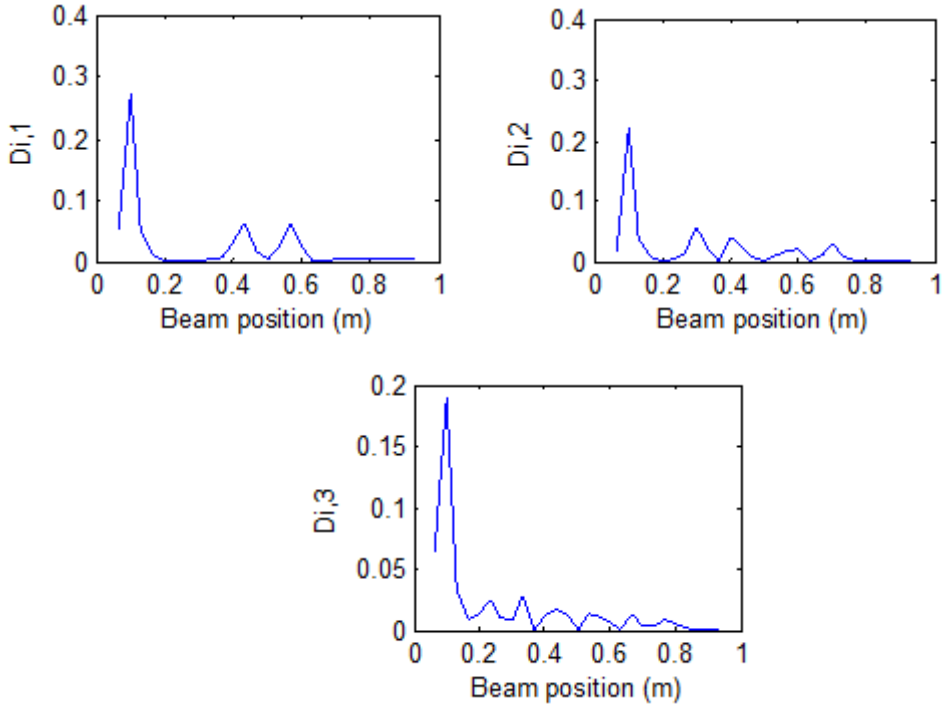

(a) Damage at 0.07m

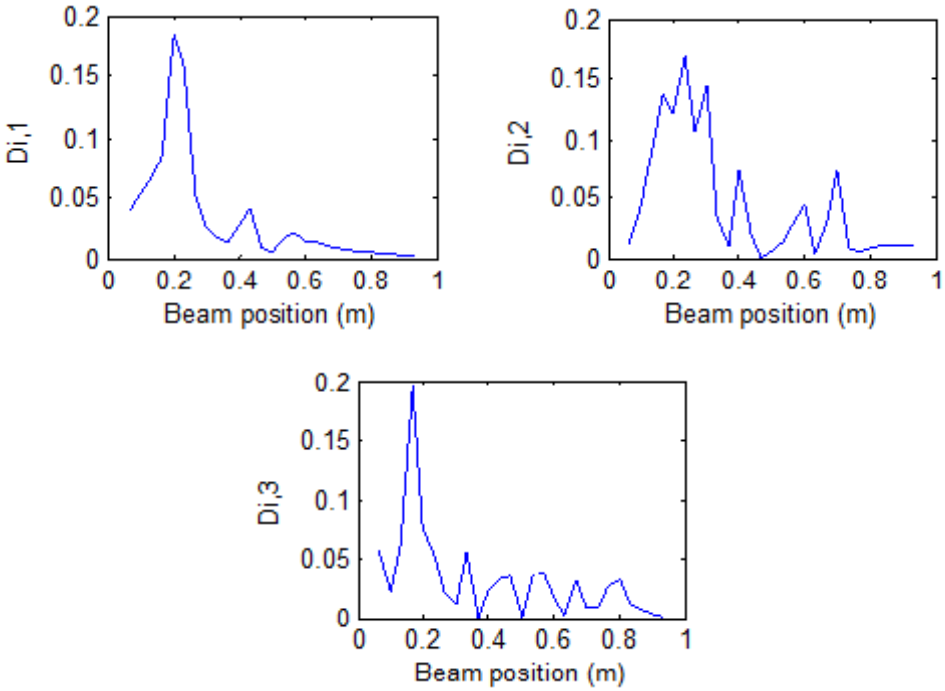

(b) Damage at 0.21m

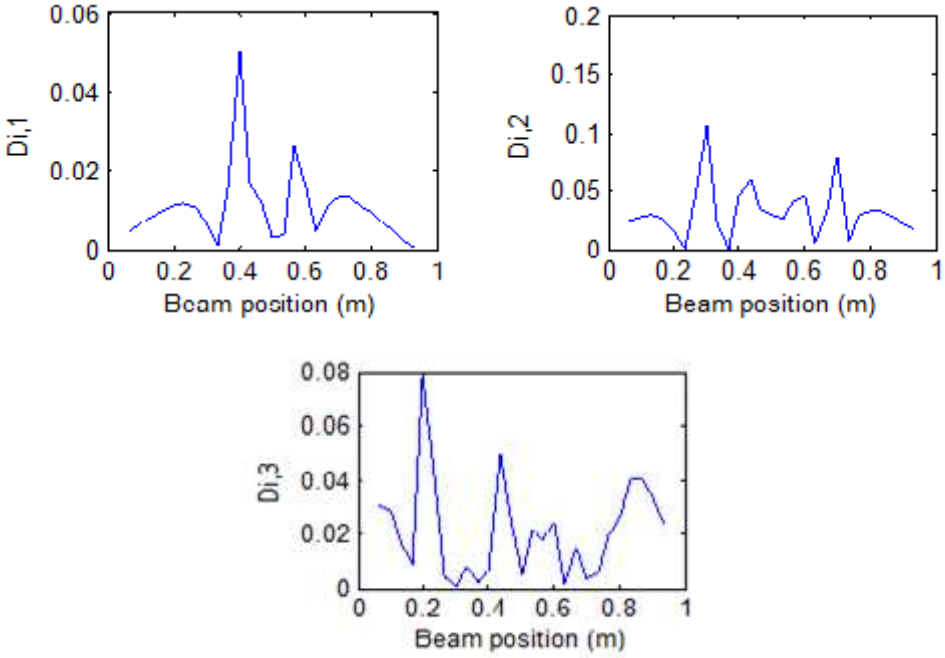

(c) Damage at 0.5m

Figure 4.15 Curvature difference due to single damage from mode shape and one-pin ABC frequency

It can be observed that the ABC frequency curvature-based index does not exhibit a consist performance for different damage locations. Although at the location of the damage the index does exhibit abnormal (increased) values, some spurious peaks appear in some other locations, which could lead to confusing results. With reference to Fig. 4.14, it can be observed that the spurious peaks appear around the peak regions in the original ABC frequency curvature profiles.

Summarising the above exploratory evaluation, although the ABC frequency curvature-based index shows certain correlation with the location of damage, it cannot yield conclusive results in its current direct curvature-analogy form. A more rigorous formulation would be required, possibly by decomposing the mode shape contribution in the ABC frequencies.

4.8 Conclusions

In this Chapter, the sensitivities of ABC frequencies to damage (stiffness reduction) are studied. On this basis, a methodology for the selection of ABC frequencies in a finite element model updating / damage identification procedure is proposed.

The existing anti-resonance (one-pin ABC) frequency sensitivity expression is extended to formulate the two-pin ABC frequency sensitivity expression, which includes the contributions of the natural frequencies and mode shape coordinates at the pin locations. Numerical examples demonstrate that the ABC sensitivity formulas for both one-pin and two-pin ABC frequencies match closely the actual sensitivities as calculated directly from the changes of the respective ABC frequencies corresponding to a particular damage.

The mode shape contribution (ratio) in the ABC frequency sensitivity is adopted as a classifying criterion for the selection of the ABC frequencies in a FE model updating procedure, such that those with higher mode shape contributions are employed, subjected to a desirable number limit.

Numerical studies on the above proposed selection criterion are carried out for different damage scenarios, with or without prior knowledge about damage positions. Results demonstrate that in both situations, the ABC frequencies selected using the proposed criterion consistently give rise to better updating results. Furthermore, it is verified through numerical studies that the general rule regarding the number of modal data to be included in a FE model updating procedure, i.e., being 2-3 times of the number of unknown parameters, also applies in the case with ABC frequencies.

The effectiveness of using ABC frequencies with the proposed selection method for FE modelling updating is further examined with real measured ABC frequencies, using GA as the parameter search engine. Results demonstrate that with the selected ABC frequencies, both the damage location and severity can be identified reliably, with an average percentage error in the identified stiffness at only 1.38%.

The possibility of formulating an ABC frequency-based damage index for a direct assessment of damage is explored by using a simple analogy to the mode shape curvature. Preliminary results indicate that, although such an ABC frequency curvature-based index shows certain correlation with the location of damage, it cannot yield conclusive outcome in its direct curvature-analogy form. Future effort in developing ABC frequency-based damage indicator will have to involve more rigorous formulation, possibly by firstly decomposing the mode shape contribution in the ABC frequencies.

5 Frequency Characteristics of Bridge Dynamic Response under Moving Trainloads

5.1 Introduction

While expanding reliable modal dataset for structural identification by resorting to additional frequency information has been the main theme of the previous chapters, understanding the frequency characteristics of structures in a dynamic environment is equally important both for possible extraction of modal information under the dynamic working condition and for control/moderation of the dynamic responses. Railway bridges represent such a class of structures whereby the dynamic characteristics under a normal working condition (under moving trains) can differ significantly from a static condition. The present and the next chapter will be devoted to the evaluation/identification of the dynamic characteristics of railway bridges from a frequency perspective. Such evaluation will lead to improved understanding and quantification of the dynamic, particularly the resonance effects which will be of special focus here, and it will also potentially facilitate real time monitoring of the structural conditions for possible future developments.

As described in the review chapter, the dynamic response of railway bridges is complicated due to the involvement of moving loads and moving masses. Comparing to road traffic, the trainload excitation is characterised by a unique pattern of frequency spectrum, which tends to play a dominant role in the dynamic response of the bridge. Moreover, the dynamic properties of railway bridges, especially the natural frequencies of small- to medium-size bridges, can be altered significantly due to moving carriage masses.

A potentially effective way of analyzing bridge dynamic response under passing trainload is to examine into the frequencies of the excitation load in conjunction with the frequency characteristics of the responding system. However, such studies are

still limited. As shown in Chapter 2, those that fall into this category may be loosely divided into two groups, one concerns the variation of the natural frequencies of the responding bridge during the passage of a laden train/vehicle (e.g. Li et al 1999, 2003, Yang and Chang 2009, Kim et al 2010, Schubert et al 2010), and the other deals with the frequency contents in the trainload excitation, including driving frequencies and dominant frequencies, and their general effect in the bridge response (e.g., Paultre et al. 1995, Fryba 2001, Yang and Lin 2005, Ju et al. 2009). Despite the identification of these frequency factors, the understanding of their influence on the bridge response remains to be rather general.

This Chapter aims to provide a comprehensive evaluation of the frequency characteristics of a railway bridge response under trainload, with a special interest in examining the significance and the variation trend of key frequency components in the response arising from the trainload, namely the driving frequencies and dominant frequencies mentioned above. To incorporate the influence of the moving mass, the analysis is carried using a finite element model, in which a moving vehicle is simulated with a moving mass block which is coupled with the bridge via surface contact. For simplicity while withholding the primary frequency characteristics, the vehicle dynamics and track irregularities are not considered.

5.2 Overview of background theories

5.2.1 Natural frequencies of bridge-moving train system

The natural frequencies of the bridge during the passage of a train (or a vehicle as a specialised case) may be established on the basis of the dynamic equation for the bridge coupled with the vehicle via its static and inertial loads, as follows:

$$m_b \frac{\partial^2 w_b}{\partial t^2} + EI \frac{\partial^4 w_b}{\partial x^4} + c_b \frac{\partial w_b}{\partial t} = P(x,t) \tag{5.1}$$

where EI, m_b, c_b are the flexural stiffness, mass per unit length and damping coefficient of the bridge, w_b is the bridge vertical displacement, and $P(x,t)$ is the interacting force between the vehicle and the bridge.

The interacting force of the i-th wheel-axle set can be expressed as (Li et al. 2003):

$$P(x,t) = \delta[x-(Vt-a_i)]\left(P_{0,i} - m_c \frac{\partial^2 w_b}{\partial t^2} + c_c \dot{w}_i + k_c w_i\right) \tag{5.2}$$

where δ is the Dirac delta function, $P_{0,i}$ is the static weight borne by the i-th wheel-axle set, a_i is the distance between the first and i-th wheel-axle sets, i.e. $a_i = (i-1)L_c$, w_i is the displacement within the suspension spring, m_c is the mass of a wheel-axle set, c_c, k_c are spring damping and stiffness of vehicle's suspension system, respectively.

The solution of the motion equation can be obtained by modal superposition. Denoting the n-th mode shape as $\phi_n(x)$ and the generalised modal coordinate as $q_{bn}(t)$,

$$w_b(x,t) = \sum_n \phi_n(x) q_{bn}(t) \tag{5.3}$$

For a simply supported bridge (beam), the mode shapes can be expressed in a sinusoidal form, thus:

$$w_b(x,t) = \sum_n \sin\frac{n\pi x}{L_b} q_{bn}(t) \tag{5.4}$$

where L_b is the bridge length.

Substituting Eq. (5.2) and (5.4) into Eq.(5.1), and then integrating with respect of L_b yields:

$$\ddot{q}_{bn}(t) + 2\xi_{bn}\omega_{bn}\dot{q}_{bn}(t) + \omega_{bn}^2 q_{bn}(t) = \frac{2}{m_b L_b} P_{bn}(t) \tag{5.5}$$

where ω_{bn} is the n-th bridge natural frequency, ξ_{bn} is the n-th bridge damping ratio, $P_{bn}(t)$ is the generalised modal force and can be expressed as:

$$P_{bn}(t) = \sum_{i=K}^{M} \sin\frac{n\pi(vt - a_i)}{L_b} \left[P_{0,i} - m_s \sum_{k=1}^{\infty} \sin\frac{k\pi(vt - a_i)}{L_b} \ddot{q}_{bk}(t) + c_c \dot{w}_i + k_c w_i \right] \tag{5.6}$$

A numerical integration method, such as the Wilson-θ method, can be employed to obtain the bridge natural frequencies at each time step. The results will allow the variation of the bridge frequency to be plotted against time or the position of the moving train.

5.2.2 Driving frequencies

For a single vehicle (single point) dynamic moving load, Eq. (5.2) reduces to:

$$P(x,t) = f_c(t)\delta(x - Vt) \tag{5.7}$$

$$f_c(t) = -m_c g + k_c(w_c - w_b) \tag{5.8}$$

where $f_c(t)$ is the sum of the vehicle weight and the elastic force of the suspension system, k_c is the stiffness between moving mass and the beam, w_c and w_b are the dynamic deflections of the moving mass and the beam, respectively.

Substituting Eq. (5.4) and (5.7) into Eq. (5.1), and ignoring the damping term yields:

$$\ddot{q}_{bn} + \omega_{bn}^2 q_{bn} = \frac{f_c(t)\int_0^L \delta(x - Vt)\phi_n(x)dx}{m_b \int_0^L \phi_n^2(x)dx} \tag{5.9}$$

Substituting Eq.(5.8), Eq.(5.9) may be re-written as:

$$\ddot{q}_{bn} + \omega_{bn}^2 q_{bn} + \frac{2\omega_c^2 m_c}{m_b L_b} \sin\frac{n\pi Vt}{L_b} \sum_j \sin\frac{j\pi Vt}{L_b} q_{bj} - \frac{2\omega_c^2 m_c}{m_b L_b} \sin\frac{n\pi Vt}{L_b} q_c = \frac{-2m_c g}{m_b L_b} \sin\frac{n\pi Vt}{L_b} \tag{5.10}$$

If the mass of the passing vehicle is small and may be ignored, the above equation reduces to:

$$\ddot{q}_{bn} + \omega_{bn}^2 q_{bn} = \frac{-2m_c g}{m_b L_b} \sin\frac{n\pi Vt}{L_b} \tag{5.11}$$

Assuming a zero initial condition, the solution to the above equation is obtained as:

$$q_{bn}(t) = \frac{\Delta}{1 - S_n^2} \left[\sin\frac{n\pi Vt}{L} - S_n \sin(\omega_{bn} t) \right] \tag{5.12}$$

where $\Delta = \dfrac{-2m_c g L^3}{n^4 \pi^4 EI}$ is the static deflection due to the passing vehicle with respect to the n-th mode, and $S_n = \dfrac{n\pi V}{L\,\omega_{bn}}$ is a relative speed parameter.

Finally, the displacement response of the bridge can be represented as:

$$w_b(x,t) = \sum_n \frac{\Delta}{1 - S_n^2} \left\{ \sin\frac{n\pi x}{L_b} \left[\sin\frac{n\pi V}{L_b} t - S_n \sin\omega_{bn} t \right] \right\} \tag{5.13}$$

Let:

$$f_{dr} = (n\pi V / L_b) / 2\pi = nV / 2L_b \tag{5.14}$$

From Eq. (5.13) it can be seen that the above frequencies will be present in the bridge dynamic responses, in addition to the natural frequencies of the bridge structure (Note that L_b / V is effectively the duration of the vehicle passing over the bridge). Such frequencies are the so-called “driving frequencies”.

5.2.3 Dominant frequencies

Assuming one generic load per carriage, the repeated wheel-axle loads from a moving train may be represented in the following simplified form (e.g., Xia and Zhang 2006):

$$P(t) = \sum_{j}^{N_c} f_c(t)\delta(t - jt_c) \tag{5.15}$$

where N_c is the number of carriages, $f_c(t)$ denotes the generic wheel-axle load, t_c represents the time interval between the repeated loads, $t_c = L_c / V$, with L_c been the length of a carriage.

The load described by Eq. (5.15) will manifest on the frequency spectrum as having peak frequencies at $n \times (1/t_c) = nV / L_c$. For a real trainload, despite the increased complexity due to multiple wheel-sets from each carriage, the frequencies arisen from the trainload is still dominated by nV / L_c (Ju et al, 2009). These frequencies are called the "dominant frequencies" in the trainload, which can be expressed as:

$$f_{do,n} = nV / L_c \tag{5.16}$$

In fact, the velocity ratios underlying the "driving frequencies" and "dominant frequencies", i.e., $V / 2L_b$ and V / L_c, have been examined in past researches when studying bridge resonance under moving trainloads (e.g. Li and Su, 1999, Yau, 2001, Xia et al, 2006, Dinh et al, 2009, Flener and Karoumi, 2009, etc.). It is widely recognised that when these ratios or their multiples become closer to the bridge natural frequencies, resonant response to a certain degree will occur (Fryba, 2001, Xia et al, 2006). However, few researches have been carried out to investigate the variation of the relative significance of these frequencies (including different orders) under different train-bridge parameter combinations, and the subsequent effect on the resonance amplitude.

5.3 Numerical model set-up and verification

It is generally understood that the actual significance of “driving” and “dominant” frequencies in the bridge dynamic response will depend upon the closeness of these frequencies to the natural frequencies of the bridge system, which in turn are affected by the moving vehicle mass. However, different orders of the driving and dominant frequencies can stretch over a large frequency span. In this section, a finite element model is developed to describe a generalized bridge-moving train system. The model is subsequently employed to investigate the effects of the trainload excitation frequencies on the bridge response under different combinations of the influencing parameters.

5.3.1 FE model set-up

A generic finite element configuration for the bridge (represented by a beam) and moving load/mass system is illustrated in Fig. 5.1. The bridge may be modelled by solid elements to facilitate the attachment of the moving objects through a contact algorithm. It is possible to model the detailed wheel-axle sets and the associated suspension system in each carriage if necessary, as shown in the Fig. 5.1(a). For the main purpose of evaluating the primary frequency characteristics, a simplified scheme with each carriage being represented by a single mass and a point load is adopted herein. The masses are coupled with the bridge via surface-to-surface contact, as shown in Fig. 5.1(b). It should be anticipated, however, that the detailed response time histories and some secondary frequency contents could be affected. An example comparison of the frequency contents in the bridge response between a single- and a multiple-mass representation of a carriage will be given later.

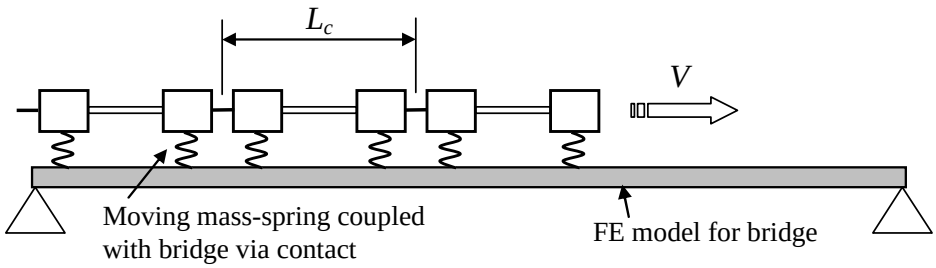

a) General FE model configuration

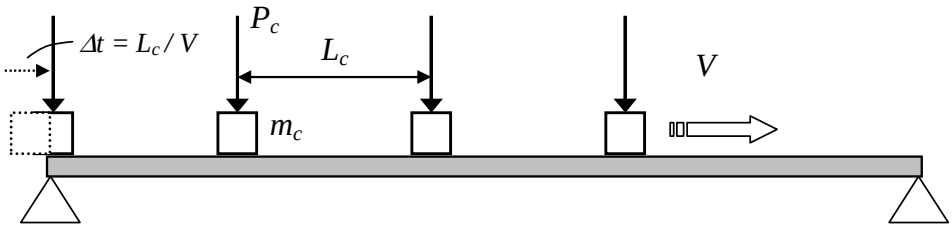

b) Simplified FE model with equalled spaced moving mass/load via surface contact

Figure 5.1 Schematic of a general FE model for bridge dynamic response under a moving train

In the present analysis, a simply-supported railway bridge of 8m length, which was actually measured in a field study, is considered as a prototype for the basic model set-up. In order to facilitate the use of the contact algorithm available in ANSYS, the 8-m bridge is modelled using 2D solid elements. The mass per unit length of the bridge is estimated to be 2 x 10^3 kg, and the flexural rigidity (EI) is assumed such that the resulting fundamental natural frequency of the bridge model matches that of the measured bridge, which is 14.2 Hz. In the model the flexural rigidity is selected as 6.81×10^8 N.m^2. A nominal damping ratio of 1% is considered in the model and the respective coefficients in the Rayleigh damping model are calculated so that the above target damping ratio is satisfied for the first two modes.

For simplicity, each mass block is modelled essentially as a point mass with a nominal size of 0.1×0.1m. A particular amount of mass can be obtained by specifying an appropriate density. The force exerted on the bridge by a carriage is achieved by

imposing a vertical load on the moving mass. The vertical load is assigned independently, so that the effects of the moving load and moving mass may be examined separately, where appropriate. For example, in order to check the adequacy of ignoring the moving mass while considering the moving load, we can simply assign a zero mass while keep the target level of the moving vehicle load.

Fig. 5.1(b) shows an overall view of the generalized train-bridge model in ANSYS11. A mesh convergence study indicates that a mesh grid size of 10 mm is enough to obtain accurate bridge responses. The involvement of multiple carriages (moving masses) is realized by starting the masses one after another at pre-calculated time intervals.

In the FE model, which is developed using ANSYS11, the moving mass and the bridge is coupled via the surface-to-surface contact, such that the bridge (beam) top surface is selected as the target, while the bottom of the moving mass is the contact. The Young's modulus of the moving mass is modelled essentially as a rigid body ($E=1.5\times10^6$ GPa herein) to avoid any sensible deformation after applying the vehicle load. Furthermore, as suggested by Metrisin (2008), in order to avoid any excessive penetration of the contact pair, the effect of initial penetration or gap is defined to ramp interference fit over several steps (keyopt(9)=4), and no separation is permitted during the processing procedure (keyopt(12)=4) when defining contact pair properties. After defining the contact pair, the initial contact status is checked to ensure that the defined contact pair is in place and the initial penetration is zero.

5.3.2 Verification of FE model

5.3.2.1 Bridge natural frequency variation due to moving mass

The above beam-moving mass model is firstly verified by analyzing the natural frequencies of the system while a single mass moves from one end of the beam to another. Fig. 5.2(a) depicts the variation of the fundamental natural frequency of the

8-m bridge when the amount of the moving mass is 20% of the bridge mass and the moving speed is set at 40m/s. An appreciable reduction in the fundamental frequency of the system is observed, and the maximum reduction takes place when the mass reaches the mid-span and it amounts to almost 10% in this particular case. For a comparison, Fig. 5.2(b) shows the variation of the bridge fundamental frequency adapted from Li et al. (2003). A similar trend is observed.

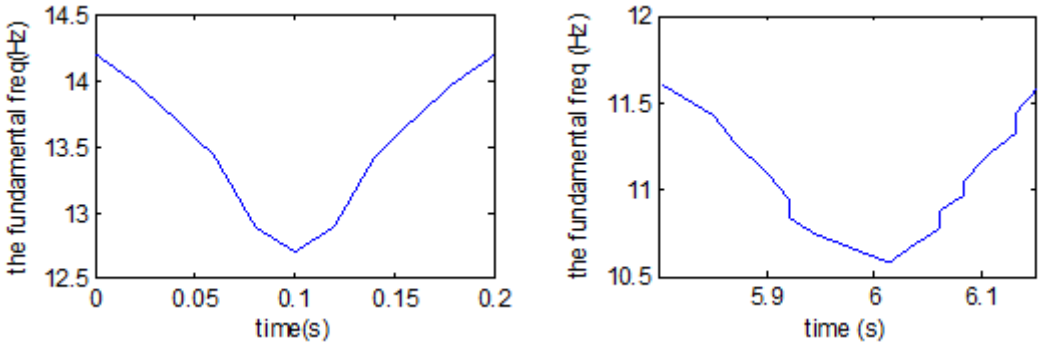

a) Present FE model **b) Truncated curve from Li et al. (2003)**

Figure 5.2 Variations of the fundamental system frequency during the passage of a single moving mass

Another scenario with two overlapped moving masses is also examined. This happens when the beam length is larger than the distance between two successive moving masses, thus more than one moving mass will act on the beam at the same time. For convenience, the bridge length is kept as 8m, with the distance between trainloads is artificially adjusted to 4m. The other properties are kept the same with the previous case. Fig. 5.3(a) depicts the variation of bridge fundamental frequency, and the result from Li et al. (2003) for a similar condition (but with many carriages) is shown in Fig. 5.3(b). It can be found that similar variation of bridge fundamental frequency under two overlapped moving masses can be obtained in the present FE analysis.

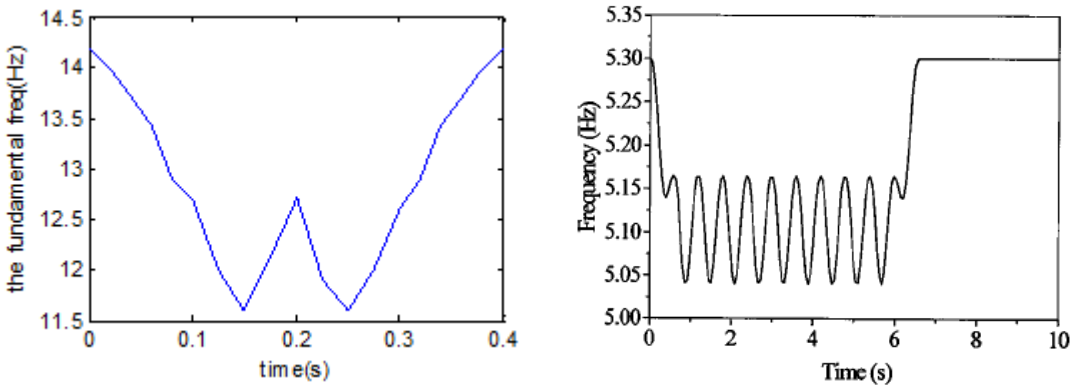

a) Present FE model **b) After Li et al. (2003)**

Figure 5.3 Variations of the fundamental system frequency during the passage of multiple moving mass

5.3.2.2 Comparison with measured bridge dynamic response

The dynamic responses measured from the reference bridge mentioned earlier, shown here in Fig. 5.4, are employed for verification of the FE model predictions. The recorded responses included the displacement and acceleration time histories at the mid-span of the bridge. One of the recorded scenarios involved 8 carriages, with the distance between adjacent carriages being approximately 20m. From the time history records, it was identified that the speed of the train was approximately 45m/s.

Figure 5.4 A short-span bridge used in field measurements

The above trainload parameters are considered in the FE analysis. The mass of the carriages was not known; therefore an estimated amount is determined through trial analysis so that the predicted response amplitudes are comparable to the measured peak response. Fig. 5.5 compares the simulated and measured mid-span displacement time histories and their corresponding frequency spectra.

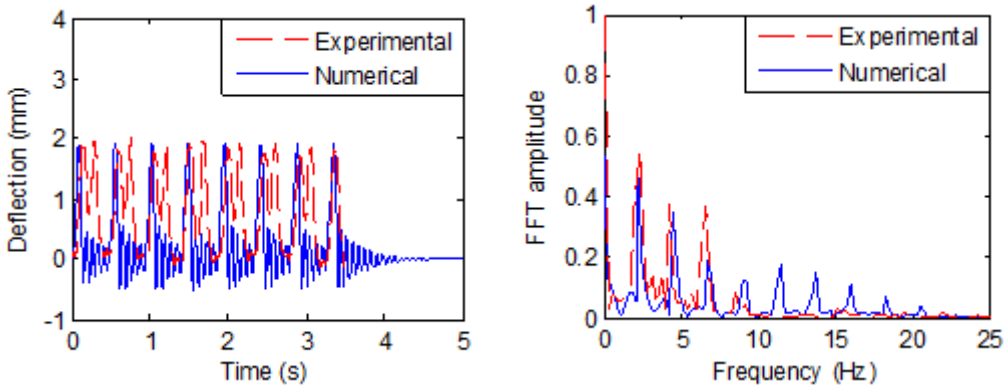

(a) Time histories **(b) Frequency spectra**

Figure 5.5 Comparison between computed and measured mid-span displacement responses

It can be found that overall response patterns compare well between the computed and measured responses. As can be expected from the simplification of each carriage into one single mass in the FE model, the numerical time histories show only one peak during the passage of each "carriage", while the measured response exhibits double peaks. On the frequency spectra, the first few dominant frequencies in the numerical results correlate well with their experimental counterparts; however the numerical results exhibit a few more frequency peaks into higher frequency range. This may be attributable to the differences in the intermittent free vibration responses between the numerical and measured results.

For further verification of the simplification of each carriage into a single mass/load in representing the primary frequency characteristics in the bridge response, another analysis is performed in which each carriage is simulated via two wheelsets (two mass blocks in the model). The resulting response time histories and the frequency spectra are compared with those using the generalised single mass per carriage representation in Fig. 5.6. As can be seen, although the refined model simulates the

bridge response more realistically in the time domain, the frequency components are very similar to those from the generalized model. It can therefore be concluded that the generalized model is indeed a suitable choice for an investigation into the frequency characteristics under different train-bridge parameter combinations.

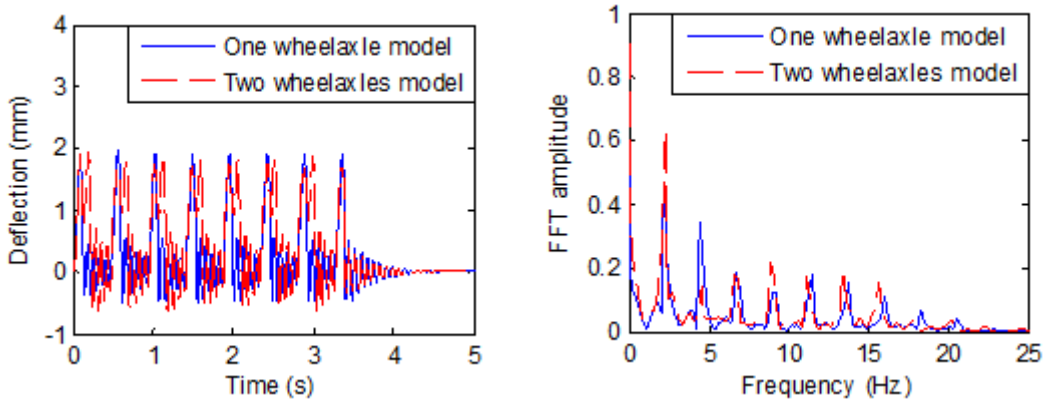

Figure 5.6 Comparison of frequencies in the simulated response using two different FE model settings

In the next section, the FE model with equally spaced moving masses will be employed to investigate the frequency characteristics in the bridge response. The frequencies in the bridge response under a single carriage are firstly studied as a special case to examine the driving frequency contribution with and without considering the moving mass effect.

5.4 Frequency characteristics of bridge response to a single moving mass

The bridge dynamic response to a single moving vehicle contains the so-called "driving frequencies". A series of numerical simulations using the FE model described in Section 5.3 are performed to demonstrate the potential significance of the driving frequencies in the bridge response.

For a direct comparison, firstly the bridge is assigned the same properties as used in Yang and Lin (2005), which has simply supported ends, length 25m, rigidity EI 3.3×10^9 N.m^2, mass per unit length 4800 kg/m. The bare bridge has a natural frequency of 2.3 Hz. As mentioned earlier, in the FE model, the moving mass is

modelled as a point mass with a nominal size of 0.1m×0.1m, while the moving load is applied on top of the mass so as to accommodate the movement. The speed of the moving load is assumed to be 5m/s, 10 and 20m/s, which corresponds to a basic driving frequency equal to $V/2L_b$ = 0.1, 0.2 and 0.4 Hz, respectively. A nominal amount of moving mass equal to 10% of the bridge mass is considered.

Fig. 5.7 illustrates the displacement, velocity and acceleration time histories of the forced vibration phase of the bridge response, as well as their corresponding FFT spectra.

As can be observed from Fig. 5.7, the deflection response is essentially featured by the movement of the vehicle from one end of the bridge to the other. This manifests in the FFT spectrum by a low frequency band encompassing the basic driving frequency of 0.1, 0.2 and 0.4 Hz for the three speeds, respectively. The above basic driving frequencies are markedly visible from the velocity and acceleration FFTs. These observations are consistent with those made by Yang and Lin (2005). Because the basic driving frequencies for all the three speeds considered here are much lower than the fundamental frequency of the bridge (2.3Hz), the deflections are essentially governed by the static deflection under the moving load; however noticeable vibration at the natural frequency appear in the velocity and more so in the acceleration responses. Furthermore, the velocity and acceleration tend to increase as the speed increases, due to the fact that the basic driving frequency becomes closer to (though still much lower than) the natural frequency of the bridge.

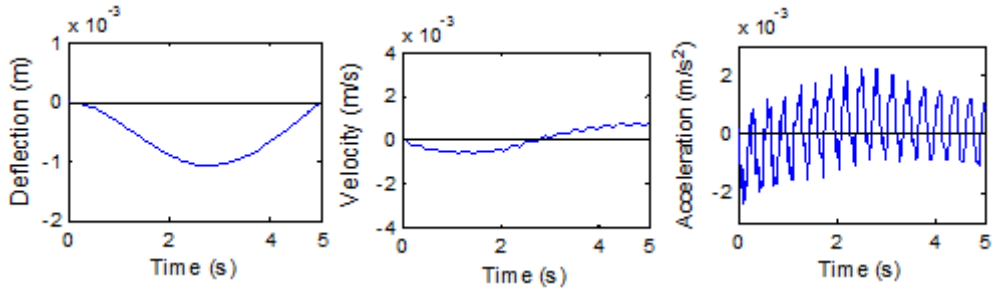

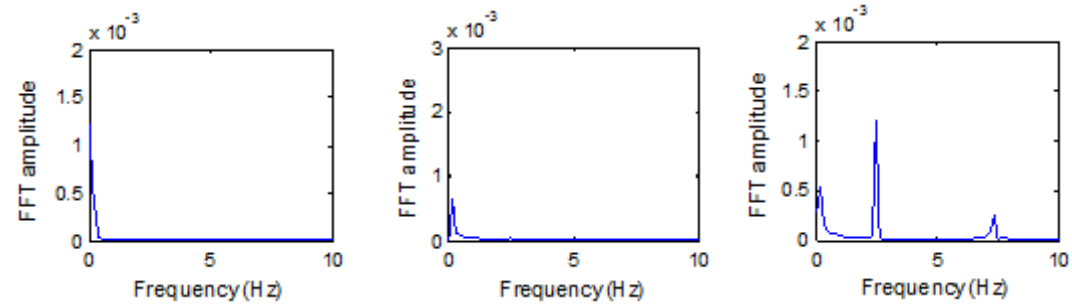

(a) Moving speed 5 m/s (upper: time histories; lower: FFT spectra)

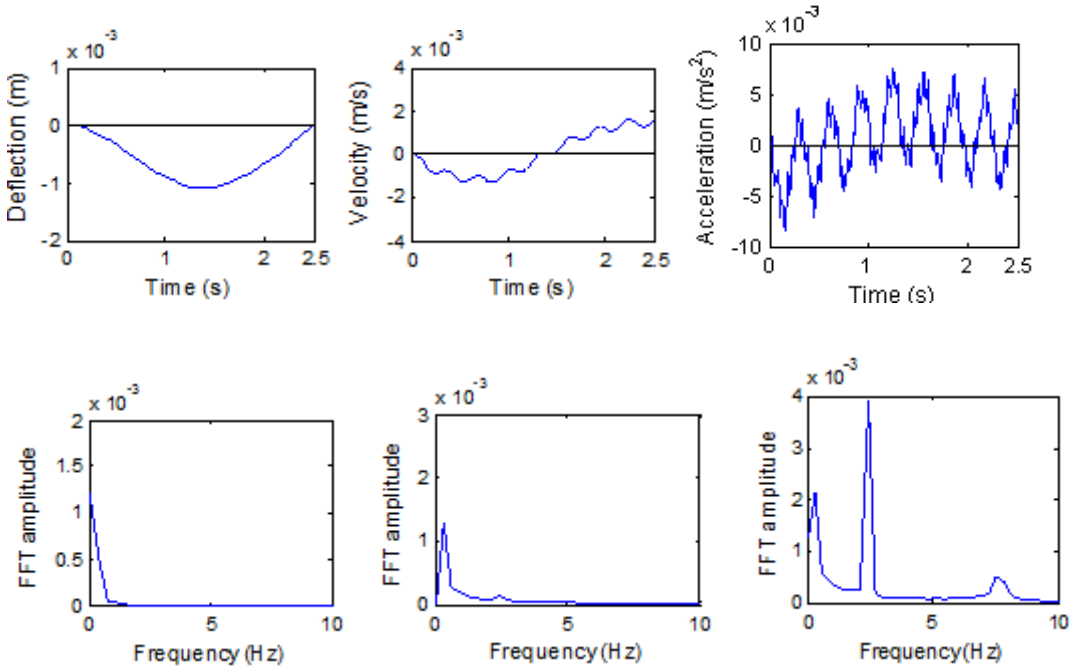

(b) Moving speed 10 m/s (upper: time histories; lower: FFT spectra)

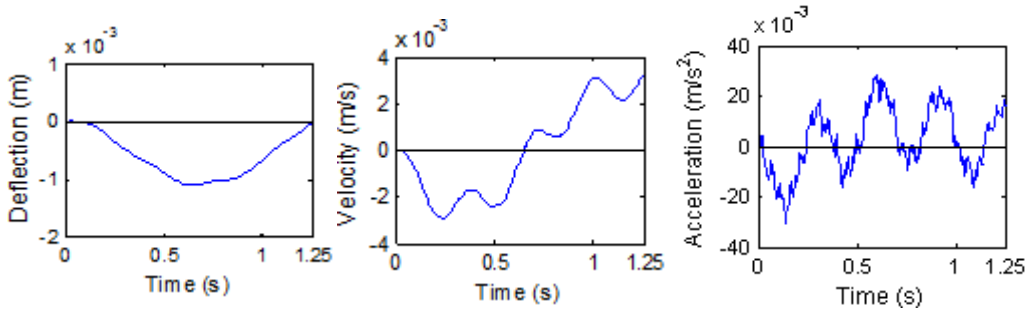

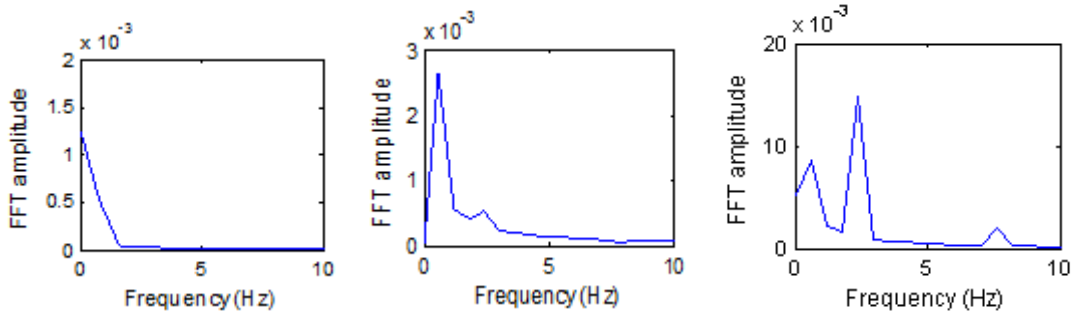

(c) Moving speed 20 m/s (upper: time histories; lower: FFT spectra)

Figure 5.7 Mid-span displacement, velocity and acceleration responses for different moving load speeds, with moving mass = 10% bridge mass

Because of the predominance of the basic driving frequency in the global response of the bridge, it can be envisaged that as this frequency, i.e., $f_{dr1} = V/2L_b$, gets closer to the bridge fundamental frequency, the dynamic response of the bridge will increase. This leads to the concept of the "critical speed". Critical speed is a term used to describe the condition under which the bridge approaches the maximum (global) response when subjected to a single moving load. Without considering the moving mass, it can be shown that (e.g. Fryba, 1999, Yang et al. 2004):

$$V_{cr} = 2 f_{b1} L_b \tag{5.17}$$

where V_{cr} is the critical speed, f_{b1} is the bridge fundamental frequency, L_b is the bridge length.

With the identification of the driving frequencies associated with a single carriage, especially the basic (first order) driving frequency $f_{dr1} = V/2L_b$, the above critical speed may be established simply by viewing it as a resonance condition such that the excitation - driving frequency matches the natural frequency of the bridge, $f_{dr1} = f_{b1}$, and hence Eq. (5.17).

A particular usefulness of viewing the critical speed from the perspective of resonance is that, when the moving mass of the carriage is taken into account, the

critical speed will automatically decrease as the natural frequency of the bridge decreases with the increase of the moving mass. In this respect, the modified critical speed may be estimated by adopting a modified "effective" natural frequency when the moving carriage mass is involved. For simplicity, the modified natural frequency when the moving mass reaches the mid-span of bridge, f_{b1m}, may be utilised, thus:

$$V_{cr,m} = 2 f_{b1m} L_b \tag{5.18}$$

More detailed discussion on the determination of the critical speed when a significant moving mass is involved will be presented in the next Chapter, and it will be demonstrated that simply using f_{b1m} to represent the effective mass-loaded frequency can yield a reasonable estimation of the mass-loaded critical speed to an accuracy within about 10%, even when a very heavy vehicle mass is involved.

To give an example, Fig. 5.8 illustrates the amplitude deflection (mid-span) versus speed curve based on the numerical simulations on the 8-m bridge described in Section 5.3 for a) without considering the vehicle mass, and b) considering a vehicle mass of 250% of the bridge mass, respectively. To allow for a direct comparison, the moving load is kept the same in both cases, being 400kN. The critical speed according to Eq. (5.17) is found to be 224 m/s for case "a" using the bare bridge frequency f_{b1} = 14 Hz, and this agrees well with the numerical results without considering the moving mass. It is, however, far away from the actual critical speed for case "b" when a heavy vehicle mass is involved. Using the mass loaded frequency $f_{b1m} \approx$ 6 Hz, the critical speed accordingly to Eq. (5.18) is found to be about 100 m/s, which matches well the corresponding numerical result as indicated in the figure.

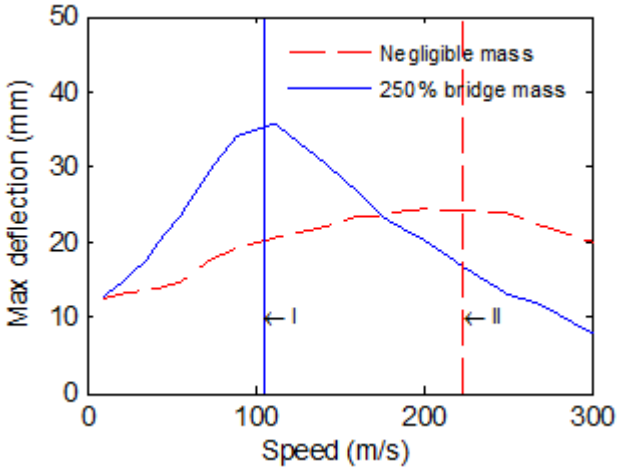

Figure 5.8 Variation of amplitude deflection of the bridge with vehicle speed

Although from Fig. 5.8 the amplitude deflection of the bridge does not appear to increase considerably upon the "resonance" at the critical speed, the bridge acceleration, and to a lesser extent the velocity, tends to exhibit drastic increase under such a condition. Fig. 5.9 and 5.10 show the bridge mid-span deflection, velocity and acceleration time histories when the vehicle moves at about the critical speed, considering a small and very large vehicle mass (case "a" and "b" mentioned previously), respectively. For a comparison, the responses when the vehicle moves at one or two other speeds are also included.

For case "a" (Fig. 5.9), it can be observed that when the vehicle moves at the critical speed, the displacement response (represented by the mid-span deflection) reaches the maximum at the time when the vehicle exits the bridge (0.035s in this case). At this point the bridge mid-span velocity approaches zero; however, the acceleration (slope of the velocity) appears to increase drastically and reaches about 200m/s^2 (~20g) momentarily around the end of the forced response. For the comparative case with the vehicle moving at half of the critical speed (Fig. 5.9b), the spiky acceleration at the end of the forced response no longer occurs, although the maximum acceleration, which takes place while the vehicle is still on the bridge, is still quite large.

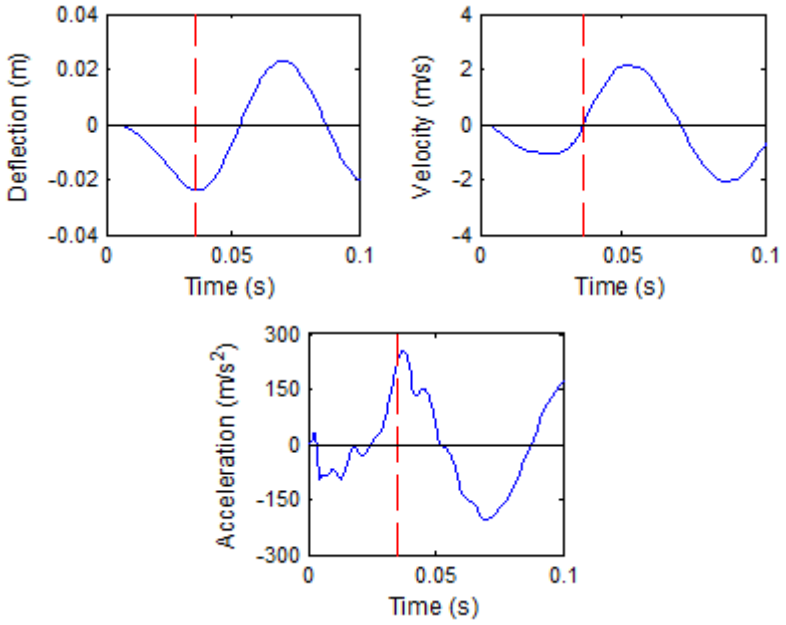

a) Bridge mid-span response at critical speed (224 m/s)

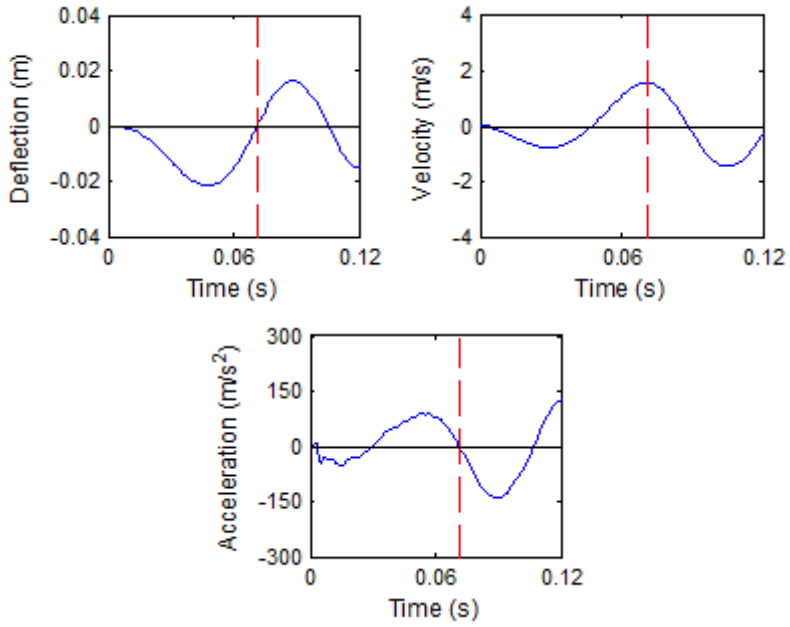

b) Bridge mid-span response at half critical speed (112 m/s)

Figure 5.9 Bridge mid-span responses at representative speeds, ignoring moving mass; dashed line marks end of forced response

For case "b" (Fig. 5.10) where the influence of a heavy vehicle mass is taken into account, the general trend is similar to the situation described above for case "a". In particular, under the critical speed the slope of velocity around the time when the

vehicle exit the bridge becomes even steeper than in case “a”, prompting a maximum acceleration to reach as high as 50g. It is noteworthy that, when the speed reduces to a quarter of the critical speed, the maximum acceleration reduces to below the order of 1.0 g.

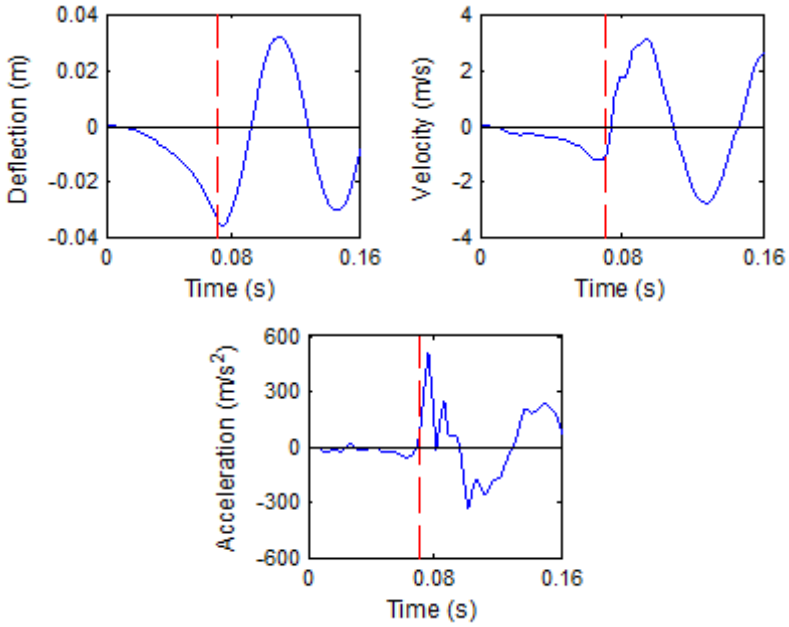

a) Bridge mid-span response at near critical speed (100 m/s)

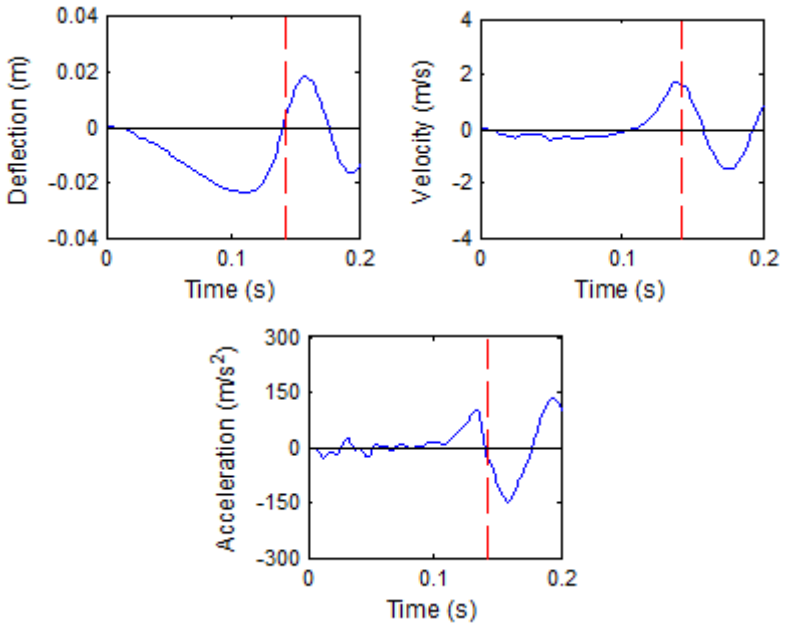

b) Bridge mid-span response at half critical speed (50 m/s)

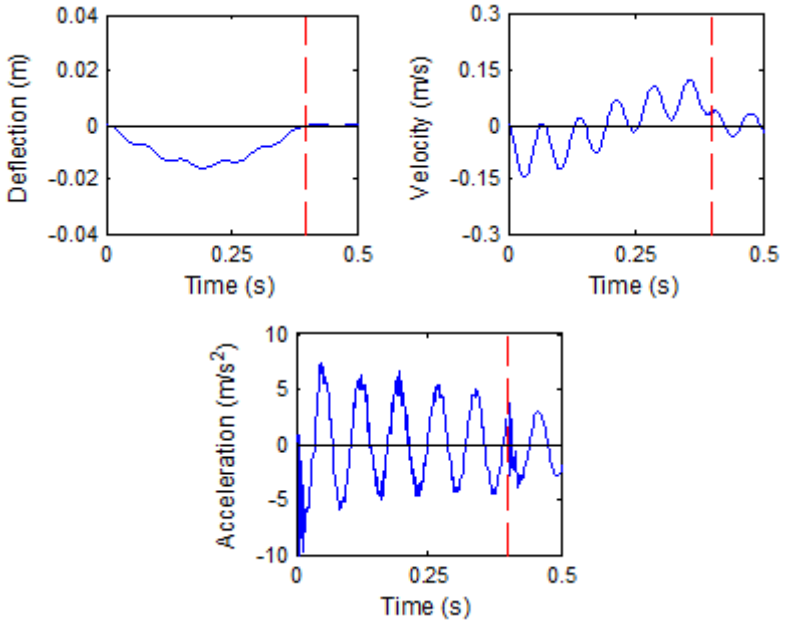

c) Bridge mid-span response at quarter critical speed (25 m/s)

Figure 5.10 Bridge mid-span responses at representative speeds, considering a heavy (250%) moving; dashed line marks end of forced response

It should be noted that in practice the critical speed $V_{cr} = 2 f_{b1} L_b$ under a single moving vehicle is not normally attainable in road traffic. However, it is possible to reach such speeds in the case of railway bridges especially in the case of high speed trains. As will be demonstrated in the sections that follow, when multiple carriages are involved the frequency characteristics and subsequently the resonant phenomena will be overwhelmed by the repeated carriage loads, while the "driving frequency" or critical-speed induced resonance would become less significant.

5.5 Frequency characteristics of bridge response under multiple carriages

The dynamic response of railway bridges is anticipated to be more closely associated with the repeated load caused by the passage of multiple carriages, in other words the so-called "dominant frequencies". Such frequencies play an important role in

determining the bridge dynamic response to a passing train, as discussed in general in some previous studies (e.g., Li and Su 1999, Xia et al. 2006, Garinei and Risitano, 2008, Flener and Karoumi, 2009, Ju et al. 2009).

To study the bridge response under multiple carriages, ten moving blocks are considered in the FE model herein, and each block is assigned a typical carriage mass of 40,000kg, while a 400kN load is applied on each moving block. The distance between two adjacent blocks is 20m. In the FE model the moving blocks are initially all placed at the same location at the left end of the bridge model. The first block is set to move at the start time of the calculation, and the remaining moving masses are scheduled to start moving one after another with a specified time lag, which is constant for equally-spaced moving blocks and is determined in accordance with the carriage distance (20m in the case herein) and the moving speed.

The 8m prototype bridge is firstly used to investigate the bridge responses and corresponding frequencies. Two other bridge cases with different lengths will be modelled subsequently, to represent a medium and a relatively long span case, respectively. The consideration of different bridge lengths also stems from the need of observing the dominant frequency characteristics. In fact, findings by Ju et al. (2009) about the dominant frequencies stem from the excitation characteristics related to repeated pulse loads at a given point. Their observations on the dominant frequency effect in a bridge response seem to be applicable mainly to short bridges, where the bridge length is not longer than the carriage length. This, however, may not be applicable when the bridge length increases, such that individual carriage loads overlap. It can be expected that as overlapping enhances, the effective load will transit from a repeated pulse character to a pattern as shown in Fig. 5.11. Further discussion on load patterns and their implication on the frequency contents will be given in Section 5.6. From this point of view, it can be understood that the ratio between the length of the bridge and that of the carriage is an important and very useful factor in classifying the bridge response and frequency characteristics.

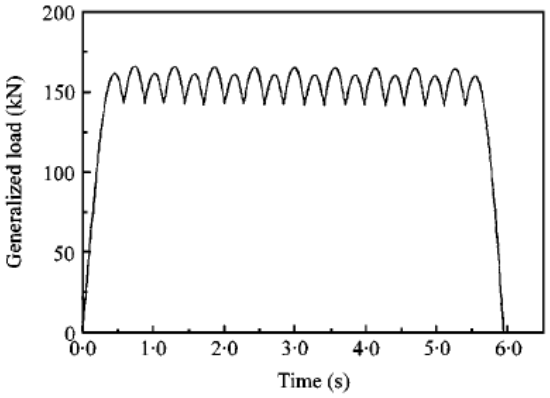

Figure 5.11 Generalized load against time (after Li et al. 1999, 2003)

5.5.1 Frequency characteristics of 8-m short span bridge

Consider a nominal carriage length of 20m, only one moving block will act on the 8-m bridge during the passage period. As mentioned before, the bridge has a total weight of 16,000kg, and for a carriage mass of 40,000 kg this gives rise to a carriage to bridge mass ratio of 2.5, which is indeed very high. Three different speeds of the train are investigated, namely 20m/s, 50m/s and 100m/s. For the carriage length of 20m, these speeds correspond to dominant frequencies of around 1n Hz, 2.5n Hz and 5n Hz (n = 1, 2, …), respectively.

Fig. 5.12 and 5.13 show the bridge displacement and acceleration responses and corresponding FFT curves. Both the displacement and acceleration frequency spectra exhibit clear spectral peaks at the anticipated dominant frequencies. From the mid-span deflection response it can be observed that pronounced resonance effect occurs under the speed of 50 m/s, apparently due to the repeated carriage loads or the "dominant frequencies". On the other hand, at the speed of 100m/s which marks the critical speed under a single moving load as discussed earlier in Section 5.4, no successive increase of the response occurs between carriage loads, and the maximum response is essentially governed by that induced from a single carriage. This comparison clearly demonstrates a very different resonance phenomenon that is clearly associated with the "dominant frequencies", and relatively speaking the

significance of the "driving frequency" which is associated with each individual carriage tends to diminish.

The influence of the critical speed has become less significant, as can be expected; however, it is worth noting that the acceleration spikes upon the exit of each individual carriage when the train moves at such a speed still occurs in this short-bridge scenario.

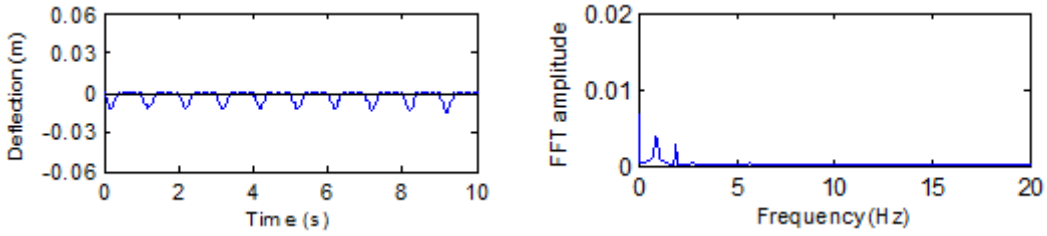

(a) Speed = 20m/s (expected dominant frequencies at 1Hz interval)

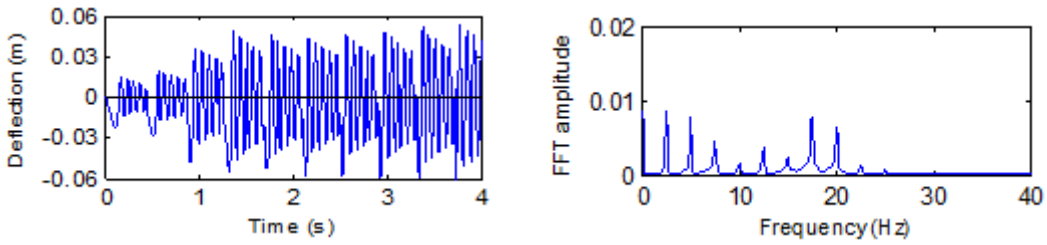

(b) Speed = 50m/s (expected dominant frequencies at 2.5Hz interval)

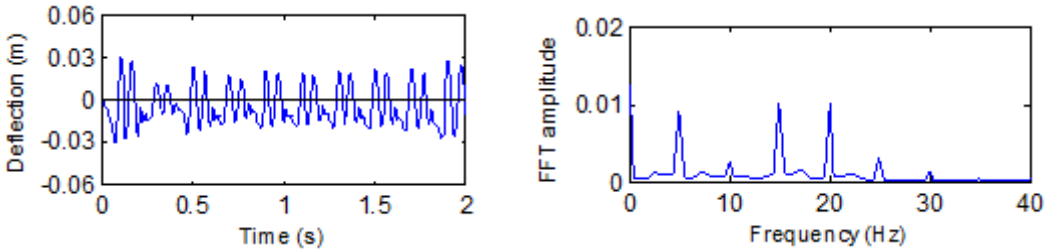

(c) Speed = 100m/s (expected dominant frequencies at 5Hz interval)

Figure 5.12 8-m bridge displacement time histories (left) and FFT spectra (right) under different train speeds

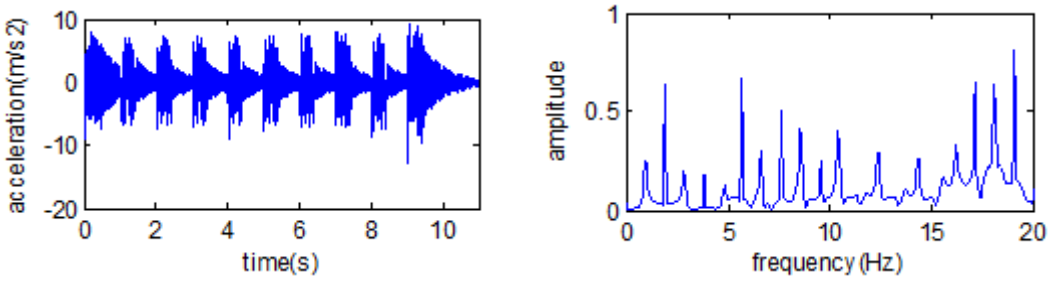

(a) Speed 20m/s

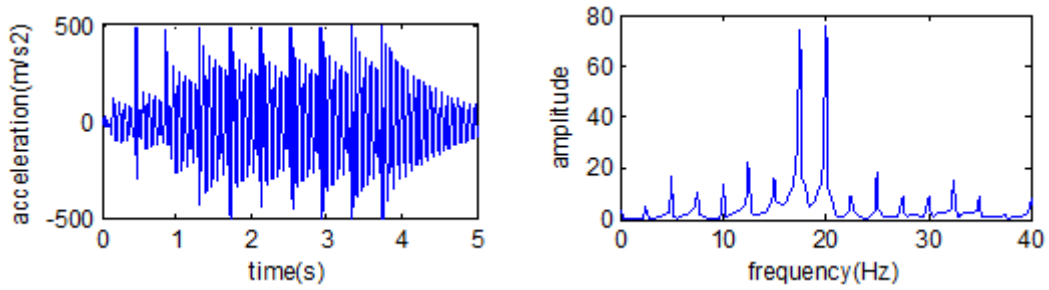

(b) Speed 50m/s

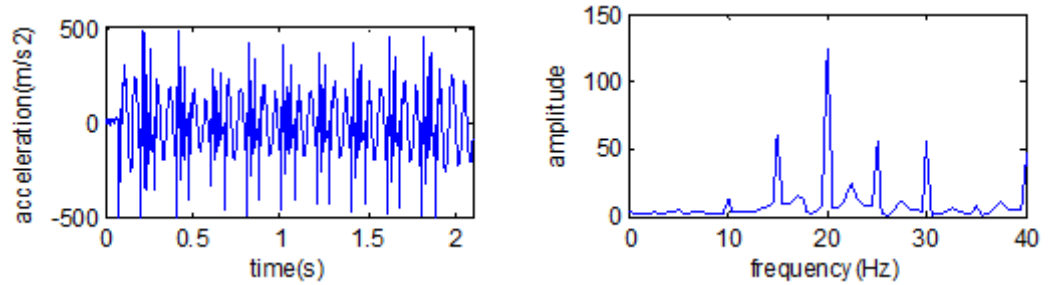

(c) Speed 100m/s

Figure 5.13 8-m bridge acceleration time histories (left) and FFT spectra (right) under different train speeds

5.5.2 Frequency characteristics of 40-m medium span bridge

A bridge length of 40m is then chosen to represent a “medium length” bridge for which more than one carriage may act at the same time. Comparing to the 8-m bridge case, when the bridge length is increased to 5 times longer, the mass per unit length and the sectional stiffness should also be increased by a reasonable proportion to be realistic. Herein the mass per unit length is increased to 2 times larger, and the sectional stiffness is increased such that with the increased mass the bridge

fundamental frequency will be around 10Hz, similar to a bridge of this size used by Li et al, (2003).

Normally another FE model will have to be set up to accommodate the increased length. Herein we adopted an equivalent approach using the same bridge model for the previous 8-m length, and convert all parameters by observing a set of scaling laws, such that while the length is scaled down by a factor of 40/8 = 5, the total mass of the 40m bridge and the time dimension (and hence the frequencies) are maintained as in the 40m bridge. In satisfying these scaling objectives, the mass per unit length in the 8-m model is scaled up by a factor of 5 x 2 = 10 (resulting in the same total weight as the 40m bridge), and the sectional stiffness is adjusted by changing the sectional property such that the bridge fundamental frequency is equal to that of the 40m bridge, i.e., 9.9Hz. Correspondingly, the distance between the carriages is scaled down by the length scale of 5, to become 4m, and the speeds are scaled down by the same length factor of 5, to become 4m/s, 10m/s and 20 m/s for the actual 20m/s, 50m/s, and 100 m/s, respectively. In this way, the dynamic response of the scaled 8-m bridge will have identical characteristics as the 40m bridge, except that the absolute response amplitude will have to be scaled up by the length scale factor of 5.

It should be noted that the increase of the bridge length does not affect the trainload dominant frequencies as these frequencies are associated only with the speed and the carriage length. Recall that these frequencies are 1n, 2.5n and 5n Hz, respectively. The basic driving frequency would be 0.25, 0.625, and 1.25 Hz for the three speeds respectively.

Fig. 5.14 and 5.15 present the bridge dynamic response and their FFT curves (after converted to the 40-m bridge scale). Similar to the 8-m bridge case, the bridge fundamental frequency is not significantly excited when the speed is low (e.g. 20m/s in this case), and in such a case the response is overwhelmed by the dominant frequencies due to repeated point loads. With the increase of the speed, the peaks around the natural frequency of the bridge (9.8Hz) tend to be significantly amplified, and this is apparently attributable to the fact that the first natural frequency of the

bridge falls within the first few dominant frequencies, and as a result increased degree of resonance occurs. This observation is supported by the significantly increased acceleration amplitudes as the speed increases, even though the amplitude of the displacement does not increase markedly. It should be noted that the 100-m/s speed is still far less than the critical speed for this 40-m bridge (the critical speed would be around 600m/s), therefore no abnormal acceleration spikes occur as in the case of the 8-m bridge.

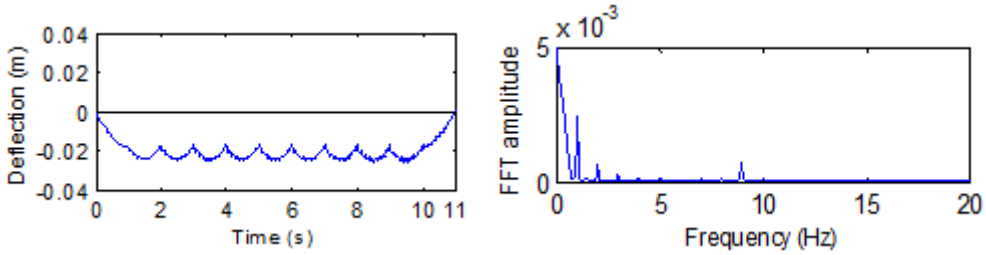

(a) Speed = 20m/s (expected dominant frequencies at 1Hz interval)

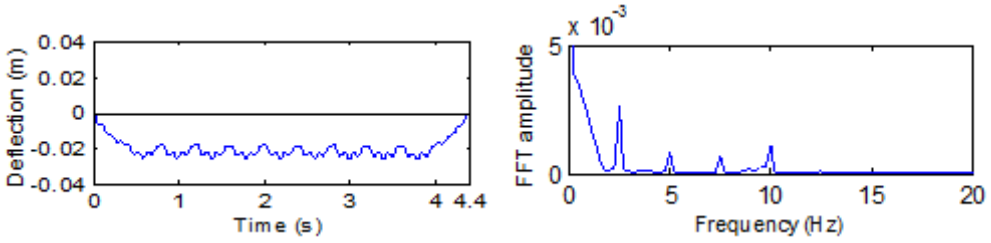

(b) Speed = 50m/s (expected dominant frequencies at 2.5Hz interval)

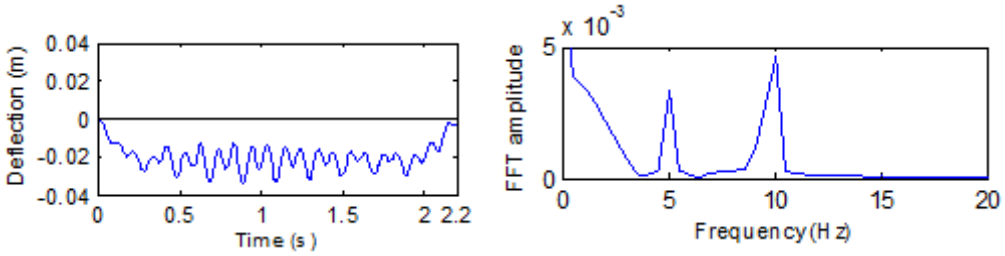

(c) Speed = 100m/s (expected dominant frequencies at 5Hz interval)

Figure 5.14 40-m bridge displacement time histories (left) and FFT spectra (right) under different train speeds

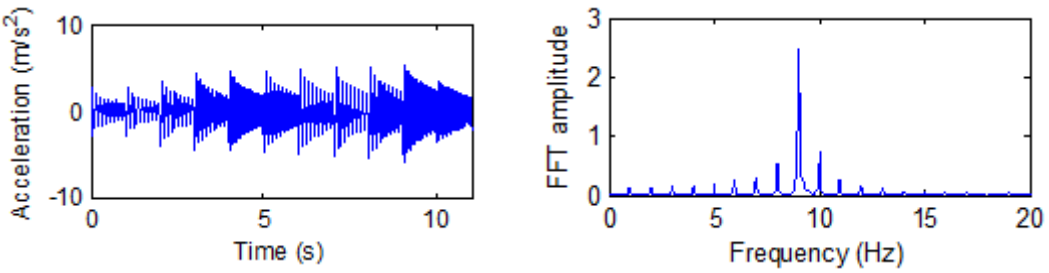

(a) Speed 20m/s (expected dominant frequencies at 1Hz interval)

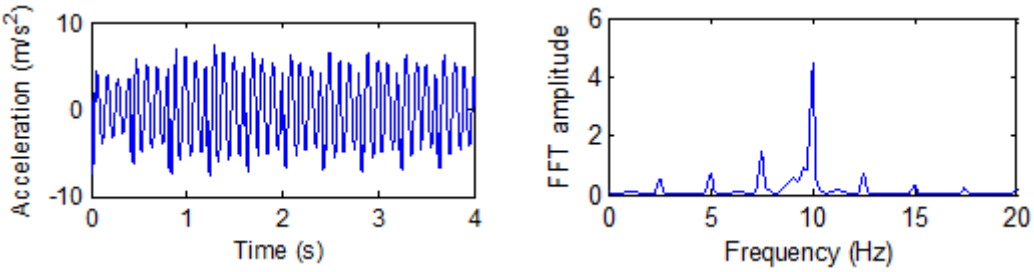

(b) Speed 50m/s (expected dominant frequencies at 2.5Hz interval)

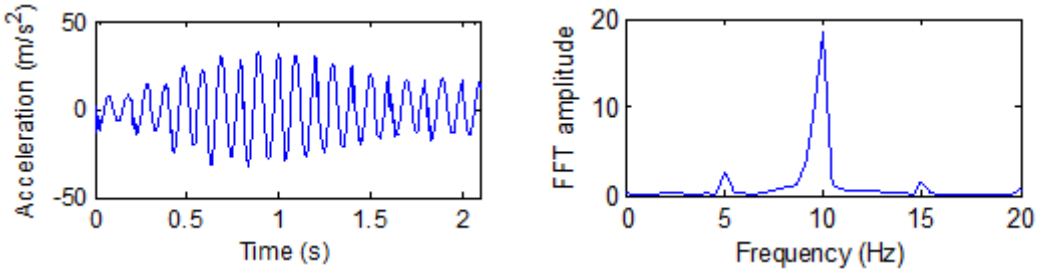

(c) Speed 100m/s (expected dominant frequencies at 5Hz interval)

Figure 5.15 40-m bridge acceleration time histories (left) and FFT spectra (right) under different train speeds

5.5.3 Frequency characteristics of 80-m long span bridge

The 80-m bridge is employed to represent a "long" bridge such that multiple carriages (in this case 4) can act on the bridge simultaneously. Again an equivalent approach is adopted, using the basic 8-m bridge model by following appropriate scaling laws as described in the previous section. The target 80-m bridge is assumed to have a mass per unit length equal to 3.5 times of the original 8-m bridge, while the

fundamental frequency is assumed to be around 5 Hz, typical of bridges of this size. Accordingly, when the 8-m bridge is used to represent the 80-m bridge, the mass per unit length in the equivalent 8-m model is increased to 35 times larger in order to preserve the total weight of the 80-m bridge. The sectional stiffness is modified so as to result in a fundamental frequency to be actually 4.9Hz. On the other hand, the distance between moving mass is reduced to 20/10=2m, and the speed is reduced to 2, 5 and 10m/s for the actual 20, 50 and 100m/s, respectively. The damping coefficient is kept to be 1% for the first two modes. Fig. 5.16 and 5.17 depict the bridge dynamic responses and corresponding FFT curves.

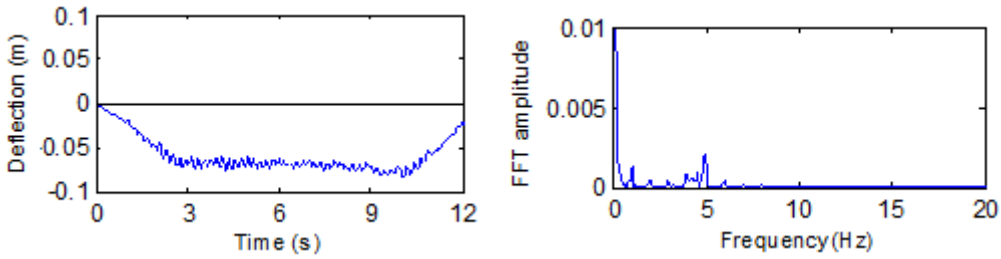

(a) Speed = 20m/s

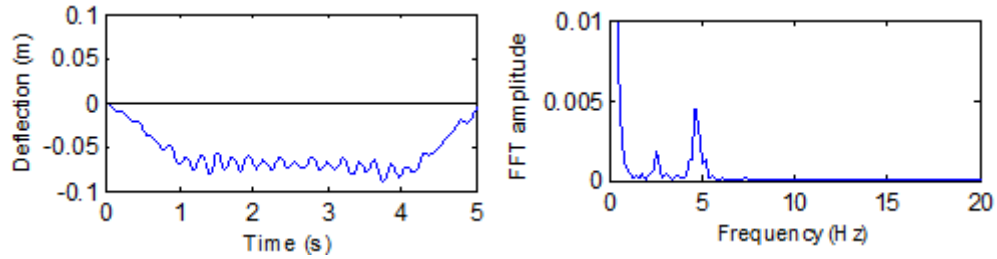

(b) Speed = 50m/s

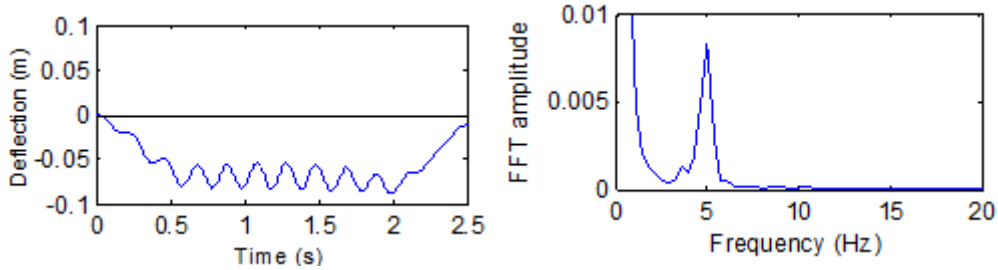

(c) Speed = 100m/s

Figure 5.16 80-m bridge displacement time histories (left) and FFT spectra (right) under different train speeds

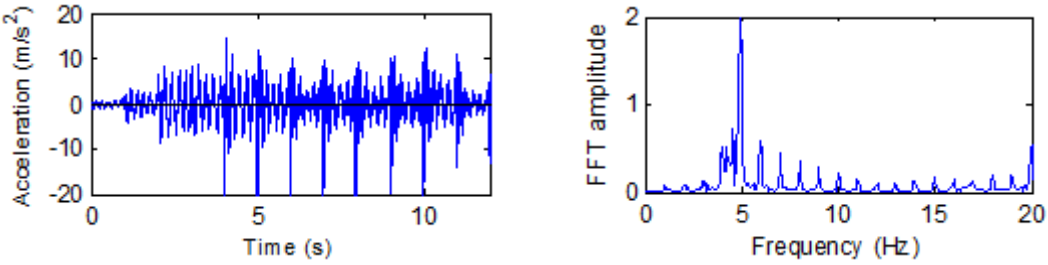

(a) Speed 20m/s

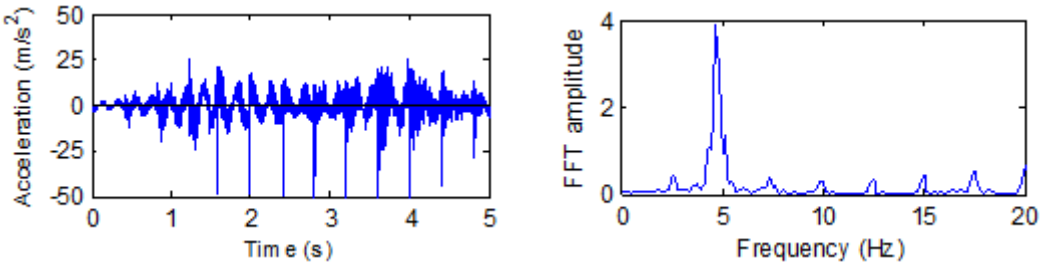

(b) Speed 50m/s

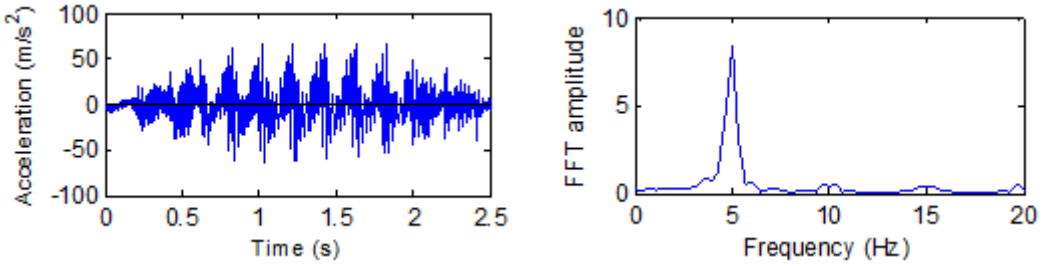

(c) Speed 100m/s

Figure 5.17 80-m bridge acceleration time histories (left) and FFT spectra (right) under different train speeds

It can be observed that the resonance effect, herein at around 5Hz, is more significantly excited. This may be explained as such that, with increase of the bridge-to-carriage length ratio, the excitation frequencies tend to concentrate to the lowest few dominant frequencies. As the natural frequency of the bridge also reduces, resonance becomes inevitably more significant.

5.6 Discussion of the bridge response from the perspective of frequency contents in the generalized trainload

For a typical trainload involving multiple carriages, it has been demonstrated the "dominant frequencies" are a primary character both in the repeated carriage load as well as in the bridge response. It has also been shown that, as the bridge length increases, the primary frequency contents in the response tend to become increasingly concentrated in the lower few dominant frequencies. In this section, further insight into this trend is provided by analysing the variation of the frequency contents in different trainload scenarios.

5.6.1 Generalization of trainload patterns and analysis of their FFT

Considering the bending response of the bridge, the load from each carriage as it moves from one end of the bridge to another may be generalized as a half sine pulse, with a duration of T_b as depicted in Fig. 5.18. When multiple carriages are involved, the load will consist of a series of such pulses with an interval between consecutive pulses being T_c. For a train speed V, $T_b = L_b / V$, $T_c = L_c / V$, where L_b, L_c are the bridge length and the carriage length, respectively.

When the length of the bridge is smaller than the carriage length (such as in the case of the 8m bridge), there will be a clear separation between consecutive pulses. On the other hand, when the bridge length is larger than the carriage length (such as the cases of 40m and 80m bridge), the pulses due to each individual carriage will overlap, giving a wavy trapezoid shape of the load. Thus, the overall pattern of the trainload, and hence the frequency distribution, depends only on the relative values of T_b and T_c, which in turn depends on the length ratio $\alpha_L = L_b / L_c$. The absolute frequency values are then determined by the speed V, e.g., the first dominant frequency $f_{do1} = V / L_c$. Therefore, for a characterisation of the frequency distribution, the length ratio α_L is a key parameter.

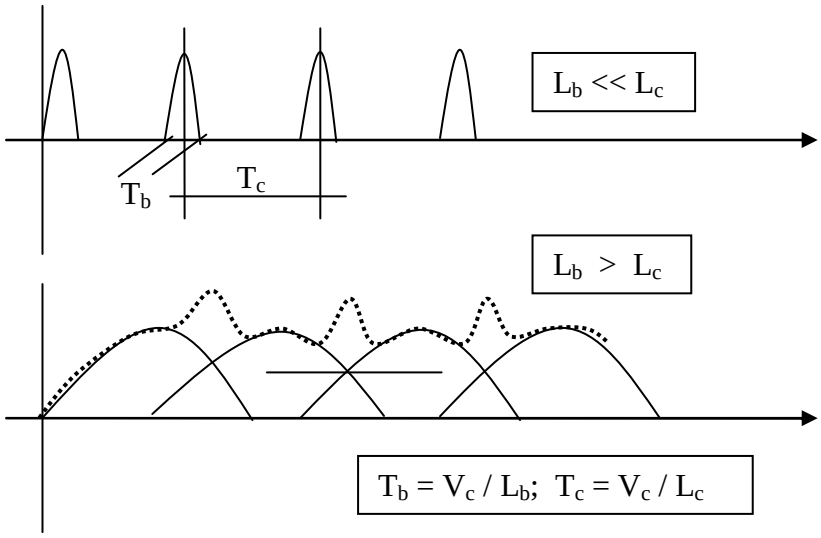

Figure 5.18 Generalisation of the trainload patterns

In what follows, the variation of the frequency spectrum is examined for different characteristic α_L values. For convenience in numerical calculations, a fixed velocity of 50 m/s and a carriage length of 20m are assumed, with ten carriages. The theoretical "dominant frequencies" are thus fixed at $(V / L_c)n = (1/T_c)n = 2.5n$ Hz, where *n* is a positive integer.

i) $\alpha_L = L_b / L_c \to 0$: let T_b = 0.02s, T_c = 0.4s (L_b = "1m", L_c = 20m, V = 50m/s)

This scenario represents a lower-bound situation with essentially a "point" bridge, such that the load resembles a string of impulses, as shown in Fig. 5.19(i). The frequency spectrum is a typical repeated impulse character with almost equal peaks for all orders of the "dominant frequencies" at a constant interval of $1/T_c$ = 2.5Hz.

ii) $\alpha_L < 1.0$: let T_b = 0.16s, T_c = 0.4s (L_b = 8m, L_c = 20m, V = 50m/s)

This case is analogous to the analysed 8-m short bridge, with the load pattern as depicted in Fig. 5.19(ii). It can be clearly seen that, as the duration T_b increases with respect to the time interval T_c, the spectral peaks at higher order "dominant"

frequencies reduce sharply. As a matter of fact, only the first three dominant frequencies may be considered as significant in this particular case.

It is worth noting that the driving frequencies, which are presumably associated with the duration, with the first frequency equal to $1/2T_b$ = 3.2 Hz, finds no trace in the frequency spectrum in the multiple carriage scenario. This is also true when the duration further increases as in the cases that follow.

iii) $\alpha_L = 1.0$: let T_b = 0.4s, T_c = 0.4s (L_b = 20m, L_c = 20m, V = 50m/s)

This is a dividing scenario where the bridge length is equal to the carriage length. The frequency spectrum still shows the character of equally spaces peaks at an interval of 2.5 Hz, but it is increasingly dominated by the first few frequencies.

iv) $\alpha_L > 1.0$: let T_b = 1s, T_c = 0.4s (L_b = 50m, L_c = 20m, V = 50m/s)

When the bridge length is greater than the carriage length, the generalized individual carriage load pulses overlap one another, see Fig. 5.19(iv). The spectrum near zero frequency is the result of the overall trapezoidal load shape in the positive domain, while frequencies at the expected intervals of 2.5 Hz are visible, with the first two peaks at 2.5 and 5 Hz being dominant.

v) $\alpha_L >> 1.0$: let T_b=2s, Tc=0.4s (L_b = 50m, L_c = 20m, V = 50m/s)

As depicted in Fig. 5.19(v), in this case the overlapping intensifies (with actually 4 carriages on the bridge at one time). The frequency spectrum exhibits generally a similar character as in the previous case with $\alpha_L = 2.5$, with concentration of spectral power at the lowest dominant frequency of 2.5 Hz.

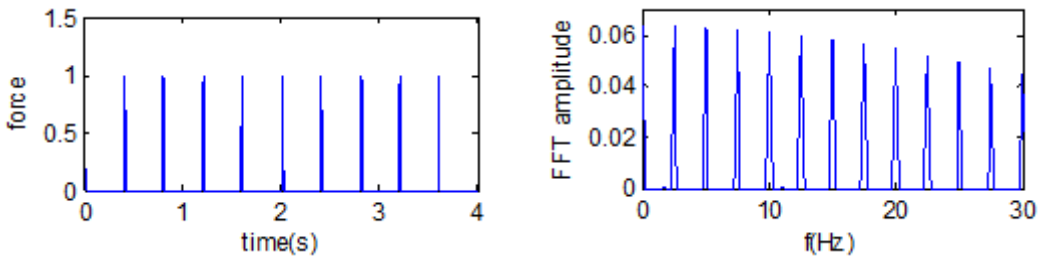

Time history **FFT spectrum**

i) Tb = 0.02s, Tc = 0.4s ($\alpha_L = 0.05$)

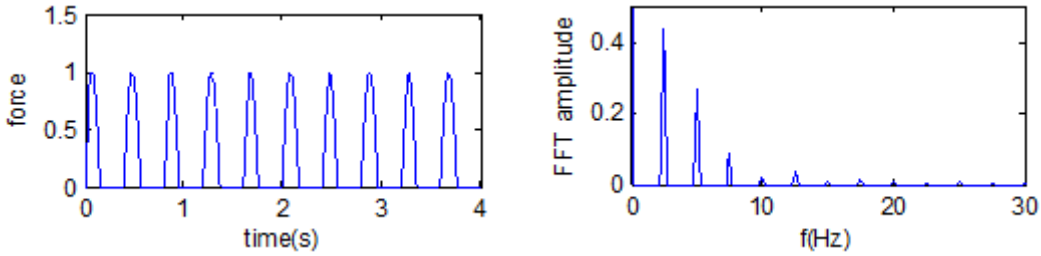

Time history **FFT spectrum**

ii) Tb = 0.16s, Tc = 0.4s ($\alpha_L = 0.4$)

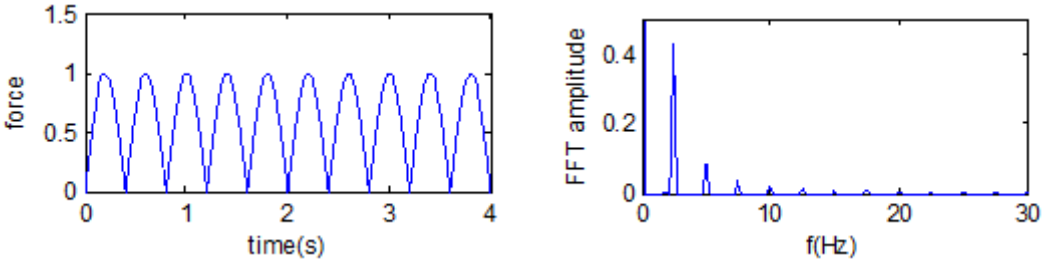

Time history **FFT spectrum**

iii) Tb = 0.4s, Tc = 0.4s ($\alpha_L = 1.0$)

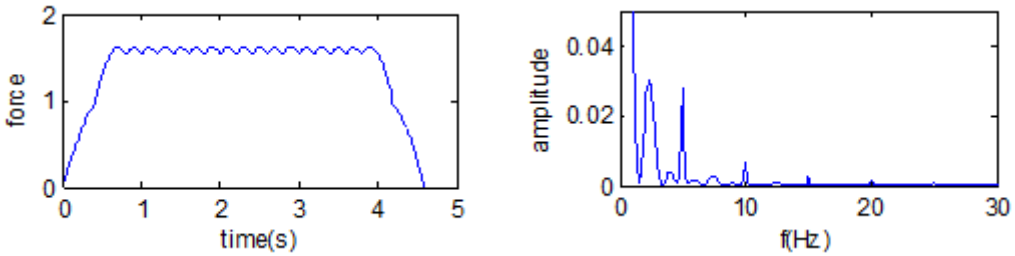

Time history **FFT spectrum**

iv) Tb = 1.0s, Tc = 0.4s ($\alpha_L = 2.5$)

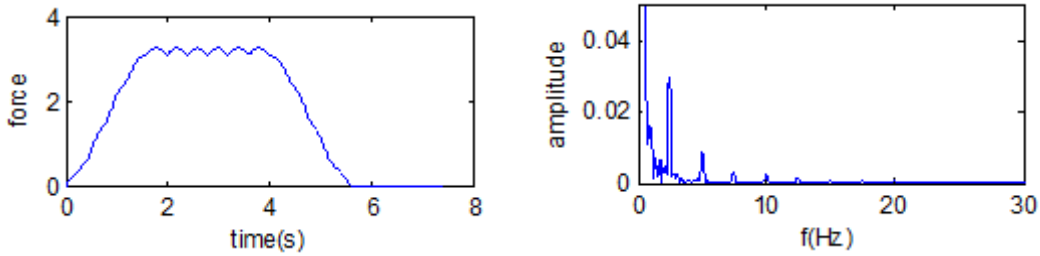

Time history **FFT spectrum**

v) Tb = 2.0s, Tc = 0.4s ($\alpha_L = 5.0$)

Figure 5.19 Different patterns of generalized trainload and corresponding frequency spectra

5.6.2 Further discussion of the frequency characteristics of bridge response

Having clarified the frequency contents in the various combinations of the repeated load patterns, much of the characteristics in the bridge responses presented in Section 5.5 become explicable from the view point of frequency contents in the trainload excitation.

The 8-m bridge case falls into the loading scenario ii) in Section 5.6.1. The frequency spectra of the displacements for the 20m/s and 50m/s speeds show clear consistency with the frequency spectra of the generalized load patterns, with higher peaks appear at the lowest few "dominant frequencies". The frequency spectra of the acceleration responses also exhibit clear peaks at the dominant frequencies, but over a wider frequency range, i.e., involves higher order as well as lower order dominant frequencies.

The obvious magnification of the spectral peaks at around 13 Hz in the case of 100m/s moving speed is apparently attributable to the resonance effect, as the first natural frequency of the bridge is around this value when a moving mass is present on the bridge. At this level of speed, the first few dominant frequencies, which carry much of the excitation energy, come closer to the bridge fundamental natural

frequency, and as a result, if the resonance is excited its effect will be considerably amplified.

The above general discussions are equally applicable in longer-length bridges, as in the cases of 40m and 80m bridges analyzed in Section 5.5. As the overlapping of individual carriage load pulses occur and intensifies, the energy in the dynamic excitation becomes increasingly concentrated in the lowest few dominant frequencies, especially the first dominant frequency, causing the dynamic deflection to exhibit primary frequencies at the first two dominant excitation frequencies. When the speed increases (to 100m/s herein), the 1^{st} or 2^{nd} dominant frequency gets closer to the natural frequency of the bridge (around 5 Hz for the 80m bridge and 10 Hz for the 40m bridge), causing markedly more significant resonance effect around the natural frequency both in the displacement and acceleration responses. On the other hand, when the speed is low and a number of dominant frequencies are below the resonance frequency, the frequency spectra in the acceleration response maintains a repeated pulse load character, and this is consistent with the discussion on the 8-m bridge in the previous paragraph.

It is worth noting that the resonance effect in terms of the absolute response amplitude appears to be more pronounced in the acceleration response than in the displacement. For example in the case of the 40m bridge, the mid-span deflection under different speeds exhibits only some steady increase; however, the acceleration amplitude increases by one order of magnitude at the speed of 100m/s as compared to that under 20m/s. Significantly increased acceleration could have a range of negative effects on the bridge structure as well as the railway track and the moving carriages.

The above described trend of concentration of the primary frequencies towards the first few dominant frequencies as the bridge span length increases can be comprehensively illustrated by plotting the frequency spectrum of the (displacement) response against the span ratio (bridge-to-carriage length ratio). Fig. 5.20 shows such a plot under a fixed speed of 100 m/s.

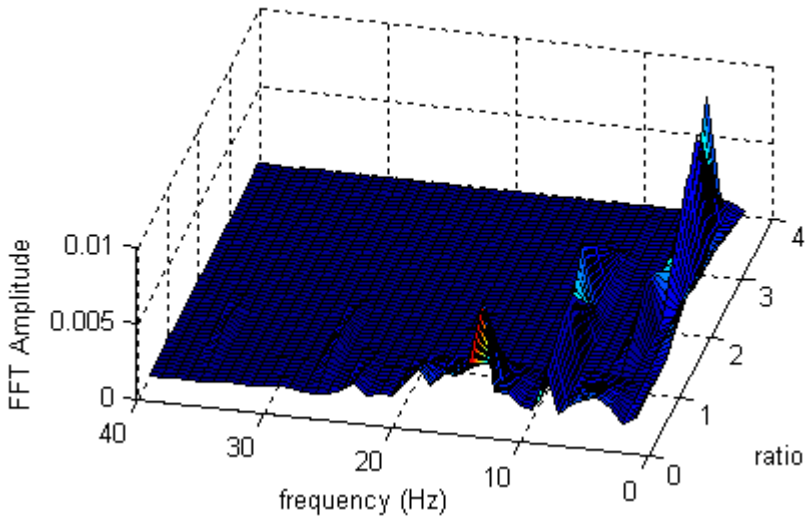

Figure 5.20 Effect of bridge-to-carriage length ratio on frequency spectrum of (displacement) response

It can be immediately observed that, as the bridge length (ratio) increases the primary frequencies tend to become increasingly concentrated to the first 1-2 dominant frequencies. Resonance tends to occur when one of the dominant frequencies is closer to the bridge fundamental frequency; and the resonant effect, when occurs, appears to be more significant in longer bridges. These observations are consistent with the discussion on the variation of the frequencies in the trainload with the bridge length. It should be noted in Fig. 5.20 the natural frequency of the bridge is not constant but reduces with increase of the bridge length.

5.7 Conclusions

The frequency characteristics of railway bridges under trainload excitation are investigated. The following conclusions may be made:

1) The dynamic response of a railway bridge to passing trains is closely associated with the frequency characteristics of the imposed trainload, particularly the "dominant frequencies" in the general case with multiple carriages, and the "driving frequencies" when only a single vehicle/carriage is involved.

2) For the special case with only a single vehicle (represented by a single mass and load), the dynamic effect can be conveniently described via the "driving frequency", $V/2L_b$, and hence may also be viewed as a normalised speed with respect to (two times of) the bridge length. The basic driving frequency tends to appear in the bridge velocity and acceleration response in a persistent manner, irrespective of the amount of mass involved.

3) For typical trainload with multiple carriages, the dynamic speed effect is overwhelmed by the repeated passage of carriages (or wheel sets); thus the "dominant frequency", V/L_c, which may also be viewed as the normalized speed with respect to the carriage length, becomes a governing factor instead of the "driving frequency". However, the effect of repeated load pulses is rather complicated in that it involves a distribution of frequencies at equal intervals of V/L_c. Examination of the frequency spectrum reveals that the distribution of the spectral peaks at nV/L_c is not uniform and it depends closely upon the bridge-to-carriage length ratio, $\alpha_L = L_b/L_c$. As α_L increases the spectral peaks become increasingly more concentrated at the lowest few dominant frequencies, and eventually dominated by the basic frequency at V/L_c when α_L is larger than 1.0.

However, it should be noted that in the present study, a simple bridge-train model is employed for the investigation. Such a model is advantageous for characterising the primary factors involved in the frequency contents of the bridge response; however, for more detailed expressions involving practical bridge-train interactions, the dynamics of the train carriages and the irregularities of the track-bridge surface should be incorporated in the bridge-train model and this should be considered in the future investigation.

6 Analysis of Bridge Resonance under Moving Trainloads with Involvement of Trainload Mass

6.1 Introduction

As discussed in Chapter 5, the dynamic response of railway bridges to moving trains may be characterised in terms of the various frequencies involved. As far as the global bridge response is concerned, it is generally understood that when one of the dominant frequencies from trainload excitation coincides with the fundamental natural frequency of the bridge, resonance could occur. However, such a general criterion is of little practical use due to the fact that a typical trainload would involve numerous dominant frequencies (at equal intervals); consequently for a given bridge there could be many train speeds that satisfy the above resonance condition. A method is therefore needed to identify the most or more critical dominant frequencies. This chapter presents the development of a new resonance severity indicator, called Z-factor, for the assessment of the resonance effect.

The involvement of the effective vehicle mass changes the dynamics of the responding bridge-vehicle system, and consequently causes variations to bridge dynamic responses, including the resonance phenomenon. The potential effect of the moving mass on the bridge response is generally recognized but a systematic study relating the varying dynamic system properties, particularly the resonant frequencies, to the characteristics of the excitation is lacked.

Moreover, based on information in the review chapter, in the special case with a single moving vehicle, where the resonance condition is traditionally viewed in the context of the “critical speed”, previous researches have suggested that the critical speed would become smaller when the moving mass was considered (e.g. Esmailzadeh and Ghorashi, 1995). Some studies tend to suggest that the modified critical speed may still be correlated to the modified resonant frequency of the

system (e.g. Dehestani, et al. 2009, etc.). However, no specifics were given concerning the actual calculation of the modified critical speed. Therefore, the potential significance of the critical speed, which is associated with a single moving load, on the bridge resonance under multiple moving loads, needs to be clearly understood.

Following an extensive theoretical discussion of the basic dynamic and resonance problems in Section 6.2, Section 6.3 presents the numerical investigation of the critical speed under a single moving vehicle and its variation with the vehicle mass. An empirical method is proposed to evaluate the modified critical speed in relation to the varied bridge resonant frequency. Section 6.4 examines numerically the bridge resonance phenomenon under typical trainload with multiple moving loads and masses. Parametric calculations are conducted to demonstrate the resonance phenomenon and the appropriateness of the proposed method, particular the developed Z-factor, for the identification of the actual resonance speeds and the assessment of the resonance severity.

6.2 Theoretical formulation

6.2.1 Critical speed of a single moving load

Critical speed is a term used to describe the condition under which a bridge reaches the maximum (global) response when subjected to a single moving load (e.g. Fryba 1999; Yang et al. 2004). Without considering the moving mass, the critical speed can be established mathematically (Fryba 1995; Yang et al. 2004), as:

$$V_{cr} = 2 f_1 L \tag{6.1}$$

where f_1 is the bridge fundamental frequency, L is the bridge length.

On the other hand, the dynamic characteristic of a single moving load may be represented by the so-called “driving frequency” as discussed extensively in Chapter 5, which has a base value of

$$f_{dr1} = V / 2L \tag{6.2}$$

Comparing Eq. (6.1) and (6.2), it can be observed that the critical speed is just the speed at which the driving frequency equals the bridge fundamental frequency, i.e., $f_{dr1} = f_1$. From this point of view, the critical speed may be interpreted as a resonance effect of the bridge under the excitation of a single moving load.

When the mass of the vehicle is also taken into account, the bridge dynamic response may be represented by a beam-moving mass system. The equation of motion (un-damped) of such a beam can be expressed as follows (Dehestani et al. 2009):

$$m_b \frac{\partial^2 w_b}{\partial t^2} + EI \frac{\partial^4 w_b}{\partial x^4} + M[V^2 \frac{\partial^2 w_b}{\partial x^2} + 2V \frac{\partial^2 w_b}{\partial t \partial x} + \frac{\partial^2 w_b}{\partial t^2}]\delta(x - Vt) = -Mg\delta(x - Vt) \tag{6.3}$$

in which the 3rd term describes the inertial effect due to the moving mass. M, EI, m_b, c_b are the flexural stiffness, mass per unit length and damping coefficient of the bridge, respectively, w_b is the bridge vertical displacement, and V is the speed of moving mass.

Using Eq. (6.3), the bridge deflection under a moving vehicle at different speeds can be calculated using numerical techniques, such as the Runge-Kutta method. The critical speed can be identified when bridge deflection reaches the maximum value. Results show the critical speed becomes smaller when the moving mass is involved (Esmailzadeh and Ghorashi 1995, Dehestani et al. 2009).

As a matter of fact, the change of the critical speed due to the vehicle mass may be deduced by the change (decrease) of the resonance frequency of the responding system due to the involvement of the moving mass. Thus,

$$V_{cr,m} = 2 f_m L \tag{6.4}$$

where $V_{cr,m}$ is the critical speed considering the effect of moving mass, and f_m is defined as the effective natural frequency of the bridge during the passage of the moving vehicle.

The calculation of the critical speed then becomes a matter of finding such an effective (or equivalent) natural frequency of the bridge-vehicle system. For simply-supported or fixed-ends, the bridge-vehicle system will attain the lowest fundamental frequency, f_{m1}, when the vehicle approaches the mid-span of the bridge. The effective natural frequency, f_m, should lie between f_{m1} and f_1. Introducing an effective frequency ratio α, such that $f_m = \alpha f_{m1}$, Eq. (6.4) can be re-written as:

$$V_{cr,m} = 2\alpha f_{m1} L \tag{6.5}$$

where α is within (1, f_1 / f_{m1}).

Herein numerical calculations using the FE model are carried out to examine the variation of the critical speed with the amount of the moving mass, and hence the factor α. The general FE model is developed for the analysis of a generic beam-bridge subjected to a series of moving loads representing a moving train, as schematically illustrated in Chapter 5 in Fig. 5.1a), where the moving vehicles are represented by loaded mass blocks while spring elements may be added to represent the vehicle suspension system. For simplicity and without affecting the main frequency characteristics, herein the mass blocks are attached directly on the bridge surface using a surface-to-surface contact approach, as shown in Fig. 5.1b).

For a single vehicle scenario, only one mass block is needed. The bridge is assigned an arbitrary length of 8m and a mass of 16,000 kg, while the stiffness is specified such that the bare bridge has a fundamental natural frequency of 14 Hz. For such a bridge, the critical speed for a moving vehicle without considering the vehicle mass can be calculated according to Eq. (6.1), $V_{cr} = 2 f_1 L = 2 \times 14 \times 8 = 224$ m/s.

Using the FE model, different amounts of the vehicle mass, in terms of the vehicle-to-bridge mass ratio, are simulated. For each amount of the mass ratio, the response

of the bridge is analysed under different moving speeds, and the critical speed, $V_{cr,m}$, for which the bridge attains the maximum (mid-span) response, is identified. Besides, for each mass ratio, f_{m1} can be calculated using the FE model by placing the mass at the mid-span. Substituting these parameters into Eq. (6.5), the corresponding effective frequency ratio α can be established. Fig. 6.1 shows the variation of α with the vehicle-to-bridge mass ratio.

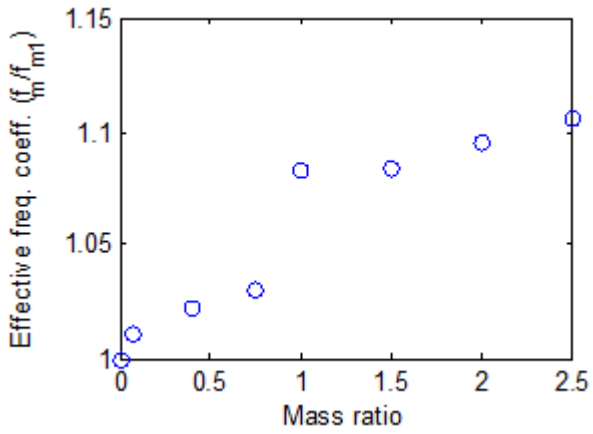

Figure 6.1 Correlation between vehicle-bridge mass ratio and effective frequency ratio α

From Fig. 6.1 it can be found that when the vehicle-to-bridge mass ratio is small, in particular smaller than 1.0 in the short span bridge example herein, the value of α may be approximately taken as equal to unity, which means the lower-bound natural frequency with the moving mass, f_{m1}, can be used directly as the effective bridge frequency to obtain the critical speed. When the vehicle-to-bridge mass ratio is large than 1.0, however, α tends to become noticeably larger than unity, indicating that the effective frequency would be markedly higher than the lower-bound frequency, and this should be considered in the calculation of the critical speed. For the mass ratio ranging from 1.0 to 2.5, α is approximately equal to 1.1.

Extending from the above analysis for a simply-supported condition, the bridge with both ends fixed is also analysed to examine the moving mass effect on the critical speed. The fundamental natural frequency is about 31Hz, so according to Eq. (6.1)

the theoretical critical speed would be about 500m/s without considering the moving mass. Fig. 6.2 depicts the correlation between vehicle-bridge mass ratio and the effective frequency ratio α. Similar observation as for the simply-supported case can be observed, i.e., when the mass ratio is smaller than 1.0 α is close to unity, and when the mass ratio is larger than 1.0 α increases to about 1.1.

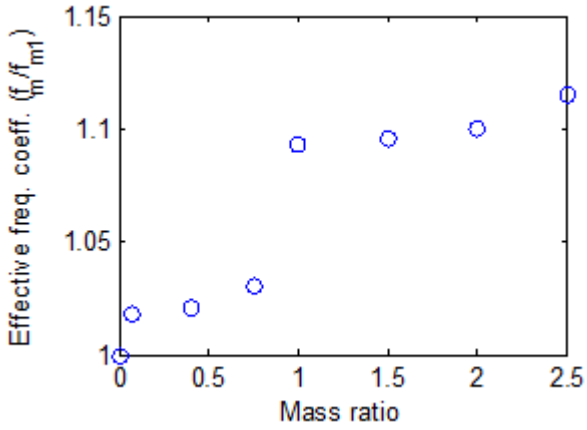

Figure 6.2 Correlation between vehicle-bridge mass ratio and frequency ratio α for a bridge with fixed-fixed ends

6.2.2 Bridge resonance under multiple carriages

The dynamic effect of a typical trainload with multiple carriages is characterised by the "dominant frequencies" arising from repeated carriage loads, and they are dependent upon the time interval between two consecutive carriages t_C, rather than t_L, i.e.,

$$f_{do,n} = nV / L_c \tag{6.6}$$

where L_C is the carriage length (noting $L_C / V = t_C$), n is a positive integer. Consequently, the resonance is expected to exhibit a very different feature as compared to the "critical speed" phenomenon under a single moving vehicle. It is understood (e.g. Ju and Lin 2003) that when a specific dominant frequency coincides with one of the first few bridge natural frequencies, especially the first bridge natural

frequency, resonance to a certain degree would occur. This establishes a necessary condition for the bridge resonance under a trainload with multiple carriages. However, in many situations especially with relatively short bridges, the trainload tends to have similar spectral amplitudes at a number of equally spaced dominant frequencies as expressed in Eq. (6.6), and not all such frequencies will cause resonance effect. Therefore, the actual resonant frequencies need to be identified, and from there the critical resonance speed can be determined.

Li and Su (1999) studied the amplification-suppression phenomenon between consecutive moving loads when a series of such loads move on the bridge at certain resonant speeds. Assuming the bridge response is governed by the fundamental mode, the dynamic response can be expressed using a generalized co-ordinate as:

$$w_b(x,t) = q(t)\phi(x) \tag{6.7}$$

where $q(t)$ is the generalized co-ordinate which expresses the bridge vertical response with time, and $\phi(x) = \sin(\pi x / L_b)$ is the bridge fundamental mode shape. Thus, the equation of motion of the bridge under multiple moving loads may be written in a generalised form as:

$$\ddot{q}(t) + 2\xi\omega\dot{q}(t) + \omega^2 q(t) = \frac{2}{mL_b}\sum_{i=K}^{M+K} \sin\frac{\pi(vt - a_i)}{L_b} P_i \tag{6.8}$$

where M denotes the number of carriages currently acting on the bridge. The solution of $q(t)$ may be sought by first examining the forced vibration of the bridge under a single moving load and the free vibration after the passage of the single load, and subsequently using the principle of superposition. For the convenience of the superposition operation, let's consider the single moving load be the i-th load in the moving load series, and let $a_i = (i-1)L_c$ be the distance of the i-th load from the first load, and $t = 0$ be the time when the first moving load enters the bridge. Thus, the forced vibration due to the i-th moving load takes place when $(a_i / v) \le t \le (a_i / v + L_b / v)$. Specializing Eq. (6.8) for the i-th single moving load

only, the solution can be expressed as the combination of a particular (forced or steady-state) term and a homogeneous (free or transient) term, as:

$$q(t) = \frac{y_{st}}{1-\beta^2}\sin\frac{\pi(vt-a_i)}{L_b} - y_{st}\frac{\beta}{1-\beta^2}e^{-\xi\omega(t-a_i/v)}\sin\omega(t-\frac{a_i}{v}) \tag{6.9}$$

where $y_{st} = PL_b^3/48EI$ is the static mid-span deflection with moving load P acting on the mid-span. $\beta = \pi v/L_b\omega$,with ω being the bridge fundamental frequency; it should be noted that when the carriage mass is considered, ω is understood to be the mass-loaded bridge frequency. ξ is the damping ratio.

The free vibration after the passage of the single (i-th) moving load, i.e., $t \geq t' = a_i/v + L_b/v$, is determined by the displacement $q_i(t')$ and velocity $\dot{q}_i(t')$ at the end of forced vibration period t':

$$q(t) = e^{-\xi\omega(t-t')}\left[\frac{\dot{q}_i(t') + \xi\omega q_i(t')}{\omega}\sin\omega(t-t') + q_i(t')\cos\omega(t-t')\right] \tag{6.10}$$

Substituting $q_i(t')$ and $\dot{q}_i(t')$ from Eq. (6.9) into Eq. (6.10) yields:

$$q(t) = -e^{-\xi\omega(t-a_i/v-L_b/v)}\frac{y_{st}\beta}{1-\beta^2}\sin\omega(t-\frac{a_i}{v}-\frac{L_b}{v}) - e^{-\xi\omega(t-a_i/v)}\frac{y_{st}\beta}{1-\beta^2}\sin\omega(t-\frac{a_i}{v}) \tag{6.11}$$

With Eq. (6.9) and (6.11), the bridge response under a series of moving loads can be obtained using superposition. Consider a generic scenario of K-1, for which (K-1) moving loads have crossed the bridge, while M moving loads are acting on the bridge; M is determined by the bridge-to-carriage length ratio, $M = \mathrm{Int}(L_b/L_c)$. It follows $(a_{K-1}/v + L_b/v) \leq t \leq (a_K/v + L_b/v)$, and the bridge response can be expressed in accordance with the solution by Li and Su (1999) as:

$$\begin{aligned} q(t) = {} & \frac{y_{st}}{1-\beta^2}\times\sum_{i=K}^{M+K-1}\sin\frac{\pi(vt-a_i)}{L_b} - \frac{y_{st}\beta}{1-\beta^2}\times\sum_{i=K}^{M+K-1}e^{-\xi\omega(t-a_i/v)}\sin\omega(t-\frac{a_i}{v}) \\ & - \frac{y_{st}\beta}{1-\beta^2}\times\sum_{i=1}^{K-1}e^{-\xi\omega(t-a_i/v-L_b/v)}\sin\omega(t-\frac{a_i}{v}-\frac{L_b}{v}) - \frac{y_{st}\beta}{1-\beta^2}\times\sum_{i=1}^{K-1}e^{-\xi\omega(t-a_i/v)}\sin\omega(t-\frac{a_i}{v}) \end{aligned} \tag{6.12}$$

In the above equation, the first two terms represent the bridge vibration due to the acting M moving loads, while the last two terms are the bridge free vibration due to the preceding K-1 moving loads. Note that the 2nd and 4th terms can be combined to yield a summation from i=1 to (M+K-1).

It is clear that the first term in Eq. (6.12), i.e., the "steady state" term of the bridge forced vibration, does not increase as the moving loads pass over the bridge. Thus the bridge resonance can be analyzed by only investigating the remaining terms in Eq. (6.12).

As stated earlier, the prior condition for the resonance to occur is that one of the dominant frequencies from multiple moving loads, expresses in Eq. (6.6), equals the bridge fundamental frequency, i.e.,

$$n\frac{v_{re}}{L_c} = f_1 = \frac{\omega}{2\pi} \tag{6.13}$$

where v_{re} is defined as "resonant speed" herein, rearrange,

$$v_{re} = \frac{f_1 L_c}{n} = \frac{\omega L_c}{2\pi n} \tag{6.14}$$

Substituting the above specific resonant speed and $a_i = (i-1)L_c$ into Eq. (6.12), the last three terms can be re-written as:

$$q_r(t) = \left(-y_{st}\frac{\beta_{re}}{1-\beta_{re}^2}e^{-\xi\omega t}\right)\times\left[\left(\sum_{i=1}^{M+K-1} e^{\xi\omega a_i / v_{re}}\right)\times\sin\omega t + \left(\sum_{i=1}^{K-1} e^{\xi\omega(a_i/v_{re}+L_b/v_{re})}\right)\times\sin\omega\left(t-\frac{L_b}{v_{re}}\right)\right] \tag{6.15}$$

where, $\beta_{re} = \dfrac{\pi v_{re}}{L_b\omega}$ (6.16)

or

$$q_r(t) = \left(-y_{st}\frac{\beta_{re}}{1-\beta_{re}^2}e^{-\xi\omega t}\right)\times\left[\left(\sum_{i=1}^{M+K-1} e^{2\pi n(i-1)\xi}\right)\times\sin\omega t + \left(\sum_{i=1}^{K-1} e^{2\pi n[(i-1)+L_b/L_c]\xi}\right)\times\sin\left(\omega t - 2\pi n\frac{L_b}{L_c}\right)\right] \tag{6.17}$$

where $\beta_{re} = \dfrac{L_c}{2nL_b}$ (6.18)

It can also be deduced that under the resonant speed of Eq. (6.14), the time interval between two consecutive moving loads is $L_c / v_{re} = 2\pi n / \omega$, this makes the sine functions in Eq. (6.15) repeat themselves while their coefficients cumulate as the consecutive moving loads pass over the bridge. As noted by Li and Su (1999), this means the response of the bridge under a series of moving loads at the "resonance" speed will always tend to increase. It is the rate of increase between the consecutive moving loads that determines the severity of the resonance effect.

From Eq. (6.15) it can be readily shown that when $\cos(\omega L_b / v_{re}) = 1$, the two sine terms get in phase; and when $\cos(\omega L_b / v_{re}) = -1$, they are out of phase. Thus, as Li and Su (1999) suggests, $\cos(\omega L_b / v_{re}) = 1$ may be used to identify the most serious bridge resonance, while $\cos(\omega L_b / v_{re}) = -1$ sets out the condition by which the most significant suppression effect (minimum bridge response) occurs.

Recalling Eq. (6.14), it follows $\omega L_b / v_{re} = 2\pi n L_b / L_c$, thus it becomes clear that only at special combinations of the bridge and carriage lengths (L_b / L_c = integer or at 0.5 interval, respectively) the maximum resonance or suppression as mentioned above would take place. For all other and more general length combinations, the value of $\cos(\omega L_b / v_{re}) = \cos(2\pi n L_b / L_c)$ could be anything between -1 and 1; therefore in such cases the severity of the resonance effect can not be determined using above condition.

For simplicity, herein we ignore damping, and consequently Eq.(6.15) can be re-written as:

$$q_r(t) = \left(-y_{st} \frac{\beta_{re}}{1-\beta_{re}^{\ 2}} \right) \times \left[(M+K-1) \times \sin\omega t + (K-1) \times \sin\omega (t - \frac{L_b}{v_{re}}) \right] \quad (6.19)$$

Hence,

$$q_r(t) = A_{k-1}\sin(\omega t - \theta_{k-1}) \qquad \text{with } (a_{K-1} + L_b)/v \le t \le (a_K + L_b)/v \tag{6.20}$$

where A_{k-1} represents the bridge response amplitude for the (K-1)-th scenario when (K-1) moving loads have left the bridge, while M moving loads act on the bridge,

$$A_{k-1} = \frac{y_{st}\beta_{re}}{1-\beta_{re}^2}\sqrt{\left[(M+K-1)+(K-1)\cos(\omega\frac{L_b}{v_{re}})\right]^2 + \left[(K-1)\sin(\omega\frac{L_b}{v_{re}})\right]^2} \tag{6.21}$$

$$\text{and } \tan(\theta_{k-1}) = \frac{(K-1)\sin(\omega\dfrac{L_b}{v_{re}})}{(M+K-1)+(K-1)\cos(\omega\dfrac{L_b}{v_{re}})}$$

Now consider the immediate next (K-th) scenario, i.e., next moving load enters the bridge, or in other words K moving loads have left the bridge, $q_r(t)$ becomes:

$$q_r(t) = A_k\sin(\omega t - \theta_k) \qquad \text{with } (a_K + L_b)/v \le t \le (a_{K+1} + L_b)/v \tag{6.22}$$

$$\text{where } A_k = \frac{y_{st}\beta_{re}}{1-\beta_{re}^2}\sqrt{\left[(M+K)+K\cos(\omega\frac{L_b}{v_{re}})\right]^2 + \left[K\sin(\omega\frac{L_b}{v_{re}})\right]^2} \tag{6.23}$$

By comparing amplitudes of bridge responses using Eq. (6.21) and (6.23), the change of bridge response under consecutive moving loads can be evaluated. For convenience of the mathematical expression, the squared amplitude is employed. Thus, the amplitude (squared) difference under consecutive moving loads can be expressed as:

$$\begin{aligned}(A_k)^2 - (A_{k-1})^2 &= \left(\frac{y_{st}\beta_{re}}{1-\beta_{re}^2}\right)^2 \times \left\{\left[(M+K)+K\cos\frac{\omega L_b}{v_{re}}\right]^2 + \left[K\sin\frac{\omega L_b}{v_{re}}\right]^2 - \left[(M+K-1)+(K-1)\cos\frac{\omega L_b}{v_{re}}\right]^2 - \left[(K-1)\sin\frac{\omega L_b}{v_{re}}\right]^2\right\} \\ &= \left(\frac{y_{st}\beta_{re}}{1-\beta_{re}^2}\right)^2 \times 2(M+2K-1)(1+\cos\frac{\omega L_b}{v_{re}})\end{aligned} \tag{6.24}$$

Let

$$Z = \left(\frac{\beta_{re}}{1-\beta_{re}^{\,2}} \right)^2 \times \left(1+\cos\frac{\omega L_b}{v_{re}} \right) = Z_a \times Z_b \tag{6.25}$$

It follows

$$\frac{(A_K)^2 - (A_{K-1})^2}{y_{st}^2} = Z\left[2(M + 2K - 1)\right] \tag{6.26}$$

The coefficient Z, along with its components Z_a, Z_b as expressed in Eq. (6.25), represents the rate of increase of the bridge response amplitudes as the moving loads pass over the bridge at a potential resonance speed. Therefore, it can serve as a direct indicator of the severity of the resonance at such a speed. From Eq. (6.25) it can also be seen that Z is a non-negative coefficient; this further confirms the observation mentioned earlier that the bridge response will tend to always increase under a series of moving loads at a resonant speed.

It should be pointed out that the above derivations are valid under the strict condition that the moving load travel at a resonance speed, i.e., Eq. (6.13) holds. Substituting Eq. (6.13) and (6.18) into Eq. (6.25) yields:

$$\begin{aligned} Z = Z_a \times Z_b &= \left[\frac{L_c / 2nL_b}{1-\left(L_c / 2nL_b\right)^2} \right]^2 \times \left[1+\cos\left(2\pi n \frac{L_b}{L_c} \right) \right] \\ &= \left[\frac{2nL_b / L_c}{(2nL_b / L_c)^2 - 1} \right]^2 \times \left[1+\cos\left(2\pi n \frac{L_b}{L_c} \right) \right] \end{aligned} \tag{6.27}$$

Eq. (6.27) is significant as it shows that, when the resonance condition is met, i.e., $v = v_{re} = \omega L_c / 2\pi n$ (or $f_1 L_c / n$), the relative severity of the actual resonance is entirely determined by the bridge-to-carriage length ratio L_b / L_c. Since for any given bridge-train system, L_b / L_c is a constant, Z value can be obtained for different orders of resonant speeds (with different n values) as a function of L_b / L_c. Figure 6.3 depicts the relationship between *Z*, Z_a, Z_b and L_b / L_c.

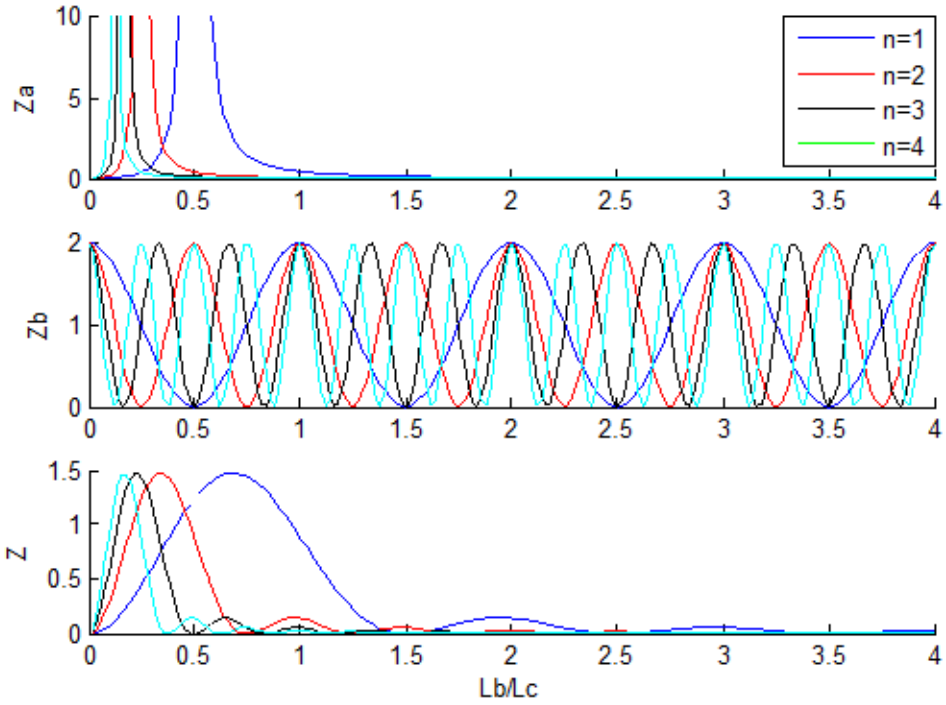

Figure 6.3 Za, Zb, and Z as functions of Lb/Lc

The following may be observed from Fig. 6.3:

1) While Z_b oscillates in the range of (0, 2) as the ratio L_b / L_c increases, Z_a is localised around the singularities at $L_b / L_c = 1/2n$, with the largest singular ratio at 0.5.

2) As a result, the Z value is dominated by Z_a and tends to concentrate in the lower L_b / L_c ratio range up to about 1.5. For longer bridges with L_b / L_c >1.5, the resonance effect due to the excitation of multiple moving loads, or essentially the dominant frequencies associated with the repeated loads, appear to diminish. However, it should be mentioned that even with small resonance effect when L_b / L_c >1.5, the dynamic bridge response amplitude may not be small, since it is obtained using Z times static deflection.

3) Significant resonance effect to be excited by a higher order dominant frequency, i.e., $n \geq 2$, would be possible only for very short bridges with $L_b / L_c \leq 0.7$; and in

this range, especially when $L_b / L_c \le 0.5$, the bridge could be excited into certain level of resonance at more than one occasion of n, which implies that there exists more than one critical resonance speed. On the other hand, for $L_b / L_c > 0.7$ (and less than 1.5), significant resonance effect is only associated with the first order dominant frequency, or n=1. This observation echoes very well the conclusion made from the examination of the frequency characteristic in the trainload patterns for different bridge-carriage length ratios in Chapter 5.

To give an example, let's consider a standard carriage length L_c = 20m, and two cases of bridges:

a) $L_b = 8\,\text{m}$, $f_1 = 14\,\text{Hz}$, thus $L_b / L_c = 0.4$. From Fig. 6.3, significant Z could arise from three different n values, i.e., n=1, Z=0.95; n=2, Z=1.37; and n=3, Z=0.33. Recall Eq. (6.14), the corresponding resonance speeds can be found as $v_{re} = f_1 L_c / n = 280/n$ =280 m/s, 140m/s, and 93.3 m/s, respectively.

b) $L_b = 18\,\text{m}$, $f_1 = 7\,\text{Hz}$; thus $L_b / L_c = 0.9$. From Fig. 6.3, significant Z could only arise from n = 1, resulting in Z = 1.17. The corresponding resonance speed is $v_{re} = f_1 L_c / n = 140/n$ =140 m/s. Less significant but still appreciable resonance may be excited at n = 2, with Z = 0.12; but it is noteworthy that the corresponding speed is reduced to a more attainable level of 70 m/s.

Comparing to the use of $\cos(\omega L_b / v_{re})$, as suggested in Li and Su (1999), the Z factor developed above is a much more robust and stable indicator of the resonance effect associated with the excitation of multiple moving loads at a potential resonance speed. Further examination in this regard will be illustrated in the next section.

It should be pointed out that the current discussion is restricted to the situation whereby the dynamic response is governed by the fundamental mode of the bridge, and the resonance effect is also confined to the resonance at the fundamental mode frequency, i.e., when one of the dominant frequencies from the multiple moving load excitation coincides with the fundamental mode frequency of the bridge.

Therefore, the observations may be considered as applicable for relatively small to medium length bridges.

When the carriage mass is involved, the bridge fundamental frequency f_1 will be altered. If the alteration is not significant or the change may be considered as constant (this could happen only with relatively long bridges which may be considered as being constantly loaded with a given number of carriage masses), the discussions presented in this section are still generally applicable, provided that the natural frequency of the bridge is replaced with the mass-loaded frequency. On the other hand, if the variation of the effective mass of the system is significant and the frequency of the system can not be treated as a constant, strictly speaking there will be no clearly defined resonance speeds ($v_{re} = f_1 L_c / n$). In such cases, similar to the situation discussed in the earlier section for the critical speed under a single moving vehicle, an effective natural frequency of the bridge-moving mass system may be used to determine the resonance speeds under multiple carriages. The corresponding resonance severity can then be established using the *Z* factor expressed in Eq. (6.25). This will be demonstrated in the numerical examples in the section that follows, along with general verification of the effectiveness of the *Z* factor where the moving mass is negligible.

6.3 Numerical analysis of bridge response under multiple trainloads considering vehicle mass

In this section two illustrative examples, including short-span and medium-span bridge cases, are firstly provided to demonstrate the effectiveness of *Z* in Eq. (6.25) in the assessment of the bridge resonance under the excitation of multiple moving loads, without the involvement of the carriage mass. The numerical model is similar to that described earlier (Fig.5.1).

6.3.1 Moving mass negligible

The properties of a bridge-train system as used in Li and Su (1999) are firstly employed to allow for a direct comparison. The bridge is 32m-long with a fundamental frequency at 5.3Hz, and the train is modelled using a series of 20 moving loads with an interval distance of 21m. Based on these parameters, the resonant speeds v_{re} can be calculated using Eq. (6.14), and the corresponding Z can be obtained using Eq. (6.25). For an observation, the values of $\cos(\omega L_b / v_{re})$, as used by Li and Su for identifying the maximum and minimum resonance effects, are also calculated. The results are summarised in Table 6.1.

Table 6.1 Z and cos(wLb/Vre) values at (potential) resonant speeds

n	1	2	3	4	5
v_{re} (m/s)	111.3	55.65	37.1	27.83	22.26
Z	0.0015	0.0556	0.0012	0.0125	0.0012
$\cos(\omega L_b / v_{re})$	-0.99	0.96	-0.9	0.83	-0.73

From Table 6.1, Z reaches the maximum value at n equals 2, and the corresponding resonance speed is 55.65 m/s. This indicates that the severest bridge resonance will occur under the above speed, and it is the 2nd dominant excitation frequency that causes the resonance. For this particular case, the prediction by means of $\cos(\omega L_b / v_{re})$ is consistent with the above result. However, as discussed earlier, the criterion of $\cos(\omega L_b / v_{re})$ is suited for the detection of the maximum and minimum resonance effect where the above cosine value approaches 1.0 or -1.0, which happens to be the case in this example. Otherwise, as will be shown in the 8-m bridge case slightly later, this cosine criterion will become meaningless.

Fig. 6.4 shows the variation of the mid-span deflection of the above bridge with the moving speed and damping ratio. From the Fig. 6.4(a), where the damping is ignored, it can be found clearly that the most serious bridge resonance is excited at 55m/s, and the next appears at about 28 m/s. These results agree perfectly with the

predictions the Z factor mentioned above. Results for lightly damped systems with a damping ratio being 1%, 2% and 4%, respectively, as shown in Fig. 6.4(b), appear to exhibit the same order of resonances at the respective resonance speeds as in the un-damped system, while the response amplitudes reduce as the damping increases, as can be expected. This indicates that the *Z*-factor is equally applicable in lightly damped systems.

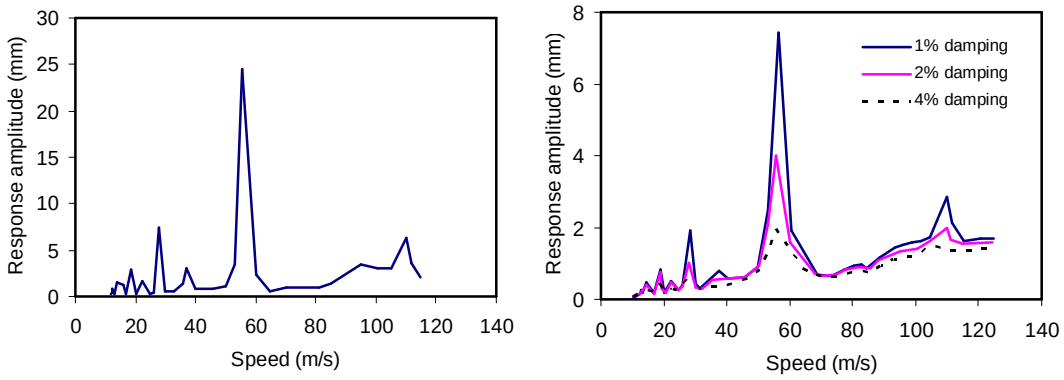

a) Without damping **b) With damping (1%, 2% and 4% respectively)**

Figure 6.4 Variation of mid-span deflection with moving speed for a 32-m bridge without considering carriage mass (after Li and Su 1999)

Next, a bridge with 8m length, which is described in Chapter 5, is employed to demonstrate the effectiveness of Z in Eq. (6.25) in short-span bridge scenarios, without the involvement of carriage mass. The train model including 10 carriages with an interval distance of 20m is considered in the study. A small nominal mass density is assigned to the mass block to effectively eliminate the carriage mass effect. Meanwhile the force exerted on the bridge is retained as 400 kN, corresponding to the assumed standard carriage weight. By doing so, the obtained bridge deflections are comparable to the results when the full carriage mass is taken into account. In the analysis, bridge responses without considering damping and with light damping ratio (1%) are both obtained.

Using Eq. (6.14), the resonant speeds v_{re} can be calculated, then the corresponding Z can be obtained using Eq. (6.25), similar to above medium-span bridge case. The values of $\cos(\omega L_b / v_{re})$ are also calculated. The results are summarised in Table 6.2.

Table 6.2 Z and cos(wLb/Vre) values at (potential) resonant speeds

n	1	2	3	4	5
v_{re} (m/s)	280	140	93	70	56
Z	0.94	1.37	0.33	0.02	0.14
$\cos(\omega L_b / v_{re})$	-0.81	0.31	0.31	-0.81	1

It can be observed that Z reaches the maximum value at n equals to 2, and the corresponding resonance speed is 140m/s. This means the 2nd dominant frequency can cause the severest bridge resonance. Meanwhile the least serious bridge resonance will occur at n equals to 4, this corresponds 70m/s resonance speeds. On the other hand, the values of $\cos(\omega L_b / v_{re})$ tend to give a rather different picture, with the highest value corresponding to n = 5, i.e., at 56m/s resonance speed.

Fig. 6.5 depicts the variation of mid-span deflections of the above bridge with speed. From the figure it can be seen clearly that, with or without damping, the most serious bridge resonance occurs at around 140m/s, and this is followed by bridge resonance at around 280m/s, i.e., the 1st dominant frequency approaches bridge fundamental frequency. No obvious resonance actually occurs at the 70m/s resonance speed. All the above results agree very well with the prediction from the *Z*- factor, whereas the values of $\cos(\omega L_b / v_{re})$ becomes meaningless in this case.

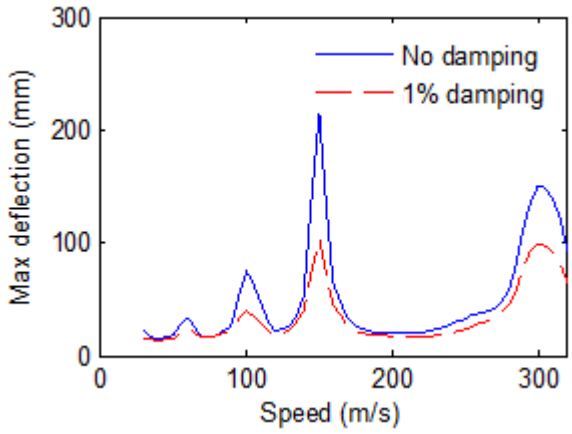

Figure 6.5 Variation of mid-span deflection with moving speed for 8-meter bridge without considering carriage mass

6.3.2 Moving mass significant

As mentioned in the Formulation section, when the moving carriage mass becomes significant, a modified bridge resonance frequency, i.e., the effective fundamental frequency of the bridge-moving mass system, needs to be established before the *Z*-factor may be applied for the determination of the resonance effect. In what follows, two bridge cases with two different levels of the carriage-to-bridge mass ratio are analysed using the FE model and the results are examined.

The first case is a 40m long bridge with a fundamental frequency of around 10Hz, and a train model including 10 carriages with an interval distance of 20m is considered. The mass of the bridge is set to 100,000kg, while the mass of each carriage is selected as 40,000kg, which represents the normal mass of a single laden carriage in a typical high-speed train. Thus, the carriage-to-bridge mass ratio is 40%. Other parameters are the same to those in above short-span bridge case. The range of variation of the natural frequency of the bridge system considering the moving mass is found to be 9 ~ 10Hz.

Based on the results shown in Fig. 6.3, for the present bridge with L_b/L_c = 2.0, the most significant resonance effect can be expected to associate with the first order

dominant frequency, i.e., n= 1, and the corresponding Z value is 0.14. For the determination of the resonance speed, use can be made of Eq. (6.14) keeping in mind that the effective natural frequency of the loaded bridge is reduced from the 10 Hz for the bare bridge. Trial analysis indicates that the lowest fundamental frequency of the present bridge-carriage system is about 9Hz. For the determination of the resonance speed, an effective natural frequency of the mass loaded bridge is estimated to be approximately 9.3Hz. Thus the corresponding resonance speeds can be calculated using the effective bridge frequency. For a comparison, the resonance speeds as calculated using the bare bridge frequency are also listed. Table 6.3 summarises the Z and $\cos(\omega L_b / v_{re})$ values at different resonant speeds with n from 1 to 5.

Table 6.3 Z and cos(wLb/Vre) values at resonant speeds

n	1	2	3	4	5
v_{re} (m/s)	200	100	67	50	40
$v_{re,m}$ (m/s)	**186**	**93**	**62**	**46.5**	**37.2**
Z	0.14	0.03	0.01	0.008	0.005
$\cos(\omega L_b / v_{re})$	1	1	1	1	1

For the particular case under consideration, $\cos(\omega L_b / v_{re})$ yields a value of 1.0 at all five resonant speeds, which does not provide any indication of the relative resonance effects at these different speeds. On the other hand, the *Z* values indicate clearly that the highest resonance occurs when *n* equals 1 while the moving speed is about 186 m/s (using the effective natural frequency) or 200 m/s (using bare bridge natural frequency).

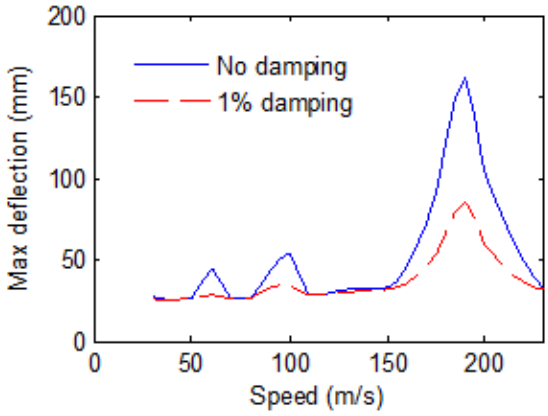

Figure 6.6 Variation of maximum mid-span deflection with moving speed for 40-m bridge considering carriage mass

The results from the FE model analysis are shown in Fig. 6.6 in terms of the variation of mid-span deflection with moving speed, without or with consideration of (1%) damping. It can be found clearly that the severest resonance does occur at around 186 m/s, followed by resonances at around 90m/s and 60m/s. These results agree very well with the predictions using the *Z* factor.

Fig. 6.7 shows the computed bridge mid-span deflection time histories with 1% damping for moving speeds of 200 m/s, 190m/s and 100 m/s, respectively. It can be seen clearly that much more serious resonance is excited at 190 m/s as compared to that at 100 m/s.

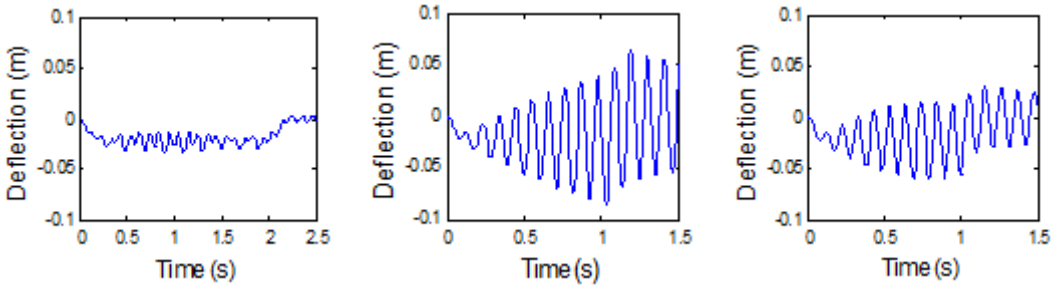

a) 100 m/s **b) 190 m/s** **c) 200 m/s**

Figure 6.7 Mid-span deflection time histories of the 40-m bridge under different moving speeds

The next case to be examined is the 8-m short-span bridge, assuming a self mass of 16,000 kg. With a 40,000 kg carriage mass, a high carriage-bridge mass ratio of 2.5

is attained. Comparing to a fundamental frequency of 14Hz for the bare bridge, the coupled bridge-moving mass system now has a natural frequency varying from 14 Hz to the lowest of 6Hz when the mass moves to the mid-span. Clearly, with such large variation of the natural frequency, calculating the resonance speeds using Eq. (6.14), i.e., $v_{re} = f_1 L_c / n$ with the bare bridge natural frequency would not make sense.

Recall the evaluation presented in Section 6.2.1 about the critical speed, the effective natural frequency for a short bridge with large moving masses would be around 1.1 times the lowest system frequency, i.e., 1.1 × 6 = 6.6 Hz. The corresponding resonance speeds, $v_{re,m} = f_{1,m} L_c / n$, and the associated *Z* values are shown in Table 6.4. For a comparison, the "resonance" speeds as calculated from the bare bridge frequency, i.e., $v_{re,0} = f_{1,0} L_c / n$, are also listed in the table.

Table 6.4 Z and $\cos(2\pi n L_b / L_c)$ values at resonant speeds

n	1	2	3	4	5
$v_{re,0}$ (m/s)	280	140	93	70	56
$v_{re,m}$ (m/s)	**132**	**64**	**43**	**34**	**26**
Z	0.94	1.37	0.33	0.02	0.14
$\cos(2\pi n L_b / L_c)$	-0.81	0.31	0.31	-0.81	1

The results in Table 6.4 tend to indicate that the highest resonance effect (highest Z) will take place at a resonance speed of around 64 m/s with its 2nd dominant frequency coinciding with the effective natural frequency of the bridge-carriage system, and this is followed by that at 132 m/s with on its 1st dominant frequency, and then 43 m/s with its 3rd dominant frequency.

For verification, the computed amplitude mid-span deflections for the bridge-moving mass system under different moving speeds, using the finite element model, are

illustrated in Fig. 6.8. It can be immediately observed that the highest resonance peak indeed takes place at around 60 m/s. The 2nd and 3rd resonance peaks appear to occur at around 120m/s and 40 m/s, respectively. These results are in good agreement with the predictions using the Z factor in association with the effective natural frequency of the bridge-mass system. It is worth noting that the calculations based on the bare bridge frequency, as shown in Table 6.4, fail to predict the actual resonance responses, as expected.

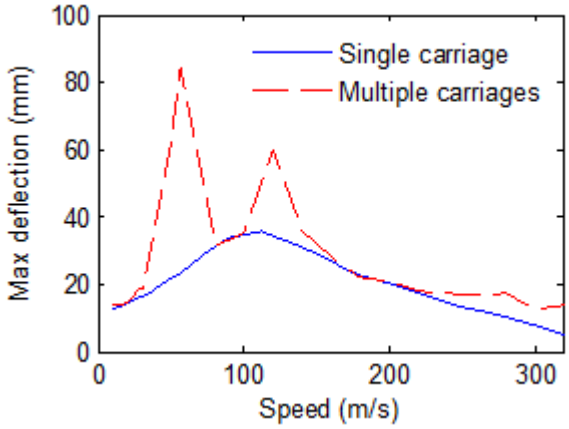

Figure 6.8 Variation of maximum mid-span deflection with moving speed for 8-m bridge considering carriage mass

Shown in Fig. 6.8 is also the amplitude response curve when the bridge is subjected to a single carriage of the same load and mass as used in the multiple carriage analysis. It can be observed in the single carriage situation the peak amplitude occurs at a different speed from the resonance in the multiple carriage situation. This is explicable by the fact that the dynamic response of the bridge under multiple carriages is influenced by the superposition of bridge responses due to consecutive carriages. The critical speed for the single carriage load herein is found to be around 105 m/s, and this is consistent with the prediction using Eq. (6.26), i.e. $V_{cr,m} = 2\beta f_{m0} L_B = 2\times 1.1\times 6\times 8 = 105.6$ m/s. Understandably, the maximum resonance effect under a single carriage load is considerably lower than its counterpart under multiple carriage loads.

Fig. 6.9 shows the mid-span deflection time histories when the bridge is subjected to the series of moving carriages at three selected speeds. The severity of the resonance effect under the speed of about 60 m/s is remarkable, and it is followed by resonance effect at 120m/s, the least serious resonance effect occurs at 40m/s, these results are consistent to predictions using Z-factor, which are listed in Table 6.4.

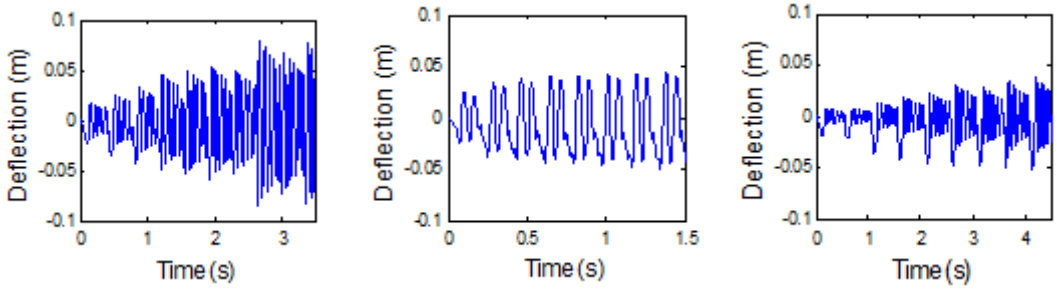

a) 60 m/s **b) 120 m/s** **c) 40 m/s**

Figure 6.9 Mid-span deflection time histories for the 8-m bridge under different resonance speeds

6.4 Conclusions

The resonance of railway bridges under trainload excitation is investigated in light of the frequency characteristics of the excitation, as well as the varying resonance frequency of the bridge-vehicle system when the vehicle mass is involved. Based on the results, the following conclusions may be drawn:

1) For the basic scenario where only a single carriage (represented by a single mass and load) is involved, the variation of the dynamic effect with speed may be interpreted by means of the "driving frequency" of the excitation, which is an apparent frequency associated with the duration of the load moving over the bridge, i.e., $V/2L_b$. The classical definition of the critical speed then becomes simply a resonant condition such that the above driving frequency matches the bridge natural frequency. It is clear that the critical speed reduces as the amount of moving mass increases. The modified critical speed can still be well predicted using the above

resonance condition, with however the consideration of an effective bridge frequency instead of the bare bridge natural frequency, using a coefficient α as proposed in this study.

2) For typical trainload with multiple carriages, the dynamic effect is overwhelmed by the repeated passage of carriages; thus the apparent "dominant frequencies" with a basic value of V / L_c, which may also be looked upon as the normalized speed with respect to the carriage length, becomes a governing factor. As there exist a cluster of dominant frequencies at equal intervals of V / L_c, thus leading to a series of resonant speeds, a resonance indicator, the *Z*-factor, is developed for the assessment of the bridge resonance severity at different resonant speeds. It is found that the *Z*-factor is essentially only dependent upon the length ratio between the bridge and the carriage. The resonance effect is shown to be markedly more severe in shorter bridges.

4) With the *Z*-factor, for a given bridge (effectively the ratio L_b / L_c and the natural frequency), the relative resonance severity at different orders of the dominant frequencies, which correspond to resonance speeds, can be predicted conveniently. When the carriage mass effect is involved, the *Z*-factor can still be used effectively to predict the resonance effect, provided that an appropriate effective natural frequency is employed in the establishment of the resonance speeds.

It should be mentioned that when deriving the Z-factor, only the fundamental mode has been considered, whereas damping is ignored. Although numerical results demonstrate that the resonance severity of light damped system can still be predicted using the Z-factor, for systems with large damping and involving vibrations from more than one mode, the Z-factor may need be modified accordingly and this should be investigated further in the future.

7 Conclusions and recommendations for further research

7.1 Conclusions

The research presented in this thesis deals with structural dynamic system identification in a broader frequency-based framework. The thesis contains two major parts. The first part deals with a) the experimental aspects of extracting ABC frequencies from physical tests, and b) the effective use of such frequencies in structural parameter identification and FE model updating. The second part is devoted to the characterisation of a complex variant dynamic system, especially the railway bridges, from a frequency perspective, and subsequently quantification of the resonance effects.

Specific conclusions on the various sub-topics have been included in the individual chapters. A summary of the major conclusions is presented in what follows.

A) Regarding the experimental extraction of ABC frequencies

1) Extraction of ABC frequencies involves the inversion of FRF matrices. Hence, it requires high quality FRF data, and this poses challenging demands on all aspects involved in the procedure, from the modal testing operation, data acquisition, signal processing, to more advanced treatment on the FRF data.

2) The Singular Value Decomposition (SVD) technique is found to be an effective method in improving the quality of the FRF curves, and hence the accuracy and reliability of the ABC frequencies. The implementation of the SVD technique for the purpose of ABC frequency extraction, however, requires particular attention because of the special requirement of preserving the “valley” (anti-resonance) regions.

3) The presence of multiplicative noises in the FRF data, particularly in terms of the singular value distributions, is found to be linked (at least partly) to the involvement of support vibration. This points a possible way of controlling such noises from the

root cause during an experiment. When comes to applying the SVD technique in processing the FRF data, the determination of the rank should be carefully considered, especially in cases where appreciable amount of multiplicative noises is involved, so that useful FRF information around the anti-resonance regions is not adversely affected while effectively removing the multiplicative noises in the FRF data.

4) With careful implementation of modal testing, data acquisition and signal processing procedures, it has been concluded that all one-pin and two-pin ABC frequencies from the first few modes may be extracted with good quality, and the accuracy of extracted ABC frequencies can be comparable to natural frequencies of similar orders.

B) Regarding effective selection of ABC frequencies for structural identification and FE model updating

1) By extending the expression of sensitivity of anti-resonances, the sensitivity of ABC frequencies to damage is formulated. Numerical examples demonstrate that the ABC sensitivity formulas for both one-pin and two-pin ABC frequencies match closely the actual sensitivities as calculated directly from the changes of the respective ABC frequencies corresponding to a particular damage. This paves the way for the proposal of using the mode shape contribution in the ABC frequency sensitivity as a criterion for the selection of ABC frequencies in finite element model updating.

2) Numerical studies on the above proposed selection criterion demonstrate that, with or without prior knowledge about damage positions, the ABC frequencies selected using the proposed criterion consistently give rise to better updating results. Furthermore, it is verified through numerical studies that the general rule regarding the number of modal data to be included in a FE model updating procedure, i.e., being 2-3 times of the number of unknown parameters, also applies in the case with ABC frequencies.

3) The effectiveness of using ABC frequencies with the proposed selection method for FE modelling updating is verified also using experiments with real measured ABC frequencies, using GA as the parameter search engine. Results demonstrate that with the selected ABC frequencies extracted from the test beam and properly configured GA, both the damage location and severity can be identified reliably.

4) A preliminary formulation of an ABC frequency-based damage index, using an analogy to the mode shape curvature, for a direct assessment of damage is explored. Preliminary results show certain correlation between the index and the location of damage; however, to yield conclusive identification results more rigorous formulation will be required.

C) On the frequency characterisation of railway bridges under moving trains and resonance quantification

1) A finite element model with a moving load / mass representation through contact proves to be an effective approach for a comprehensive evaluation of the frequency characteristics in bridge response under trainload.

2) Based on simplified theoretical analysis in conjunction with the numerical studies using the above FE model, it has been systematically demonstrated that the dynamic response of railway bridge is closely associated with the frequencies in the trainload excitation, especially the 'driving frequencies' in the case when single vehicle is involved, and the 'dominate frequencies' with multiple vehicles.

3) In the special case of only a single vehicle, the dynamic effect can be described using the 'driving frequency', $V/2L_b$, and a resonant condition can occur when the driving frequency matches the bridge natural frequency. This is equivalent to the classical definition of the critical speed. When significant moving mass is involved, the modified critical speed can still be established using the above resonant condition, with however an effective bridge natural frequency instead of the bare bridge frequency, using a proposed coefficient α.

4) Under typical trainload with multiple vehicles, the dynamic effect is overwhelmed by the 'dominate frequency', V / L_c. Results from examining frequency spectrum demonstrate that the distribution of the spectral peaks at nV / L_c is not uniform and it depends closely upon the bridge-to-carriage length ratio, $\alpha_L = L_b / L_c$. As α_L increases the spectral peaks become increasingly more concentrated at the lowest few dominant frequencies, and eventually dominated by the basic frequency at V / L_c when α_L is larger than 1.0;

5) A resonance indicator, the Z-factor, is developed for the determination of resonant speeds and resonance severity with involvement of vehicle mass influence. The *Z*-factor represents the rate of increase of the bridge response amplitudes as the consecutive moving loads pass over the bridge at a potential resonance speed. With the *Z*-factor, for a given bridge (effectively the ratio L_b / L_c and the natural frequency), the relative resonance severity at different orders of the dominant frequencies, which correspond to resonance speeds, can be predicted conveniently. When the carriage mass effect is involved, the *Z*-factor can still be used effectively to predict the resonance effect, provided that an appropriate effective natural frequency is employed in the establishment of the resonance speeds.

7.2 Recommendations for further research

Further research along the line of acquiring and utilizing ABC frequencies for structural damage identification and FE model updating should move towards real-life structure applications, including investigation of the accuracy and reliability of extracting ABC frequencies in more complex structural and measurement environment, and with field test validations.

The possibility of formulating ABC frequency-based damage indicator for fast damage assessment should be further studied. One possible approach would be using more rigorous formulation in order to separate the mode shape contribution in the ABC frequencies, and from there to construct sensible and unique damage indicators.

Further work on the variant dynamic system as represented by railway bridges under moving trains is recommended towards interactive FE model updating for the coupled structure-moving load & mass system using the comprehensive frequency data in the measured responses. Influences from complexity of moving loads from wheel-axle sets and the effects of the rail track irregularities should also be examined in more quantitative terms and included in the model where necessary.

8 References

Agneni, A., Crema, L.B., Masroddi, F.(2000). Damage Detection from Truncated Frequency Response Functions. European COST F3 Conference on System Identification and Structural Health Monitoring, Madrid, Spain, 137-146.

Ahmadian, H., Mottershead, J.E., Friswell, M.I. (1997). Substructure modes for damage detection. Structural damage assessment using advanced signal processing procedures. Processings of DAMAS 97, University of Sheffield, UK, 257-268.

Allemang, R.J., Brown, D.L. (1998). A unified matrix polynomial approach to modal identification. Journal of Sound and Vibration, 211(3), 301-322.

Akin, J.E. Mofid, M (1989). Numerical solution for response of beams with moving mass. Journal of structural engineering, 115, 120-131.

Ambrogio, W.D., Fregolent, A.(2000). The Use of Antiresonances for Robusta Model Updating. Journal of Sound and Vibration, 236(2), 227-243.

Avitabile, P. (2001). Experimental modal analysis – A simple non-mathematical presentation. Journal of Sound and Vibration. February, 2001.

Begg, R.D., Mackenzie, A.C., Dodds, C.J., Loland, O. (1976). Structural Integrity Monitoring using Digital Processing of Vibration Signals. Proc. 8th Annual Offshore Technology Conference, Houston, TX, 305-311.

Biggs, J.M. (1964). Introduction to structural dynamics. McGraw-Hill, New York, N.Y.

Bolotin, V.V. (1964). The dynamic stabilitya of elastic systems. Holden Day, Inc., San Francisco, California, USA.

Cadzow, J.A. (1982). Spectral estimation an overdetermined rational approach. Proceedings of the IEEE, 70(9), 907-939.

Cakar, O., Sanliturk, K.Y.(2002). Elimination of noise and transducer effects from measured response data. Proceedings of ESDA2002: 6th Biennial Conference on Engineering Systems Design and Analysis, Istanbul, Turkey.

Carcaterra, A., Ambrogio, W.D. (1995). An iterative rational fraction polynomial technique for modal identification. Meccanica, 30, 63-75.

Carrasco, C, et al. (1997). Localization and Quantification of Damage in a Space Truss Model using Modal Strain Energy. Smart Systems for Bridges, Structures and Highways, Proceedings of SPIE, 3043, 181-192.

Dehestani, M., Mofid, M., Vafai, A. (2009). Investigation of critical influential speed for moving mass problems on beams. Applied Mathematical Modelling, 33, 3885-3895.

Dinh, V.N., Kim, K.D., Warnitchai, P. (2009). Dynamic analysis of three-dimensional bridge-high speed train interactions using a wheel-rail contact model. Engineering Structures, 31(12), 3090-3106.

Doebling, S.W., Farrar, C.R., Prime, M.B., Shevitz, D.W. (1996). Damage Identification and Health Monitoring of Structural and Mechanical Systems from Changes in Their Vibration Characteristics: A Literature Review. Los Alamos National Laboratory.

Doebling, S.W., Farrar, C.R. (1997). Using statistical analysis to enhance modal-based damage identification. Structural damage assessment using advanced signal processing procedures, Proceedings of DAMAS 97, University of Sheffield, UK, 199-210.

Duggan, D.M., Wallace, E.R., Caldwell, S.R. (1980). Measured and Predicted Vibrational Behavior of Gulf of Mexico Platforms. Proc. 12th Annual Offshore Technology, 92-100.

Esmailzadeh, E., Ghorashi, M. (1995). Vibration analysis of beams traversed by uniform partially distributed moving masses. Journal of Sound and Vibration, 184(1), 9-17.

Flener, E.B., Karoumi, R. (2009). Dynamic testing of a soil-steel composite railway bridge. Engineering Structures, 31(12), 2803-2811.

Forsythe, G.E. (1957). Generation and use of orthogonal polynomials for data-fitting with a digital computer. Journal of SIAM, 74-88.

Fox, C.H.J. (1992). The location of defects in structures: A comparison of the use of natural frequency and mode shape data. Proc. Of the 10th International Modal Analysis Conference, 522-528.

Friswell, M.I., Mottershead, J.E. (1995). Finite element model updating in structural dynamics. Dordrecht, The Netherlands, Kluwer.

Fryba, L.(1972). Vibration of solids and structures under moving loads. Noordhoff International Publishing, Groningen, The Netherlands.

Fryba, L. (1987). Dynamic interaction of vehicles with tracks and roads. Vehicle System Dynamics, 16(3), 129 – 138.

Fryba, L (1999). Vibration of solids and structure under moving loads. 3rd ed, London, Tomas Telford.

Fryba, L (2001). A rough assessment of railway bridges for high speed trains. Engineering structures 23, 548-556.

Gandomi, A.H., Sahab, M.G., Rahaei, A., Safari Gorji, M.(2008). Development in Mode Shape-Based Structural Fault Identification Technique. World Applied Science Journal, 5(1), 29-38.

Garcia, G.V., Osegueda, R., Meza, D. (1998). Comparison of the damage detection results utilizing an ARMA model and FRF model to extract the modal parameters.

Smart Systems for Bridges, Structures and Highways, Proceedings of SPIE, 325(3), 244-252.

Garcia, G.V., Osegueda, R. (1999). Damage detection using ARMA model coefficients. Smart Systems for Bridges, Structures and Highways, Proceedings of SPIE, 671(3), 244-252.

Garinei, A., Risitano, G.(2008). Vibrations of railway bridges for high speed trains under moving loads varying in time. Engineering Structures, 30(3), 724-732.

Gordis, J.H.(1996). Omitted Coordinate Systems and Artificial Constraints in Spatially Incomplete Identification. Modal Analysis, 11, 83-95.

Gordis, J.H.(1999). Artificial Boundary Conditions for Model Updating and Damage Detection. Mechanical Systems and Signal Processing, 13(3), 437-448.

Gomes, H.G., Silva, N.R.S. (2008). Some comparisons for damage detection on structures using genetic algorithms and modal sensitivity method. Applied Mathematical Modelling, 32, 2216-2232.

Hanson, D., Waters, T.P., Thompson, D.J., Randall, R.B., Ford, R.A.J.(2007). The Role of Anti-resonance Frequencies from Operational Modal Analysis in Finite Element Model Updating. Mechanical Systems and Signal Processing, 21(1), 74-97.

He Jimin, Fu Zhifang (2001). Modal analysis. Butterworth-Heinemann, Oxford.

Hearn, G., Testa, R.B.(1991). Modal Analysis for Damage Detection in Structures. Journal of Structural Engineering, 117(10),3042-3063.

Inglis, C.E. (1934). A mathematical treatise on vibration in railway bridges. The University press, Cambridge, England.

Jeffcott, H.H. (1929). On the vibrations of beams under the action of moving loads. Phil. Magazine, 7,8(48), 66-97.

Jones K., Turcotte. J.(2002). Finite Element Model Updating using Antiresonant Frequencies. Journal of Sound and Vibration, 252(4): 717-727.

Ju, S.H. Lin, H.T. (2003). Resonance characteristics of high-speed trains passing simply supported bridges. Journal of sound and vibration, 267(5), 1127-1141.

Ju, S.H., Lin, H.T., Huang, J.Y (2009). Dominant frequencies of train-induced vibrations. Journal of Sound and Vibration, 319, 247-259.

Ju, S.H., Lin, H.T (2003).Numerical investigation of a steel arch bridge and interaction with high-speed trains. Engineering Structures, 25, 241-250.

Ju, S.H. Lin, H.T (2003). Resonance characteristics of high-speed trains passing simply supported bridges. Journal of sound and vibration, 267, 1127-1141.

Juang, J.N., Pappa, R.S. (1986). Effects of noise on modal parameters identified by the eigensystem realization algorithm. Journal of Guidance, Control and Dynamics, 9(3), 294-303.

Kim, J.H., Jeon, H.S., Lee, C.W. (1992). Application of the modal assurance criteria for detecting and locating structural faults. Proc. of the 10th International Modal Analysis Conference, 536-540.

Kim, B.H., Lee, J., Lee, D.H.(2010). Extracting modal parameters of high-speed railway bridge using the TDD technique. Mechanical Systems and Signal Processing, 24(3), 707-720.

Koh, B.H., Dyke, S.J. (2007). Structural health monitoring for flexible bridge structures using correlation and sensitivity of modal data. Computers and Structures 85, 117-130.

Lallement, G., Cogan, S.(1992). Reconciliation between measured and calculated dynamic behaviours. Proceedings of the 10th IMAC, 487-493.

Law, S.S., Shi, Z.Y., Zhang, L.M.(1998). Structural Damage Detection from Incomplete and Noisy Modal Test Data. Journal of Engineering Mechanics, 124(11), 1280-1287.

Leutenegger, T.(1999). Structural Testing of Fatigued Structures. Smart Structures and Integrated Systems. 3668, 987-997.

Li, S., Shelley, S.J., Brown, D.L.(1995). Perturbed Boundary Condition Testing Concepts. 13th International Modal Analysis Conference (IMAC), Nashville, Tennessee, 13-16.

Li J.Z., Su M.B. (1999). The resonant vibration for a simply supported girder bridge under high speed trains. Journal of Sound and Vibration, 224(5), 897-915.

Li, J.Z., Su, M.B., Fan, L.C.(2003). Natural Frequency of Railway Girder Bridges under Vehicle Loads. Journal of Bridge Engineering, 8(4), 199-203.

Liu, K., De Roeck, G., Lombaert, G. (2009). The Effects of Dynamic Train-Bridge Interaction on The Bridge Response During a Train Passage. Journal of Sound and Vibration, 325, 240-251.

Liu, K., Roeck, G.D., Lombaert, G. (2009). The effect of dynamic train-bridge interaction on the bridge response during a train passage. Journal of Sound and Vibration, 325(1), 240-251.

Lou, P. (2007). Finite element analysis for train-track-bridge interaction system. App Mech, 71, 707-728.

Lowan, A.N. (1935). On transverse oscillations of beams under the action of moving variable loads. Phil. Magazine, 19(127), 708-715.

Lu, Y., Mao, L., Tu, Z.G.(2008). Practical Considerations in FE Model Updating with Artificial Boundary Condition Frequencies. The 10th Int. Symposium on Structural Engineering for Young Experts, Changsha, China.

Lu, Y., Tu, Z.G.(2008). Artificial Boundary Condition Approach for Structural Identification: A Laboratory Perspective. Proc., 26th International Modal Analysis Conference, Orlando, Florida.

Maeck, J., De Roeck, G. (1999). Damage Detection on a Prestressed Concrete Bridge and RC Beams Using Dynamic System Identification. Damage Assessment of Structures, Proceedings of the International Conference on Damage Assessment of Structures, Dublin, Ireland, 320-327.

Majka, M., Hartnett, M.(2008). Effects of Speed, Load and Damping on The Dynamic Response of Railway Bridge and Vehicles. Computers and Structures, 86, 556-572.

Mao, L. and Lu, Y. (2011). Critical speed and resonance criteria of railway bridge response to moving trains. Journal of Bridge Engineering, ASCE (In Press). doi:10.1061/ (ASCE)BE.1943-5592.0000336)

Mehrjoo, M., Khaji, N. (2008) . Damage detection of truss bridge joints using artificial neural network. Expert systems with applications 35, 1122-1131.

Metrisin, J.T (2008). Guidelines for obtaining contact convergence. 2008 International ANSYS Conference. Pittsburgh, U.S.A.

Modena, C., Sonda, D., Zonta, D.(1999). Damage Localization in Reinforced Concrete Structures by using Damping Measurement. Damage Assessment of Structures, Proceedings of the International Conference on Damage Assessment of Structures, Dublin, Ireland, 132-141.

Mottershead, J.E., Friswell, M.I.(1993). Model Updating in Structural Dynamics: A Survey. Journal of Sound and Vibration, 167(2), 347-375.

Mottershead, J.E.(1998). On the Zeros of Structural Frequency Response Functions and Their Sensitivities. Mechanical Systems and Signal Processing, 12(5), 591-597.

Mroz, Z., Lekszynski, T.(2000). Identification of Damage in Structures using Parameter Dependent Modal Response. Proceedings of ISMA25, Noise and Vibration Engineering, Leuven, Belgium.

Natke, H.G, et al.(1997). Modal-Aided Diagnosis based on Symptoms. Structural Damage Assessment using Advanced Signal Processing Procedures, 363-375.

Pandey, A.K., Biswas, M, Samman, M.M. (1991). Damage Detection from Changes in Curvature Mode Shapes. Journal of Sound and Vibration, 145(2), 321-332.

Paultre, P., Proulx, J., Talbot, M. (1995). Dynamic testing procedures for highway bridges using traffic loads. Journal of Structural Engineering, 121, 362-376.

Perera, R., Ruiz, A. (2008). A multistage FE updating procedure for damage identification in large-scale structures based on multi-objective evolutionary optimization. Mechanical Systems and Signal Processing 22, 970-991.

Pickrel, C.R. (1996). Estimating the rank of measured response data using SVD and principle response functions. Proceedings of the Second International Conference on Structural Dynamics Modelling, Test Analysis and Correlation DTA/NAFEMS, 89-100.

Qiao, P.Z., Lu, K., Lestari, W.Y., Wang, J.L. (2007). Curvature Mode Shape-Based Damage Detection in Composite Laminated Plates. Composite Structures, 80: 409-428.

Rade, D.A., Lallement, G.(1998). A Strategy for the Enrichment of Experimental Data as Applied to an Inverse Eigensensitivity-based FE Model Updating Method. Proceedings of the 12th IMAC, 127-132

Rahimzadeh, R.F., Ali, N (2008). Dynamic behaviour and modal control of Euler-Bernoulli Beams under moving mass. Journal of Applied Mathematics, 1(1), 293-304.

Ratcliffe, C.P.(1997). Damage Detection using a Modified Laplacian Operator on Mode Shape Data. Journal of Sound and Vibration, 204(3), 505-517.

Reynolds, P., Pavic, A. (2008). Quality assurance procedures for the modal testing of building floor structures. Experimental Techniques, 24(4): 36-41.

Richardson, M.H. (1999). Structural dynamics measurements. SD2000.

Richardson, M.H., Formenti, D.L. (1982). Parameter estimation from frequency response measurements using rational fraction polynomials. Proc. of the 1st International Modal Analysis Conference, 167-186.

Ruotolo, R., Surace, C.(1997). Damage Assessment of Multiple Cracked Beams: Results and Experimental Validation. Journal of Sound and Vibration, 206, 567-588.

Sanliturk, K.Y., Cakar, O. (2005). Noise elimination from measured frequency response functions. Mechanical Systems and Signal Processing, 19, 615-631.

Schubert, S., Gsell, D., Steiger, R, Feltrin, G. (2010). Influence of asphalt pavement on damping ratio and resonance frequencies of timber bridges. Engineering Structures, 32(10), 3122-3129.

Shi, Z.Y., Law, S.S.(1998). Structural Damage Localization from Modal Strain Energy Change. Journal of Sound and Vibration, 218(5), 825-844.

Shi, Z.Y., Law, S.S., Zhang, L.M.(2000). Structural Damage Detection from Modal Strain Energy Change. Journal of Engineering Mechanics, 126(12), 1216-1223.

Sohn, H., Farrar, C.R., Hemez, F.M., Shunk, D.D., Stinemates, D.W., Nadler, B.R., Czarnecki, J.J (2004). A Review of Structural Health Monitoring Literature: 1996-2001. Los Alamos National Laboratory.

Srinivasan, M.G., Kot, C.A. (1992). Effects of damage on the modal parameters of a cylindrical Shell. Proc. Of the 10th Modal Analysis Conference, 529-535.

Stokes, G.G.(1849). Discussion of a differential equation relating to the breaking of railway bridges. Trans, Cambridge Phil. Soc., 8(5), 707-735.

Stubbs, N., Broome, T.H., Osegueda, R. (1990). Monitoring and Evaluating Civil Structures using Measured Vibration. Proc. 14th International Modal Analysis Conference, 84-90.

Stubbs, N., Osegueda, R. (1990). Global Damage Detection in Solids-Experimental Verification. The International Journal of Analytical and Experimental Modal Analysis, 5(2), 81-97.

Stubbs, N., Sikorsky, C., Park, S.C., Bolton, R. (1999). Verification of a Methodology to Non-destructively Evaluate the Structural Properties of Bridges. Structural Health Monitoring 2000, Stanford University, Palo Alto, California, 440-449.

Taghi, M., Baghmisheh, V.(2008). Crack detection in beam-like structures using genetic algorithms. Applied soft computing 8,1150-1160.

Timoshenko, S.P. (1922). On the forced vibrations of bridges. Phil. Magazine, 6(43), 1018-1019.

Timoshenko, S.P., Young, D.H. (1955). Vibration problems in Engineering, 3rd Edition, D.Van Nostrand, New York, N.Y.

Tu, Z.G., Lu, Y.(2008). FE Model Updating using Artificial Boundary Conditions with Genetic algorithms. Computers and Structures, 86(7-8), 714-727.

Tufts, D.W., Kumerasan, R. (1982). Singular value decomposition and improved frequency estimation using linear prediction. IEEE Transactions on Acoustics, Speech and Signal Processing, 30(4), 671-675.

Tufts, D.W., Kumerasan, R., Kirsteins, I. (1982). Data adaptive signal estimation by singular value decomposition of a data matrix. Proceedings of the IEEE, 70(6), 684-685.

Vandiver, J.K. (1975). Detection of Structural Failure on Fixed Platforms by Measurement of Dynamic Response. Journal of Petroleum Technology, 305-310.

Wang, M.L., Satpathi, D., Heo, G.(1997). Damage Detection of a Model Bridge using Modal Testing. Structural Health Monitoring, Current Status and Perspectives, Stanford University, Palo Alto, California, 589-600.

West, W.M.(1984). Illustration of the use of Modal Assurance Criterion to detect Structural Changes in an Orbiter Test Specimen. Proc. Air Force Conference on Aircraft Structural Integrity, 1-6.

Willis, R.(1849). Appendix to the report of the commissioners appointed to inquire into the application of iron to bridge structures. H.M. Stationary office, London, England.

Worden, K., Fieller, N.R.J. (1999). Damage detection using outlier analysis. Journal of Sound and Vibration, 229(3), 647-667.

Wu Y.S, Yang Y.B (2003). Steady-state response and riding comfort of trains moving over a series of simply supported bridges. Engineering Structures, 25, 251-265.

Xia, H. Zhang, N. Guo, W.W (2006). Analysis of resonance mechanism and conditions of train-bridge system. Journal of sound and vibration, 297, 810-822.

Yan, Y.J., Cheng, L., Wu, Z.Y., Yam, L.H.(2007). Development in Vibration-based Structural Damage Detection Technique. Mechanical Systems and Signal Processing, 21, 2198-2211.

Yang, Y.B, Lin, C.W (2004). Vehicle-bridge interaction dynamics and potential applications. Journal of Sound and Vibration, 284, 205-226.

Yang, Y.B. Chang, K.C (2009). Extracting the bridge frequencies indirectly from a passing vehicle: parametric study. Engineering Structures, 31, 2448-2459.

Yang, Y.B. Yau, J.D. Wu, Y.S (2004). Vehicle-bridge interaction dynamics. World Scientific Publishing Co.Pte.Ltd.

Yau Jong Dar (2001). Resonance of continuous bridges due to high speed trains. Journal of Marine Science and Technology, 9(1), 14-20.

Yuen, M.M.F. (1985). A numerical study of the eigenparameters of a damaged cantiléver. Journal of Sound and Vibration, 103, 301-310.

Zhai, W, Cai, Z. (1997). Dynamic interaction between a lumped mass vehicle and a discretely supported continuous rail track. Computers and Structures, 63(5), 987-997

Zak, A., Krawczuk, M., Ostachowicz, W. (1999). Vibration of a Laminated Composite Plate with Closing Delamination. Structural Damage Assessment using Advanced Signal Processing Procedures. Proceedings of DAMAS, University College, Dublin, Ireland, 17-26.

9 Appendix

List of Publications:

Mao, L., Lu, Y. Experimental extraction of artificial boundary condition frequencies for structural identification. (to be submitted).

Mao, L., Lu, Y. (2012). Critical speed and resonance criteria of railway bridge response to moving trains. Journal of Bridge Engineering, ASCE (In Press). doi:10.1061/ (ASCE)BE.1943-5592.0000336).

Lu, Y., Mao, L., Woodward, P. (2012). Frequency characteristics of railway bridge response to moving trains with consideration of train mass. Journal of Engineering Structures. (Accepted).

Currie, D. Petrie, N., Mao, L., Lu Y. (2012) A Benchmark study of dynamic damage identification of plates. Engineering and Computational Mechanics - ICE Proceedings Journals (In Press).

Mao. L, Lu, Y. (2011) Extraction of artificial boundary frequencies for damage identification. 9th International Conference on Damage Assessment of Structures (DAMAS2011), 11–13 July 2011, St Anne's College, University of Oxford, UK.

Mao. L., Lu, Y., and Woodward, P. (2011) Resonance of railway bridge under moving trainload considering the effect of vehicle mass. Railway Engineering 2011, 29th - 30th June 2011, London, UK.

Mao, L., Woodward, P., Lu, Y. (2011) Structural fault detection using artificial boundary frequencies - some recent progress. Structural Faults and Repair 2011, 15-17 June 2011, Edinburgh, UK.

Lu, Y., Mao, L., Woodward, P.(2010) Identification of dynamic characteristics of railway bridge response to moving trainload. The 11th International Symposium on Structural Engineering (ISSE-11), 20-22 Dec 2010, Guangzhou, China.

Mao, L., Woodward, P., Lu, Y. (2009) Dynamic behaviour of railway bridges - a perspective from field dynamic measurements. Proc., Railway Engineering 2009, London.

Lu, Y., Mao, L., Tu, Z.G. (2008) Practical considerations in FE model updating with artificial boundary condition frequencies. The Tenth Intl. Symposium on Structural Engineering for Young Experts, Changsha, China, 19-21 October 2008.